Scuola Internazionale Superiore di Studi Avanzati

PhD course in Theory and Numerical Simulation of Condensed Matter

Lattice dynamics with Fully Relativistic Pseudopotentials for magnetic systems, with selected applications

Candidate
Andrea Urru

Supervisor
Prof. Andrea Dal Corso

A thesis submitted for the degree of *PhilosophiæDoctor*

Trieste, November 2020

"If you expect science to give all the answers to the wonderful questions about what we are, where we're going, what the meaning of the universe is... you could easily become disillusioned and look for a mystic answer... We're exploring, trying to find out as much as we can about the world. People ask: 'Are you looking for the ultimate physics laws?' No, I'm not. I'm just looking to find out more about the world. If it turns out there is an ultimate law which explains everything, so be it; that would be very nice to discover. If it turns out it's like an onion, with millions of layers... then that's the way it is. But whatever way it comes out, it's nature, and she's going to come out the way she is! Therefore we shouldn't pre-decide what it is we're going to find, except to try to find out more. If you think that you are going to get an answer to some deep philosophical question, you may be wrong - it may be that you can't get an answer to that particular problem by finding out more about the character of nature. But I don't look at it like that; my interest in science is to find out more about the world, and the more I find out, the better."

Richard P. Feynman

Foreword

The following manuscript reports the Thesis submitted for the degree of *Philosophiæ Doctor* and it is based on the research activity carried out during four years of PhD at the International School for Advanced Studies (SISSA) in Trieste, under the supervision of Prof. Andrea Dal Corso.

The Thesis is conceived to be read at two levels: at a first level, corresponding to Chapters 1-4, we provide the reader with an appropriate background, and we report the main outcomes of the research work, based on the papers published, listed in the List of Publications. At a second, more complete level, corresponding to the additional part reported in Appendices A-I, we give both some pedagogical introductions on particular topics (e.g. the antilinear operators and the action of symmetry operators on scalar and spinor wave functions), as well as additional proofs and derivations of some particularly important equations presented in the Chapters. In this way, our aim is to provide the reader with a work that is as self-contained as possible.

Trieste, 30^{th} October 2020

Andrea Urru

Acknowledgments

All good things come to an end. I am convinced this short sentence encloses in a dense way my feelings now that my PhD journey is reaching a conclusion. In few days I will leave Trieste, a piece of my life, and a piece of my heart too, I must admit. It will not be easy.

I spent four wonderful years in Trieste, and I will certainly keep in my happiest memories all the moments I lived here. There are many people I shared my time with, and I would like to dedicate a few lines to thank them.

On the scientific side, my biggest and most heartfelt thanks goes to my supervisor, Prof. Andrea Dal Corso. I owe Andrea much, and I am very grateful to him, because he introduced me to the topics of my PhD with care, passion, and sharing his scientific knowledge with me in depth. Moreover, I thank him for his careful supervision of my work, for being always present to discuss, and for the patience and the accuracy in proofreading this Thesis, as well as the papers we published.
Thanks to Prof. Stefano Baroni, for his suggestions and for having involved me in the Quantum `ESPRESSO` team, giving me the chance to include my work in the main Quantum `ESPRESSO` package, and to be part of the teaching staff at the Summer School in Lubiana in 2019. I would like to thank also Prof. Paolo Giannozzi and Pietro Delugas for useful discussions and help.
Thanks to Prof. Stefano de Gironcoli for being always available to discuss and for letting me build and improve my teaching experience by including me in the teaching staff of the PhD course on problem solving in solid state physics.
Thanks to all the staff of the Condensed Matter sector, for everything I had the possibility to learn from them in the PhD courses and in all the activities proposed, journal clubs, internal workshops, group meetings.
Finally, I would like to thank also Prof. Vincenzo Fiorentini, my previous advisor during my bachelor and master degrees studies, with whom I kept on sharing my passion for physics during these years.

Life in SISSA would have not been the same without my colleagues, Claudio, Giulia, Karla, Lorenzo C., Matteo F., Matteo W., Silvia, and Yusuf, with whom I spent most of my time. You, guys, inspired me a lot, I am very grateful to you. I think by keeping in touch so closely we motivated and pushed each other to raise the bar to the best of our possibilities. I feel blessed to have met you. To share a part of my life with you has been a great pleasure to me, and now that this journey has come to an end I feel very sad, lost, and quite confused too. I will keep in my happiest and deepest memories the moments we lived together, and I look forward to meet you again, hopefully sometime soon!

Thanks to all my colleagues of the Condensed Matter sector, for contributing to make the scientific and social life in SISSA so enjoyable: among them, I would like to acknowledge in particular Matteo S., Lorenzo G., Davide, Cristiano, and Mattia.

A special thanks goes to my officemates, Matteo F., Lorenzo C., and Yusuf, for the nice time we spent together in our room 401 and for your motivation in doing science, which I have the utmost admiration for and I got inspired by. Matteo, I know we both are gonna miss each other, we are going to miss our *"Andreeeea"* and *"Maréé́é!"*, our jokes and our laughs. It has been so hard to say you goodbye, and I am going to miss you so much, I hope to meet you again very soon.

Life in Trieste has been remarkably embellished by my flatmates, who happened to be among my dearest fellows of the PhD course, Claudio and Matteo W. . Claudio, your friendship has supported me so much, especially during the first months in Trieste, when everything was new for both of us: with you I always felt at home, as though we were part of the same family, I am very grateful to you for the time we spent together. We shared many moments together, but I think the most peculiar aspect of our friendship is how I got inspired from you in developing an increasing interest in cooking: you know I was not a great fan of cooking, to say the least, but nevertheless you were able to transfer a part of your genuine passion for cooking to me, I will be always grateful for it.
Matteo, you are one of the people with whom I shared the widest variety of moments: from ping pong, our very first common passion, to physics, to games of course. Thank you very much for being such a nice mate, and for the even stronger connection we developed during the lockdown, living in close contact for much time, helping each other to keep calm and somehow relaxed although the rest of the situation was far from being ideal or easy to cope with. I will remember for a very long time the evenings during the lockdown, spent playing together at *DBZ Budokai Tenkaichi 2*, and for the many many matches with *Pokémon cards* we played during summer.
I acknowledge also Matteo S. and Angela, whom I lived with for a short period of time while changing house: thank you for your kindness and care when we shared the same apartment, for your friendship, and the sushi-based lunchs of course!

A substantial part of my time in Trieste has been spent practicing the sport I love the most, table tennis. I enjoyed this sport in its full beauty thanks to a fellow at SISSA, Sabine, who inspired me to start practicing. Sabine, one of my most heartfelt thanks goes to you: the inspiration I got from you changed significantly the way I approached life here. Starting from not being even able to handle a racket properly, it has been a pleasure to benefit of your suggestions to improve my game and to have had the chance to face you several times. I will especially remember for long time our last "official" match, that final at the SISSA Games, particularly that last return of serve I pushed directly to the net, which meant the temporary end of our "rivalry". I look forward to meet you again in the future and, hopefully, we will be able to play again.

Thanks to Lorenzo G., a fellow of the PhD course and, especially, a dear friend of mine. Table tennis, our common passion, let us get in touch, but soon we discovered to share many more passions and interests. Lorenzo, thank you for the deep friendship, the long chats we have had, the passions we shared, and that slice of summer we spent at my place, we have

had a great time there. Thank you also for teaching me with so much patience and care the technique of the strokes in table tennis, letting me raise my level.

Thanks to all the people I met in the Trieste-Sistiana table tennis team, for helping me developing and improving my game and for all the nice time we spent together, both at the gym and around in Friuli-Venezia Giulia playing local tournaments and championship matches.

Thanks to all the Directive Boards of the SISSA Club, a nonprofit cultural and sport organization, which I had the pleasure to be part of for a long time during these years.

Thanks to all my long-time friends Marco, Gabriella, Alessio, Michele, Cristiano, and Salvatore, for being always present in my life. I would like to acknowledge also Roberto, with whom I had the pleasure to spend two full F1 GP weekends in Monza 2017 and Spa 2019: thank you for the very exciting adventures we lived during those two weekends, I am sure we will remember them for a long time, and I look forward to repeat this experience soon.

My last thanks goes to my mother and to my sister, who always supported me and stood by me unconditionally, and to my father, whose memory and spiritual presence has always guided me wisely, especially in the toughest moments.

List of publications

The main outcomes of the work presented in this Thesis have been published in the following papers in international peer-reviewed journals:

- A. Urru and A. Dal Corso,
  Clean Os(0001) electronic surface states: A first-principle fully relativistic investigation,
  Surf. Science **671**, 17-26 (2018).

- A. Urru and A. Dal Corso,
  Spin-polarized electronic surface states of Re(0001): An ab-initio investigation,
  Surf. Science **686**, 22-29 (2019).

- A. Urru and A. Dal Corso,
  Density functional perturbation theory for lattice dynamics with fully relativistic ultrasoft pseudopotentials: The magnetic case,
  Phys. Rev. B **100**, 045115 (2019).

- P. Giannozzi, O. Baseggio, P. Bonfà, R. Car, I. Carnimeo, C. Cavazzoni, S. de Gironcoli, P. Delugas, F. Ferrari Ruffino, A. Ferretti, T. Gorni, N. Marzari, I. Timrov, A. Urru, and S. Baroni,
  `Quantum ESPRESSO` *toward the exascale*,
  J. Chem. Phys. **152**, 154105 (2020).

- A. Urru and A. Dal Corso,
  Lattice dynamics effects on the magnetocrystalline anisotropy energy: application to MnBi,
  Phys. Rev. B **102**, 115126 (2020).

Other publications by the same author are listed below:

- F. Belviso, V. E. P. Claerbout, A. Comas-Vives, N. S. Dalal, F. Fan, A. Filippetti, V. Fiorentini, L. Foppa, C. Franchini, B. Geisler, L. M. Ghiringhelli, A. Groß, S. Hu, J. Íñiguez, S. K. Kauwe, J. L. Musfeldt, P. Nicolini, R. Pentcheva, T. Polcar, W. Ren, Fa. Ricci, Fr. Ricci, H. S. Sen, J. M. Skelton, T. D. Sparks, A. Stroppa, A. Urru, M. Vandichel, P. Vavassori, H. Wu, K. Yang, H. J. Zhao, D. Puggioni, R. Cortese, and A. Cammarata,
  Viewpoint: Atomic-Scale Design Protocols toward Energy,Electronic, Catalysis, and Sensing Applications,
  Inorg. Chem. 2019, **58**, 22, 14939-14980 (2019).

- A. Urru, F. Ricci, A. Filippetti, J. Íñiguez, and V. Fiorentini,
  A three-order-parameter, bistable, magnetoelectric multiferroic metal,
  Nat. Commun. **11**, 4922 (2020).

Contents

Introduction

Quantum Mechanics and *Special Relativity* are two of the basic theories of modern physics. The relevance of Quantum Mechanics in condensed matter physics and in chemistry has been evident since its foundation, the first achievements being the explanation of the electronic structure of atoms and molecules. Originally, many properties addressed in chemistry and in condensed matter physics have been accurately studied at the non-relativistic level. However, relativistic effects become increasingly important as the speed v of a particle (or the average speed, if we consider a quantum particle) approaches the speed of light, c. In atomic systems, the ratio v/c ($c = 1/\alpha \approx 137$ in atomic units, α being the fine structure constant) becomes rapidly non-negligible for the electrons in the inner shells of heavy elements, which results in visible effects also for the valence electrons. In the Bohr model, in a hydrogen-like atom with nuclear charge Z, the $1s$ electron has a speed Z (in atomic units), therefore the ratio $v/c \approx Z/\alpha$ increases with the atomic number: as a consequence, relativistic effects can be considered small only for elements up to the first row of transition metals [1].

Two of the most outstanding predictions of the relativistic theory, the spin and the *spin-orbit coupling* (SOC), have paved the way for important research fields, such as *spintronics* [2,3] and *spin-orbitronics* [4], which promise important scientific progress. Among the most remarkable discoveries, that have had a relevant impact for technological applications, we mention the Rashba effect [5], the spin-Hall effects [6–8], the spin-orbit torque effect [4], magnetic skyrmions [9], and topological insulators [10–12]. From a more general point of view, SOC is responsible for the coupling between the lattice and the magnetic structure, and may lead to magnetocrystalline anisotropy, which is responsible for the existence of a easy axis for magnetic moments in magnetically ordered systems. Magnetocrystalline anisotropy can give rise to interesting phenomena, such as the spin-reorientation transition [13].

Since the formulation of Dirac equation in 1928 [14], several attempts have been made to account for relativistic effects in realistic systems. In 1928, Darwin and Gordon proposed a solution of the Dirac equation for one-electron atoms [15, 16]. In many-electron atoms, relativistic effects were initially included using *perturbation theory*, a widely used approach that later had been refined into the *quasi-relativistic method* [17], which consisted in including the mass-velocity and Darwin corrections in a non-relativistic Hamiltonian during the self-consistent steps, whereas the spin-orbit term was added at the end as a first-order perturbation. Further approaches, devoted to capture the exchange and correlation effects, include the Dirac-Hartree [18], the Dirac-Slater [19–21], and the Dirac-Fock [22–24] methods. For a more detailed explanation of the methods mentioned above and for a more extensive bibliography, we refer the interested reader to Ref. [25].

Alongside to the progress on relativistic *ab initio* methods for atomic and molecular systems, similar techniques were developed for extended systems. At the beginning, the relativistic corrections were computed using perturbation theory [26–28]. Few years later, extensions of the most well known methods, such as the orthogonalized plane-wave [29], the augmented plane-wave [30], the Korringa-Kohn-Rostocker [31, 32], the pseudo-plane wave [33], and the *Density Functional Theory* (DFT) methods, to the relativistic regime were presented. Few years after the original formulation of DFT by P. Hohenberg, W. Kohn, and L. J. Sham [34,35], a relativistic extension, which allowed to deal also with magnetic systems, was proposed and resulted in single-particle Dirac-like self-consistent equations [36]. A very efficient method to include relativistic effects in DFT calculations is the *pseudopotentials* (PPs) technique, where PPs are constructed by solving relativistic DFT equations for atoms. Essentially, all modern PPs adopt a *scalar relativistic* (SR) approach, which is based on a j-average of the solutions of the Dirac equation and introduces a simplification in that it requires only one radial wave function for each orbital angular momentum l, but neglects spin-orbit coupling. The *fully relativistic* (FR) PP approach [37–40], instead provides two different radial wave functions for each $l > 0$ (obtained for $j = l + 1/2$ and $j = l - 1/2$, respectively), and includes spin-orbit splitting effects. Remarkably, in the FR scheme, relativistic effects are encoded in the PPs, which are then used in a scheme of non-collinear non-relativistic Kohn-Sham equations, based on two-component spinor wave functions, an approach that was shown to give the same electronic structure, to order α^2, as an all-electron FR four-component Dirac-like equation [37, 40].

In solid state physics, the equilibrium properties of materials are usually related to the response of the system to an external perturbation. From the microscopic point of view, and within DFT, the responses of the electronic charge density and of the free energy of the system, induced by a given external perturbation, allow to predict the macroscopic response of the material. In the case of small perturbations, meaning that the induced variation of the free energy is small compared to the free energy itself, it is reasonable to assume that we are in the so-called *linear response* regime, where the density response varies linearly with the perturbation. In this approach, the free energy is expanded up to the second order in the perturbation: in particular, we are interested in the second-order derivatives of the free energy, also called *susceptibilities*, which can be linked to the macroscopic material properties. Some well known examples are, e.g., the electric and the magnetic susceptibilities which correspond to the second-order derivatives with respect to the electric and magnetic field, respectively. In the Born-Oppenheimer approximation, the free energy at equilibrium is replaced by the total energy of the electrons, $E_{\rm tot}$, therefore we are interested in the second-order derivatives of the electronic total energy. Different approaches based on the calculation of $E_{\rm tot}$ by first-principles techniques have been developed to cope with external perturbations in periodic systems. One of the first to be used has been the so-called *direct method* [41], which handles the perturbed system on the same footage as the unperturbed one: the response is obtained from a direct comparison of the two systems. The main drawback of such approach is its high computational cost to deal with long-wavelength perturbations, for which the simulation of large supercells is needed. In 1987 a new scheme, based on perturbation theory, was proposed to study the linear response of crystals [42]. The method combines the linear response approach with the computational techniques typical of

DFT: the response of the system is addressed with perturbation theory and is computed by iterating the calculation, based on a solid-state rephrasing of the Sternheimer equation for atomic polarizabilities, up to self-consistency. The approch, known as Density Functional Perturbation Theory (DFPT) [43], allows to overcome the main limitations of the previously developed techniques: remarkably, the calculation of the linear response does not require the use of any supercell. DFPT has been conceived for a generic perturbation: in its current implementation, it has been applied, e.g., both to static perturbations, such as the lattice dynamics for ionic displacements [42–49], and homogeneous electric fields [43], as well as to time-dependent perturbations (using the Liouville-Lanczos approach), applied to the study of the electron energy loss spectroscopy [50] and the spin fluctuations [51, 52]. With particular emphasis on its implementation for lattice dynamics, we mention that after its first formulation for the plane waves norm-conserving PPs scheme [42, 44], generalized to deal with metallic systems as well [45], DFPT has been extended to the ultrasoft (US) [46, 47] and, more recently, to the Projector Augmented-Wave [48] schemes. Later, in Ref. [49] it was shown that spin-orbit effects could be included in DFPT for lattice dynamics by using the FR PPs approach, already successfully implemented for the DFT ground state calculations.

The work presented in this Thesis is based on the FR PPs technique, as implemented in the Density Functional Theory (DFT) scheme [34, 35]. We start by providing a methodological background on the main theoretical aspects of DFT in Chapter 1, with particular attention to relativistic effects in condensed matter and to the PPs theory, and we explain how relativistic effects are addressed in the SR and FR PPs schemes.

A first part of the project has been devoted to study two surfaces where the SOC has a relevant effect on the electronic structure and can result in Rashba split surface states. Following the literature of the past decades, where several surfaces of $5d$ metals, such as Au, Ir, and Pt, have been studied, showing the presence of Rashba split states, we have studied the electronic structure of clean Os(0001) and Re(0001) surfaces, focusing our attention on the characterization of surface states and resonances and on the calculation of their spin polarization. The main outcomes of this part of the project are presented and discussed in Chapter 2.

The second part of the project has been oriented towards a methodological development in the FR DFPT for lattice dynamics. Since its first formulation, DFPT has been always conceived by assuming time-reversal invariance, which turns out to be helpful in the computational implementation of the theory. Such assumption yields physically correct results for time-reversal-invariant, i.e. non-magnetic, systems. Remarkably, also the lattice dynamics of magnetic systems, if described within the local spin density approximation (LSDA), can be studied with this assumption, because the LSDA Hamiltonian, being real, is time-reversal invariant (a net magnetization is obtained by allowing the two spin-polarized (spin-up and spin-down) channels, to have a different number of electrons). Yet, in the non-collinear formulation, the Hamiltonian is not time-reversal invariant in presence of magnetization, therefore the DFPT formulated by assuming time-reversal invariance works only at zero magnetization. The aim of the project has been to extend the formulation of non-collinear DFPT to cover the case of time-reversal symmetry breaking, and, in particular, we followed the recent developments of DFPT for the calculation of magnons [52]. Notably, we consider the general case of metallic systems: in Chapter 3 we present the more general formulation

with US PPs presented in 2007 in Ref. [49], we provide the explicit formulation for the magnetic case as well, and moreover we extend the symmetrization of the induced densities and the dynamical matrix to include also the symmetry operations that require the time-reversal operation. The new formulation has been implemented and tested. The tests were based on a comparison between the phonon frequencies computed with the new method and those computed with the frozen phonon (direct) method. The systems studied at this stage are fcc Ni and a monatomic ferromagnetic Pt nanowire, simulated in the idealized form of an infinite chain [53]. In addition to the purely quantitative shifts of the phonon frequencies, the possible lowering of symmetry due to the magnetic order may lift the degeneracy of the phonon modes along some high-symmetry lines and high-symmetry points in the BZ: fcc Ni and the Pt nanowire are well suited systems in this respect, being both ferromagnetic and having both simple enough structures that let the effects to be immediately understandable. Moreover, magnetocrystalline anisotropy can influence the phonon frequencies, which as a result may depend on the orientation of the magnetization of the system.

As a further step, the new formulation has been applied to a more realistic system, MnBi. The choice of this compound has been motivated by the sizable magnetocrystalline anisotropy, due to the simultaneous presence of a strong magnetism carried by Mn, and the large SOC brought by Bi, reported by experiments. MnBi is even more interesting because it undergoes a spin-reorientation transition at $T \approx 90$ K, due to a change of the sign of the magnetocrystalline anisotropy constant, a fact that has been reported since the first experimental studies on this compound. In Chapter 4 we study the lattice dynamics of MnBi and we compute the contribution to the magnetocrystalline anisotropy energy of the vibrational free energy difference, obtained with the harmonic approximation from the phonon dispersions corresponding to two phases with different orientation of the magnetization.

Chapter 1

Theoretical and methodological background

The theoretical description of a condensed matter system, made of N electrons and M nuclei, has its natural starting point in the many-body *Schrödinger equation*. The presence of both nuclei and electrons, and the correlation effects between electrons, force us to deal with the *many-body wave function*, which becomes rapidly numerically untractable as N and M increase. As a consequence, several approximations have to be introduced to solve the quantum-mechanical problem. One of them is the *Born-Oppenheimer* approximation, which separates the nuclear and electronic degrees of freedom. A complete description of such an approximation is beyond the scope of this work, hence we will revise here only its fundamental aspects. Once the nuclear and electronic degrees of freedom have been decoupled, the electronic problem has to be solved. Correlation effects prevent the possibility to further separate the electronic degrees of freedom, leaving a many-body problem whose complexity grows with increasing number of electrons. To make the electronic problem solvable from a computational point of view is the aim of *ab initio methods*, such as *Density Functional Theory* (DFT), whose basic features will be briefly discussed below.

In this chapter we start mentioning the Born-Oppenheimer approximation, then we will present the fundamental aspects of DFT (in the collinear and non-collinear formalism) and we will discuss also the solution of the *Kohn-Sham equations* via plane waves. Finally we will focus on the description of relativistic effects, such as the spin-orbit coupling, showing how they can be included in the DFT framework via the pseudopotential theory. In particular, we will focus on the *fully relativistic ultrasoft pseudopotentials*.

1.1 The Born-Oppenheimer approximation

A quantum-mechanical system made up of M nuclei and N electrons can be described by the Schrödinger equation:

$$[T_{\rm I} + T_{\rm e} + V_{\rm Ie} + V_{\rm ee} + V_{\rm II}]\,\Phi(\mathbf{R}_1,\ldots,\mathbf{R}_M,\mathbf{r}_1,\ldots,\mathbf{r}_N) = E\,\Phi(\mathbf{R}_1,\ldots,\mathbf{R}_M,\mathbf{r}_1,\ldots,\mathbf{r}_N), \quad (1.1)$$

where $T_{\rm I}$ ($T_{\rm e}$) is the ionic (electronic) kinetic energy, whereas $V_{\rm ee}$, $V_{\rm Ie}$, and $V_{\rm Ie}$ are the electron-electron, ion-electron, and ion-ion interaction energy operators, and read:

$$V_{\rm ee} = \frac{1}{2}\sum_{\substack{i,j=1\\ i\neq j}}^{N}\frac{1}{|\mathbf{r}_i-\mathbf{r}_j|}, \quad (1.2)$$

$$V_{\rm Ie} = -\sum_{I=1}^{M}\sum_{i=1}^{N}\frac{Z_I}{|\mathbf{R}_I-\mathbf{r}_i|}, \quad (1.3)$$

$$V_{\rm II} = \frac{1}{2}\sum_{\substack{I,J=1\\ I\neq J}}^{M}\frac{Z_I\,Z_J}{|\mathbf{R}_I-\mathbf{R}_J|}. \quad (1.4)$$

$\Phi(\mathbf{R}_1,\ldots,\mathbf{R}_M,\mathbf{r}_1,\ldots,\mathbf{r}_N)$ in Eq. (1.1) is the many-body wave function, where $\mathbf{R}_I$, $I = 1,\ldots,M$ ($\mathbf{r}_i$, $i = 1,\ldots,N$) are the ionic (electronic) spatial coordinates. In order to simplify the problem, the solution may be written using the variables separation technique:

$$\Phi(\mathbf{R}_1,\ldots,\mathbf{R}_M,\mathbf{r}_1,\ldots,\mathbf{r}_N) = \sum_j F_j(\mathbf{R}_1,\ldots,\mathbf{R}_M)\,\Psi_j(\mathbf{R}_1,\ldots,\mathbf{R}_M,\mathbf{r}_1,\ldots,\mathbf{r}_N), \quad (1.5)$$

where $\{\Psi_j\}$ is a complete basis set. The expansion given by Eq. (1.5) can lead to a complete separation of the nuclear and electronic degrees of freedom in the extreme approximation of fixed nuclei. A different approximation, which preserves the complete separation of variables, is the *Born-Oppenheimer* (BO) approximation. The nuclei are not considered fixed, but being much more massive than electrons, they are slower, so one can neglect the gradient of the electronic wave function with respect to the nuclear coordinates ($\nabla_{\mathbf{R}_i}\Psi_j$). As a consequence, the problem can be completely separated into two equations, one for the nuclear wave function $F_j(\mathbf{R}_1,\ldots,\mathbf{R}_M)$, the other for the electronic wave function $\Psi_j(\{\mathbf{R}_1,\ldots,\mathbf{R}_M\},\mathbf{r}_1,\ldots,\mathbf{r}_N)$, which depends parametrically on the nuclear coordinates, while the electronic total energy represents the potential energy surface for the nuclei.

1.2 The electronic problem

Following the BO approximation we can write the electronic problem in the following way:

$$H\left[\{\mathbf{R}\}\right]\Psi\left(\{\mathbf{R}\},\mathbf{r}_1,\mathbf{r}_2,\ldots,\mathbf{r}_N\right) = E\,\Psi\left(\{\mathbf{R}\},\mathbf{r}_1,\mathbf{r}_2,\ldots,\mathbf{r}_N\right), \quad (1.6)$$

where $\Psi\left(\{\mathbf{R}\},\mathbf{r}_1,\mathbf{r}_2,\ldots,\mathbf{r}_N\right)$ is the many-body wave function. The Hamiltonian $H\left[\{\mathbf{R}\}\right]$, where the nuclear coordinates $\{\mathbf{R}\}$ enter as simple parameters, reads as (we use Hartree

atomic units):

$$H\left[\{\mathbf{R}\}\right] = \sum_{i=1}^{N} -\frac{1}{2}\nabla_i^2 + \frac{1}{2}\sum_{\substack{i,j=1 \\ i\neq j}}^{N} \frac{1}{|\mathbf{r}_i - \mathbf{r}_j|} - \sum_{I=1}^{M}\sum_{i=1}^{N} \frac{Z_I}{|\mathbf{R}_I - \mathbf{r}_i|} + \frac{1}{2}\sum_{\substack{I,J=1 \\ I\neq J}}^{M} \frac{Z_I\, Z_J}{|\mathbf{R}_I - \mathbf{R}_J|}, \tag{1.7}$$

where Z_I is the charge of the I-th nucleus. The ion-ion interaction energy does not depend on the electronic coordinates: its contribution to the total electronic energy is a constant (once $\{\mathbf{R}\}$ are given), hence it can be added to the total energy after the solution of the electronic problem.

From the many-body wave function a physical quantity of interest, the electronic density, can be computed:

$$n(\mathbf{r}) = N \int d^3r_2 \ldots \int d^3r_N \, |\Psi\left(\{\mathbf{R}\}, \mathbf{r}, \mathbf{r}_2, \ldots, \mathbf{r}_N\right)|^2. \tag{1.8}$$

$n(\mathbf{r})$ plays a central role in the simplification of the many-body problem carried out by theoretical approaches such as the DFT, briefly described below.

1.2.1 The total energy functional

Let us consider a set of N interacting electrons, described by the Hamiltonian (1.7). We write $H\left[\{\mathbf{R}\}\right]$ in the following compact form:

$$H = T + U + v_{\text{ext}}, \tag{1.9}$$

where T, U, and v_{ext} are the kinetic energy, electron-electron interaction energy, and external potential energy operators, respectively. In particular, the latter corresponds to the electron-ion interaction energy (third term of Eq. (1.7)) and we can write:

$$v_{\text{ext}}(\mathbf{r}) = \sum_{i=1}^{N} V_{\text{ext}}(\mathbf{r}_i), \tag{1.10}$$

where

$$V_{\text{ext}}(\mathbf{r}_i) = -\sum_{I=1}^{M} \frac{Z_I}{|\mathbf{R}_I - \mathbf{r}_i|}. \tag{1.11}$$

The total energy can be calculated as the expectation value of the Hamiltonian on the ground state $\Psi\left(\{\mathbf{R}\}, \mathbf{r}_1, \mathbf{r}_2, \ldots, \mathbf{r}_N\right)$; given the expression of the electronic density, it reads:

$$E_{\text{tot}} = \langle\Psi|T + U|\Psi\rangle + \int d^3r \, V_{\text{ext}}(\mathbf{r})\, n(\mathbf{r}). \tag{1.12}$$

In 1964 P. Hohenberg and W. Kohn [34] proved that, if an N-electrons system is described by the Hamiltonian (1.7), then the following, *Hohenberg-Kohn* (HK) *theorems*, hold:

1. $V_{\text{ext}}(\mathbf{r})$ is, up to a constant, a unique functional of the electronic density $n(\mathbf{r})$. Since V_{ext} fixes H, it follows that the total energy itself is a unique functional of $n(\mathbf{r})$, and it is written as:
$$E_{\text{tot}}[n(\mathbf{r})] = F[n(\mathbf{r})] + \int d^3r\, V_{\text{ext}}(\mathbf{r})\, n(\mathbf{r}). \tag{1.13}$$
Here, the contribution given by V_{ext} is system-dependent. Conversely, $F[n(\mathbf{r})]$ (corresponding to the expectation value of $T + U$) is a *universal functional*, valid for *any* number of particles and *any* external potential.

2. Once the external potential $V_{\text{ext}}(\mathbf{r})$ is given, the total energy functional has a minimum at the ground state density $n_0(\mathbf{r})$.

1.2.2 The Kohn-Sham formulation

The HK theorems do not provide an expression for the universal functional $F[n(\mathbf{r})]$. In 1965 a further, crucial simplification of the theoretical scheme, currently found in the implementation of DFT in electronic structure codes, was achieved. W. Kohn and L. J. Sham [35], proposed to introduce a non-interacting electron gas with the same ground state density as the interacting system and to compute a part of the total energy using such auxiliary system. They wrote the total energy functional in the following way:

$$E_{\text{tot}}[n(\mathbf{r})] = T_{\text{s}}[\{\psi_i\}] + E_{\text{H}}[n(\mathbf{r})] + E_{\text{xc}}[n(\mathbf{r})] + E_{\text{ext}}[n(\mathbf{r})]. \tag{1.14}$$

$n(\mathbf{r})$ is the electronic density and can be expressed in terms of the one-particle wave functions:

$$n(\mathbf{r}) = \sum_i f_i \left\langle \psi_i | \mathbf{r} \right\rangle \left\langle \mathbf{r} | \psi_i \right\rangle, \tag{1.15}$$

where the sum is performed over all the states and f_i is the occupation number (1 or 0 if the state $|\psi_i\rangle$ is occupied or empty, respectively). Therefore, the complete total energy functional can be expressed, in the Kohn-Sham framework, as a functional of $|\psi_i\rangle$. In Eq. (1.14), $T_{\text{s}}[\psi_i]$ is the kinetic energy of the non-interacting electron gas. It is an implict functional of $n(\mathbf{r})$, and an explicit functional of the one-particle orbitals $|\psi_i\rangle$:

$$T_{\text{s}}[\{\psi_i\}] = \sum_i f_i \left\langle \psi_i \right| -\frac{1}{2}\nabla^2 \left| \psi_i \right\rangle. \tag{1.16}$$

$E_{\text{H}}[n(\mathbf{r})]$ is the *Hartree energy functional*, given by:

$$E_{\text{H}}[n(\mathbf{r})] = \frac{1}{2}\int d^3r \int d^3r' \, \frac{n(\mathbf{r})\, n(\mathbf{r}')}{|\mathbf{r} - \mathbf{r}'|}, \tag{1.17}$$

E_{ext} is the expectation value of V_{ext}, and $E_{\text{xc}}[n(\mathbf{r})]$ is the so-called *exchange-correlation energy functional*: it is the difference between the total energy of the interacting system and the terms explicitly written above for the non-interacting system, T_{s}, E_{H}, and E_{ext}.

Since $\langle \psi_i | \psi_j \rangle = \delta_{ij}$, the second HK theorem can be recast into the following constrained minimization condition using the Lagrange multipliers technique:

$$\frac{\delta}{\delta \psi_i^*(\mathbf{r})} \left(E_{\text{tot}}[n(\mathbf{r})] - \epsilon_i \left\langle \psi_i | \psi_i \right\rangle \right) = 0, \tag{1.18}$$

where δ identifies the functional derivative. Eq. (1.18) leads to a set of one-particle Schrödinger equations, known as *Kohn-Sham* (KS) *equations*, whose solutions are the wave functions $|\psi_i\rangle$:

$$\left[-\frac{1}{2}\nabla^2 + V_{\mathrm{KS}}\right] |\psi_i\rangle = \epsilon_i \, |\psi_i\rangle \, . \tag{1.19}$$

In particular, the *KS potential* V_{KS} is defined as:

$$V_{\mathrm{KS}}(\mathbf{r}) = V_{\mathrm{H}}(\mathbf{r}) + V_{\mathrm{xc}}(\mathbf{r}) + V_{\mathrm{ext}}(\mathbf{r}), \tag{1.20}$$

where:

$$V_{\mathrm{H}}(\mathbf{r}) = \int d^3r' \, \frac{n(\mathbf{r}')}{|\mathbf{r} - \mathbf{r}'|}, \tag{1.21}$$

$$V_{\mathrm{xc}}(\mathbf{r}) = \frac{\delta E_{\mathrm{xc}}}{\delta n(\mathbf{r})}. \tag{1.22}$$

1.2.3 The exchange-correlation energy functional

DFT is a formally exact theory, but it does not provide any analytic expression for E_{xc}. However, in their work Kohn and Sham proved that if $n(\mathbf{r})$ is sufficiently slowly-varying, then $E_{\mathrm{xc}}[n(\mathbf{r})]$ can be written as:

$$E_{\mathrm{xc}}[n(\mathbf{r})] = \int d^3r \, n(\mathbf{r}) \, \epsilon_{\mathrm{xc}}(n(\mathbf{r})), \tag{1.23}$$

where $\epsilon_{\mathrm{xc}}(n(\mathbf{r}))$ is the exchange-correlation energy of a *homogeneous* electron gas with density $n(\mathbf{r})$. Over time, several approximations of E_{xc} have been proposed. One of the simplest and most widely used ones is the *Local Density Approximation* (LDA), where E_{xc} is written in the following way:

$$E_{\mathrm{xc}}^{\mathrm{LDA}}[n(\mathbf{r})] = \int d^3r \, n(\mathbf{r}) \, \epsilon_{\mathrm{xc}}^{\mathrm{hom}}(n(\mathbf{r})). \tag{1.24}$$

$\epsilon_{\mathrm{xc}}^{\mathrm{hom}}(n(\mathbf{r}))$ is the exchange-correlation energy of a homogeneous gas of interacting electrons with uniform charge density n, and is evaluated at each point $\mathbf{r}$ with the local charge density of the inhomogeneous system, $n(\mathbf{r})$. In the 80s, the value of $\epsilon_{\mathrm{xc}}^{\mathrm{hom}}(n)$ has been computed for some values of the density n with Monte Carlo techniques [54]. Later, further theoretical works proposed interpolation recipes for $\epsilon_{\mathrm{xc}}^{\mathrm{hom}}(n(\mathbf{r}))$ [55–57].

LDA is, in principle, appropriate to describe systems with a slowly-varying electron density. In practice, it turns to be a good choice for a rather wide variety of materials and it has successfully predicted several materials properties [58]. However, a well known drawback of LDA is its tendency to overestimate the binding energies. In extended solids, this leads to an underestimation of the lattice parameters and, similarly, to an overestimation of cohesive energies. Phonon frequencies and elastic moduli are also often overestimated. A first attempt to correct the overbinding issue has been made with the *Generalized Gradient Approximation* (GGA), where ϵ_{xc} depends on the local density $n(\mathbf{r})$ and on its gradient $\nabla n(\mathbf{r})$:

$$E_{\mathrm{xc}}^{\mathrm{GGA}}[n(\mathbf{r})] = \int d^3r \, n(\mathbf{r}) \, \epsilon_{\mathrm{xc}}^{\mathrm{GGA}}(n(\mathbf{r}), \nabla n(\mathbf{r})). \tag{1.25}$$

Several expressions for $\epsilon_{\rm xc}^{\rm GGA}(n(\mathbf{r}), \nabla n(\mathbf{r}))$ have been proposed in literature [59–65]: nowadays, one of the most widely used parametrizations of the GGA functional is the one proposed by Perdew, Burke, and Ernzerhof, known as PBE [65]. GGA has been proved to perform generally better than LDA, especially in atomic and molecular systems, where the prediction of ionization energies, electron affinities, and atomization energies becomes more accurate [64]. In solids, the success of GGA is more controversial: while, in general, the estimation of lattice constants is improved with respect to LDA, GGA often overcorrects the overbinding typical of LDA and results in an overestimation of the lattice constants. More recently, a corrected PBE functional, known as PBEsol [66], has been developed to improve the description of exchange in solids, which as a result provides a better agreement with experiments for equilibrium properties of densely packed solids and their surfaces.

1.2.4 The self-consistent field method

The HK theorems imply that the total energy is a functional of the electronic charge density, $n(\mathbf{r})$. In the KS formulation, given in Eqs. (1.19)-(1.22), the KS potential is a functional of $n(\mathbf{r})$ itself: since $n(\mathbf{r})$ is, in turn, computed from the KS orbitals, it follows that the KS hamiltonian depends on its eigenfunctions. From a practical point of view, it is possible to deal with such a loop by using an iterative procedure known as *Self-Consistent Field* method (SCF): an initial guess for the charge density, $n_{\rm in}^{(0)}(\mathbf{r})$ (computed using randomized atomic wave functions), is used to compute the KS potential. By diagonalizing $H_{\rm KS}$, the set of single-particle orbitals $\{|\psi_i\rangle\}$ and, in turn, a new estimation of the charge density, $n_{\rm out}^{(0)}(\mathbf{r})$, are obtained. A new trial density $n_{\rm in}^{(1)}(\mathbf{r})$ is obtained from a linear combination of the densities $n_{\rm in}^{(0)}(\mathbf{r})$ and $n_{\rm out}^{(0)}(\mathbf{r})$ and is used to recompute $V_{\rm KS}$: $H_{\rm KS}$ is then diagonalized to get a new estimate of the density, $n_{\rm out}^{(1)}(\mathbf{r})$. The iterative procedure described is repeated until the absolute difference between two consecutive solutions, which can be defined e.g. as

$$\int d^3r \, |n_{\rm out}^{(j)}(\mathbf{r}) - n_{\rm in}^{(j)}(\mathbf{r})|^2, \tag{1.26}$$

where j labels the iteration, is lower than a given threshold.

1.3 Spin density functional theory

So far, the wave functions adopted in the DFT approach have been considered as scalar quantities. In order to include the interaction with an external magnetic field, or to deal with magnetic systems, it is necessary to include the spin variables, which leads to the so-called *spin density functional theory*.

1.3.1 Local spin density approximation

The most immediate way to include the spin variables consists into introducing two different sets of single-particle orbitals, $|\psi_i^\sigma\rangle$, with $\sigma = \{\uparrow, \downarrow\}$ being the spin variable: $\uparrow$ and $\downarrow$ identify two opposite orientations along an arbitrary quantization axis, and are usually referred to as *spin up* and *spin down* channels. The two channels may have different occupation numbers,

$f_i^{\uparrow}$ and $f_i^{\downarrow}$, in such a way that if the number of occupied states in the two channels is different, the system has a non-zero net magnetization. The charge density and the magnitude of the magnetization density [1] are written in terms of the two sets of single-particle wave functions as:

$$n(\mathbf{r}) = n^{\uparrow}(\mathbf{r}) + n^{\downarrow}(\mathbf{r}), \tag{1.27}$$

$$m(\mathbf{r}) = \mu_{\mathrm{B}}(n^{\uparrow}(\mathbf{r}) - n^{\downarrow}(\mathbf{r})), \tag{1.28}$$

where μ_{B} is the Bohr magneton, and:

$$n^{\uparrow}(\mathbf{r}) = \sum_i f_i^{\uparrow} \, \langle \psi_i^{\uparrow} | \mathbf{r} \rangle \, \langle \mathbf{r} | \psi_i^{\uparrow} \rangle \,, \tag{1.29}$$

$$n^{\downarrow}(\mathbf{r}) = \sum_i f_i^{\downarrow} \, \langle \psi_i^{\downarrow} | \mathbf{r} \rangle \, \langle \mathbf{r} | \psi_i^{\downarrow} \rangle \,. \tag{1.30}$$

The wave functions $|\psi_i^{\uparrow}\rangle$ and $|\psi_i^{\downarrow}\rangle$ are determined with a generalized KS scheme. In particular, in the LDA scheme, the exchange-correlation energy E_{xc} is written as a functional of $n^{\uparrow}(\mathbf{r})$ and $n^{\downarrow}(\mathbf{r})$:

$$E_{\mathrm{xc}}[n^{\uparrow}(\mathbf{r}), n^{\downarrow}(\mathbf{r})] = \int d^3r \, n(\mathbf{r}) \, \epsilon_{\mathrm{xc}}^{\mathrm{hom}}(n^{\uparrow}(\mathbf{r}), n^{\downarrow}(\mathbf{r})). \tag{1.31}$$

In this scheme, a different set of KS equations is provided for each of the two sets of wave functions:

$$\left[-\frac{1}{2}\nabla^2 + V_{\mathrm{H}} + V_{\mathrm{xc}}^{\uparrow} + V_{\mathrm{ext}} \right] |\psi_i^{\uparrow}\rangle = \epsilon_i^{\uparrow} \, |\psi_i^{\uparrow}\rangle \,, \tag{1.32}$$

$$\left[-\frac{1}{2}\nabla^2 + V_{\mathrm{H}} + V_{\mathrm{xc}}^{\downarrow} + V_{\mathrm{ext}} \right] |\psi_i^{\downarrow}\rangle = \epsilon_i^{\downarrow} \, |\psi_i^{\downarrow}\rangle \,, \tag{1.33}$$

where the exchange-correlation potentials for the two spin channels are defined as:

$$V_{\mathrm{xc}}^{\uparrow}(\mathbf{r}) = \frac{\delta E_{\mathrm{xc}}}{\delta n^{\uparrow}(\mathbf{r})}, \tag{1.34}$$

$$V_{\mathrm{xc}}^{\downarrow}(\mathbf{r}) = \frac{\delta E_{\mathrm{xc}}}{\delta n^{\downarrow}(\mathbf{r})}. \tag{1.35}$$

1.3.2 Non-collinear spin density functional theory

A more general formulation that provides a magnetization density field that, at any point in space, can point in different directions, is the *non-collinear* spin density functional theory. In this framework, the one-particle wave functions are described by the spinors:

$$\begin{pmatrix} |\psi_i^{\uparrow}\rangle \\ |\psi_i^{\downarrow}\rangle \end{pmatrix}. \tag{1.36}$$

[1] In this approach, since the wave functions are considered as scalar quantities, it is not possible to define a magnetization density as a vector field, only its magnitude is accessible.

If their components are indicated with the short-hand notation $|\psi_i^\sigma\rangle$, the 2×2 spin density matrix is defined as:

$$n^{\sigma\sigma'}(\mathbf{r}) = \sum_i f_i \, \langle\psi_i^\sigma|\mathbf{r}\rangle \, \langle\mathbf{r}|\psi_i^{\sigma'}\rangle \, . \tag{1.37}$$

The density and the magnetization density are then defined by multiplying the spin density matrix with the identity matrix or the Pauli matrices σ_α, respectively:

$$n(\mathbf{r}) = \sum_\sigma n^{\sigma\sigma}(\mathbf{r}), \tag{1.38}$$

$$m_\alpha(\mathbf{r}) = \mu_\mathrm{B} \sum_{\sigma\sigma'} n^{\sigma\sigma'}(\mathbf{r}) \, \sigma_\alpha^{\sigma\sigma'}, \tag{1.39}$$

where α indicates the cartesian component.

The total energy functional can be decomposed in a similar way to what described in the previous section:

$$E_\mathrm{tot}[\{\psi_i^\sigma\}] = T_s[\{\psi_i^\sigma\}] + E_\mathrm{H}[n(\mathbf{r})] + E_\mathrm{xc}[n^{\sigma\sigma'}(\mathbf{r})] + E_\mathrm{ext}[n^{\sigma\sigma'}(\mathbf{r})], \tag{1.40}$$

where the external energy functional is written as:

$$E_\mathrm{ext}[n^{\sigma\sigma'}(\mathbf{r})] = \sum_{\sigma\sigma'} \int d^3r \, V_\mathrm{ext}^{\sigma\sigma'}(\mathbf{r}) \, n^{\sigma\sigma'}(\mathbf{r}), \tag{1.41}$$

whereas the Hartree energy is expressed as in Eq. (1.17), and the exchange-correlation energy is tipically written in terms of the density and magnetization density fields:

$$E_\mathrm{xc}[n^{\sigma\sigma'}(\mathbf{r})] = E_\mathrm{xc}[n(\mathbf{r}), |\mathbf{m}(\mathbf{r})|]. \tag{1.42}$$

Similarly to the formulation for scalar wave functions, the total energy has been written using an auxiliary system of N non-interacting spin-1/2 particles, hence a set of N equations for single-particle orbitals can be derived using the KS scheme described above. The KS equations in the non-collinear formulation are then:

$$\sum_{\sigma'} \left[-\frac{1}{2}\nabla^2 \, \delta^{\sigma\sigma'} + V_\mathrm{ext}^{\sigma\sigma'} + (V_\mathrm{H} + V_\mathrm{xc}) \, \delta^{\sigma\sigma'} - \mu_\mathrm{B} \sum_{\alpha=1}^{3} B_{\mathrm{xc},\alpha} \, \sigma_\alpha^{\sigma\sigma'} \right] |\psi_i^{\sigma'}\rangle = \epsilon_i \, |\psi_i^\sigma\rangle \, , \tag{1.43}$$

where $\mathbf{B}_\mathrm{xc}(\mathbf{r})$ is a three-component vector field called *exchange-correlation magnetic field* and is defined as:

$$B_{\mathrm{xc},\alpha}(\mathbf{r}) = -\frac{\delta E_\mathrm{xc}}{\delta m_\alpha(\mathbf{r})}. \tag{1.44}$$

Eq. (1.44) can be specialized for the LDA and GGA schemes for the exchange and correlation functional, to get:

$$B_{\mathrm{xc},\alpha}^\mathrm{LDA}(\mathbf{r}) = -n(\mathbf{r}) \frac{\partial \epsilon_\mathrm{xc}}{\partial |\mathbf{m}(\mathbf{r})|} \frac{m_\alpha}{|\mathbf{m}(\mathbf{r})|}, \tag{1.45}$$

$$B_{\mathrm{xc},\alpha}^\mathrm{GGA}(\mathbf{r}) = -n(\mathbf{r}) \left[\frac{\partial \epsilon_\mathrm{xc}}{\partial |\mathbf{m}(\mathbf{r})|} - \nabla \cdot \frac{\partial \epsilon_\mathrm{xc}}{\partial \nabla |\mathbf{m}(\mathbf{r})|} \right] \frac{m_\alpha}{|\mathbf{m}(\mathbf{r})|}. \tag{1.46}$$

whence it follows that $\mathbf{B}_\mathrm{xc} \parallel \mathbf{m}$ at any point in space.

Collinear formulation

A simplified formulation is the *collinear* spin density functional theory, where the wave functions are written as:

$$\begin{pmatrix} |\psi_i^{\uparrow}\rangle \\ 0 \end{pmatrix}, \quad \begin{pmatrix} 0 \\ |\psi_i^{\downarrow}\rangle \end{pmatrix}. \tag{1.47}$$

As a consequence, the spin density defined in Eq. (1.37) is diagonal:

$$n^{\sigma\sigma'}(\mathbf{r}) = \begin{pmatrix} n^{\uparrow\uparrow}(\mathbf{r}) & 0 \\ 0 & n^{\downarrow\downarrow}(\mathbf{r}) \end{pmatrix}, \tag{1.48}$$

therefore the density and the magnetization density are expressed as:

$$n(\mathbf{r}) = n^{\uparrow\uparrow}(\mathbf{r}) + n^{\downarrow\downarrow}(\mathbf{r}), \tag{1.49}$$

$$\mathbf{m}(\mathbf{r}) = \begin{pmatrix} 0 \\ 0 \\ \mu_{\mathrm{B}}(n^{\uparrow\uparrow}(\mathbf{r}) - n^{\downarrow\downarrow}(\mathbf{r})) \end{pmatrix}. \tag{1.50}$$

It follows that $\mathbf{m}(\mathbf{r})$ always points along a given quantization axis, uniform in space, hence only its magnitude is physically relevant, which is at some extent similar to what we discussed above for the Local Spin Density Approximation (LSDA). As a result, all the effects related to the orientation of the magnetization, such as the magnetic anisotropy effects, are not accounted for in the collinear framework.

The total energy, external energy, and exchange-correlation energy functionals can be expressed as in Eqs. (1.40), (1.41), and (1.42) [67]. Since $\mathbf{B}_{\mathrm{xc}} \parallel \mathbf{m}$, we can write $\mathbf{B}_{\mathrm{xc}} = (0, 0, B_{\mathrm{xc},z})$, and hence the Kohn-Sham equations in the collinear formulation are:

$$\left[-\frac{1}{2}\nabla^2 + V_{\mathrm{ext}} + V_{\mathrm{H}} + V_{\mathrm{xc}} - \mu_{\mathrm{B}} B_{\mathrm{xc},z}\right] |\psi_i^{\uparrow}\rangle = \epsilon_i^{\uparrow}\, |\psi_i^{\uparrow}\rangle\,, \tag{1.51}$$

$$\left[-\frac{1}{2}\nabla^2 + V_{\mathrm{ext}} + V_{\mathrm{H}} + V_{\mathrm{xc}} + \mu_{\mathrm{B}} B_{\mathrm{xc},z}\right] |\psi_i^{\downarrow}\rangle = \epsilon_i^{\downarrow}\, |\psi_i^{\downarrow}\rangle\,. \tag{1.52}$$

The two equations allow to separately determine $|\psi_i^{\uparrow}\rangle$ and $|\psi_i^{\downarrow}\rangle$, but cannot be regarded as completely decoupled: they are implicitly coupled through the Hartree and exchange and correlation terms, which need both $|\psi_i^{\uparrow}\rangle$ and $|\psi_i^{\downarrow}\rangle$ to be computed. As a consequence, the self-consistent field approach must be carried out by solving them together. As a side note, we remark that comparing the collinear and the LSDA formulations, $V_{\mathrm{xc}}^{\uparrow}$ and $V_{\mathrm{xc}}^{\downarrow}$ of the LSDA approach correspond to $V_{\mathrm{xc}} - \mu_{\mathrm{B}} B_{\mathrm{xc},z}$ and $V_{\mathrm{xc}} + \mu_{\mathrm{B}} B_{\mathrm{xc},z}$, respectively.

1.4 Periodic solids and plane waves

In this Thesis we will focus mainly on crystalline solids. A crystalline solid is a periodic, extended system, characterized by the infinite repetition in space of a constituent unit, called *primitive cell*. A solid can be described, from a mathematical point of view, by a set of points, named *Bravais lattice*, with coordinates given by:

$$\mathbf{R}_{\mu} = n_1\, \mathbf{a}_1 + n_2\, \mathbf{a}_2 + n_3\, \mathbf{a}_3, \tag{1.53}$$

where the index μ labels the primitive cell, n_1, n_2, and n_3 are integer numbers, while $\mathbf{a}_1$, $\mathbf{a}_2$, and $\mathbf{a}_3$ are three linearly independent vectors which identify the primitive cell and are called *primitive lattice vectors*. The volume of the primitive cell can be computed directly from the primitive lattice vectors as:

$$\Omega = \mathbf{a}_1 \cdot (\mathbf{a}_2 \times \mathbf{a}_3). \tag{1.54}$$

In order to identify the position of all the atoms of a solid, we introduce an additional set of vectors $\mathbf{d}_s$, $s = 1, \ldots, N_{\text{at}}$ ($N_{\text{at}} \geq 1$ identifies the number of atoms in the primitive cell): $\mathbf{d}_s$ specifies the position of the nucleus of the s-th atom, of atomic species $\gamma(s)$, with respect to the origin of the primitive cell, therefore the positions of the atomic nuclei in space are given by $\mathbf{R}_\mu + \mathbf{d}_s$.

The potential V_{ext}, generated by the nuclear charges, has the same periodicity as the Bravais lattice,

$$V_{\text{ext}}(\mathbf{r} + \mathbf{R}_\mu) = V_{\text{ext}}(\mathbf{r}). \tag{1.55}$$

As a consequence, the electronic charge density $n(\mathbf{r})$ and, in turn, the KS potential V_{KS} are invariant with respect to a translation of a direct lattice vector $\mathbf{R}_\mu$:

$$n(\mathbf{r} + \mathbf{R}_\mu) = n(\mathbf{r}), \tag{1.56}$$

$$V_{\text{KS}}(\mathbf{r} + \mathbf{R}_\mu) = V_{\text{KS}}(\mathbf{r}), \tag{1.57}$$

therefore also the whole KS Hamiltonian is lattice-periodic, and we can apply Bloch's theorem to write the single-particle wave functions in the following way:

$$\psi_{\mathbf{k}v}(\mathbf{r}) = e^{i\mathbf{k}\cdot\mathbf{r}}\, u_{\mathbf{k}v}(\mathbf{r}), \tag{1.58}$$

where $u_{\mathbf{k}v}$ is a lattice-periodic function. $\mathbf{k}$ is a three-dimensional vector, defined in the *reciprocal space* and it labels the wave functions $\psi_{\mathbf{k}v}(\mathbf{r})$: the specific way adopted to describe the system, usually represented by a given *boundary condition* on the wave functions, imposes constraints that determine a set of allowed wave vectors. In solid state physics, we usually adopt the so-called *Born-von Kármán Periodic Boundary Conditions* (PBCs): the solid is modeled as an extended system made up of N_j unit cells along the direction $\mathbf{a}_j$ ($j = 1, 2, 3$) [2] and the following conditions are imposed on the wave functions:

$$\psi_{\mathbf{k}v}(\mathbf{r} + N_j\, \mathbf{a}_j) = \psi_{\mathbf{k}v}(\mathbf{r}). \tag{1.59}$$

Given Bloch's theorem, PBCs imply that:

$$e^{iN_j\, \mathbf{k}\cdot\mathbf{a}_j} = 1, \tag{1.60}$$

hence, after introducing the vectors $\mathbf{b}_j$ such that $\mathbf{a}_i \cdot \mathbf{b}_j = 2\pi\, \delta_{ij}$, the allowed wave vectors are expressed as:

$$\mathbf{k} = \frac{m_1}{N_1}\, \mathbf{b}_1 + \frac{m_2}{N_2}\, \mathbf{b}_2 + \frac{m_3}{N_3}\, \mathbf{b}_3, \tag{1.61}$$

where m_j are integers such that $0 \leq m_j < N_j$.

[2] So, overall the system is made up of $N = N_1\, N_2\, N_3$ unit cells and has a volume $V = N\, \Omega$

In order to solve the KS equations, it is useful to expand the wave functions on a given basis set. One of the most widely used is the Plane Waves (PWs) basis set: PWs are indeed an orthogonal basis by construction and represent the most natural choice while dealing with crystalline solids. The translational invariance of the Bravais lattice imposes further constraints on the wave vectors that enter in the expansion of a lattice-periodic function in the PWs basis set. Indeed, PWs $e^{i\mathbf{k}\cdot\mathbf{r}}$ are lattice-periodic only for a given set of wave vectors $\mathbf{G}$, called *reciprocal lattice vectors* and defined by the condition $e^{i\mathbf{G}\cdot\mathbf{R}_\mu} = 1$. The $\mathbf{G}$ vectors form a lattice in the reciprocal space, its primitive vectors being $\mathbf{b}_1$, $\mathbf{b}_2$, and $\mathbf{b}_3$ introduced above. The Wigner-Seitz primitive cell of the reciprocal lattice is called *Brillouin Zone* (BZ): all the wave vectors $\mathbf{k}$ allowed in PBCs can be refolded into it and, as a consequence, a band index v needs to be introduced to label the wave functions, $\psi_{\mathbf{k}v}(\mathbf{r})$.

The periodic part of the wave function can be expanded in PWs, to get:

$$\psi_{\mathbf{k}v}(\mathbf{r}) = \frac{1}{\sqrt{V}} \sum_{\mathbf{G}} c_{\mathbf{k}+\mathbf{G}\,v}\, e^{i(\mathbf{k}+\mathbf{G})\cdot\mathbf{r}}, \tag{1.62}$$

where V is the volume of the solid. If we substitute $\psi_{\mathbf{k}v}(\mathbf{r})$ given by Eq. (1.62) into Eq. (1.19), we obtain the following expression for the KS equations in reciprocal space:

$$\sum_{\mathbf{G}'} \left[\frac{1}{2}|\mathbf{k}+\mathbf{G}|^2\,\delta_{\mathbf{G}\mathbf{G}'} + V_{\mathrm{KS}}(\mathbf{G}-\mathbf{G}')\right] c_{\mathbf{k}+\mathbf{G}'\,v} = \epsilon_{\mathbf{k}v}\, c_{\mathbf{k}+\mathbf{G}\,v}, \tag{1.63}$$

where $V_{\mathrm{KS}}(\mathbf{G}-\mathbf{G}')$ ($V_{\mathrm{KS}} = V_{\mathrm{H}} + V_{\mathrm{xc}} + V_{\mathrm{ext}}$) is the matrix elements of the KS potential between two PWs with wave vectors $\mathbf{k}+\mathbf{G}$ and $\mathbf{k}+\mathbf{G}'$, hence it corresponds to the $\mathbf{G}-\mathbf{G}'$ Fourier component of the KS potential defined in real space:

$$\begin{aligned} V_{\mathrm{KS}}(\mathbf{G}-\mathbf{G}') &= \frac{1}{\Omega}\int_\Omega d^3r\, e^{-i(\mathbf{k}+\mathbf{G})\cdot\mathbf{r}}\, V_{\mathrm{KS}}(\mathbf{r})\, e^{i(\mathbf{k}+\mathbf{G}')\cdot\mathbf{r}} \\ &= \frac{1}{\Omega}\int_\Omega d^3r\, e^{-i(\mathbf{G}-\mathbf{G}')\cdot\mathbf{r}}\, V_{\mathrm{KS}}(\mathbf{r}). \end{aligned} \tag{1.64}$$

The charge density can be written in terms of the single-particle wave functions (Eq. (1.15)) and, following the expansion in PWs introduced above, it reads:

$$n(\mathbf{r}) = \frac{1}{V}\sum_{\mathbf{k}v}\sum_{\mathbf{G}\,\mathbf{G}'} f_{\mathbf{k}v}\, c^*_{\mathbf{k}+\mathbf{G}'\,v}\, c_{\mathbf{k}+\mathbf{G}\,v}\, e^{i(\mathbf{G}-\mathbf{G}')\cdot\mathbf{r}}, \tag{1.65}$$

or, equivalently:

$$n(\mathbf{r}) = \sum_{\mathbf{G}} n(\mathbf{G})\, e^{i\mathbf{G}\cdot\mathbf{r}}. \tag{1.66}$$

The PWs expansion in Eq. (1.62) is formally exact, but it requires an infinite number of PWs. Clearly, in order for such an approach to be computationally affordable, the number of basis elements has to be finite: in electronic structure codes, this is usually achieved by considering only the PWs with $\mathbf{G}$ vectors such that:

$$\frac{1}{2}|\mathbf{k}+\mathbf{G}|^2 < E_{\mathrm{cut}}, \tag{1.67}$$

where E_{cut} is a kinetic energy cut-off that is chosen accordingly to the desired accuracy on the wave functions, which naturally affects the accuracy of computed quantities such as, e.g., the ground state energy and the forces. The representation of the wave functions with a truncated basis set implies that also the charge density is computed with a limited number of PWs. By comparing Eqs. (1.65) and (1.66) it follows that the kinetic energy cut-off for the charge density is 4 times larger than the one for the wave functions, namely:

$$\frac{1}{2}|\mathbf{G}|^2 < 4\,E_{\text{cut}}. \tag{1.68}$$

1.5 Ionic forces: the Hellmann-Feynman theorem

In solid state physics we often are interested in equilibrium properties of solids. Ionic forces are important quantities in this respect, since their calculation, together with an appropriate minimization algorithm, allow to get the equilibrium structure of the solid. In the BO approximation, the ionic forces $\mathbf{f}$ are computed as the derivative of the total energy of the electrons with respect to the ionic displacements $\mathbf{u}$, namely:

$$f_{\mu s\alpha} = -\frac{dE_{\text{tot}}}{du_{\mu s\alpha}}. \tag{1.69}$$

The total derivative of the total energy can be computed by exploiting the Hellmann-Feynman (HF) theorem [68, 69]. If we consider the total energy $E_{\text{tot}} = E_{\text{tot},\lambda}[\{\psi_i\}]$, written in the KS DFT formalism as a functional of the single-particle orbitals $|\psi_i\rangle$, and dependent on the parameter λ, its total derivative, computed with the chain rule, reads:

$$\begin{aligned}
\frac{dE_{\text{tot}}}{d\lambda} &= \frac{\partial E_{\text{tot}}}{\partial\lambda} + \sum_i \int d^3r \left(\frac{\delta E_{\text{tot}}}{\delta\psi_i^*(\mathbf{r})} \frac{d\psi_i^*(\mathbf{r})}{d\lambda} + \frac{\delta E_{\text{tot}}}{\delta\psi_i(\mathbf{r})} \frac{d\psi_i(\mathbf{r})}{d\lambda} \right) \\
&= \frac{\partial E_{\text{tot}}}{\partial\lambda} + \sum_i \epsilon_i \int d^3r \left(\frac{d\psi_i^*(\mathbf{r})}{d\lambda} \psi_i(\mathbf{r}) + \psi_i^*(\mathbf{r}) \frac{d\psi_i(\mathbf{r})}{d\lambda} \right) \\
&= \frac{\partial E_{\text{tot}}}{\partial\lambda} + \sum_i \epsilon_i \frac{d}{d\lambda} \langle\psi_i|\psi_i\rangle \\
&= \frac{\partial E_{\text{tot}}}{\partial\lambda},
\end{aligned} \tag{1.70}$$

where the second line follows from Eq. (1.18). The partial derivative of E_{tot} is then further expressed using the HF theorem, therefore:

$$\begin{aligned}
\frac{dE_{\text{tot}}}{d\lambda} &= \frac{\partial E_{\text{tot}}}{\partial\lambda} \\
&= \sum_i \left\langle \psi_i \middle| \frac{\partial V_{\text{KS}}}{\partial\lambda} \middle| \psi_i \right\rangle.
\end{aligned} \tag{1.71}$$

1.6 The smearing technique

DFT is a ground state theory, because the second HK theorem derives from the variational principle of quantum mechanics, which is valid only for the ground state. As a consequence,

the occupation numbers of the states $|\psi_{\mathbf{k}v}\rangle$ have no thermal broadening, therefore $f_{\mathbf{k}v}$ is 1 or 0. Equivalently, if we identify with ϵ_{F} the Fermi energy, $f_{\mathbf{k}v}$ can be expressed as a Fermi-Dirac function at zero temperature, $\theta(\epsilon_{\mathrm{F}} - \epsilon_{\mathbf{k}v})$. Being $\theta(\epsilon_{\mathrm{F}} - \epsilon_{\mathbf{k}v})$ discontinous, convergence issues on the BZ summations may show up. This is especially true for metals, where the presence of a Fermi surface would require a very dense **k**-points mesh in order to converge the BZ summations. Moreover, due to the discontinuity of $\theta(\epsilon_{\mathrm{F}} - \epsilon_{\mathbf{k}v})$, in metals one or more states with energy close to ϵ_{F} that are occupied at a given iteration of the self-consistent loop, may be empty at the next iteration (or viceversa): as a consequence, the charge density can be subject to evident variations during the SCF iterative procedure, leading to convergence issues.

A method widely used to overcome this shortcoming is the *smearing technique*: the idea is to remove the discontinuity by smoothing out the Fermi-Dirac function at $T = 0$ K. In practice, this is achieved by approximating the Dirac's δ function, i.e. the derivative of $\theta(\epsilon_{\mathrm{F}} - \epsilon_{\mathbf{k}v})_{T=0}$, by a smearing function:

$$f(\epsilon) = \frac{1}{\eta}\,\tilde{\delta}\left(\frac{\epsilon}{\eta}\right), \tag{1.72}$$

where η is called *smearing parameter*. Many kinds of smearing functions can be used: gaussian [70], gaussian combined with polynomials, the most well known methods being the Methfessel-Paxton [71] and the Marzari-Vanderbilt [72] methods, and the Fermi-Dirac broadening [3].

The use of the smearing technique introduces a difficulty when applying the HF theorem to compute the ionic forces. The occupation numbers $f_{\mathbf{k}v}$ are not fixed, therefore the KS energy functional $E[n(\mathbf{r})]$ is not variational because $\partial E/\partial f_{\mathbf{k}v} \neq 0$. As a result, the HF theorem cannot be applied and an additional term in the forces appears. To solve this issue, it has been proposed [73] to substitute the energy functional with the Mermin free energy:

$$F = E - T_{\mathrm{el}}\, S, \tag{1.73}$$

where S is the entropy and is given by:

$$S = -k_{\mathrm{B}} \sum_{\mathbf{k}v} \left[f_{\mathbf{k}v} \ln f_{\mathbf{k}v} + (1 - f_{\mathbf{k}v}) \ln(1 - f_{\mathbf{k}v}) \right]. \tag{1.74}$$

We remark that the smearing technique mentioned above corresponds to a fictitious thermal broadening (with temperature T_{el}) of the electronic occupation function: in the original KS formulation, where no smearing is used, the fictitious temperature of the electronic system is $T_{\mathrm{el}} = 0$. If Eq. (1.72) is adopted, the entropic contribution in the free-energy reads [45]:

$$E_{\mathrm{met}} = \sum_{\mathbf{k}v} \eta\, \tilde{\theta}_1\left(\frac{\epsilon_{\mathrm{F}} - \epsilon_{\mathbf{k}v}}{\eta}\right), \tag{1.75}$$

that is usually included in the kinetic energy functional. The function $\tilde{\theta}_1(x)$ introduced is:

$$\tilde{\theta}_1(x) = \int_{-\infty}^{x} dy\, y\, \tilde{\delta}(y). \tag{1.76}$$

[3] We are not going to discuss these methods in detail here: the interested reader is encouraged to check out the references indicated.

The derivative of the entropic contribution with respect to the atomic displacement cancels the extra term in the forces coming from the derivative of the occupation function and, as a result, the HF theorem is still valid.

1.7 Symmetrization

Several physical quantities of interest depend on integrals of periodic functions over the BZ. These integrals are calculated taking a uniform mesh of points, an idea proposed in 1976 by H. J. Monkhorst and J. D. Pack [74]. In the basis of the primitive vectors of the reciprocal lattice, the **k**-points of the mesh are given by:

$$\mathbf{k} = \frac{m-1}{N_{k_1}}\,\mathbf{b}_1 + \frac{p-1}{N_{k_2}}\,\mathbf{b}_2 + \frac{q-1}{N_{k_3}}\,\mathbf{b}_3, \tag{1.77}$$

where N_{k_1}, N_{k_2}, and N_{k_3} are the number of **k**-points along $\mathbf{b}_1$, $\mathbf{b}_2$, and $\mathbf{b}_3$, respectively, and m, p, and q, are integers such that $1 \leq m < N_{k_1}$, $1 \leq p < N_{k_2}$, and $1 \leq q < N_{k_3}$.

Besides translational invariance, crystalline solids may possess a further set of symmetries: the complete set of symmetries forms the so-called *space group* of the crystal. We identify the symmetries with the symbol $\{\mathcal{S}|\mathbf{f}\}$, where $\mathcal{S}$ is a rotation (proper or improper) and $\mathbf{f}$ is a translation. The action of $\{\mathcal{S}|\mathbf{f}\}$ is defined in the following way:

$$\{\mathcal{S}|\mathbf{f}\}\mathbf{r} = \mathcal{S}\mathbf{r} + \mathbf{f}. \tag{1.78}$$

The element $\{\mathcal{S}|\mathbf{f}\}$ belongs to the space group of the crystal if it leaves the crystal invariant, i.e.:

$$\{\mathcal{S}|\mathbf{f}\}(\mathbf{R}_\mu + \mathbf{d}_s) = \mathbf{R}_{\bar{\mu}} + \mathbf{d}_{\bar{s}}, \tag{1.79}$$

for every μ and s, and with $\gamma(\bar{s}) = \gamma(s)$.

Bloch's theorem implies that (for a general discussion on the action of symmetry operators on wave functions the interested reader is referred to Appendix B):

$$\begin{aligned} \mathcal{O}_{\{\mathcal{S}|\mathbf{f}\}^{-1}}\psi_{\mathbf{k}v}(\mathbf{r}) &= \psi_{\mathbf{k}v}(\{\mathcal{S}|\mathbf{f}\}\mathbf{r}) \\ &= \psi_{\mathcal{S}^{-1}\mathbf{k}v}(\mathbf{r}), \end{aligned} \tag{1.80}$$

which allows to reduce the summations over the whole BZ to a smaller portion of the BZ, called *Irreducible Brillouin Zone* (IBZ): the reduction procedure is often called *symmetrization*. As an example, we mention the symmetrization of the charge density. If we consider $n(\mathbf{r})$ as written in Eq. (1.15), it can be symmetrized using Eq. (1.80) to get:

$$n(\mathbf{r}) = \frac{1}{N_S}\sum_{\{\mathcal{S}|\mathbf{f}\}}\left(\sum_{\mathbf{k}\in\mathrm{IBZ}}\sum_{v}\omega_{\mathbf{k}}\, f_{\mathbf{k}v}\,|\psi_{\mathbf{k}v}(\{\mathcal{S}|\mathbf{f}\}\mathbf{r})|^2\right), \tag{1.81}$$

where N_S is the number of symmetries $\mathcal{S}$ in the space group of the crystal, whereas $\omega_{\mathbf{k}}$ is the *weight factor*, corresponding to the number of points $\mathbf{k}'$ of the *star* of $\mathbf{k}$, obtained from $\mathbf{k}$ by applying the symmetry operations $\mathcal{S}$, namely $\mathbf{k}' = \mathcal{S}\mathbf{k}$. Eq. (1.81) is usually written in the following compact form:

$$n(\mathbf{r}) = \frac{1}{N_S}\sum_{\{\mathcal{S}|\mathbf{f}\}} n^{\mathrm{NS}}(\{\mathcal{S}|\mathbf{f}\}\mathbf{r}), \tag{1.82}$$

where we introduced the so-called *non-symmetrized* charge density $n^{\rm NS}(\mathbf{r})$, defined as:

$$n^{\rm NS}(\mathbf{r}) = \sum_{\mathbf{k}\in {\rm IBZ}} \sum_{v} \omega_{\mathbf{k}}\, f_{\mathbf{k}v}\, |\psi_{\mathbf{k}v}(\mathbf{r})|^2. \tag{1.83}$$

While dealing with magnetic systems, also the magnetization density $\mathbf{m}(\mathbf{r})$ needs to be symmetrized. In a magnetic solid, the set of symmetries that leave the crystal invariant (including also the magnetization density) is called *magnetic space group*: it contains the symmetries $\{\mathcal{S}|\mathbf{f}\}$ introduced above and, in addition, it may contain also symmetries that require the time-reversal operation $\mathcal{T}$, so that $\{\mathcal{T}\mathcal{S}|\mathbf{f}\}$ is a symmetry of the crystal [4]. In order to distinguish the two cases we introduce a variable $\tau(\mathcal{S})$, such that $\tau = 0$ ($\tau = 1$) if $\{\mathcal{S}|\mathbf{f}\}$ ($\{\mathcal{T}\mathcal{S}|\mathbf{f}\}$) is a symmetry of the crystal. After introducing the non-symmetrized magnetization density $\mathbf{m}^{\rm NS}(\mathbf{r})$, similarly to Eq. (1.83):

$$m_\alpha^{\rm NS}(\mathbf{r}) = \mu_{\rm B} \sum_{\mathbf{k}\in {\rm IBZ}} \sum_{v} \omega_{\mathbf{k}}\, f_{\mathbf{k}v} \sum_{\sigma\,\sigma'} \psi^{*\sigma}_{\mathbf{k}v}(\mathbf{r})\, \sigma_\alpha^{\sigma\sigma'}\, \psi^{\sigma'}_{\mathbf{k}v}(\mathbf{r}), \tag{1.84}$$

the full, symmetrized, magnetization density reads:

$$m_\alpha(\mathbf{r}) = \frac{1}{N_S} \sum_{\{\mathcal{S}|\mathbf{f}\}} (-1)^{\tau(\mathcal{S})} \sum_{\beta} \tilde{S}^{-1}_{\alpha\beta}\, m_\beta^{\rm NS}(\{\mathcal{S}|\mathbf{f}\}\mathbf{r}), \tag{1.85}$$

where $\tilde{S}$ is the proper part of S.

1.8 Pseudopotentials theory: an overview

The expansion of the wave functions on a given basis set is computationally affordable only if a truncated basis is used. Unavoidably, basis set reduction implies inaccuracies in representing the wave functions, hence a good compromise between computational cost and accuracy is necessary. The effort made during the years to optimize such aspect led to the development of the *pseudopotentials theory*. While a detailed and complete description of the theoretical aspects of the pseudopotentials theory is far beyond the scope of this Thesis, in this Section we highlight the milestones that lead to the current formulation.

It is well known that core states vary on short length scales, hence a high number of PWs is needed to accurately represent them. This affects also the valence states which, being orthogonal to the core states, present oscillations near the atomic nuclei. This issue has been faced since the early 1940s, when C. Herring proposed [75] to expand the eigenfunctions in plane waves orthogonalized to the core states. In 1959, J. C. Phillips and L. Kleinman specialized the method to crystals and molecules [76]: they considered the smooth part of symmetrized Bloch functions and showed that it is the solution of an equation similar to the starting Schrödinger equation, with an additional term in the potential. The auxiliary wave function introduced is usually called *pseudowave function* and the modified potential is referred to as *pseudopotential*. Briefly, the idea behind the pseudopotential scheme is to find a modified potential and proper auxiliary wave functions that solve a Schrödinger equation with the same eigenvalues as the exact ones. Clearly, the complexity of the task lies in developing proper techniques to construct such auxiliary wave functions and potentials.

[4] This is the case of a symmetry $\{\mathcal{S}|\mathbf{f}\}$ that leaves the charge density invariant, but changes the sign of the magnetization density, i.e. $\mathbf{m}(\mathbf{r}) = -\mathbf{m}(\{\mathcal{S}|\mathbf{f}\}\mathbf{r})$.

1.8.1 The atomic pseudopotential

We recall from previous sections that in DFT the KS potential is written as:

$$V_{\mathrm{KS}} = V_{\mathrm{H}} + V_{\mathrm{xc}} + V_{\mathrm{ext}}. \tag{1.86}$$

Considering an atomic system, the radial part of the wave functions solves the KS equation:

$$\left[T_l + V_{\mathrm{KS}}\right] |\psi_{nl}\rangle = \epsilon_{nl}\ |\psi_{nl}\rangle\,, \tag{1.87}$$

where n and l are the principal and orbital quantum numbers, respectively, and:

$$T_l = -\frac{1}{2}\frac{d^2}{dr^2} + \frac{l(l+1)}{2r^2} \tag{1.88}$$

is the kinetic energy operator that contains the centrifugal contribution.

In the pseudopotential scheme, we look for a potential V_{ps}^l such that:

$$\left[T_l + V_{\mathrm{ps}}^l\right] |\phi_l\rangle = \widetilde{\epsilon}_l\ |\phi_l\rangle\,. \tag{1.89}$$

The pseudopotential V_{ps}^l must be devised in such a way that:

- the pseudowave function $|\phi_l\rangle$ is identical to the all-electron (AE) wave function for $r \geq r_c^l$, where r_{c}^l is called *core radius*, and it is nodeless for $r < r_c^l$;
- $\widetilde{\epsilon}_l$ is equal to the exact energies ϵ_{nl}.

V_{ps}^l is usually tailored to reproduce the tail of V_{KS} for $r \geq r_c^l$, by writing it as:

$$V_{\mathrm{ps}}^l = V_{\mathrm{eff}} + \Delta V_{\mathrm{ps}}^l, \tag{1.90}$$

where V_{eff}, called *effective potential*, is a l-independent, function that matches V_{KS} for $r \geq r_c^l$, whereas ΔV_{ps}^l is a l-dependent, localized function, different from zero for $r < r_c^l$, called *non-local component* of the pseudopotential. V_{eff} contains also the screening contributions given by V_{H} and V_{xc}, therefore it is affected by the valence charge density distribution, which usually varies in a significant way depending on the system studied. A more effective way to improve the *transferability* of the pseudopotential is to *descreen* V_{eff} by subtracting the Hartree and exchange-correlation contributions computed with the valence charge density $n_v(\mathbf{r})$. In this way, we have a more transferable, *local*, component of the pseudopotential:

$$V_{\mathrm{loc}} = V_{\mathrm{eff}} - V_{\mathrm{H}}[n_v(\mathbf{r})] - V_{\mathrm{xc}}[n_v(\mathbf{r})], \tag{1.91}$$

whereas V_{H} and V_{xc} can be then recomputed with the actual charge density.

The freedom in the choice of the pseudowave function and of the core radius r_c^l has led to develop several pseudization techniques. As an example, among the most well known methods we mention the Kerker [77], the Troullier-Martins [78, 79], and the Rappe-Rabe-Kaxiras-Joannopoulos (RRKJ) [80] techniques, which require the pseudowave function to obey a given set of constraints, such as the continuity of the function and of a given number of its derivatives at r_c^l. Once the pseudowave functions have been constructed, the non-local

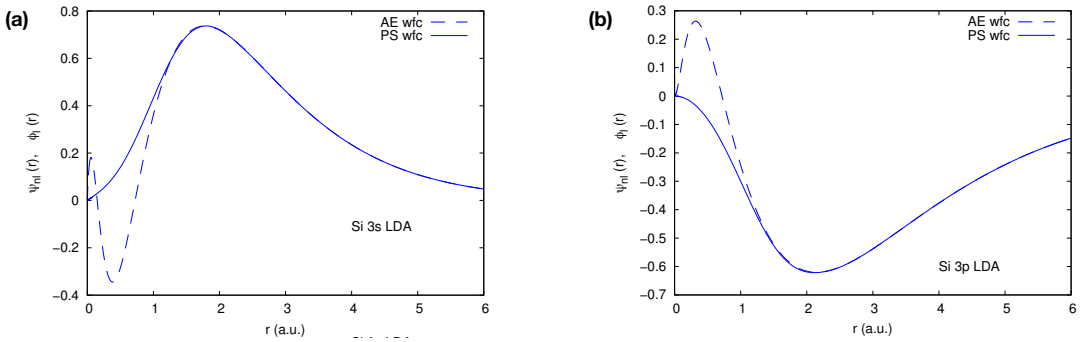

Figure 1.1: AE (dashed line) and pseudo (PS, continuous line) radial wave functions for the $3s$ (a) and $3p$ (b) states of Si in the configuration $3s^2 3p^2$.

part of the pseudopotential can be obtained by inverting the KS equation. Since $|\phi_l\rangle$ are nodeless, we can write:

$$\Delta V_{\rm ps}^l = \frac{1}{\phi_l} \left[\epsilon_l - T_l - V_{\rm eff}\right] \phi_l. \tag{1.92}$$

As an example, we report in Fig. 1.1 the radial pseudowave functions compared to the AE wave functions for Si in the configuration $3s^2 3p^2$. For $r \geq r_c^l$, the pseudowave functions match the AE wave functions. In the core region ($r < r_c^l$), the pseudowave functions are smooth and nodeless: they deviate sensibly from the AE wave functions, which have 2 and 1 nodes, respectively, and show an oscillating behavior.

1.8.2 Norm-conserving pseudopotentials

The approach described above guarantees that the pseudo eigenvalues $\widetilde{\epsilon}_l$ match the AE eigenvalues ϵ_{nl}. However, to have a good transferability of the pseudopotential, the matching between the pseudo and AE eigenvalues is required to extend to wider energy ranges. This goal can be achieved if the pseudopotential has the same scattering properties as the real potential: in particular, in this case the so-called *logarithmic derivative* of the wave function, a common quantity in scattering theory, defined as:

$$\begin{aligned} f_l(\epsilon) &= \frac{d}{dr} \ln \psi_{\epsilon\, l}(r) \Big|_{r=R} \\ &= \frac{1}{\psi_{\epsilon\, l}(r)} \frac{d\psi_{\epsilon\, l}(r)}{dr} \Big|_{r=R}, \end{aligned} \tag{1.93}$$

is the same for the pseudo and the AE wave functions. In the practical construction of a pseudopotential, the logarithmic derivatives $f_l(\epsilon)$ of the pseudo and AE wave functions coincide at the atomic eigenvalues. From the scattering theory it is possible to prove that $f_l(\epsilon)$ fulfills the following relationship:

$$-2\pi \left|\psi_{\epsilon\, l}(r)\right|^2 \frac{df_l(\epsilon)}{d\epsilon} \Big|_{r=r_c^l} = 4\pi \int_0^{r_c^l} dr \left|\psi_{\epsilon\, l}(r)\right|^2. \tag{1.94}$$

The most straightforward way to have a good matching of the logarithmic derivatives is to impose that the quantity in the right-hand side of Eq. (1.94) is the same for the pseudo and the AE wave functions, which provides the following, *norm-conserving* condition [81]:

$$\int_0^{r_c^l} dr\,|\phi_l(r)|^2 = \int_0^{r_c^l} dr\,|\psi_{nl}(r)|^2. \tag{1.95}$$

1.8.3 Kleinman-Bylander pseudopotentials

In a solid, the pseudopotential is written as a sum over the ions of the corresponding atomic pseudopotential. If $\mathbf{R}_I$ are the positions of the ions, the local part of the pseudopotential is written as:

$$V_{\rm loc}(\mathbf{r}) = \sum_I V_{\rm loc}^{\gamma(I)}(\mathbf{r}-\mathbf{R}_I), \tag{1.96}$$

where $V_{\rm loc}^{\gamma(I)}$ is the local part of the atomic pseudopotential. The non-local part of the pseudopotential in three dimensions is written starting from the l-dependent radial part $\Delta V_{\rm ps}^l$ introduced before, in the following way [81]:

$$V_{\rm NL}(\mathbf{r},\mathbf{r}') = \sum_I \sum_l \sum_{m_l} \Delta V_{\rm ps}^{l\,\gamma(I)}(|\mathbf{r}-\mathbf{R}_I|)\,\delta(|\mathbf{r}-\mathbf{R}_I| - |\mathbf{r}'-\mathbf{R}_I|)\,\langle \mathbf{r}-\mathbf{R}_I|Y_{lm_l}\rangle\,\langle Y_{lm_l}|\mathbf{r}'-\mathbf{R}_I\rangle\,, \tag{1.97}$$

where l and m_l are the orbital and azimuthal quantum numbers, and $|Y_{lm_l}\rangle$ are spherical harmonics. Although being formally correct, this formulation turned out to be computationally expensive: in 1982, L. Kleinman and D. M. Bylander [82] noticed that when computing the matrix elements of $V_{\rm NL}$ between two PWs, the semi-local form of Eq. (1.97) (i.e. non-local in the angular variables, but local in the radial coordinate) required to compute and to store a number of integrals that increases quadratically with the size of the PWs basis set adopted. They proposed to write $V_{\rm NL}$ in real space in a *fully separable* form, non-local in the radial variable as well. In particular, they introduced the states $|\chi_l\rangle = \Delta V_{\rm ps}^l\,|\phi_l\rangle$, where $|\phi_l\rangle$ are the atomic pseudowave functions, and then wrote the non-local part of the pseudopotential in three dimensions as:

$$V_{\rm NL}(\mathbf{r},\mathbf{r}') = \sum_I \sum_l \sum_{m_l} \frac{1}{r^2}\,\frac{\langle \mathbf{r}-\mathbf{R}_I|\chi_l\,Y_{lm_l}\rangle\,\langle Y_{lm_l}\,\chi_l|\mathbf{r}'-\mathbf{R}_I\rangle}{\langle\chi_l|\phi_l\rangle}. \tag{1.98}$$

In this way, the number of integrals needed when computing the matrix elements of $V_{\rm NL}$ increases linearly with the number of PWs used.

The local and non-local parts, given by Eqs. (1.96) and (1.98), are then introduced in the KS equation for the extended system and the eigenvalues $\epsilon_{\mathbf{k}v}$ and the eigenfunctions $|\psi_{\mathbf{k}v}\rangle$ are computed. Since condition (1.95) holds, the charge density in the norm-conserving (NC) case is written as:

$$n(\mathbf{r}) = \sum_{\mathbf{k}v} f_{\mathbf{k}v}\;\langle\phi_{\mathbf{k}v}|\mathbf{r}\rangle\,\langle\mathbf{r}|\phi_{\mathbf{k}v}\rangle\,. \tag{1.99}$$

1.8.4 Ultrasoft pseudopotentials

In order to improve the accuracy of the technique, which tipically means enlarging the energy covered by the pseudopotential, a multi-projector form of the non-local part was proposed:

$$V_{\mathrm{NL}}(r, r') = \sum_{ij} B_{ij} \langle r|\beta_i\rangle \langle \beta_j|r'\rangle \,, \tag{1.100}$$

where:

$$B_{ij} = \langle \phi_i|\chi_j\rangle \,, \tag{1.101}$$

$$|\beta_i\rangle = \sum_j (B^{-1})_{ji} |\chi_j\rangle \,, \tag{1.102}$$

and the functions $|\chi\rangle$ are obtained in the following way:

$$|\chi_i\rangle = (\epsilon_i - T_l - V_{\mathrm{eff}}) |\phi_i\rangle \,. \tag{1.103}$$

i and j are indices that run from 1 to N_ϵ, the number of energies used in the construction of the pseudopotential for each l. The additional condition $B_{ij} - B_{ji} = 0$ has to be imposed in order for V_{NL} to be symmetric. The quantity $B_{ij} - B_{ji}$ can be written as [83]:

$$B_{ij} - B_{ji} = (\epsilon_i - \epsilon_j)\, q_{ij}, \tag{1.104}$$

where q_{ij} has been defined as:

$$q_{ij} = \langle \psi_i|\psi_j\rangle - \langle \phi_i|\phi_j\rangle \,, \tag{1.105}$$

where $|\phi_i\rangle$ are the pseudowave functions, while $|\psi_i\rangle$ are the all-electron wave functions. The norm-conservation condition given in Eq. (1.95) corresponds to have $q_{ii} = 0$. In order for V_{NL} to be hermitian, this condition has to be generalized to the condition $q_{ij} = 0$, $i \neq j$. As a consequence, it would be possible to build a pseudopotential that:

- is hermitian,
- is NC,
- is accurate in a wider range of energies than usual NC pseudopotentials.

However, the generalized norm-conserving condition is indeed difficult to satisfy. In 1990, Vanderbilt proposed to relax both the condition $q_{ij} = 0$ for $i \neq j$ and the norm-conserving condition, Eq. (1.95), which led to the so-called *ultrasoft* (US) scheme [83]. He noticed that the matrix $D_{ij} = B_{ij} + \epsilon_j q_{ij}$ is hermitian and recast V_{NL} in the form:

$$V_{\mathrm{NL}} = \sum_{ij} D_{ij} |\beta_i\rangle \langle \beta_j| \,. \tag{1.106}$$

By further introducing a non-local overlap operator S, defined as:

$$S = \mathbb{1} + \sum_{ij} q_{ij} |\beta_i\rangle \langle \beta_j| \,, \tag{1.107}$$

he wrote the KS equation as:

$$[T_l + V_{\text{eff}} + V_{\text{NL}}] \, |\phi_k\rangle = \epsilon_l \, S \, |\phi_k\rangle \, . \tag{1.108}$$

These equations lead to the following consequences:

- the pseudowave functions are not orthogonal to each other, while they fulfill the generalized orthogonality condition:

$$\langle \phi_i | \, S \, | \phi_j \rangle = \delta_{ij}; \tag{1.109}$$

- due to the relaxation of the norm-conserving condition, the charge density associated to the k-th eigenfunction cannot be computed as $\langle \phi_k | r \rangle \, \langle r | \phi_k \rangle$, but an additional term, called *augmentation charge*, has to be introduced:

$$n_k(r) = \langle \phi_k | r \rangle \, \langle r | \phi_k \rangle + \sum_{ij} Q_{ij}(r) \, \langle \phi_k | \beta_i \rangle \, \langle \beta_j | \phi_k \rangle \, , \tag{1.110}$$

  where $Q_{ij}(r)$ is the function integrated to compute q_{ij}, i.e.:

$$Q_{ij}(r) = \langle \psi_i | r \rangle \, \langle r | \psi_j \rangle - \langle \phi_i | r \rangle \, \langle r | \phi_j \rangle \, . \tag{1.111}$$

Passing to a periodic solid, we define the projectors $|\beta^I_{\tau l m_l}\rangle$ in the following way:

$$\langle \mathbf{r} | \beta^I_{\tau l m_l} \rangle = \frac{1}{r} \, \langle \mathbf{r} - \mathbf{R}_I | \beta_{\tau l} \, Y_{l m_l} \rangle \, . \tag{1.112}$$

The non-local part of the pseudopotential is written as:

$$V_{\text{NL}}(\mathbf{r}, \mathbf{r}') = \sum_I \sum_{\tau \, l \, m_l} \sum_{\tau' \, l' \, m'_l} D^{\gamma(I)}_{\substack{\tau l m_l \\ \tau' l' m'_l}} \, \langle \mathbf{r} | \beta^I_{\tau l m_l} \rangle \, \langle \beta^I_{\tau' l' m'_l} | \mathbf{r}' \rangle \, , \tag{1.113}$$

where

$$D^{\gamma(I)}_{\substack{\tau l m_l \\ \tau' l' m'_l}} = D^{\gamma(I)}_{\tau\tau'} \delta_{ll'} \delta_{m_l m'_l}, \tag{1.114}$$

while τ and τ' are the energy indices, called i and j above.

The charge density is then obtained by summing Eq. (1.110) over the occupied states:

$$n(\mathbf{r}) = \sum_{\mathbf{k}v} f_{\mathbf{k}v} \, \langle \phi_{\mathbf{k}v} | \mathbf{r} \rangle \, \langle \mathbf{r} | \phi_{\mathbf{k}v} \rangle + \sum_I \sum_{mn} \rho^I_{mn} Q^I_{mn}(\mathbf{r}), \tag{1.115}$$

where we introduced again the composite indices $m = \{\tau l m_l\}$ and $n = \{\tau' l' m'_l\}$. The coefficients ρ^I_{mn}, called *partial occupations*, are defined as:

$$\rho^I_{mn} = \sum_{\mathbf{k}v} f_{\mathbf{k}v} \, \langle \phi_{\mathbf{k}v} | \beta^I_m \rangle \, \langle \beta^I_n | \phi_{\mathbf{k}v} \rangle \, , \tag{1.116}$$

whereas the *augmentation functions* $Q^I_{mn}(\mathbf{r})$ are obtained by generalizing the radial functions $Q(r)$ to three dimensions in the following way:

$$Q^I_{mn}(\mathbf{r}) = \frac{1}{r^2}\left(\langle\psi_{\tau l}\, Y_{lm_l}|\mathbf{r}-\mathbf{R}_I\rangle\,\langle\mathbf{r}-\mathbf{R}_I|\psi_{\tau' l'}\, Y_{l'm'_l}\rangle - \langle\phi_{\tau l}\, Y_{lm_l}|\mathbf{r}-\mathbf{R}_I\rangle\,\langle\mathbf{r}-\mathbf{R}_I|\phi_{\tau' l'}\, Y_{l'm'_l}\rangle\right). \tag{1.117}$$

$Q^I_{mn}(\mathbf{r})$ can be factorized into the product of a radial part, $Q^I_{mn}(r)$, and an angular part that depends on the spherical harmonics with angular numbers $\{l, m_l\}$ and $\{l', m'_l\}$. The radial augmentation functions $Q^I_{mn}(r)$ depend on the AE wave functions, hence they present rapid oscillations in the core region, which increase the cut-off of the PWs needed to expand the charge density. This shortcoming can be avoided by pseudizing $Q_{mn}(r)$ itself. In practice, this is done by introducing a new set of functions $\widetilde{Q}^L_{mn}(r)$ that have the same L-th momentum as $Q_{mn}(r)$ [84], namely:

$$\int_0^{+\infty} dr\, r^L\, \widetilde{Q}^L_{mn}(r) = \int_0^{+\infty} dr\, r^L\, Q_{mn}(r). \tag{1.118}$$

The angular part of $Q^I_{mn}(\mathbf{r})$ is addressed by exploiting the properties of the spherical harmonics, in particular by writing the product of two spherical harmonics as a linear combination of spherical harmonics. As a final result, $Q_{mn}(\mathbf{r})$ is pseudized in the following way [84]:

$$\widetilde{Q}_{mn}(\mathbf{r}) = \sum_{LM} c(l\, m_l, l'\, m'_l, L\, M)\, \widetilde{Q}^L_{mn}(r)\, Y_{LM}(\Omega), \tag{1.119}$$

where $|l-l'| \leq L \leq l+l'$ and $-L \leq M \leq L$, while $c(l\, m_l, l'\, m'_l, L\, M)$ are the Clebsch-Gordan coefficients.

The fact that the charge density contains also the augmentation term implies that, when written in the PWs basis set, the kinetic energy cut-off needed to describe it accurately is, in general, higher than $4\, E_{\text{cut}}$. From a practical point of view, the cut-offs for the wave functions and the charge density are not related anymore and the convergence with respect to both of them must be studied.

The charge density, Eq. (1.115), is often written in an alternative way as:

$$n(\mathbf{r}) = \sum_{\mathbf{k}v} f_{\mathbf{k}v}\, \langle\phi_{\mathbf{k}v}|K(\mathbf{r})|\phi_{\mathbf{k}v}\rangle\,, \tag{1.120}$$

introducing the non-local kernel $K(\mathbf{r}, \mathbf{r}_1, \mathbf{r}_2)$:

$$K(\mathbf{r}, \mathbf{r}_1, \mathbf{r}_2) = \delta(\mathbf{r}-\mathbf{r}_1)\,\delta(\mathbf{r}-\mathbf{r}_2) + \sum_I \sum_{m\,n} Q^I_{mn}(\mathbf{r})\,\langle\mathbf{r}_1|\beta^I_m\rangle\,\langle\beta^I_n|\mathbf{r}_2\rangle\,. \tag{1.121}$$

As a side note, we remark that the NC framework can be obtained as a particular case of the US formulation by dropping the augmentation term in Eq. (1.121):

$$K(\mathbf{r}, \mathbf{r}_1, \mathbf{r}_2) = \delta(\mathbf{r}-\mathbf{r}_1)\delta(\mathbf{r}-\mathbf{r}_2), \tag{1.122}$$

which implies that the overlap matrix is $S = \mathbb{1}$.

Due to the generalized orthogonality condition, the KS equations become a generalized eigenvalue problem. Moreover, due to the augmentation charge contribution, the constrained minimization of the total energy functional:

$$\frac{\delta}{\delta\phi^*_{\mathbf{k}v}(\mathbf{r})}\left(E[n(\mathbf{r})] - \epsilon_{\mathbf{k}v}\left\langle\phi_{\mathbf{k}v}|S|\phi_{\mathbf{k}v}\right\rangle\right) = 0, \tag{1.123}$$

produces the following additional term in the KS potential:

$$\left(\int d^3r'\, V_{\text{eff}}(\mathbf{r}')\, Q_{mn}(\mathbf{r}')\right)|\beta^I_m\rangle\,\langle\beta^I_n|\,, \tag{1.124}$$

which is usually introduced in the non-local potential by defining the screened D coefficients [83, 84]:

$$\widetilde{D}^I_{mn} = D^{\gamma(I)}_{mn} + \int d^3r'\, V_{\text{eff}}(\mathbf{r}')\,\widetilde{Q}^I_{mn}(\mathbf{r}'). \tag{1.125}$$

$D^{\gamma(I)}_{mn}$ must be obtained by descreening the $\widetilde{D}^I_{mn}$ coefficients of the generating atomic configuration, as explained for the effective potential above.

The generalized orthogonality condition affects also the calculation of the forces. When applying the HF theorem to compute $\partial E_{\text{tot}}/\partial\lambda$, the derivative of the orthonormalization constraint, namely $\partial/\partial\lambda\,\langle\psi_i|S|\psi_i\rangle = 0$, must be properly taken into account. In particular:

$$\left\langle\frac{\partial\psi_i}{\partial\lambda}\middle|S|\psi_i\right\rangle + \langle\psi_i|S\middle|\frac{\partial\psi_i}{\partial\lambda}\right\rangle = -\left\langle\psi_i\middle|\frac{\partial S}{\partial\lambda}\middle|\psi_i\right\rangle, \tag{1.126}$$

therefore the total derivative of E_{tot} (Eq. (1.71)) reads:

$$\frac{dE_{\text{tot}}}{d\lambda} = \sum_i\left\langle\psi_i\middle|\frac{\partial V_{\text{KS}}}{\partial\lambda} - \epsilon_i\frac{\partial S}{\partial\lambda}\middle|\psi_i\right\rangle. \tag{1.127}$$

1.8.5 Projector augmented-wave pseudopotentials

A further step forward in the pseudopotentials theory was made in 1994 by the work of P. E. Blöchl [85]. The new method, named Projector Augmented-Wave method (PAW) resulted from the need to combine the versatility of the Augmented-Plane-Wave (APW) methods, which supply information about the wave functions in the core region (a feature that the pseudopotentials scheme did not have in the NC and US schemes), with the simplicity of the pseudopotentials formalism.

In Ref. [85], Blöchl proposed a generalization of the mapping technique of the pseudowave function into the AE wave function. He introduced a transformation operator T such that:

$$|\psi_i\rangle = T\,|\widetilde{\psi}_i\rangle\,. \tag{1.128}$$

As a consequence, the expectation value of a given operator A can be obtained either from the AE wave function via $\langle A\rangle = \langle\psi_i|A|\psi_i\rangle$, or from the pseudowave functions via $\langle A\rangle = \langle\widetilde{\psi}_i|\widetilde{A}|\widetilde{\psi}_i\rangle$ by defining the transformed operator $\widetilde{A} = T^\dagger\,A\,T$. The total energy can then be expressed

as a functional of the pseudowave functions and the KS equation for $|\widetilde{\psi}_i\rangle$ can be obtained by the constrained minimization condition:

$$\frac{\delta}{\delta\widetilde{\psi}_i^*(\mathbf{r})}\left(E[\{T\,|\widetilde{\psi}_i\rangle\}] - \epsilon_i\,\langle\widetilde{\psi}_i|T^\dagger\,T|\widetilde{\psi}_i\rangle\right) = 0. \tag{1.129}$$

Since the aim of the PAW method is to reconstruct the information about the AE wave functions in the core region, though keeping the advantages given by the formulation with pseudowave functions, the operator T is written as the sum of the identity operator and a sum of a set of local, atom-centered operators T_I, namely:

$$T = \mathbb{1} + \sum_I T_I. \tag{1.130}$$

T_I acts only within the atomic core region, also called *augmentation region* or *PAW sphere*. In order to pursue the reconstruction of the AE wave function, Blöchl proposed the following form for the local operator T:

$$T_I = \sum_I \sum_m \left(|\psi_m^I\rangle - |\phi_m^I\rangle\right)\langle\beta_m^I|\,, \tag{1.131}$$

where $|\psi_m^I\rangle$ and $|\phi_m^I\rangle$ are the atomic AE and pseudowave functions, while $|\beta_m^I\rangle$ are a set of projectors defined in a way similar to the NC and the US schemes.

Given the definition of the transformation T, the generic operator A transforms into:

$$\widetilde{A} = A + \sum_I \sum_{m\,n} \left(\langle\psi_m^I|A|\psi_n^I\rangle - \langle\phi_m^I|A|\phi_n^I\rangle\right)|\beta_m^I\rangle\,\langle\beta_n^I|\,, \tag{1.132}$$

i.e. a pseudized operator that coincides with A outside the PAW sphere, while inside the core region is properly devised to fulfill the condition:

$$\langle\widetilde{\psi}_i|\widetilde{A}|\widetilde{\psi}_j\rangle = \langle\psi_i|A|\psi_j\rangle\,. \tag{1.133}$$

Eq. (1.132) can be applied to any operator A. As an example, we mention the main results obtained while applying it to some of the ubiquitous operators in DFT, e.g. the identity operator and the charge density.

- The identity operator transforms in the following way:

$$\begin{aligned}\langle\psi_k|\mathbb{1}|\psi_j\rangle &= \langle\widetilde{\psi}_k|\widetilde{\psi}_j\rangle + \sum_I \sum_{m\,n}\left(\langle\psi_m^I|\psi_n^I\rangle - \langle\phi_m^I|\phi_n^I\rangle\right)\langle\widetilde{\psi}_k|\beta_m^I\rangle\,\langle\beta_n^I|\widetilde{\psi}_j\rangle \\ &= \langle\widetilde{\psi}_k|\widetilde{\psi}_j\rangle + \sum_I \sum_{m\,n} q_{mn}^I\,\langle\widetilde{\psi}_k|\beta_m^I\rangle\,\langle\beta_n^I|\widetilde{\psi}_j\rangle \\ &= \langle\widetilde{\psi}_k|S|\widetilde{\psi}_j\rangle\,,\end{aligned} \tag{1.134}$$

  similarly to the US case. The overlap matrix S is defined as in Eq. (1.107).

- The charge density transforms in the following way:

$$\begin{aligned} n(\mathbf{r}) &= \sum_{\mathbf{k}v} f_{\mathbf{k}v}\ \langle\psi_{\mathbf{k}v}|\mathbf{r}\rangle\,\langle\mathbf{r}|\psi_{\mathbf{k}v}\rangle \\ &= \sum_{\mathbf{k}v} f_{\mathbf{k}v}\ \langle\widetilde{\psi}_{\mathbf{k}v}|\mathbf{r}\rangle\,\langle\mathbf{r}|\widetilde{\psi}_{\mathbf{k}v}\rangle + \sum_{\mathbf{k}v}\sum_{I}\sum_{m\,n} f_{\mathbf{k}v}\ \left(\langle\psi^I_m|\mathbf{r}\rangle\,\langle\mathbf{r}|\psi^I_n\rangle - \langle\phi^I_m|\mathbf{r}\rangle\,\langle\mathbf{r}|\phi^I_n\rangle\right) \\ &\quad \times \langle\widetilde{\psi}_{\mathbf{k}v}|\beta^I_m\rangle\,\langle\beta^I_n|\widetilde{\psi}_{\mathbf{k}v}\rangle \\ &= \widetilde{n}(\mathbf{r}) + \sum_{I}\sum_{m\,n}\rho^I_{mn}\,Q^I_{mn}(\mathbf{r}), \end{aligned} \tag{1.135}$$

  that is similar to Eq. (1.115) reported for the US scheme.

The application of Eq. (1.132) can be extended to the KS Hamiltonian as well, leading to the total energy functional. While a comprehensive discussion is outside the scope of this work, we refer the interested reader to Refs. [85,86] for a detailed derivation. Here we simply report the final result, that is the KS equation obtained from Eq. (1.129):

$$\left[-\frac{1}{2}\nabla^2 + \widetilde{V}_{\text{eff}} + \sum_{I}\sum_{mn}\left(D^{1I}_{mn} - \widetilde{D}^{1I}_{mn} + \int d^3r'\widetilde{V}_{\text{eff}}(\mathbf{r}')Q^I_{mn}(\mathbf{r}')\right)|\beta^I_m\rangle\,\langle\beta^I_n|\right]|\psi_{\mathbf{k}v}\rangle = \epsilon_{\mathbf{k}v}S\,|\psi_{\mathbf{k}v}\rangle\,, \tag{1.136}$$

where the PAW D coefficients are given by:

$$D^{1I}_{mn} = \left\langle\psi^I_m\right| -\frac{1}{2}\nabla^2 + V_{\text{KS}}\left|\psi^I_n\right\rangle \tag{1.137}$$

$$\widetilde{D}^{1I}_{mn} = \left\langle\phi^I_m\right| -\frac{1}{2}\nabla^2 + \widetilde{V}_{\text{eff}}\left|\phi^I_n\right\rangle + \int_{\Omega_I} d^3r'\,\widetilde{V}_{\text{eff}}(\mathbf{r}')\,Q^I_{mn}(\mathbf{r}'), \tag{1.138}$$

and Ω_I indicates the PAW sphere of atom I.

1.9 Relativistic effects in electronic structure

Relativistic effects in condensed matter systems are relevant whenever the ratio v/c becomes non negligible. Near the nucleus, $v/c = Z\,\alpha$ (in atomic units), therefore relativistic effects become increasingly important for heavy elements. One of the most well known relativistic effects is the radial contraction of the inner s and p shells. Such contraction implies a more effective screening of the potential for the d and f orbitals (whose radial charge density distribution is more spread due to the centrifugal term proportional to $l(l+1)/r^2$), which will experience an upshift in energy and a radial expansion [87, 88]. A further important relativistic effect, experienced by the electrons with $l > 0$, is the *spin-orbit coupling* (SOC), which splits energy levels with the same orbital angular momentum according to the total angular momentum number j ($j = l \pm 1/2$).

Relativistic effects allow to explain several physical and chemical facts. As an example, we mention the explanation of the yellow color of gold. Early studies [1, 89] reported a comparison between relativistic and non-relativistic calculations on the band structure of gold, and showed that the excitation energies from the $5d$ band to the half-filled $6s$ band were

sensibly different in the two cases. More recently the calculation of the frequency-dependent dielectric constant [90, 91] showed that relativistic calculations are able to reproduce the lower bound of the optical absorption near 2 eV, whereas non-relativistic calculations are not and wrongly predict an absorption onset at 3.6 eV. Among the consequences of relativity, we further mention the effect on the bond lengths [1, 92] and the lattice parameters.

The exact method to systematically include all the relativistic effects is to solve the *Dirac equation* [14] which, for a free particle, reads:

$$i\hbar\frac{\partial\psi}{\partial t} = H\psi, \tag{1.139}$$

$$H = c\boldsymbol{\alpha}\cdot\mathbf{p} + \beta mc^2, \tag{1.140}$$

where $\mathbf{p}$ is the momentum, β is a 4×4 matrix:

$$\beta = \begin{pmatrix} \mathbb{1}_{2\times 2} & 0 \\ 0 & -\mathbb{1}_{2\times 2} \end{pmatrix}, \tag{1.141}$$

and $\boldsymbol{\alpha}$ is a set of three 4×4 matrices, with components:

$$\alpha_i = \begin{pmatrix} 0 & \sigma_i \\ \sigma_i & 0 \end{pmatrix}, \tag{1.142}$$

where σ_i are the Pauli matrices.

In presence of a potential, Eq. (1.139) turns out to be rather challenging to solve, since its solutions are four-component spinors. A common approach consists in performing a low-energy expansion (typically, in powers of v/c), of the Dirac equation. The first-order expansion of Eq. (1.139) gives the Schrödinger equation or, in presence of an external magnetic field $\mathbf{B}$, the *Pauli equation*:

$$\left\{\frac{1}{2m}\left[(\mathbf{p}+e\,\mathbf{A})^2 + e\,\hbar\,\boldsymbol{\sigma}\cdot\mathbf{B}\right] + V\right\}\psi = \epsilon\,\psi, \tag{1.143}$$

where $\mathbf{A}$ is the vector potential, while $\boldsymbol{\sigma}$ identifies a set made up of the three Pauli matrices. The second-order expansion gives three additional terms: the first two, called *mass-velocity* (mv) and *Darwin* (D) terms, are known in condensed matter physics as *scalar relativistic corrections*, and read:

$$H_{\mathrm{mv}} = -\frac{p^4}{8m^3c^2}, \tag{1.144}$$

$$H_{\mathrm{D}} = \frac{\hbar^2}{8m^2c^2}\,\nabla^2 V, \tag{1.145}$$

whereas the third term is the *spin-orbit* (SO) correction:

$$H_{\mathrm{SO}} = \frac{1}{2m^2c^2}\,\frac{1}{r}\,\frac{dV}{dr}\,\mathbf{S}\cdot\mathbf{L}. \tag{1.146}$$

In this approach, the relativistic corrections are used as a perturbation to the non-relativistic Schrödinger equation: perturbation theory is a well known technique and is

used, for instance, to discuss the fine structure of the hydrogen-like atoms. However, such approaches are accurate enough only for light atoms: concerning the relativistic corrections, the perturbation parameter $v/c = Z\,\alpha$ is small (enough for the second-order expansion mentioned above to be accurate) only for atoms up to the first row of transition metals. For heavier atoms, the perturbation v/c is not small and, in principle, many more terms in the perturbative expansion must be considered: for instance, $v/c \approx 0.58$ for the $5d$ metal Hg. It is clear that, in these cases, a complete solution of the Dirac equation is desirable.

The solutions of the Dirac equation are four-component spinors, usually written in terms of two-component spinors in the following way:

$$\psi = \begin{pmatrix} \psi_A \\ \psi_B \end{pmatrix}. \tag{1.147}$$

ψ_A and ψ_B are called *large* and *small* components because if the expression (1.147) is plugged into the time-independent Dirac equation, the two components are then related by the following relationship:

$$\psi_B = \frac{1}{E' + 2mc^2 - V}\, c\,\boldsymbol{\sigma}\cdot\mathbf{p}\,\psi_A, \tag{1.148}$$

where $E' = E - mc^2$ and V is the external potential. Eq. (1.148) implies that $\psi_B \propto v/c\,\psi_A$, whence ψ_B is called small component.

1.9.1 Scalar Relativistic and Fully Relativistic approaches

In presence of a central potential, the eigenfunction components ψ_A and ψ_B can be factorized into a radial function and a two-component *spin-angle function*. The Dirac Hamiltonian does not commute with the orbital angular momentum $\mathbf{L}$ or the spin angular momentum $\mathbf{S}$ separately, but it commutes with their sum, the total angular momentum $\mathbf{J} = \mathbf{L} + \mathbf{S}$. As a consequence, the angular part of ψ is the eigenfunction of the total angular momentum J^2 and of the azimuthal total angular momentum J_z, and can be written using two two-component spin-angle functions (see Appendix C for a more detailed discussion). The radial parts of ψ satisfies the radial Dirac equations. For the large component, the radial equation (see e.g. Ref. [93] for a complete discussion and the derivation) reads:

$$-\frac{\hbar^2}{2M}\left(\frac{d^2R_k}{dr^2} + \frac{2}{r}\frac{dR_k}{dr} - \frac{l(l+1)}{r^2}R_k\right) - \frac{\hbar^2}{2M^2c^2}\frac{dV}{dr}\left(\frac{dR_k}{dr} + \frac{1-k}{r}R_k\right) + V\,R_k = E\,R_k, \tag{1.149}$$

where: $M = m[1 - (V - E')/2mc^2]$, R_k is the radial function, and $k = -l$ or $k = l+1$ if the total angular momentum quantum number j is $j = l - 1/2$ or $j = l + 1/2$, respectively. Since two possible values of k are allowed for each l, two different radial functions are expected. Two different approaches are possible at this stage:

- *Scalar Relativistic* (SR): in order to simplify the problem, the quantum number k is substituted by a j-averaged k, called $\bar{k}$. Since $\bar{k} = 1$, the k-dependent term of Eq. (1.149), which represents the spin-orbit interaction, drops off. As a result, there is only one radial function.

- *Fully Relativistic* (FR): no simplifications are assumed. The complete Dirac equation, for both the large and the small component, is solved, to get two radial functions for each $l > 0$, one for $j = l + 1/2$ and one for $j = l - 1/2$.

1.9.2 Relativistic Pseudopotentials

In a practical *ab initio* approach based on plane waves, the shortcomings described in Section 1.8 affect the radial eigenfunctions of the Dirac equation in a similar way, hence a pseudopotentials-based theory is desirable. We remark that in the relativistic case, the goal is to find an appropriate $V_{\rm NL}$ that is able to reproduce the large-component of the Dirac eigenfunctions for $r \geq r_c$, which are then pseudized for $r < r_c$ in order to have both the pseudized wave function and the pseudopotential smooth enough to be represented with a reasonable number of plane waves.

At a first stage, the small component of the wave function can be neglected, hence the original four-component spinor problem is simplified into a two-component one. In the SR approach an additional simplification holds: the two large component radial functions are averaged, and we recover the SR wave function approach. In the FR approach, instead there are two different radial wave functions for each orbital angular number $l > 0$ and both of them have to be pseudized. The pseudopotential $V_{\rm NL}$ is written as a 2×2 matrix, and the most natural way to do it consists in generalizing the NC formalism by using the spin-angle functions, as proposed by L. Kleinman in 1980 [37]. However, when first proposed, the FR pseudopotential was written in a semilocal way, non-local only in the angular variables [94]. Further developments [38, 39] led to a fully separable form of $V_{\rm NL}$:

$$V_{\rm NL}^{\sigma_1\sigma_2}(\mathbf{r},\mathbf{r}') = \sum_I \sum_l \sum_j \sum_{m_j=-j}^{j} E_{lj}^{\gamma(I)} \, \langle \mathbf{r}|\beta_{lj}^I \, Y_{l\,1/2}^{Ijm_j\sigma_1}\rangle \, \langle \beta_{lj}^I \, Y_{l\,1/2}^{Ijm_j\sigma_2}|\mathbf{r}'\rangle \, . \tag{1.150}$$

The expression can be further simplified and recast into the usual pseudopotential construction scheme based on spherical harmonics [40]. Indeed, the spin-angle functions can be written in terms of real spherical harmonics (see Appendix C for more details):

$$Y_{l\,1/2}^{jm_j\sigma} = \sum_{m_l=-l}^{l} c_{m_j m_l}^{lj\sigma} \, Y'_{lm_l}, \tag{1.151}$$

where Y' indicates a real spherical harmonic function. Eq. (1.150) then becomes:

$$V_{\rm NL}^{\sigma_1\sigma_2}(\mathbf{r},\mathbf{r}') = \sum_I \sum_{ljm_l} \sum_{\substack{l'j'm'_l \\ }} D_{\substack{ljm_l \\ l'j'm'_l}}^{\gamma(I)\,\sigma_1\sigma_2} \, \langle \mathbf{r}|\beta_{lj}^I \, Y_{lm_l}^{\prime I}\rangle \, \langle \beta_{l'j'}^I \, Y_{l'm'_l}^{\prime I}|\mathbf{r}'\rangle \, , \tag{1.152}$$

where all the dependence on the spin indices has been attributed to the D coefficients of the pseudopotential, defined as:

$$D_{\substack{ljm_l \\ l'j'm'_l}}^{\gamma(I)\,\sigma_1\sigma_2} = E_{lj}^{\gamma(I)} \, f_{\substack{ljm_l \\ l'j'm'_l}}^{\sigma_1\sigma_2} \, \delta_{ll'} \, \delta_{jj'}, \tag{1.153}$$

$$f_{\substack{ljm_l \\ l'j'm'_l}}^{\sigma_1\sigma_2} = \sum_{m_j=-j}^{j} c_{m_j m_l}^{lj\sigma_1} \, c_{m_j m'_l}^{*\,l'j'\sigma_2}. \tag{1.154}$$

The ideas behind the the FR approach have been extended to the US pseudopotentials scheme [40] as well. The non-local part of the pseudopotential is first written with projectors that contain spin-angle functions:

$$V_{\mathrm{NL}}^{\sigma_1\sigma_2}(\mathbf{r},\mathbf{r}') = \sum_I \sum_{\tau l j m_j} \sum_{\substack{\tau' l' j' m'_j \\ \tau' l' j' m'_j}} D^{\gamma(I)}_{\substack{\tau l j m_j \\ \tau' l' j' m'_j}} \langle \mathbf{r}|\beta^I_{\tau l j}\, Y^{I j m_j \sigma_1}_{l\,1/2}\rangle \langle \beta^I_{\tau' l' j'}\, Y^{I j' m'_j \sigma_2}_{l'\,1/2}|\mathbf{r}'\rangle\,, \tag{1.155}$$

where τ and τ' are indices that run from 1 to N_ϵ, the number of energies used in the construction of the pseudopotential for each l and j. Then the complex spin-angle functions are transformed into real spherical harmonics, getting the following expression, used in practical implementations:

$$V_{\mathrm{NL}}^{\sigma_1\sigma_2}(\mathbf{r},\mathbf{r}') = \sum_I \sum_{\tau l j m_l} \sum_{\substack{\tau' l' j' m'_l \\ \tau' l' j' m'_l}} D^{\gamma(I)\,\sigma_1\sigma_2}_{\substack{\tau l j m_l \\ \tau' l' j' m'_l}} \langle \mathbf{r}|\beta^I_{\tau l j}\, Y^{I}_{l m_l}\rangle \langle \beta^I_{\tau' l' j'}\, Y^{I}_{l' m'_l}|\mathbf{r}'\rangle\,, \tag{1.156}$$

where:

$$D^{\gamma(I)\,\sigma_1\sigma_2}_{\substack{\tau l j m_l \\ \tau' l' j' m'_l}} = D^{l j\,\gamma(I)}_{\tau\tau'}\, f^{\sigma_1\sigma_2}_{\substack{l j m_l \\ l' j' m'_l}}\, \delta_{ll'}\, \delta_{jj'}. \tag{1.157}$$

In the following, we will adopt a short-hand notation by introducing the compact indices $m = \{\tau\, l\, j\, m_l\}$, $n = \{\tau'\, l'\, j'\, m'_l\}$.

Total energy functional, spin density, and Kohn-Sham potential

Since the wave functions are written as two-component spinors, the spin density functional theory formalism is necessary. Moreover, in the FR approach the pseudopotentials is written as a non-diagonal matrix, thus it is necessary to adopt the non-collinear formulation. If the external potential V_{ext} is modeled with the pseudopotentials formalism, the total energy functional (Eq. (1.40)), the spin density (Eq. (1.37)), and the KS equations (Eq. (1.43)) must be generalized accordingly. Once the single-particle orbitals $|\psi_i^\sigma\rangle$ are introduced, the total energy functional is written in the following compact way:

$$E[\{\psi_i^\sigma\}] = \bar{E}[\{\psi_i^\sigma\}] + F[n(\mathbf{r}), |\mathbf{m}(\mathbf{r})|], \tag{1.158}$$

where the functional $\bar{E}$ contains the kinetic energy functional, the non-local potential contribution, and the smearing contribution E_{met} mentioned in Section 1.6:

$$\bar{E}[\{\psi_i^\sigma\}] = \sum_i \sum_{\sigma_1\,\sigma_2} \left[f_i \left\langle \psi_i^{\sigma_1} \right| -\frac{1}{2}\nabla^2\, \delta^{\sigma_1\sigma_2} + V_{\mathrm{NL}}^{\sigma_1\sigma_2} \left| \psi_i^{\sigma_2} \right\rangle \right] + E_{\mathrm{met}}, \tag{1.159}$$

while the functional F is made up of the local potential contribution and the Hartree and exchange-correlation functionals:

$$F[n(\mathbf{r}), |\mathbf{m}(\mathbf{r})|] = \int d^3r\, V_{\mathrm{loc}}(\mathbf{r})\, n(\mathbf{r}) + E_{\mathrm{H}}[n(\mathbf{r})] + E_{\mathrm{xc}}[n(\mathbf{r}), |\mathbf{m}(\mathbf{r})|]. \tag{1.160}$$

The spin density is computed from the single-particle wave functions as:

$$n^{\sigma\sigma'}(\mathbf{r}) = \sum_i \sum_{\sigma_1\,\sigma_2} f_i\, \langle \psi_i^{\sigma_1}|K^{\sigma\sigma'}_{\sigma_1\sigma_2}(\mathbf{r})|\psi_i^{\sigma_2}\rangle\,, \tag{1.161}$$

where the non-local kernel $K^{\sigma\sigma'}_{\sigma_1\sigma_2}$ is (see Eq. (1.121), which here is properly generalized to the non-collinear case) [40]:

$$K^{\sigma\sigma'}_{\sigma_1\sigma_2}(\mathbf{r},\mathbf{r}_1,\mathbf{r}_2) = \delta(\mathbf{r}-\mathbf{r}_1)\delta(\mathbf{r}-\mathbf{r}_2)\delta^{\sigma\sigma_1}\delta^{\sigma'\sigma_2} + \sum_I \sum_{m\,n} \sum_{m_1\,n_1} Q^I_{mn}(\mathbf{r})\, f^{\sigma_1\sigma}_{m_1 m}\, f^{\sigma'\sigma_2}_{n n_1}\, \langle \mathbf{r}_1|\beta^I_{m_1}\rangle\, \langle \beta^I_{n_1}|\mathbf{r}_2\rangle. \tag{1.162}$$

The single-particle orbitals are the solutions of the KS equations, obtained by the constrained minimization condition applied to the total energy functional:

$$\sum_{\sigma_2} \left[-\frac{1}{2}\nabla^2\, \delta^{\sigma_1\sigma_2} + V^{\sigma_1\sigma_2}_{\mathrm{KS}} \right] |\psi^{\sigma_2}_i\rangle = \epsilon_i \sum_{\sigma_2} S^{\sigma_1\sigma_2}\, |\psi^{\sigma_2}_i\rangle\,, \tag{1.163}$$

where the KS potential is:

$$V^{\sigma_1\sigma_2}_{\mathrm{KS}}(\mathbf{r}_1,\mathbf{r}_2) = V^{\sigma_1\sigma_2}_{\mathrm{NL}}(\mathbf{r}_1,\mathbf{r}_2) + \sum_{\sigma_3\,\sigma_4} \int d^3r'\, V^{\sigma_3\sigma_4}_{\mathrm{LOC}}(\mathbf{r}')\, K^{\sigma_3\sigma_4}_{\sigma_1\sigma_2}(\mathbf{r}',\mathbf{r}_1,\mathbf{r}_2), \tag{1.164}$$

$$V^{\sigma_3\sigma_4}_{\mathrm{LOC}}(\mathbf{r}) = V_{\mathrm{eff}}(\mathbf{r})\, \delta^{\sigma_3\sigma_4} - \mu_{\mathrm{B}}\, \mathbf{B}_{\mathrm{xc}}(\mathbf{r}) \cdot \boldsymbol{\sigma}^{\sigma_3\sigma_4}. \tag{1.165}$$

Similarly to the non-relativistic case, the additional terms that appear in the KS equations because the augmentation terms in the spin density depend on the spinor wave functions, can be included in the non-local part of the pseudopotential by defining the screened D coefficients [40]:

$$\widetilde{D}^{I\,\sigma_1\sigma_2}_{m_1 n_1} = D^{\gamma(I)\,\sigma_1\sigma_2}_{m_1 n_1} + \sum_{m\,n} \sum_{\sigma_3\,\sigma_4} \sum_{\alpha=1}^{4} f^{\sigma_1\sigma_3}_{m_1 m}\, A^{\sigma_3\sigma_4}_{\alpha}\, I^{I\,\alpha}_{mn}\, f^{\sigma_4\sigma_2}_{n n_1}, \tag{1.166}$$

where $\mathbf{A}$ is a four-component vector ($\alpha = 1,\ldots,4$) of 2×2 matrices: $\mathbf{A} = (\mathbb{1}, \sigma_x, \sigma_y, \sigma_z)$. The quantity $I^{I\,\alpha}_{mn}$ is defined as:

$$I^{I\,\alpha}_{mn} = \int d^3r\, Q^I_{mn}(\mathbf{r})\, C'_{\alpha}(\mathbf{r}), \tag{1.167}$$

where the four-component vector $\mathbf{C}'$ is defined as: $\mathbf{C}' = (V_{\mathrm{eff}}, -\mu_{\mathrm{B}}B_{\mathrm{xc},x}, -\mu_{\mathrm{B}}B_{\mathrm{xc},y}, -\mu_{\mathrm{B}}B_{\mathrm{xc},z})$. The overlap matrix S appearing in the KS equations (Eq. (1.163)) can be determined from the integration of the kernel K:

$$\begin{aligned} S^{\sigma_1\sigma_2}(\mathbf{r}_1,\mathbf{r}_2) &= \sum_{\sigma_3} \int d^3r'\, K^{\sigma_3\sigma_3}_{\sigma_1\sigma_2}(\mathbf{r}',\mathbf{r}_1,\mathbf{r}_2) \\ &= \delta(\mathbf{r}_1-\mathbf{r}_2)\, \delta^{\sigma_1\sigma_2} + \sum_I \sum_{m_1\,n_1} q^{\gamma(I)\,\sigma_1\sigma_2}_{m_1 n_1}\, \langle \mathbf{r}_1|\beta^I_{m_1}\rangle\, \langle \beta^I_{n_1}|\mathbf{r}_2\rangle\,, \end{aligned} \tag{1.168}$$

where the coefficients $q^{\gamma(I)\,\sigma_1\sigma_2}_{m_1 n_1}$ are spin-dependent and follow from the generalization of the coefficients $q^{\gamma(I)}_{mn} = \int d^3r\, Q^I_{mn}(\mathbf{r})$ [40]:

$$q^{\gamma(I)\,\sigma_1\sigma_2}_{m_1 n_1} = \sum_{mn} \sum_{\sigma_3} f^{\sigma_1\sigma_3}_{m_1 m}\, q^{\gamma(I)}_{mn}\, f^{\sigma_3\sigma_2}_{n n_1}. \tag{1.169}$$

Chapter 2

Spin-polarized electronic surface states of clean Os(0001) and Re(0001) surfaces: an *ab initio* fully relativistic investigation

Surfaces can host electronic states localized on the last few layers and the surface electronic structure is a key ingredient to predict many properties of materials. Pure surface states are usually found in the gaps of the projected band structure (PBS) [95], while resonances can be present also within the PBS. Due to surface states, surfaces can have properties different from the bulk, as found e.g. in topological insulators [10–12]. Moreover, since surfaces lack inversion symmetry, even non-magnetic (i.e. time-reversal invariant) materials can have surface states with a non-vanishing spin polarization. Hence, surface states might be practically useful for instance in spintronics applications [2,3], and it is worthwhile to characterize them. The energy dispersion of surface states with respect to $\mathbf{k}_{\parallel}$, the wave vector parallel to the surface, and in some cases also their spin polarization, have been analyzed for many surfaces of different materials, by both theoretical (DFT [96–103]) and experimental (photoelectron spectroscopy, PES [104–113], angular- and spin-resolved) techniques. For instance, among the heavy metal surfaces, the L-gap surface states of Au(111) are a paradigmatic example [96–101,105,106]. Their main feature is a split parabolic energy dispersion, which can be interpreted as an effect of spin-orbit coupling and explained by the Rashba model [5]. The latter suggests that the average direction of the electron spin is perpendicular to the wavevector $\mathbf{k}_{\parallel}$ and parallel to the surface, with opposite directions in the two energy paraboloids, a property that has been proven by experiments [98], although in real materials the presence of the underlying atomic layers can give rise to a small spin component orthogonal to the surface.

Similar states have been studied in Ir(111) and Pt(111) surfaces [100,102,107–113]. Pass-

ing from Au to Pt and to Ir their behavior changes: in Au(111) they are found in a PBS gap (the so-called L-gap) and show a dispersion with positive curvature, while in Ir(111) they hybridize with bulk states and have a characteristic negative curvature [102, 112]. In Pt(111) their nature turns out to be trickier to characterize. At variance with Au(111) they are empty and resemble the Au(111) states away from $\bar{\Gamma}$, but close to $\bar{\Gamma}$ they are very close to bulk states and the predicted hybridization is quite sensitive to the technical details of the calculation [100, 102].

Re(0001) is another interesting surface used [114–116] both as a support for other metallic layers and as a reactive catalytic surface. Very recently, it has been shown that artificially constructed Fe chains on top of Re(0001) surface exhibit a spin spiral state [117]. Though having been widely studied, little information is available about its electronic structure. Os(0001) is another surface similar to the (111) surface of Ir, Pt, and Au, but little information is available about it [118]. Os(0001) and Re(0001) could have states similar to the Rashba split surface states with inverted dispersion as in Ir(111) but *a priori* one cannot exclude the presence of empty surface states in a gap analogous to the L-gap. Also the other surface states could be similar, but both the energy dispersion and their spin polarization, are poorly known. An obvious difference between the (0001) surfaces of Os and Re and the other surfaces mentioned is the position of the Fermi level, due to the lower atomic number, while more subtle differences could be due to the hexagonal close-packed (hcp) structure that on the third layer differs from the face-centered-cubic (fcc) surfaces.

In this chapter, we present and discuss the results of a first principle study of Os(0001) and Re(0001). In particular, we analyze their band structure and characterize their main surface states, including the Rashba split states. We find that they have an inverted dispersion as in Ir(111), and cross the Fermi level. For some selected states we study in detail the spin polarization. We first use symmetry considerations to determine its direction in different high-symmetry lines and points of the BZ then we follow, for the most interesting surface states, the direction of the spin polarization as a function of $\mathbf{k}_{\parallel}$. This spin polarization is potentially measurable in spin-resolved ARPES experiments.

2.1 Methods

First principle calculations were performed by means of DFT [34, 35] within the LDA scheme, as implemented in the `Quantum ESPRESSO` [119–121] and `thermo_pw` [1] packages. The Perdew and Zunger's [56] parameterization for the exchange-correlation energy has been used. Spin-orbit coupling effects are included by using the FR PAW method [122] (see Section 1.8.5), with $5d$ and $6s$ valence electrons and $5s$ and $5p$ semicore states (PPs `Os.rel-pz-spn-kjpaw_psl.1.0.0.UPF` for Os and `Re.rel-pz-spn-kjpaw_psl.1.0.0.UPF from pslibrary.1.0.0` for Re, from pslibrary.1.0.0 [2] [123]). while SR calculations are performed with the PAW PPs `Os.pz-spn-kjpaw_psl.1.0.0.UPF` and `Re.pz-spn-kjpaw_psl.1.0.0.UPF` for Os and Re, respectively, from pslibrary.1.0.0. Calculations on the bulk system,

[1] `thermo_pw` is a driver of the `Quantum ESPRESSO` (QE) routines which provides an alternative organization of the QE work-flow for the most common tasks. For more information see `https://dalcorso.github.io/thermo_pw`.

[2] See `https://dalcorso.github.io/pslibrary`

System-method	a (a.u.)	c (a.u.)
Os FR LDA (this work)	5.135	8.047
Os exp. (Ref. [124])	5.169	8.162
Re FR LDA (this work)	5.175	8.338
Re exp. (Ref. [124])	5.217	8.425

Table 2.1: Computed FR LDA and experimental lattice constants of bulk hcp Os and Re.

were performed with an hexagonal close-packed (hcp) structure at the theoretical LDA lattice constants: a comparison between the theoretical LDA and experimental geometries is reported in Table 2.1. The surfaces have been simulated by the slab method. For Os(0001) we used a 24-layers slab perpendicular to the [0001] direction, while for Re(0001) we used both a 24-layers and a 25-layers slab perpendicular to the [0001] direction in order to check the stability of the results with respect to the breaking of the inversion symmetry. The slab replicas have been separated by a vacuum space of 34 a.u. and 44 a.u. in Os(0001) and Re(0001), respectively. The slab crystal structure has been obtained from the bulk, with a further relaxation along the [0001] direction, which has the most relevant effects on the first three atomic layers: in particular, the distance between the first two layers decreases of 5.4% with respect to the idealized interlayer distance in the bulk, while the distance between the second and the third layer increases of 2.9%. At a first stage, we performed a calculation with a starting non-zero magnetization, but the self-consistent ground state of the slab ended up to be non magnetic. The pseudo wavefunctions have been expanded in a PWs basis set with a kinetic energy cut-off of 60 Ry for both systems, while the charge density with a cut-off of 360 Ry and 400 Ry for Os(0001) and Re(0001), respectively. BZ integrations have been performed using a shifted uniform Monkhorst-Pack [74] **k**-point mesh of $12 \times 12 \times 1$ and $16 \times 16 \times 1$ points for the Os(0001) and Re(0001) slabs, respectively, and $12 \times 12 \times 8$ and $16 \times 16 \times 10$ points for bulk Os and Re, respectively. The presence of a Fermi surface has been dealt with by the Methfessel-Paxton method [71] with a smearing parameter $\eta = 0.02$ Ry in both systems. With these parameters the total energy is converged within 10^{-3} Ry and the crystal parameters within 10^{-3} Å.

In Figs. 2.1 (a)-(b) we show the first two atomic layers of the 24-layers slab and the 25-layers slab, respectively. The 24-layers slab has a D_{3d} point group. In particular, the z axis, normal to the surface, is a $\bar{3}$ rotoinversion axis, while the axes [100], [110], and [010] in Fig. 2.1 (a) are two-fold rotation axes. There are also three mirror planes, $(\bar{1}20)$, $(2\bar{1}0)$, and (110) shown in Fig. 2.1 (a). The 25-layers slab has instead, a D_{3h} point group. The z axis is a $\bar{6}$ axis, while the axes [210], [120], and $[\bar{1}10]$, shown in Fig. 2.1 (b), are two-fold rotation axes. Moreover, there are three mirror planes, whose traces coincide with the C_2 axes [210], [120], and $[\bar{1}10]$. The electronic band structure was calculated along the path $\bar{\Gamma} - \bar{K} - \bar{M} - \bar{\Gamma}$ (that is along the $\bar{T}$, $\bar{T}'$, and $\bar{\Sigma}$ high-symmmetry lines) of the Surface Brillouin Zone (SBZ), shown in Figs. 2.1 (c)-(d). The small point group of **k** of the two slabs is indicated in the band structures in Figs. 2.2, 2.11 (a), and 2.11 (b), both for the high symmetry points ($\bar{\Gamma}$, $\bar{K}$, and $\bar{M}$) and for the high symmetry lines ($\bar{T}$, $\bar{T}'$, and $\bar{\Sigma}$). In particular, for the 24-layers slab, at $\bar{\Gamma}$, $\bar{K}$, and $\bar{M}$ the small group of **k** is D_{3d}, D_3, and C_{2h}, respectively. Along the high symmetry lines $\bar{T}$, $\bar{T}'$, and $\bar{\Sigma}$ it is C_2, C_2, and C_s, respectively. Along $\bar{T}$ the rotation axis

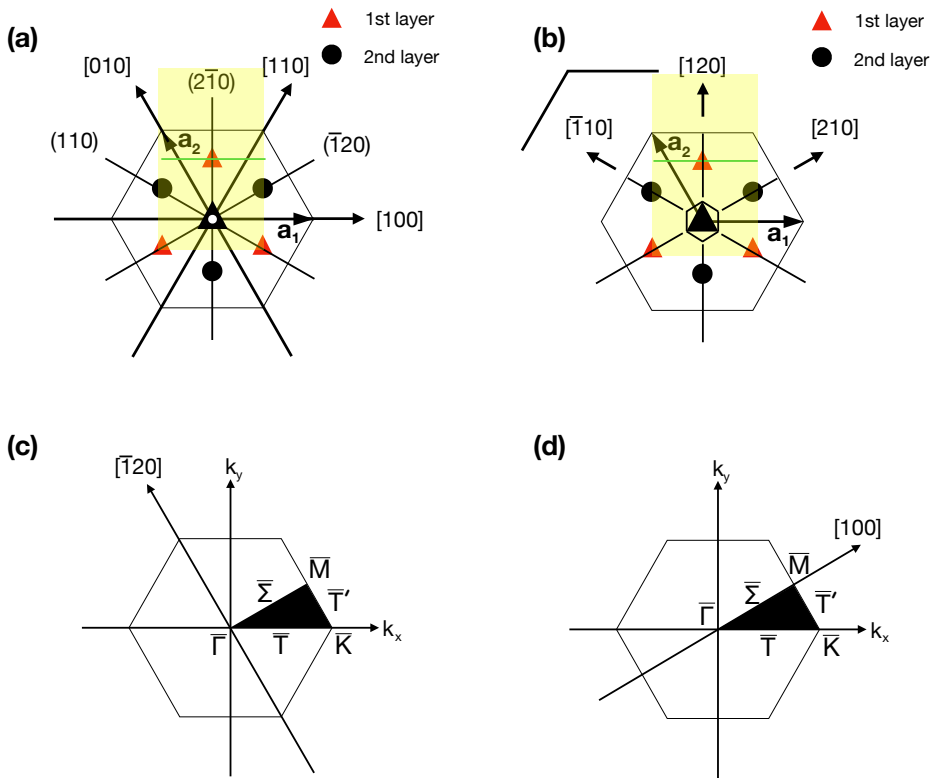

Figure 2.1: (a)-(b) Positions of the atoms in the first two atomic layers of the Re(0001) 24-layers and 25-layers slab, respectively. Arrows and solid lines indicate the C_2 rotation axes and the mirror planes, respectively. (c)-(d) Surface Brillouin Zone of Re(0001) 24-layers and 25-layers slab, respectively. The Irreducible Brillouin Zone (IBZ) and the path used to plot the electronic band structure are shown. The [$\bar{1}$20] and [100] axes are the two-fold rotation axes of the small groups of $\mathbf{k}_{\|}$ along $\bar{T}'$ for the 24-layers and along $\bar{\Sigma}$ for the 25-layers slab, respectively.

coincides with the x-axis, while along $\bar{T}'$ the rotation axis is the [$\bar{1}$20] axis, shown in Fig. 2.1 (c). Finally, along $\bar{\Sigma}$ the trace of the mirror plane of C_s is $\bar{\Sigma}$. On the other hand, for the 25-layers slab, at $\bar{\Gamma}$, $\bar{K}$, and $\bar{M}$ the small group of $\mathbf{k}$ is D_{3h}, C_{3h}, and C_{2v}, respectively, while along the high symmetry lines $\bar{T}$, $\bar{T}'$, and $\bar{\Sigma}$ it is C_s, C_s, and C_{2v}, respectively. In particular, along $\bar{T}$ and $\bar{T}'$ the mirror plane is σ_h. The two slabs have more symmetry elements than the surfaces, since they have symmetry operations that exchange the two surfaces. Removing these elements, the surface point group is C_{3v}, while the small groups of $\mathbf{k}$ are C_{3v}, C_3, and C_s for $\bar{\Gamma}$, $\bar{K}$, and $\bar{M}$ respectively and C_1, C_1, and C_s along $\bar{T}$, $\bar{T}'$, and $\bar{\Sigma}$. Actually, they are the same for both slabs.

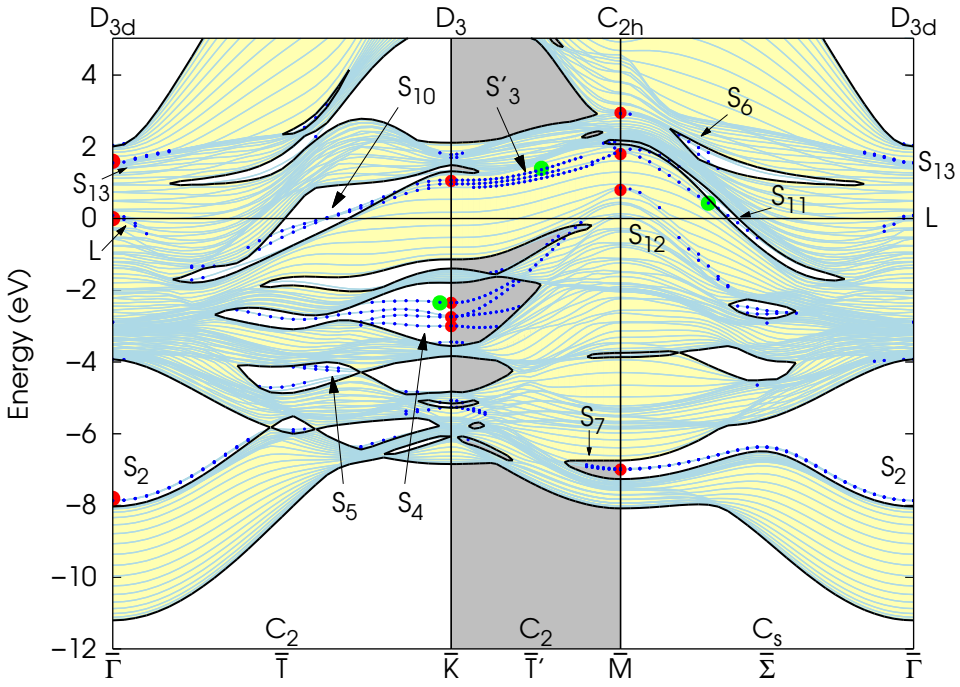

Figure 2.2: LDA FR-PAW surface band structure of Os(0001). The yellow region is the PBS, the light blue lines are the slab electronic states and the blue dots indicate surface states or resonances, defined as those having a charge density greater than 0.5 on the last two atomic layers of both surfaces. Energies are measured with respect to the Fermi energy, and the energy maximum in the figure is the computed work function (5.03 eV).

2.2 Os(0001)

2.2.1 Results

In this section we analyze the FR band structure of Os(0001), shown in Fig. 2.2. We characterize the main surface states and compare with Au(111), Pt(111), and Ir(111) (Refs. [99], [102]). A list of the main surface states, their energy and symmetry, is given in Table 2.2. Whenever possible, we use the same names as in Refs. [99] and [102]. We start our analysis from the $\bar{\Gamma}$ point, where we find two main gaps in the PBS. Taking the energy zero at the Fermi energy, the highest starts at 2 eV and is similar to the L-gap of the fcc surfaces. It is located higher in energy with respect to Au(111), Pt(111), and Ir(111), due to the lower number of electrons per cell. At $\bar{\Gamma}$ we find a second gap, between -8 eV $< E < -4$ eV, approximately at the same energy as in Pt(111) and Ir(111), although a bit wider and extending up to half of the $\bar{T}$ line and along the whole $\bar{\Sigma}$ line. As in Ir(111), and at variance with Au(111) and Pt(111), no surface states are found in the L-gap. Rashba-split surface states similar to the L-gap states of Au(111) are found around $\bar{\Gamma}$ near the Fermi energy and,

Surface State	$\mathbf{k}_\parallel$	ε (eV) Os(0001)	ε (eV) Ir(111)	ε (eV) Pt(111)	ε (eV) Au(111)	Small group of $\mathbf{k}_\parallel$	Symmetry
L	$\bar{\Gamma}$	0.08	−0.31	0.1	−0.5	D_{3d} (C_{3v})	Γ_4^-, Γ_4^+ (Γ_4)
S_2	$\bar{\Gamma}$	−7.87	−8.0	−7.4	−7.6		Γ_4^+, Γ_4^- (Γ_4)
S_{13}	$\bar{\Gamma}$	1.55	—	—	—		Γ_4^-, Γ_4^+ (Γ_4)
S'_{3a}	$\bar{K}$	1.07	—	—	—	D_3 (C_3)	$\Gamma_5 \oplus \Gamma_6$ ($2\Gamma_6$)
S'_{3b}	$\bar{K}$	0.97	—	—	—		Γ_4 ($\Gamma_4 \oplus \Gamma_5$)
S_{4a}	$\bar{K}$	−2.35	−2.7	−2.8	−3.7		Γ_4 ($\Gamma_4 \oplus \Gamma_5$)
S_{4b}	$\bar{K}$	−2.72	−3.1	−3.1	−4.0		$\Gamma_5 \oplus \Gamma_6$ ($2\Gamma_6$)
S_{4c}	$\bar{K}$	−2.74	−3.1	−3.1	−4.0		Γ_4 ($\Gamma_4 \oplus \Gamma_5$)
S_{4d}	$\bar{K}$	−2.99	−3.5	−3.7	−4.7		Γ_4 ($\Gamma_4 \oplus \Gamma_5$)
S_6	$\bar{M}$	2.93	1.6	0.6	—	C_{2h} (C_s)	$\Gamma_3^- \oplus \Gamma_4^-$($\Gamma_3 \oplus \Gamma_4$)
S_{11}	$\bar{M}$	1.90	—	—	—		$\Gamma_3^+ \oplus \Gamma_4^+$, $\Gamma_3^- \oplus \Gamma_4^-$ ($\Gamma_3 \oplus \Gamma_4$)
S_{12}	$\bar{M}$	0.86	—	—	—		$\Gamma_3^- \oplus \Gamma_4^-$($\Gamma_3 \oplus \Gamma_4$)
S_7	$\bar{M}$	−7.00	−6.7	−6.3	−6.6		$\Gamma_3^+ \oplus \Gamma_4^+$, $\Gamma_3^- \oplus \Gamma_4^-$ ($\Gamma_3 \oplus \Gamma_4$)
S_{10}	0.6 $\bar{K}$	−0.24	−0.8	−1.2	—	C_2 (C_1)	$\Gamma_3 \oplus \Gamma_4$
S_{12}	0.6 $\bar{M}$	−1.90	−2.6	−2.6	—	C_s (C_s)	$\Gamma_3 \oplus \Gamma_4$

Table 2.2: Energy and symmetry properties of the surface states discussed in the paper for the Os(0001), Ir(111), Pt(111), and Au(111) surfaces. The reported symmetry refers to the slab. In parenthesis, the symmetry relevant for the surface.

as in Ir(111), show a characteristic negative dispersion. At $\bar{\Gamma}$ there are two groups of two degenerate states, transforming as the Γ_{4+} and Γ_{4-} representations of the D_{3d} group, that extend up to 0.15 Å^{-1} along $\bar{T}$ and to 0.13 Å^{-1} along $\bar{\Sigma}$. Due to the finiteness of the slab the two surfaces are not perfectly decoupled, so the two groups of states are not exactly degenerate at $\bar{\Gamma}$, although their energy splitting is very small (≈ 0.01 eV). Neglecting this splitting it is possible to fit them with two parabolas as in the Rashba model [5]:

$$E_\pm = \frac{\hbar^2}{2m^*} k_\parallel^2 \pm \gamma_{\text{SO}}\, k_\parallel, \tag{2.1}$$

where $k_\parallel$ is the magnitude of the wave-vector parallel to the surface, m^* is the effective electron mass and γ_{SO} is the spin-orbit coupling parameter. γ_{SO} and m^* are obtained by fitting $E_+ - E_-$ as a function of $k_\parallel$ with a straight line and $E_+ + E_-$ with a parabola centered in $\bar{\Gamma}$, respectively. The fit of our data, shown in Fig. 2.3, gives: $\gamma_{\text{SO}} = (6.1 \pm 0.1) \times 10^{-9}$ eV cm, which falls between the values found in Au(111) and Ir(111) ($\gamma_{\text{SO}} = 4.5 \times 10^{-9}$ eV cm [99] and $\gamma_{\text{SO}} = 13 \times 10^{-9}$ eV cm [102] respectively). The fitted value of $m^*/m = -0.140 \pm 0.001$, where m is the electron mass, is approximately 40% lower in modulus than in Au(111) (0.24) and Ir(111) (−0.22) [3]. Along $\bar{\Sigma}$ we find $m^*/m = -0.146 \pm 0.002$ and a γ_{SO} parameter equal, within the error bar, to the one obtained along $\bar{T}$. In Fig. 2.4 (a) we show the sum of charge densities of the two degenerate states at higher energy that form the L_a band. The planar average of the charge density is maximum at the surface and decays toward the center of the slab. The contour plots suggest that it has mainly s character hybridized with some d states, as also confirmed by the projection on atomic wavefunctions. We find very small projections on the unoccupied $6p$ states.

At lower energies, at the $\bar{\Gamma}$ point, we find a group of two two-fold degenerate states within a PBS gap, similar to the S_2 states previously studied in Au(111), Pt(111), and

[3] A calculation with a 40-layer slab has been performed as well. The fit gives $\gamma_{\text{SO}} = (6.5 \pm 0.3) \times 10^{-9}$ eV cm, and $m^*/m = -0.132 \pm 0.002$.

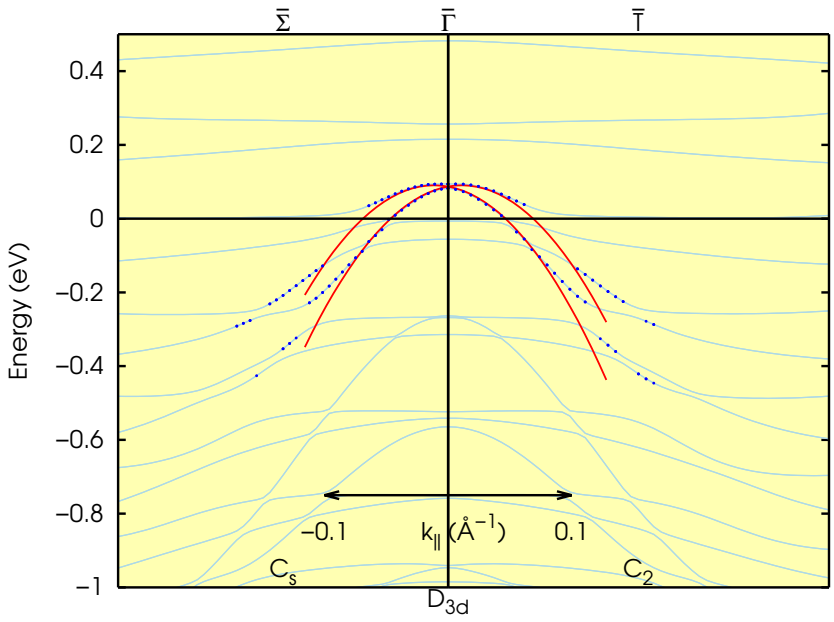

Figure 2.3: Magnification of the FR electronic band structure around $\bar{\Gamma}$. The L states are shown with blue dots. Red lines show the two Rashba parabolas that fit the energy dispersion, with the parameters reported in the main text.

Ir(111) [111]. At $\bar{\Gamma}$, the S_2 states have Γ_{4+} and Γ_{4-} symmetry, as the L states. Their energy difference is linear in $k_{\|}$, as for Rashba split states, although with a smaller value of the spin-orbit parameter. A fit performed as above gives: $\gamma_{\rm SO} = (0.288 \pm 0.003) \times 10^{-9}$ eV cm and $m^*/m = 0.732 \pm 0.005$, with identical values, within the error bar, along $\bar{T}$ and $\bar{\Sigma}$.

In Fig. 2.4 (b) we show the charge density for the S_{2a} states, those with higher energy at $\bar{\Gamma}$. The states are localized in the last two atomic layers.

Finally, in $\bar{\Gamma}$ there is another group of states, called S_{13} in Fig. 2.2, that was not discussed before. They appear in the relaxed surface and, at $\bar{\Gamma}$, they have symmetry Γ_{4+} and Γ_{4-}. In the non-relaxed surface they are not identified as surface states because their charge density (≈ 0.47) is slightly below the threshold chosen (0.5). As the L states, they are resonances, as shown by the planar average of the charge density in Fig. 2.4 (c). The contour plots, together with the analysis of the projection of the states on atomic orbitals, show that the S_{13} states have mainly d character, with main projections on the second and first atomic layers.

L, S_2, and S_{13} states extend also along a portion of the $\bar{T}$ line, where they transform as the $\Gamma_3 \oplus \Gamma_4$ representations of C_2. Along $\bar{T}$ we find other PBS gaps as well: the widest ones contain also some surface states as S_{10}, that cross the Fermi level, and S_4, at lower energies. A small energy gap, in the central part of the $\bar{T}$ line, contains the S_5 states. At variance with Au(111), Pt(111), and Ir(111) the S_{10} states are inside a PBS gap, while they were hybridized with the bulk in the other surfaces.

The main states at the $\bar{K}$ point are S_3' (3 couples of empty states) and S_4 (4 couples of occupied states). S_{3a}' have symmetry $\Gamma_5 \oplus \Gamma_6$ (D_3 group), while S_{3b}' have symmetry Γ_4 (D_3 group). The planar average and contour plots of the charge density of S_{3a}' are shown

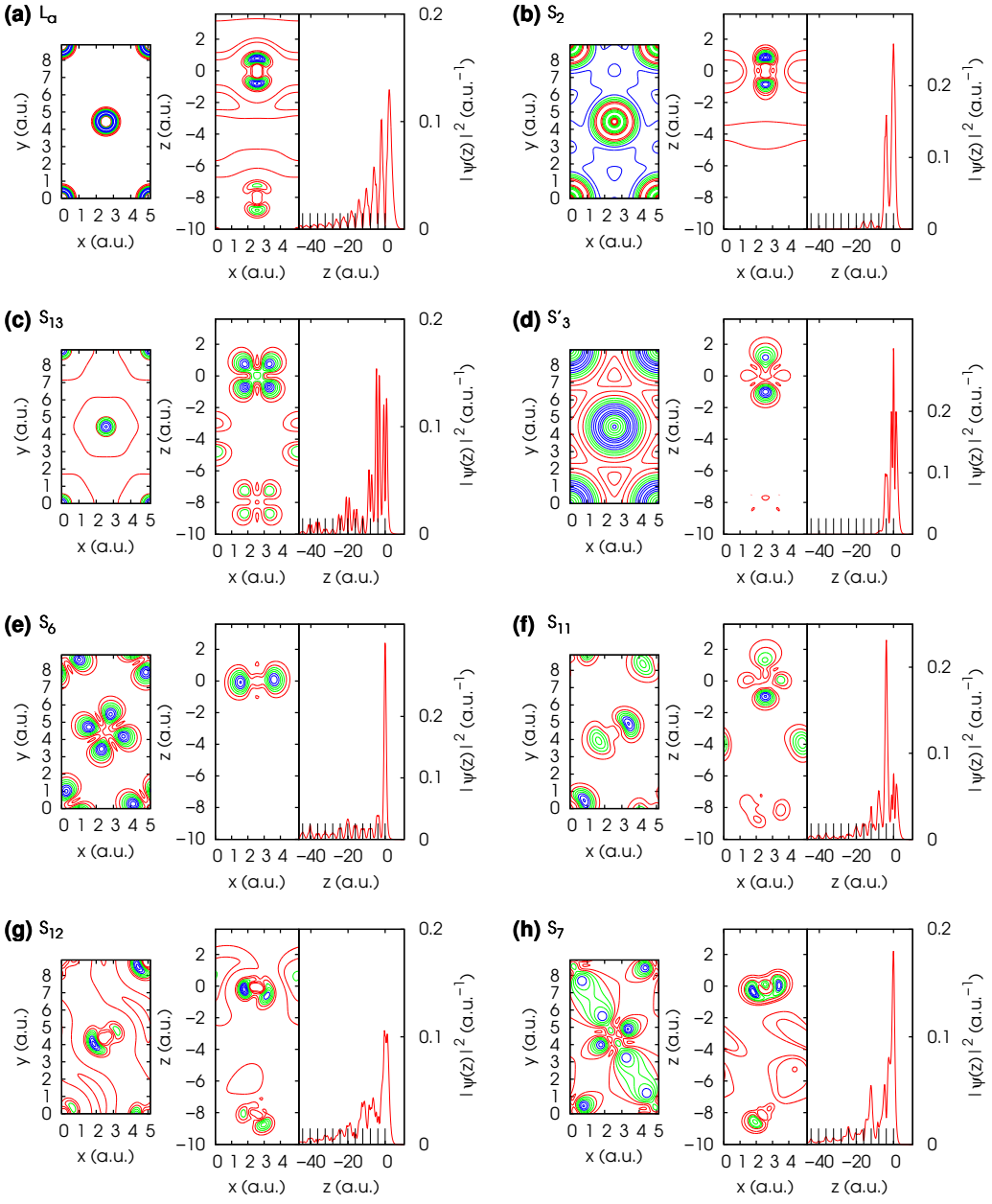

Figure 2.4: Contour plots and planar average of the charge density corresponding to the selected FR surface states indicated with red dots in Fig. 2.2. The left subplot shows the charge density contour plot in the yellow region in Fig. 2.1a, on the top atomic layer of the slab. The central subplot shows the contour plot in a plane perpendicular to the slab, whose trace is the green line in Fig. 2.1a. The contours are equally spaced and are indicated with different colors (red, green, and blue in increasing order of charge density). The first three atomic layers are shown. The right subplot shows the planar average of the charge density in one half of the slab. The vacuum is on the right; the x tics represent the positions of the atomic layers.

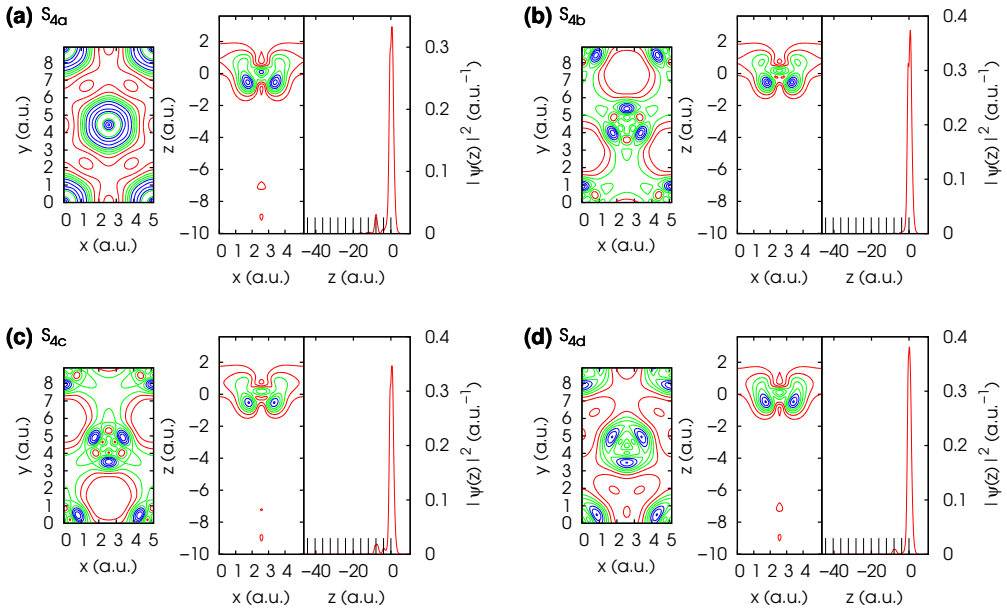

Figure 2.5: Contour plots and planar average of the charge density of the S_4 surface states at $\bar{K}$. The organization of the subplots is the same as in Fig. 2.4.

in Fig. 2.4 (d). These states are almost entirely localized in the first two layers and derive mainly from $d_{3z^2-r^2}$ states. A comparison with the S_3' states in Ir(111) shows that they have a similar character, although in Ir(111) they are in a PBS gap.

In the PBS gap located at -3.8 eV $< E < -1.8$ eV we find the S_4 states, whose charge densities are shown in Fig. 2.5. They are strongly localized on the top atomic layer, with a very small contribution in the third layer for S_{4a}, S_{4c}, and S_{4d}. To analyze in more detail their nature, in Fig. 2.6 we compare the FR S_4 states with those found in the SR scheme. In the SR case (Fig. 2.6 (a)), the S_4 states are two couples of degenerate states. Along $\bar{T}$ ($\bar{T}'$) each couple is made up of an even and an odd state with respect to the C_2 rotation about the x ($[\bar{1}20]$) axis. Their degeneracy is due to the localization of the states in the outermost atomic layers, not to symmetry. Only at $\bar{K}$, the two states at higher energy are exactly degenerate and transform as the E representation of the D_3 group, while the states at lower energy have A_1 and A_2 symmetry, respectively. The former projects with similar weights on $d_{x^2-y^2}$, d_{xy}, d_{xz}, and d_{zy} of the first layer, while the latter projects mainly on d_{xy} and $d_{x^2-y^2}$ states, with small projections on d_{xz} and d_{yz}.

In the FR band structure, along the $\bar{T}$ and $\bar{T}'$ lines all the states have symmetry $\Gamma_3 \oplus \Gamma_4$ of the group C_2, consistent with the product of the SR representation with the $D^+_{1/2}$ representation of spin ($A \otimes D^+_{1/2} = \Gamma_3 \oplus \Gamma_4$, $B \otimes D^+_{1/2} = \Gamma_3 \oplus \Gamma_4$). At $\bar{K}$ S_{4a}, S_{4c}, and S_{4d} have symmetry Γ_4 (group D_3), while S_{4b} has symmetry $\Gamma_5 \oplus \Gamma_6$. Multiplying the SR symmetries with $D^+_{1/2}$ we have $A_1 \otimes D^+_{1/2} = \Gamma_4$, $A_2 \otimes D^+_{1/2} = \Gamma_4$, $E \otimes D^+_{1/2} = \Gamma_4 \oplus \Gamma_5 \oplus \Gamma_6$ and, as a result, the FR S_4 states mix both the SR states. Another consequence of the spin-orbit effects is the anti-crossing of the states S_{4b} and S_{4c} near $\bar{K}$ ($k_\parallel = 1.59\,\text{Å}^{-1}$).

The surface states found in $\bar{K}$ extend also partly along $\bar{T}'$ but do not reach $\bar{M}$. Near $\bar{M}$ there are three gaps in the PBS. Two of them, at 2 eV and -3.8 eV, are quite narrow, while

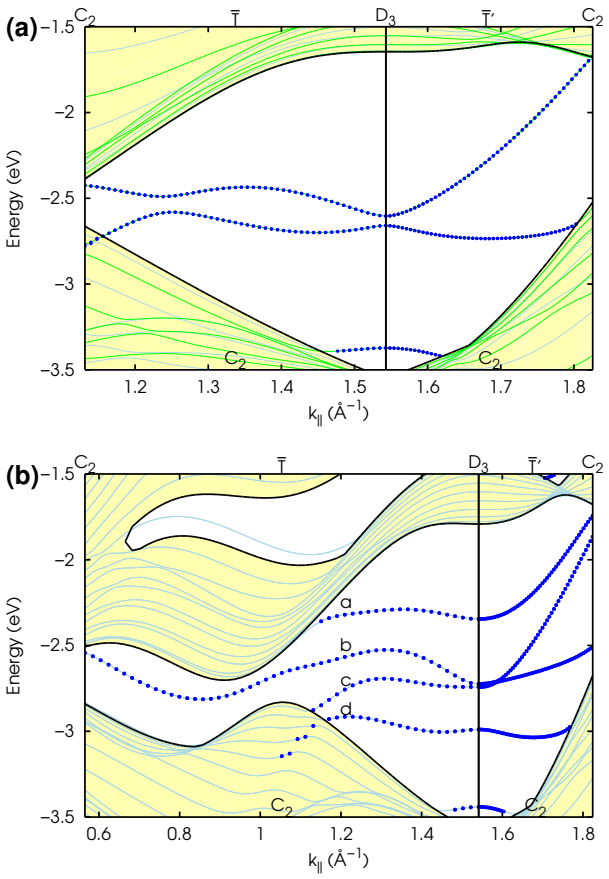

Figure 2.6: Enlarged view of the S_4 surface states around $\bar{K}$ in the SR (a) and FR (b) case, respectively.

the third one is between -7 eV $< E < -6.5$ eV. At variance with Au(111), Pt(111), and Ir(111) we do not find the gap that contained the Dirac-like S_8 states studied in Ref. [101], and S_8 states are not found in Os(0001). Moreover, the gap along $\bar{\Sigma}$ that contains the S_2 states extends up to the $\bar{M}$ point and includes also the S_7 surface states. The other surface states at $\bar{M}$ are, in decreasing order of energy, S_6, S_{11}, and S_{12}. S_6 is empty, has symmetry $\Gamma_{3-} \oplus \Gamma_{4-}$ (C_{2h} group) and is a resonance, as can be seen from the planar average of its charge density in Fig. 2.4 (e). This state, present in Au(111) (SR) band structure, disappears when spin-orbit coupling is included (see [99] for more details). It is present also in the FR band structure of Pt(111) and Ir(111), but it is not located in a PBS gap as in the SR Au(111) surface. The charge density contours of the S_6 states in Au(111) are pretty similar to those of Os(0001), both in the top atomic layer and perpendicularly to the surface. At $\bar{M}$ we find also the states S_{11} and S_{12}, that belong to the representations $\Gamma_{3+} \oplus \Gamma_{4+}$ and $\Gamma_{3-} \oplus \Gamma_{4-}$ of C_{2h} respectively. They are both resonances, with the main charge contribution coming from second (S_{11}) or first (S_{12}) layer. S_{11} have mainly $d_{3z^2-r^2}$ character, as shown by the contour plot in the plane perpendicular to the surface, and smaller components coming from first layer d_{xy} and $d_{x^2-y^2}$ states. Even though we gave them the same names as the states

present in the same energy region in Ir(111), S_{11} and S_{12} look quite different from those of Ref. [102]. S_{12} has non-negligible projections on many d states of the first six layers of the slab and small projection on s states. Finally, again at $\bar{M}$, but deeper in energy we have the S_7 states, arranged in two couples of degenerate states, with symmetry $\Gamma_{3+} \oplus \Gamma_{4+}$ and $\Gamma_{3-} \oplus \Gamma_{4-}$ respectively. In Fig. 2.4 (h) we report the contour plots and planar average of the charge density of S_7, which shows relevant contributions on the first, second and fourth layer. The S_7 states of Os(0001) are in a PBS gap and differ somewhat from those of Au(111). S_7 projects on many atomic wavefunctions: the main contributions come from d states of the first two layers and s states of the top layer.

2.2.2 Spin polarization: results and discussion

In this section we discuss the spin polarization of some of the surface states found above. The spin polarization can be obtained integrating the planar average of the magnetization density over half slab:

$$m_\alpha = \int_0^{L/2} m_\alpha(z)\, dz\,, \tag{2.2}$$

where the zero of z is taken at the center of the slab and L is its length along z, including vacuum. $m_\alpha(z)$ in Eq. 2.2 is the planar average of the magnetization density $m^\alpha_{\mathbf{k}n}(\mathbf{r})$ associated to the Bloch state $\langle \mathbf{r}|\psi_{\mathbf{k}n\sigma}\rangle$ and is defined as:

$$m_\alpha(z) = \int_A m^\alpha_{\mathbf{k}n}(x,y,z)\, dx\, dy\,, \tag{2.3}$$

where A is the yellow shaded region shown in Fig. 2.1 (a), and

$$m^\alpha_{\mathbf{k}n}(\mathbf{r}) = \mu_\mathrm{B} \sum_{\sigma_1\,\sigma_2} \sigma_\alpha^{\sigma_1\sigma_2}\ \langle \psi^{\sigma_1}_{\mathbf{k}n}|\mathbf{r}\rangle\, \langle \mathbf{r}|\psi^{\sigma_2}_{\mathbf{k}n}\rangle\,, \tag{2.4}$$

where μ_B is the Bohr magneton and σ_α are the Pauli matrices. The sum over σ_1 and σ_2 is over the spin indices.

Bulk Os and Os(0001) slab have inversion symmetry, and since Os is nonmagnetic and its Hamiltonian is time-reversal invariant, all the bands are at least two-fold degenerate. Eq. 2.4 must be generalized accordingly considering the sum of the contributions of the degenerate states to the magnetization. The surface breaks inversion symmetry, hence we expect the states to have a non-zero average spin polarization when integrating the sum of the two magnetization densities in half slab.

The crystal possesses other symmetries as well, like rotations ($\mathcal{S}$), possibly together with fractional translations ($\mathbf{f}$). They can induce some constraint on the magnetization density, leading in some cases to a vanishing spin polarization. If $\{\mathcal{S}, \mathbf{f}\}$ is an operation of the small space group of $\mathbf{k}$, or if it is when composed with time-reversal $\mathcal{T}$, the sum of the magnetization densities of degenerate states must obey the following relationship:

$$\mathbf{m}(\mathbf{r}) = \pm\tilde{\mathcal{S}}\, \mathbf{m}(\mathcal{S}^{-1}\mathbf{r} - \mathcal{S}^{-1}\mathbf{f}), \tag{2.5}$$

where $\tilde{\mathcal{S}}$ is the proper part of $\mathcal{S}$. The $\pm$ signs of Eq. 2.5 distinguish the operations that require $\mathcal{T}$ ($-$ sign) from those that do not require it ($+$ sign) and are due to the fact that $\mathcal{T}$

$\mathbf{k}_\parallel$	Slab	Surface
$\bar{\Gamma}$	$D_{3d} \otimes \{E, \mathcal{T}\}$	$C_{3v} \otimes \{E, \mathcal{T}\}$
$\bar{T}$	$C_{2h}(C_2)$	$C_s(C_1)$
$\bar{K}$	$D_{3d}(D_3)$	$C_{3v}(C_3)$
$\bar{T}'$	$C_{2h}(C_2)$	$C_s(C_1)$
$\bar{M}$	$C_{2h} \otimes \{E, \mathcal{T}\}$	$C_s \otimes \{E, \mathcal{T}\}$
$\bar{\Sigma}$	$C_{2h}(C_s)$	$C_s(C_s)$

Table 2.3: Small groups of $\mathbf{k}_\parallel$ at high symmetry points and high symmetry lines for the slab (central column) and a single surface (right column).

reverses the sign of the magnetization. For a complete derivation of Eq. (2.5), the interested reader is referred to Appendices B, E, and F.

Os(0001) space group does not contain any fractional translation, so we have $\mathbf{f} = \mathbf{0}$, and in the following we focus on the small point group of $\mathbf{k}$.

In addition to its operations one can consider the magnetic point group, obtained by multiplying the small point group operations by $\{E, \mathcal{TI}\}$ ($\mathcal{I}$ is the inversion), since $\mathcal{TI}$ leaves $\mathbf{k}$ invariant and $\mathcal{I}$ is contained in the slab point group D_{3d}. The magnetic point groups for the high symmetry lines and points of Os(0001) slab are summed up in the central column of Table 2.3. For the surface we must remove from these groups the operations that exchange the two slab surfaces, obtaining the groups listed in the right column of Table 2.3.

For a group that contains $\mathcal{T}$, Eq. 2.5 implies, using $\mathcal{S} = \mathbb{1}$, that $\mathbf{m}(\mathbf{r}) = -\mathbf{m}(\mathbf{r})$, so $\mathbf{m}(\mathbf{r}) = \mathbf{0}$. In Os(0001) this is the case for the small point group of the time-reversal invariant $\mathbf{k}$ points $\bar{\Gamma}$ and $\bar{M}$.

The states at $\bar{T}$, $\bar{T}'$, $\bar{\Sigma}$, and $\bar{K}$, have instead a non-zero magnetization density. We show it in Fig. 2.7 on the plane xy (the yellow shaded area in Fig. 2.1 (a)) for the states highlighted with green dots in Fig. 2.2 (a state in each line or point).

Along $\bar{T}$ the small magnetic point group of $\mathbf{k}_\parallel$, $C_s(C_1)$, contains $\mathcal{TI}C_{2x} = \mathcal{T}\sigma_y$ (σ_y is the mirror plane perpendicular to x), which inserted in Eq. 2.5 leads to $m_\parallel(x, y, z) = -m_\parallel(-x, y, z)$, $m_\perp(x, y, z) = m_\perp(-x, y, z)$, and $m_z(x, y, z) = -m_z(-x, y, z)$, since $\tilde{\mathcal{S}} = C_{2x}$, the two-fold rotation about x. As an example we show the state S_{4a} in Fig. 2.7 (a).

Along $\bar{T}'$ the small magnetic point group of $\mathbf{k}_\parallel$, $C_s(C_1)$, has elements $\{E, \mathcal{T}\sigma_{\bar{\Sigma}}\}$, where $\sigma_{\bar{\Sigma}}$ is the mirror plane $(\bar{1}20)$. Considering $\mathcal{T}\sigma_{\bar{\Sigma}}$ in Eq. 2.5, we find that $m_\parallel$ has opposite signs in the two sides of the mirror $\sigma_{\bar{\Sigma}}$, while $m_\perp$ and m_z have the same sign, as confirmed by the state S'_{3a} (Fig. 2.7 (b)).

Along $\bar{\Sigma}$, the small magnetic point group of $\mathbf{k}_\parallel$, $C_s(C_s)$, contains only the operations E and $\sigma_{\bar{\Sigma}}$ and not $\mathcal{T}$ or operations that require $\mathcal{T}$. Considering the operation $\sigma_{\bar{\Sigma}}$ in Eq. 2.5 one finds that $m_\parallel$ and m_z change sign in the two sides of the mirror $\sigma_{\bar{\Sigma}}$, while $m_\perp$ does not, as shown by the state S_{11} in Fig. 2.7 (c).

Finally, at the $\bar{K}$ point the small magnetic point group of $\mathbf{k}_\parallel$ is $C_{3v}(C_3)$, with operations $\{E,\ C_3,\ C_3^2,\ \mathcal{T}\sigma_y,\ \mathcal{T}\sigma_{\bar{\Sigma}},\ \mathcal{T}\sigma_{\bar{\Sigma}'}\}$, where $\sigma_{\bar{\Sigma}'}$ is the mirror plane (110). Among these, $\mathcal{T}\sigma_y$ leads to $m_\parallel(x, y, z) = -m_\parallel(-x, y, z)$, $m_\perp(x, y, z) = m_\perp(-x, y, z)$, $m_z(x, y, z) = m_z(-x, y, z)$, as along $\bar{T}$. C_3 and C_3^2 operations lead to a three-fold rotational symmetry for the m_z component, whereas $\mathcal{T}\sigma_{\bar{\Sigma}}$ and $\mathcal{T}\sigma_{\bar{\Sigma}'}$ lead to the mirror planes $(\bar{1}20)$ and (110) for the m_z

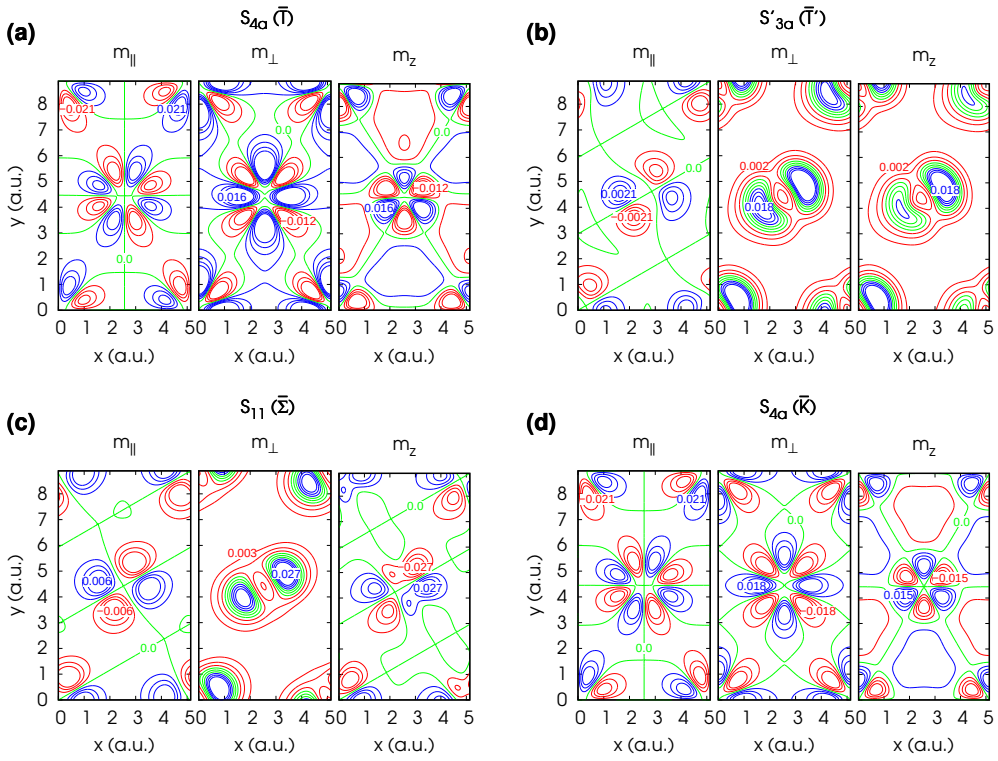

Figure 2.7: Magnetization density contour plots in the yellow region in Fig. 2.1a, on the top atomic layer of the slab, for the selected FR surface states, indicated with green dots in Fig. 2.2. The three subplots show, from left to right, the contour plot of the components parallel and perpendicular to the high symmetry line, and perpendicular to the slab. The contour levels are equally spaced and range from a minimum and a maximum value, indicated in the figure.

component, while they impose more complex constraints on $m_{\parallel}$ and $m_{\perp}$. As an example we show the state S_{4a} in Fig. 2.7 (d).

In Fig. 2.8 we show, for the same states as in Fig. 2.7, the planar averages of the components of the magnetization density. The S_{4a} states at $\bar{T}$ and $\bar{K}$ show a magnetization that vanishes after five layers below the surface, while S'_{3a} and S_{11} have some non negligible contribution also in the center of the slab. As a consequence of the symmetries discussed above, all states have a vanishing component $m_{\parallel}(z)$ parallel to the high symmetry line: as a result the spin polarization lies in a plane perpendicular to the high symmetry line. The states along $\bar{\Sigma}$ have also a vanishing z component, so their spin polarization has a fixed direction, parallel to the surface. Moreover, since $\bar{K}$ belongs both to $\bar{T}$ and $\bar{T}'$, both the components parallel to $\bar{T}$ and $\bar{T}'$ must vanish, so the states at $\bar{K}$ have only a z component. This is in agreement with the conclusions of Ref. [125].

Along $\bar{T}$ and $\bar{T}'$ the spin polarization can rotate in a plane perpendicular to the high symmetry line and we investigate its rotation for a few surface states: L, S'_3, S_{10}, shown in Fig. 2.9, and S_4, depicted in Fig. 2.10. We start our analysis from the L states (Fig. 2.9 (a)). Their spin polarization is mainly parallel to the surface and perpendicular to the high

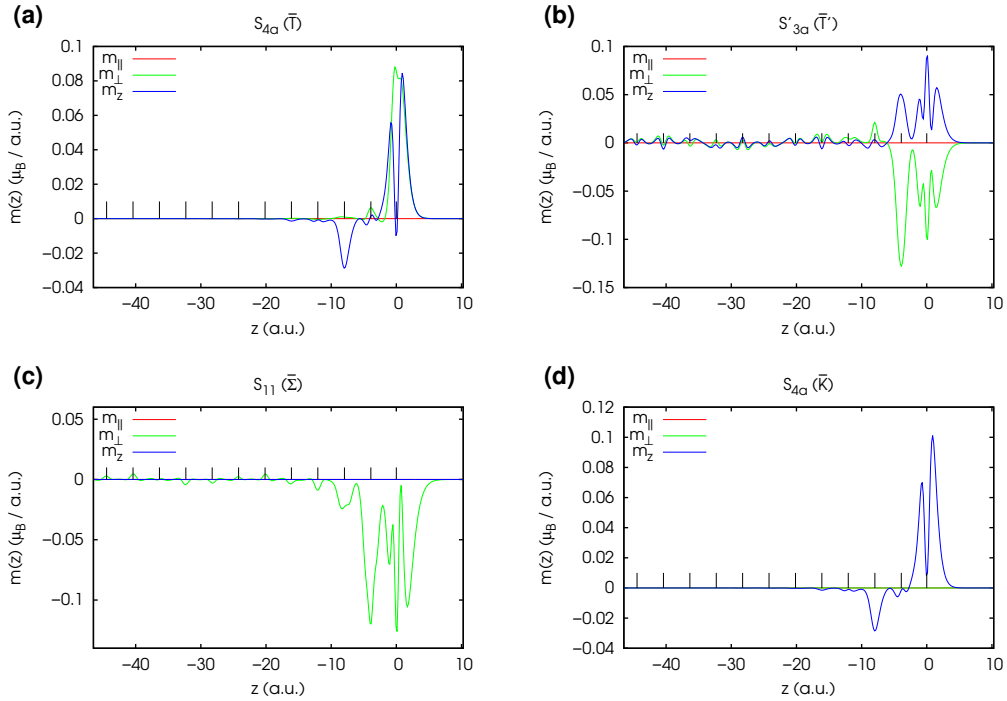

Figure 2.8: Planar average of the magnetization density for the same states as in Fig. 2.7. Only one half of the slab is shown. The vacuum is on the right of each plot, while the tics in the reference line represent the position of the atomic layers.

symmetry line, as predicted by the Rashba model, although a small component perpendicular to the surface survives along $\bar{T}$. The spin gets reverted when crossing the $\bar{\Gamma}$ point, due to the different orientation of the $\bar{M}-\bar{\Gamma}$ and $\bar{\Gamma}-\bar{K}$ lines. The spin flipping is not sudden as predicted by the Rashba model, due to the residue coupling between the two surfaces that opens a small gap at $\bar{\Gamma}$ (Fig. 2.3).

Next we consider the S'_3 states (Fig. 2.9 (b)-(d)), named S'_{3a}, S'_{3b}, and S'_{3c} in decreasing order of energy. They show a quite smooth behavior, with a slowly varying spin polarization along the $\bar{T}'$ line, although there are some differences among them. The spin of S'_{3a} state points outside the slab, the spins of S'_{3b} and S'_{3c} point towards the slab. Moreover, S'_{3b} shows a small rotation of the spin, which points mainly along z, whereas in S'_{3a} and S'_{3c} the rotation is more evident: the spin is oriented mainly along z at $\bar{K}$ and ends up with a main component perpendicular to the high symmetry line.

The spin polarization of the S_{10} states (Fig. 2.9(e)-(f)) evolves more rapidly than in the S'_3 states: in particular, the most rapid variations are found at about $k_{\parallel} = 1\,\text{Å}^{-1}$. The variations are due to the anticrossing of the two states (see Fig. 2.2).

Finally we analyze the spin polarizations of the S_4 states (Fig. 2.10), that vary rapidly with $k_{\parallel}$ and show a quite complex behavior. Due to symmetry, the $m_{\perp}$ component must vanish at $\bar{K}$, whereas m_z is not influenced by symmetry. The most regular evolution is shown by S_{4d}, for which the m_z component is almost constant and always negative; instead

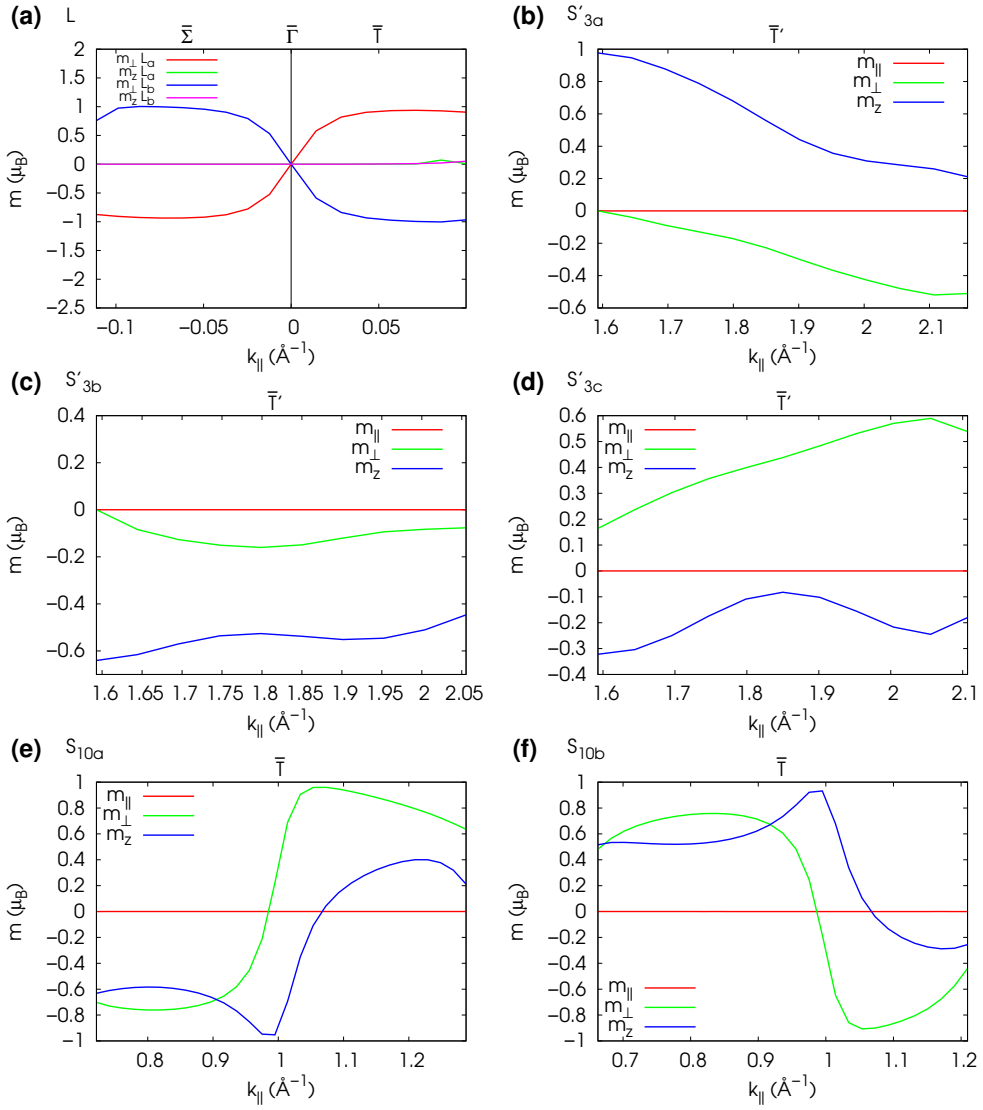

Figure 2.9: Spin polarization components as a function of $\mathbf{k}_{\parallel}$ for the FR surface states $L_{a,b}$, $S'_{3a,b,c}$ and $S_{10a,b}$.

the other states show more evident rotations of the spin, which spans a wide range of different configurations in a quite small region of the high symmetry line. In particular, the S_{4b} and S_{4c} states show a quite abrupt variation of m_z around $k_{\parallel} = 1.59\,\text{Å}^{-1}$. As for the S_{10} states, this behavior can be explained observing that at $k_{\parallel} \approx 1.59\,\text{Å}^{-1}$ S_{4b} and S_{4c} anti-cross. A more clear representation of the anti-crossing is given in the inset of Fig. 2.10 (b), in which we show a magnification of the S_{4b} and S_{4c} states around the $\bar{K}$ point.

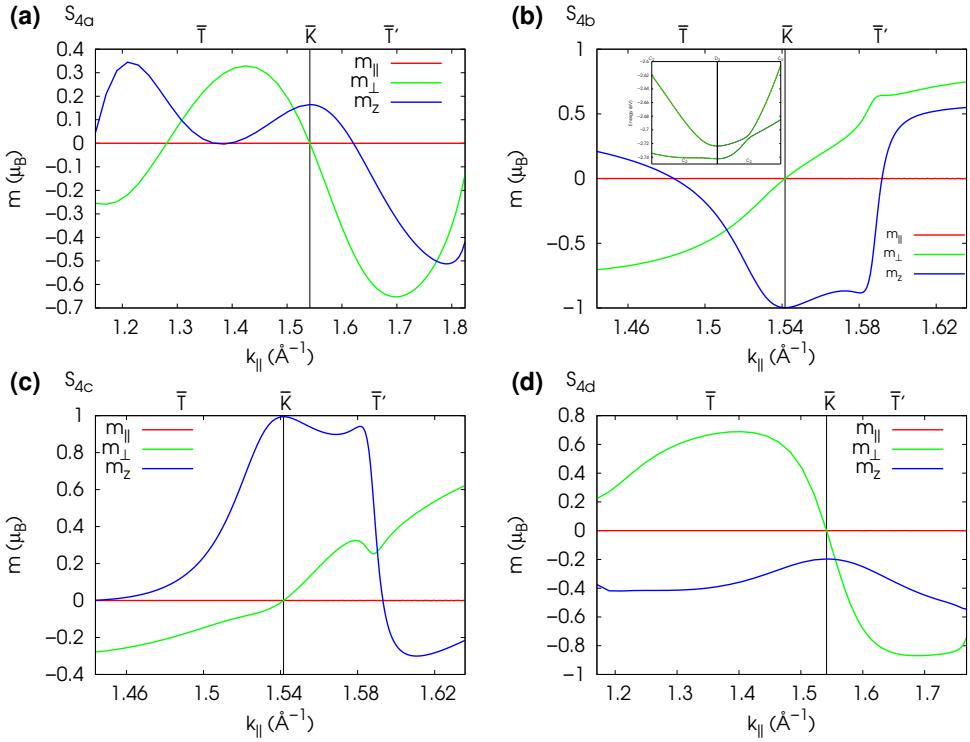

Figure 2.10: Spin polarization components as a function of $\mathbf{k}_{\|}$ for the FR surface states $S_{4a,b,c,d}$.

2.3 Re(0001)

2.3.1 Results

In this section, we analyze the Re(0001) 24-layers slab FR band structure, shown in Fig. 2.11 (a). We characterize the main surface states, indicated with red dots in Fig. 2.11 (a), and compare them with Os(0001) and other previously studied surfaces (e.g. Au(111), Pt(111), and Ir(111)). We use the same names as in Ref. [103]. Moreover, at the end of the section we discuss the band structure of a 25-layers slab (Fig. 2.11 (b)).

We start our analysis from the $\bar{\Gamma}$ point, where we find two gaps in the PBS. Taking the Fermi energy as a reference, the first is located 4 eV above it and the second approximately from -7 eV to -3 eV. The first gap, higher in energy, is similar to the L-gap of the fcc surfaces and is found in Os(0001) as well. It extends partly along the $\bar{T}$ and $\bar{\Sigma}$ lines. The second gap, deeper in energy, extends up to half of the $\bar{T}$ line and along the whole $\bar{\Sigma}$ line. Similarly to Os(0001) and Ir(111), but at variance with Au(111) and Pt(111), no surface states are found in the L-gap. Below the L-gap, near the Fermi energy, we found two couples of states (L in Fig. 2.11 (a)) that transform as the Γ_4^- and Γ_4^+ representations of the D_{3d} group. Their energy dispersion around $\bar{\Gamma}$ is parabolic with negative curvature, as for the Rashba split states in Os(0001) and Ir(111). In these surfaces we could fit their dispersion

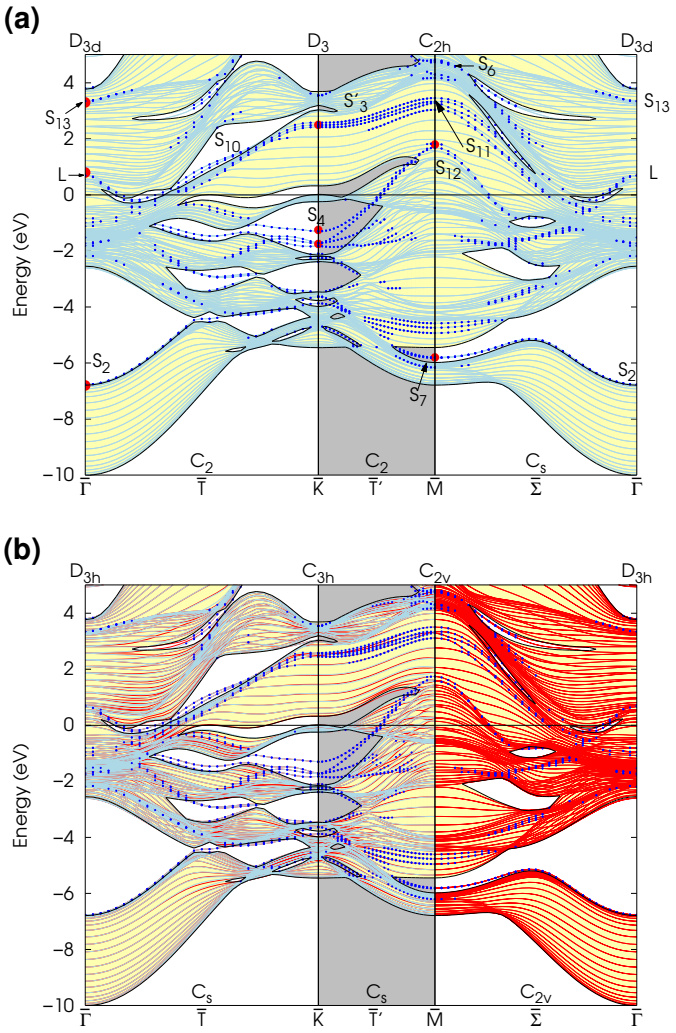

Figure 2.11: LDA FR-PAW surface band structure of Re(0001). (a) 24-layers slab band structure, (b) 25-layers slab band structure. The yellow region is the PBS, the light blue and red lines are the slab electronic states and the blue dots indicate surface states or resonances, defined as those having a charge density greater than 0.35 on the last two atomic layers of both surfaces. Energies are measured with respect to the Fermi energy, and the energy maximum in the figure is the computed work function (5.01 eV). Red dots in (a) indicate the states shown in Figs. 2.13 and 2.14.

with Eq. (2.1). However, here their dispersions do not cross at $\bar{\Gamma}$, as shown in Fig. 2.12 (a), and even neglecting this splitting it is not possible to fit them with Eq. (2.1). Nevertheless, at the Fermi energy the two states show a splitting along $\mathbf{k}_{\parallel}$, due to spin-orbit coupling: indeed, a comparison with the SR band structure (Fig. 2.12 (b)), shows that this splitting emerges only in the FR picture. Moreover, the spin texture of the L states at the Fermi energy is well predicted by the Rashba model (see Section 2.3.2 for more details), so they behave as Rashba states. In Fig. 2.13 (a) we show the contour plots and the planar average of the sum of the charge densities at $\bar{\Gamma}$ for the L_a states, the couple higher in energy. The

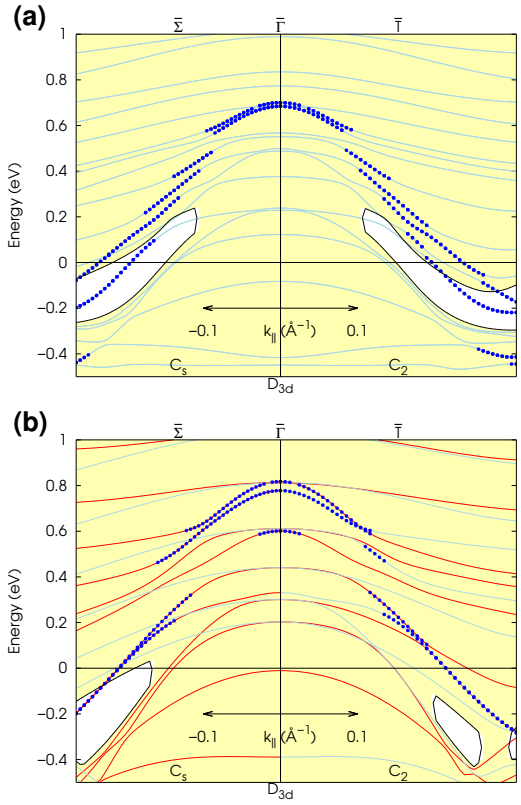

Figure 2.12: Magnification of the electronic band structure around $\bar{\Gamma}$ in the FR (a) and SR (b) case. The L states are shown with blue dots.

contour plots suggest that it has mainly s character hybridized with some d states. The planar average is maximum around the surface and shows a very slow decay towards the center of the slab, indicating that the L states are resonances. Their evident hybridization with bulk states, together with the finite size of the slab, might be responsible for the gap at $\bar{\Gamma}$ [4].

At lower energies at $\bar{\Gamma}$, there are two couples of states in a PBS gap, similar to the previously studied S_2 states of the other metal surfaces. At $\bar{\Gamma}$, they have symmetry Γ_4^+ and Γ_4^-. Their energy dispersion has a positive curvature and can be fitted with Eq. (2.1), with: $\gamma_{SO} = (0.200 \pm 0.005) \times 10^{-9}$ eV cm and $m^*/m = (0.661 \pm 0.003)$, with identical values, within the error bar, along $\bar{T}$ and $\bar{\Sigma}$. In particular, γ_{SO} is 30 % lower than in Os(0001), while the effective mass is approximately 10 % lower. The charge density contours and planar average of the S_{2a} states, those higher in energy, are shown in Fig. 2.13 (b). The states are surface states mainly localized on the first two atomic layers.

Finally, at $\bar{\Gamma}$ there are two couples of empty localized surface states called S_{13}, which have been characterized in Os(0001) surface. At $\bar{\Gamma}$ they transform as the Γ_4^+ and Γ_4^- rep-

[4] A calculation with a 40-layers slab has been performed as well: the gap at $\bar{\Gamma}$ between L_a and L_b is the same as for the 24-layers slab.

Surface State	$\mathbf{k}_\parallel$	ϵ (eV) Re(0001)	ϵ (eV) Os(0001)	ϵ (eV) Ir(111)	ϵ (eV) Pt(111)	ϵ (eV) Au(111)
L	$\bar{\Gamma}$	0.68	0.08	−0.31	0.1	−0.5
S_2	$\bar{\Gamma}$	−6.77	−7.87	−8.0	−7.4	−7.6
S_{13}	$\bar{\Gamma}$	3.35	1.55	—	—	—
S'_{3a}	$\bar{K}$	2.58	1.07	—	—	—
S'_{3b}	$\bar{K}$	2.49	0.97	—	—	—
S'_{3c}	$\bar{K}$	2.42	—	—	—	—
S_{4a}	$\bar{K}$	−1.30	−2.35	−2.7	−2.8	−3.7
S_{4b}	$\bar{K}$	−1.72	−2.74	−3.1	−3.1	−4.0
S_{4c}	$\bar{K}$	−1.73	−2.72	−3.1	−3.1	−4.0
S_{4d}	$\bar{K}$	−1.82	−2.99	−3.5	−3.7	−4.7
S_{12}	$\bar{M}$	1.68	0.86	—	—	—
S_7	$\bar{M}$	−5.80	−7.00	−6.7	−6.3	−6.6
S_{10}	0.6 $\bar{K}$	1.42	−0.24	−0.8	−1.2	—

Surface State	$\mathbf{k}_\parallel$	Small group of $\mathbf{k}_\parallel$			Symmetry		
L	$\bar{\Gamma}$	D_{3d}	$[D_{3h}]$	(C_{3v})	Γ_4^-, Γ_4^+	$[\Gamma_7, \Gamma_8]$	(Γ_4)
S_2	$\bar{\Gamma}$				Γ_4^+, Γ_4^-	$[\Gamma_7, \Gamma_8]$	(Γ_4)
S_{13}	$\bar{\Gamma}$				Γ_4^+, Γ_4^-	$[\Gamma_7, \Gamma_8]$	(Γ_4)
S'_{3a}	$\bar{K}$	D_3	$[C_{3h}]$	(C_3)	$\Gamma_5 \oplus \Gamma_6$	$[\Gamma_{11} \oplus \Gamma_{12}]$	$(2\Gamma_6)$
S'_{3b}	$\bar{K}$				Γ_4	$[\Gamma_7 \oplus \Gamma_9]$	$(\Gamma_4 \oplus \Gamma_5)$
S'_{3c}	$\bar{K}$				Γ_4	$[\Gamma_7 \oplus \Gamma_9]$	$(\Gamma_4 \oplus \Gamma_5)$
S_{4a}	$\bar{K}$				Γ_4	$[\Gamma_8 \oplus \Gamma_{10}]$	$(\Gamma_4 \oplus \Gamma_5)$
S_{4b}	$\bar{K}$				Γ_4	$[\Gamma_7 \oplus \Gamma_9]$	$(\Gamma_4 \oplus \Gamma_5)$
S_{4c}	$\bar{K}$				$\Gamma_5 \oplus \Gamma_6$	$[\Gamma_{11} \oplus \Gamma_{12}]$	$(2\Gamma_6)$
S_{4d}	$\bar{K}$				Γ_4	$[\Gamma_8 \oplus \Gamma_{10}]$	$(\Gamma_4 \oplus \Gamma_5)$
S_{12}	$\bar{M}$	C_{2h}	$[C_{2v}]$	(C_s)	$\Gamma_3^+ \oplus \Gamma_4^+$	$[\Gamma_5]$	$(\Gamma_3 \oplus \Gamma_4)$
S_7	$\bar{M}$				$\Gamma_3^+ \oplus \Gamma_4^+, \Gamma_3^- \oplus \Gamma_4^-$	$[\Gamma_5]$	$(\Gamma_3 \oplus \Gamma_4)$
S_{10}	0.6 $\bar{K}$	C_2	$[C_s]$	(C_1)	$\Gamma_3 \oplus \Gamma_4$	$[\Gamma_3 \oplus \Gamma_4]$	(Γ_2)

Table 2.4: Energy and symmetry properties of the surface states discussed in the paper, for the Re(0001), Os(0001), Ir(111), Pt(111), and Au(111) surfaces. The reported symmetry refers to the 24-layers slab. In square brackets, the symmetry for the 25-layers slab, in parentheses, the symmetry relevant for the surface.

resentations of the D_{3d} group. Similarly to Os(0001), they are resonances and they have mainly d character, with main contributions from the first two atomic layers (Fig. 2.13 (c)).

The states L, S_2, and S_{13} extend partially also along the $\bar{T}$ line, where they all transform as the $\Gamma_3 \oplus \Gamma_4$ representation of the C_2 group. Along $\bar{T}$ we find some PBS gaps as well: the widest ones host the S_{10}, S_4, and the previously mentioned S_2 states. The S_{10} states are two couples of degenerate states with symmetry $\Gamma_3 \oplus \Gamma_4$. They cross the Fermi level around $k_\parallel = 0.51\,\text{Å}^{-1}$. As in Pt(111), Ir(111), and Os(0001), they merge with the S'_3 states at $\bar{K}$. The S_4 states are located inside a PBS gap, they cross the $\bar{K}$ point and extend along the $\bar{T}'$ line as well. They have symmetry $\Gamma_3 \oplus \Gamma_4$.

At $\bar{K}$ we find four main gaps in the PBS: the highest in energy is located above 3.5 eV,

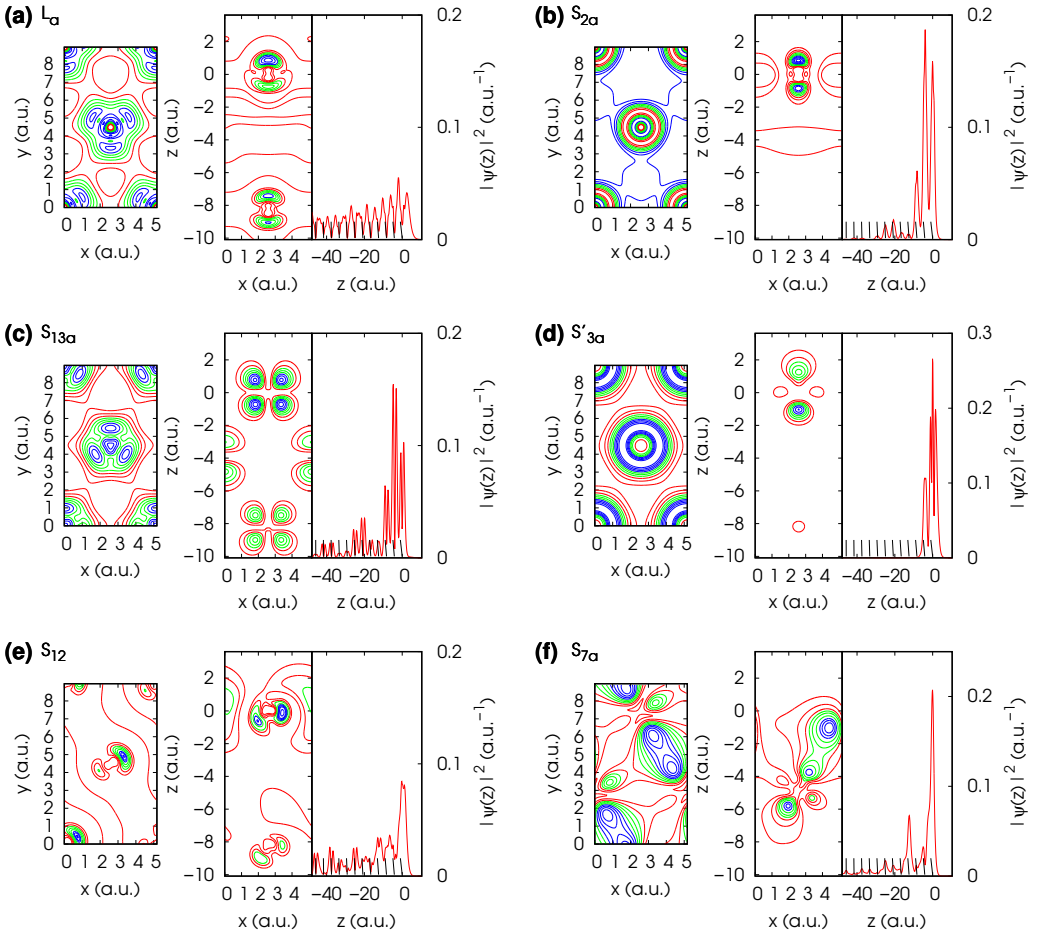

Figure 2.13: Contour plots and planar average of the charge density corresponding to the selected FR surface states indicated with red dots in Fig. 2.11. The left subplot shows the charge density contour plot in the yellow region in Fig. 2.1a, on the top atomic layer of the slab. The central subplot shows the contour plot in a plane perpendicular to the slab, whose trace is the green line in Fig. 2.1a. The contours are equally spaced and are indicated with different colors (red, green, and blue in increasing order of charge density). The first three atomic layers are shown. The right subplot shows the planar average of the charge density in one half of the slab. The vacuum is on the right; the z tics represent the positions of the atomic layers.

the second one crosses the Fermi level and does not host any surface state, the third one contains the S_4 states, while the fourth one extends down to -3.5 eV. The main surface states at $\bar{K}$ are the S'_3 and S_4 states. S'_3 are made up of three couples of empty states, that are named S'_{3a}, S'_{3b}, and S'_{3c} in decreasing order of energy. S'_{3a} transforms as the $\Gamma_5 \oplus \Gamma_6$ representation of the D_3 group, while S'_{3b} and S'_{3c} have symmetry Γ_4. As in Os(0001), they are not in a PBS gap, they are localized in the first two atomic layers and project mainly on $d_{3z^2-r^2}$ states, as can be seen from the charge density contour lines shown in Fig. 2.13 (d).

The S_4 states are located in the PBS gap found at -2 eV $< E < -0.3$ eV. S_{4a}, S_{4b}, and

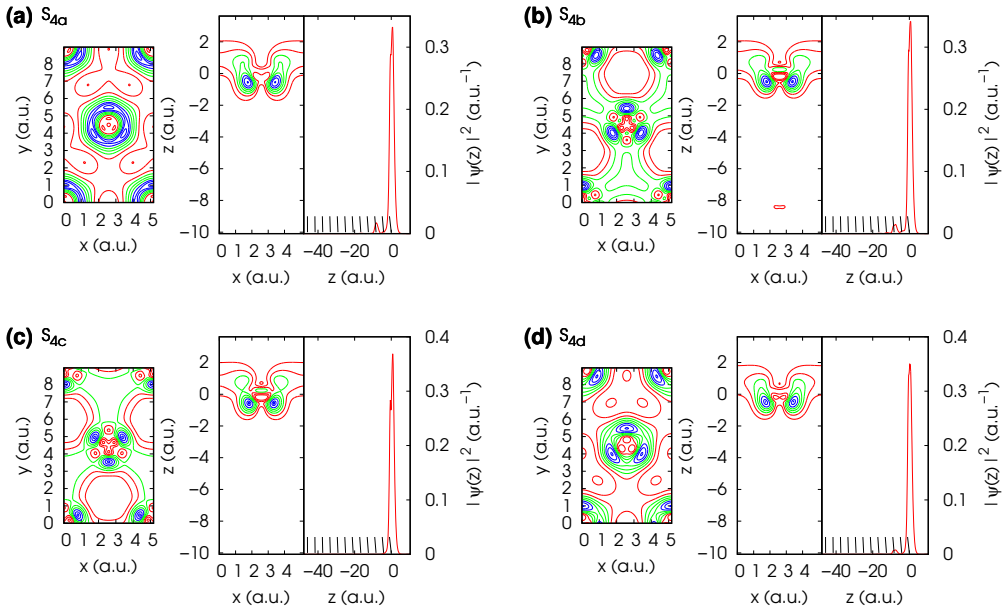

Figure 2.14: Contour plots and planar average of the charge density of the S_4 surface states at $\bar{K}$. The organization of the subplots is the same as in Fig. 2.13.

S_{4d} transform as the representation Γ_4, while S_{4c} transforms as $\Gamma_5 \oplus \Gamma_6$. In Fig. 2.14 we show their charge density, which is peaked on the top atomic layer, with a small contribution on the third atomic layer for S_{4a}, S_{4b}, and S_{4d}. They have very similar features in Os(0001), though S_{4b} and S_{4c} exchange their character, as can be argued from the symmetry and the charge density plots.

The PBS gaps and surface states described at $\bar{K}$ extend also along the $\bar{T}'$ line. Both S_3' and S_4 states, along $\bar{T}'$ have symmetry $\Gamma_3 \oplus \Gamma_4$ of the C_2 group. Moreover, S_{4b} and S_{4c} anticross near $\bar{K}$ ($\mathbf{k} \approx 1.53\,\text{Å}^{-1}$), similarly to Os(0001). Along $\bar{T}'$, near $\bar{M}$, we find another PBS gap, located around -6 eV, that hosts the S_7 states. It extends up to $\bar{M}$ and along the whole $\bar{\Sigma}$ line, as well as the S_7 states, that connect to the S_2 states at $\bar{M}$.

At $\bar{M}$, besides the previously mentioned PBS gap and S_7 states, we find the S_{12} states. They are a couple of degenerate states with symmetry $\Gamma_3^+ \oplus \Gamma_4^+$ and project on many d states (Fig. 2.13 (e)). The S_7 states, instead, are made up of two couples of states, that belong to the representations $\Gamma_3^+ \oplus \Gamma_4^+$ and $\Gamma_3^- \oplus \Gamma_4^-$ of the group C_{2h}, respectively. They have a strong contribution to the charge density (Fig. 2.13 (f)) coming from $d_{x^2-y^2}$ and d_{xy} orbitals localized in the first atomic layer.

The band structure of the 25-layers slab (Fig. 2.11 (b)) is overall very similar to the one of the 24-layers slab and the surface states are located at the same energies in both slabs. Nevertheless there are minor differences, due to the different symmetries of the two slabs. In particular, since the 25-layers slab lacks inversion symmetry (its point group is D_{3h}), only the $\mathbf{k}$ - $-\mathbf{k}$ Kramers degeneracy remains, and a spin splitting may appear, along some lines. This is the case of the lines $\bar{T}$ and $\bar{T}'$, in which states of different symmetry (in our case, even and odd with respect to the mirror plane σ_h) are split. The spin splitting is different for different states: it can be very small as, e.g., $\approx 10^{-6}$ eV for the S_4 states, or larger as

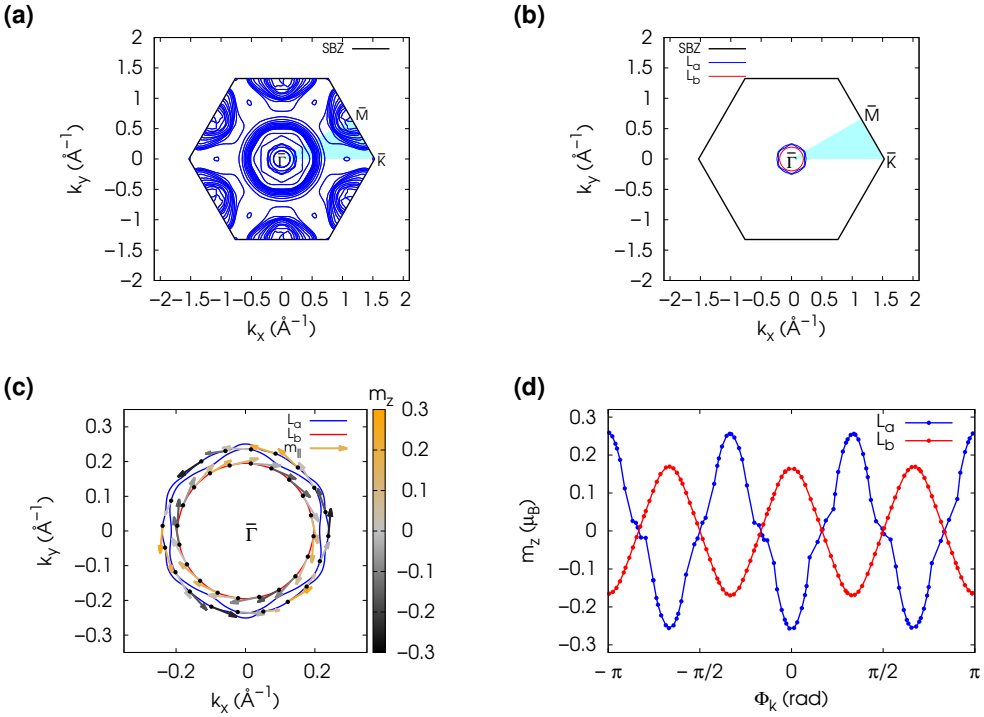

Figure 2.15: (a) Fermi surface of the Re(0001) 24-layers slab. The light blue region is the Irreducible Brillouin Zone (IBZ). (b) The $L_{a,b}$ surface states contours shown in comparison with the SBZ. (c) Magnification of the $L_{a,b}$ surface states contours at the Fermi energy. The black dots indicate the surface states, the arrows indicate the spin polarization parallel to the surface, and they are colored depending on the magnitude of the z component of the spin polarization. (d) z component of the spin polarization for the states $L_{a,b}$ as a function of $\Phi_k = \tan^{-1}(k_y/k_x)$.

$\approx$ 0.03 eV for the S_3' states, and it decreases increasing the slab thickness [5]. At variance with the states along $\bar{T}$ and $\bar{T}'$, the states along $\bar{\Sigma}$ are doubly degenerate because the C_{2v} double group has only one two-dimensional irreducible representation, Γ_5.

2.3.2 Spin polarization: results and discussion

In this section we discuss the spin polarization of some of the surface states found above. The spin polarization can be obtained integrating the planar average of the magnetization density over half slab (see Section 2.2.2 for more details, in particular Eqs. (2.2), (2.3), and (2.4)).

We start our discussion from the L states. In particular, we consider their contribution to the Fermi surface and their spin texture at the Fermi energy. The results are shown in Fig. 2.15. The Fermi surface of the slab is shown in Fig. 2.15 (a), while the contour levels of

[5] A band structure calculation of a 41-layers slab shows that the spin splittings decrease, but quite slowly: for instance, the splitting of the S_3' states decreases of about 30 %.

the L states, shown in Fig. 2.15 (b) (compared with the SBZ) are magnified in Fig. 2.15 (c): they have been obtained with a cubic interpolation of the energies of the states computed in a 14×14 square mesh of $\mathbf{k}$ points centered in $\bar{\Gamma}$. The spin polarization, computed via Eq. (2.2), is represented by arrows whose length is proportional to the component of the spin parallel to the surface. The arrows are colored according to the magnitude of the spin polarization (Eq. 2.2) perpendicular to the surface, as indicated by the color map in the Figure. The L_b states have a circular Fermi surface, whereas the shape of the L_a states is more influenced by the underlying lattice. The component of the spin polarization parallel to the surface is perpendicular to the wavevector for both states, and it rotates clockwise and counter-clockwise for the two states, respectively. This is in agreement with the prediction of the Rashba model [5], so the L states appear as Rashba split states at the Fermi level, although it has not been possible to fit their energy dispersion with Eq. (2.1). In particular, given the dependence of the Rashba spin texture on the sign of both the effective mass and the spin-orbit coupling parameter [126], our results are consistent with a Rashba model with $\gamma_{\mathrm{SO}} > 0$. Due to the presence of the underlying atomic layers, the spin polarization shows a non vanishing component perpendicular to the surface. As shown in Fig. 2.15 (d), this component oscillates around zero along the contour levels, with a period of $2\pi/3$ as a consequence of the symmetry of the lattice, with opposite phase for L_a and L_b.

Along the $\bar{T}$ and $\bar{T}'$ high symmetry lines the spin polarization can rotate in a plane perpendicular to the line, as explained in Refs. [103], [125], and previously in Section 2.3.2. In this work we consider the rotation of the spin polarization of the states S'_3, S_{10} (Fig. 2.16), and S_4 (Fig. 2.17).

The S'_3 states (Figs. 2.16 (a)-(c)) have been studied along the whole $\bar{T}'$ line: at $\bar{K}$ the states have only a non-zero z (perpendicular to the surface) component of the spin polarization, due to symmetry constraints, while at $\bar{M}$ their spin polarization vanishes because $\bar{M}$ is a time-reversal invariant point. The spin polarization of S'_{3a} is mainly perpendicular to the surface: the z component decreases along the $\bar{T}'$ line, in a similar fashion as in Os(0001). The S'_{3b} states show a more pronounced rotation: the z component changes sign along the high symmetry line, and the component perpendicular to $\bar{T}'$ spans a wide range of values, at variance with Os(0001). Finally, the S'_{3c} states have a rotating spin along $\bar{T}'$, which always points towards the center of the slab: its behaviour is similar to what shown in Os(0001).

The S_{10} states show a smooth evolution of the spin polarization in the region $0.55\,\text{Å}^{-1} < k_{\parallel} < 1\,\text{Å}^{-1}$, as shown in Figs. 2.16 (d)-(e): in particular, S_{10a} and S_{10b} have opposite spin. Around $k_{\parallel} \approx 0.55\text{Å}^{-1}$ and $k_{\parallel} \approx 1\text{Å}^{-1}$ the spin polarization rotates more rapidly, because the two states anti-cross. Overall, their behaviour is similar to that shown by Os(0001).

Finally, the S_4 states (Fig. 2.17) show a spin texture along $\bar{T}$ and $\bar{T}'$ very similar to Os(0001). In particular, the smoothest behaviour is shown by S_{4d}, for which the spin always points towards the slab. S_{4b} and S_{4c} have a rapidly varying spin, even in a very narrow range of $k_{\parallel}$ as shown in Fig. 2.17 (b)-(c), due to their mixing and anticrossing around $\bar{K}$: a comparison with Os(0001) shows that their features are exchanged, as pointed out by their symmetry (see Table 2.4).

Similar calculations have been performed for the 25-layers slab as well. The results are very similar to those discussed above, in particular for the S_4 and S_{10} states, which have the same energy dispersion in the two systems. Instead, the spin polarization of the S'_3 states

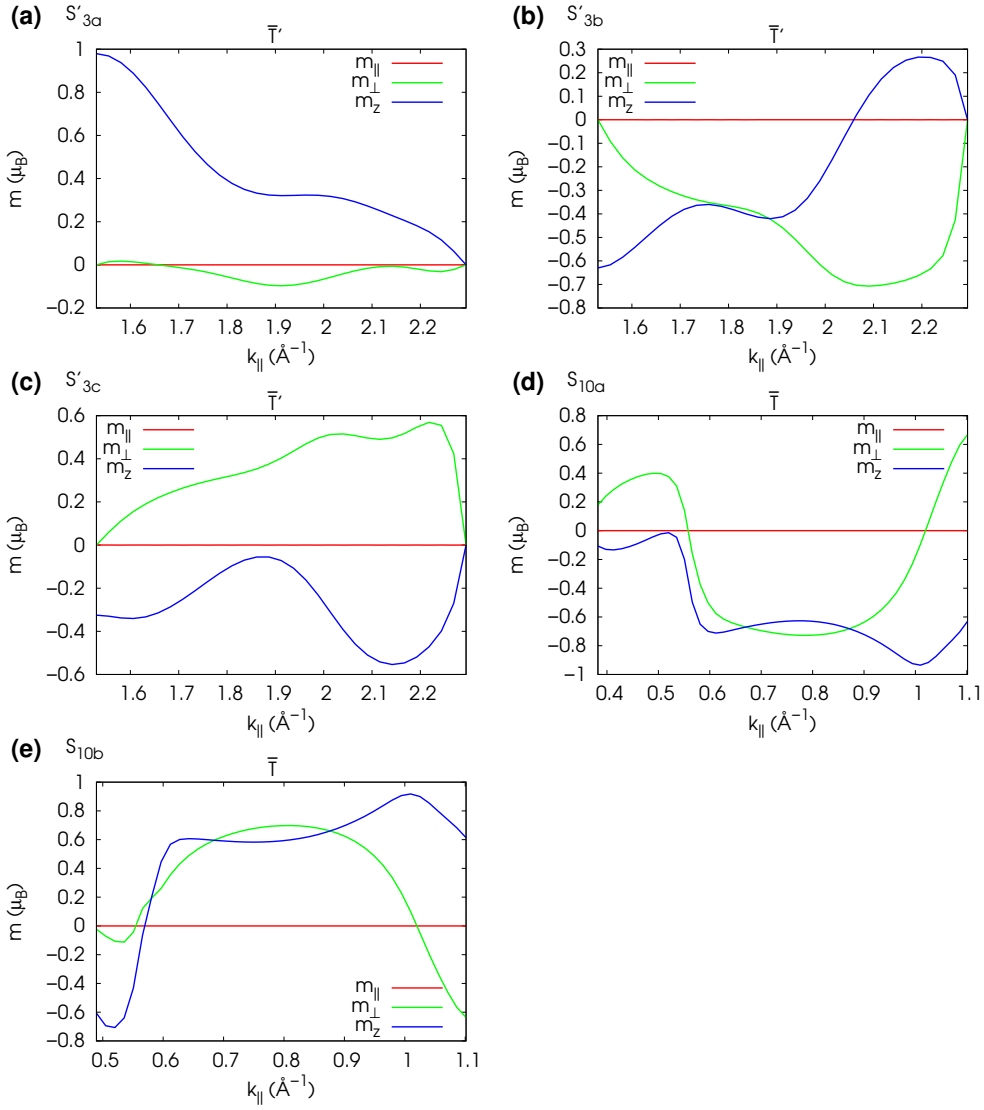

Figure 2.16: Spin polarization components as a function of $\mathbf{k}_{\parallel}$ for the FR surface states $S'_{3a,b,c}$ and $S_{10a,b}$. $m_{\parallel}$ and $m_{\perp}$ are the spin polarization components parallel to the surface: they are parallel and perpendicular to the high symmetry line, respectively. m_z is the component perpendicular to the surface.

shows a somehow different behavior, characterized by more rapid variations, which might be due to the mixing of the states caused by their non-negligible spin splitting. However, as pointed out before, the spin splitting decreases, though slowly, with increasing slab thickness, so we expect a better agreement using a thicker slab.

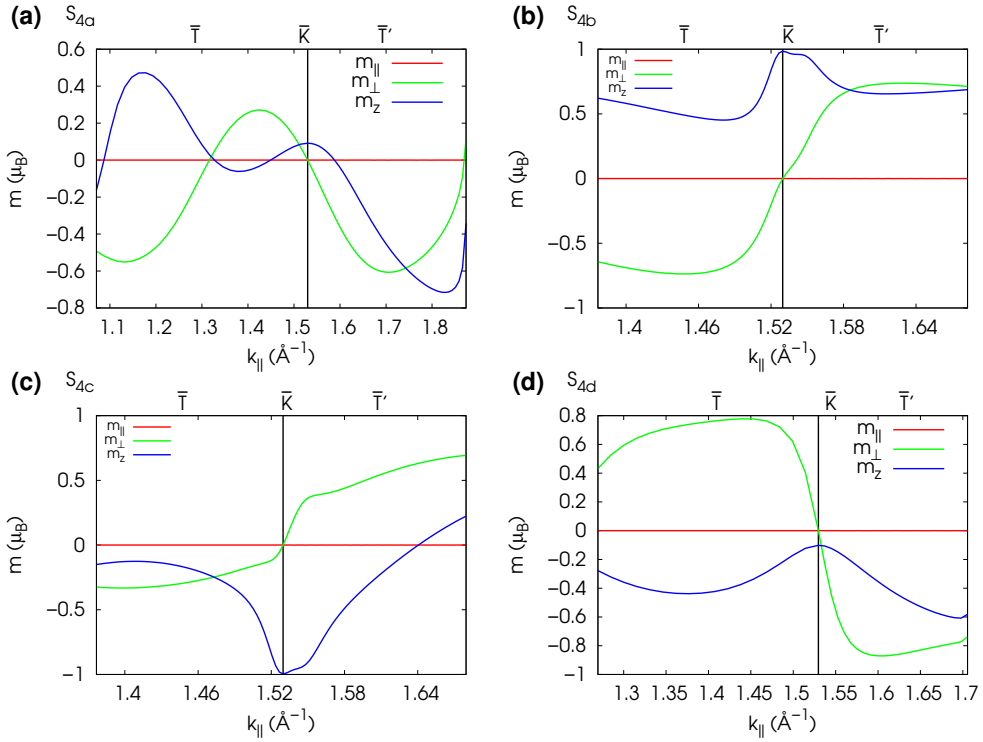

Figure 2.17: Spin polarization components as a function of $\mathbf{k}_{\parallel}$ for the FR surface states $S_{4a,b,c,d}$. The convention on $m_{\parallel}$, $m_{\perp}$, and m_z is the same as in Fig. 2.16

2.4 Closing remarks

The results presented and discussed in this work have been obtained within the DFT-LDA scheme. The Kohn-Sham eigenvalues are distinct from the quasi-particle energies, so in principle many-body corrections might be necessary for a detailed comparison with experiment. Yet, these calculations are more computationally demanding and are usually carried out only in those cases in which LDA is not sufficient to explain the experimental results. In the other surfaces mentioned, the main features of the bands, such as the presence or absence of L-gap states, are well predicted by DFT-LDA, while the exact energy positions of the surface states might have small shifts.

Chapter 3

Density Functional Perturbation Theory with Fully Relativistic Ultrasoft Pseudopotentials: the magnetic case

Density Functional Perturbation Theory (DFPT) is widely used for the computation of the linear response properties of solids, and in particular for the study of their lattice dynamics [42–49]. Some years ago, DFPT has been applied [49] to a scheme based on PWs and NC or US [83] PPs, that allow the introduction of spin-orbit effects within a FR density functional formalism [40] and can be written in a form very similar to the SR one. However, the theory presented in Ref. [49] was implemented only for time-reversal-invariant systems, and therefore applications that include spin-orbit so far have been limited to non-magnetic solids [49, 127].

In the first part of this Chapter, Section 3.2, we consider the DFPT for generic perturbations in the non-collinear FR case, as presented in Ref. [49], and we discuss its extension to deal with magnetic systems, by explicitly considering the presence of an exchange-correlation magnetic field in the Hamiltonian. DFPT equations in presence of a magnetic field have been recently written to calculate magnons with NC PPs in Refs. [51] and [52]. In Ref. [51], the charge density induced by a periodic perturbation was computed by using the response to a perturbation at wave vector $\mathbf{q}$ and the response to a perturbation at $-\mathbf{q}$, while in Ref. [52] the problem at $-\mathbf{q}$ was not solved, but the time-reversal operator was used to obtain a second Sternheimer equation with a reversed magnetic field. The two formulations are equivalent.

In Section 3.3, we generalize the theory of Ref. [52] to a phonon perturbation, avoiding the study of the response at $-\mathbf{q}$, and write it in a form suitable for both NC and US PPs.

In presence of a magnetic field, the solid is invariant upon the symmetry operations of the magnetic space group. Some of these operations require the time-reversal operator. In

Section 3.4, we discuss how to exploit these symmetries for the symmetrization of the induced charge and magnetization densities and for the dynamical matrix.

Finally, in Section 3.5, we validate our method in ferromagnetic fcc Ni first computing the phonon frequencies at the X point in the BZ via the frozen phonon method and comparing with DFPT results, and then by computing the phonon dispersions. Moreover, we apply our method to a monatomic ferromagnetic Pt nanowire and compare its vibrational properties when the magnetization is parallel or perpendicular to the wire. Also for this case, we compare the DFPT results to the frozen phonon method for a phonon perturbation with wavevector $q = \pi/a$ and $q = \pi/2a$, and then we compute by DFPT the phonon dispersion in the one-dimensional BZ.

3.1 A recap on lattice dynamics in the harmonic approximation

Within the BO adiabatic approximation, mentioned in Section 1.1, the atomic nuclei move in a potential energy given by the total energy E_{tot} of the electronic system. Conversely, the electronic total energy depends parametrically on the nuclear positions $\mathbf{R}_\mu + \mathbf{d}_s$ and the electrons are assumed to be in the ground state for each nuclear configuration.

We model a generic lattice distortion by introducing the atomic displacements $\mathbf{u}_{\mu s}$. For displacements of small amplitude $|\mathbf{u}|$ we can perform a Taylor expansion of E_{tot}. In the *harmonic approximation* this expansion is truncated at second order, and E_{tot} reads

$$E_{\text{tot}}[\{\mathbf{R}+\mathbf{u}\}] = E_{\text{tot}}[\{\mathbf{R}\}] + \sum_{\mu s\alpha} \frac{dE_{\text{tot}}}{du_{\mu s\alpha}}\, u_{\mu s\alpha} + \frac{1}{2} \sum_{\mu s\alpha} \sum_{\nu s'\beta} \frac{d^2E_{\text{tot}}}{du_{\mu s\alpha} du_{\nu s'\beta}}\, u_{\mu s\alpha}\, u_{\nu s'\beta}, \tag{3.1}$$

where α and β identify the cartesian coordinates, and the derivatives are computed at $\mathbf{u} = \mathbf{0}$. The classical dynamics of the nuclei is described by the Newton's equations of motion which, at equilibrium ($dE_{\text{tot}}/du_{\mu s\alpha} = 0$), read:

$$M_s \frac{d^2 u_{\mu s\alpha}}{dt^2} = -\sum_{\nu s'\beta} \frac{d^2E_{\text{tot}}}{du_{\mu s\alpha} du_{\nu s'\beta}}\, u_{\nu s'\beta}, \tag{3.2}$$

where M_s identifies the mass of the s-th atom in the unit cell. We look for solutions in the form of a phonon perturbation at finite wave vector $\mathbf{q}$:

$$u_{\mu s\alpha}(t) = \frac{1}{\sqrt{M_s}} \operatorname{Re}\left(u_{s\alpha}(\mathbf{q})\, e^{i\mathbf{q}\cdot\mathbf{R}_\mu}\, e^{-i\omega_{\mathbf{q}} t}\right), \tag{3.3}$$

where $\omega_{\mathbf{q}}$ is the frequency of the lattice vibration and $u_{s\alpha}(\mathbf{q})$ is the (complex) phonon mode amplitude. Eq. (3.2) thus becomes:

$$\omega_{\mathbf{q}}^2\, u_{s\alpha}(\mathbf{q}) = \sum_{s'\beta} \frac{1}{\sqrt{M_s\, M_{s'}}}\, \Phi_{\substack{s\alpha \\ s'\beta}}(\mathbf{q})\, u_{s'\beta}(\mathbf{q}), \tag{3.4}$$

where $1/\sqrt{M_s\, M_{s'}}\, \Phi_{s\alpha s'\beta}(\mathbf{q})$ is the *dynamical matrix* at wave vector $\mathbf{q}$. $\Phi_{s\alpha s'\beta}(\mathbf{q})$ is defined as:

$$\Phi_{\substack{s\alpha \\ s'\beta}}(\mathbf{q}) = \frac{1}{N} \sum_{\mu\nu} e^{-i\mathbf{q}\cdot\mathbf{R}_\mu} \frac{d^2 E_{\text{tot}}}{du_{\mu s\alpha} du_{\nu s'\beta}} e^{i\mathbf{q}\cdot\mathbf{R}_\nu}, \tag{3.5}$$

where N is the number of unit cells in the solid. As a result, $\omega_{\mathbf{q}}$ and $u_{s\alpha}(\mathbf{q})$ are the eigenvalues and the eigenvectors of the dynamical matrix, respectively.

The second-order derivatives of E_{tot}, known also as *interatomic force constants*, play a crucial role, in that they allow to compute the dynamical matrix and, ultimately, the phonon frequencies and the phonon modes. Below we start by addressing the calculation of the interatomic force constants when E_{tot} is computed within the non-collinear DFT formalism with the FR US PPs scheme, discussed in Section 1.9.2.

3.2 Formulation with generic perturbations

3.2.1 Second-order energy derivatives: introduction

If we consider a generic perturbation λ, the generalized force, computed as the first-order derivative of the total energy with respect to λ, follows directly from the HF theorem (see Section 1.5 and Eqs. (1.71) and (1.127)) and reads:

$$\frac{dE_{\text{tot}}}{d\lambda} = \sum_i \sum_{\sigma_1} \tilde{\theta}_{F,i}\, \langle \psi_i^{\sigma_1} | \phi_i^{\lambda[\mathbf{B}]\sigma_1} \rangle\,, \tag{3.6}$$

with

$$|\phi_i^{\lambda[\mathbf{B}]\sigma_1}\rangle = \sum_{\sigma_2} \left[\frac{\partial V_{\text{KS}}^{[\mathbf{B}]\sigma_1\sigma_2}}{\partial\lambda} - \epsilon_i \frac{\partial S^{\sigma_1\sigma_2}}{\partial\lambda} \right] \Big| \psi_i^{\sigma_2} \Big\rangle, \tag{3.7}$$

where the superscript $[\mathbf{B}]$ identifies the exchange-correlation magnetic field $\mathbf{B}_{\text{xc}}$ in V_{KS}. Hereafter we will adopt the total derivative symbol d to identify derivatives where the one-particle wave functions $|\psi_i^\sigma\rangle$ are considered as implicit functions of λ, whereas the partial derivative symbol ∂ will refer to derivatives computed assuming fixed wave functions. The partial derivative of the KS potential appearing in Eq. (3.7) thus reads:

$$\frac{\partial V_{\text{KS}}^{[\mathbf{B}]\sigma_1\sigma_2}}{\partial\lambda} = \frac{\partial V_{\text{NL}}^{\sigma_1\sigma_2}}{\partial\lambda} + \sum_{\sigma_3} \int d^3r\, \frac{\partial V_{\text{loc}}(\mathbf{r})}{\partial\lambda}\, K_{\sigma_1\sigma_2}^{\sigma_3\sigma_3}(\mathbf{r}) + \sum_{\sigma_3\,\sigma_4} \int d^3r\, V_{\text{LOC}}^{[\mathbf{B}]\sigma_3\sigma_4}(\mathbf{r})\, \frac{\partial K_{\sigma_1\sigma_2}^{\sigma_3\sigma_4}(\mathbf{r})}{\partial\lambda}. \tag{3.8}$$

The mixed second-order derivative of the total energy is computed by taking the derivative of Eq. (3.6), and contains three terms. The first term accounts for the change in the occupation numbers $\tilde{\theta}_{F,i}$:

$$\frac{d^2 E_{\text{tot}}^{(a)}}{d\mu d\lambda} = \sum_i \sum_{\sigma_1} \frac{d\tilde{\theta}_{F,i}}{d\mu}\, \langle \psi_i^{\sigma_1} | \phi_i^{\lambda[\mathbf{B}]\sigma_1} \rangle\,, \tag{3.9}$$

the second one keeps into account the derivatives of the energy levels ϵ_i and of the wave functions $|\psi_i^\sigma\rangle$:

$$\frac{d^2E_{\rm tot}^{(b)}}{d\mu d\lambda} = -\sum_i \sum_{\sigma_1\,\sigma_2} \tilde{\theta}_{F,i}\, \frac{d\epsilon_i}{d\mu} \left\langle \psi_i^{\sigma_1} \middle| \frac{\partial S^{\sigma_1\sigma_2}}{\partial\lambda} \middle| \psi_i^{\sigma_2} \right\rangle + \sum_i \sum_{\sigma_1} \tilde{\theta}_{F,i} \left[\left\langle \frac{d\psi_i^{\sigma_1}}{d\mu} \middle| \phi_i^{\lambda[\mathbf{B}]\sigma_1} \right\rangle + \left\langle \phi_i^{\lambda[\mathbf{B}]\sigma_1} \middle| \frac{d\psi_i^{\sigma_1}}{d\mu} \right\rangle \right], \tag{3.10}$$

and the third term contains the expectation value of the mixed second-order derivative of the potential, generalized to the US scheme:

$$\frac{d^2E_{\rm tot}^{(c)}}{d\mu d\lambda} = \sum_i \sum_{\sigma_1\,\sigma_2} \tilde{\theta}_{F,i} \left\langle \psi_i^{\sigma_1} \middle| \frac{d}{d\mu} \left(\frac{\partial V_{\rm KS}^{[\mathbf{B}]\sigma_1\sigma_2}}{\partial\lambda} \right) - \epsilon_i \frac{\partial^2 S^{\sigma_1\sigma_2}}{\partial\mu\partial\lambda} \middle| \psi_i^{\sigma_2} \right\rangle. \tag{3.11}$$

The term $d^2E_{\rm tot}^{(b)}/d\mu d\lambda$ depends on the first-order derivative of the KS orbitals, which can be computed by applying the time-independent first-order perturbation theory to the KS equations, a widely used and well known technique [43], that we briefly summarize below.

3.2.2 First-order perturbation theory: a brief introduction

In first-order perturbation theory the quantities appearing in the KS equations are expanded at first order in the external perturbation μ:

$$\epsilon_i = \epsilon_i^{(0)} + \frac{d\epsilon_i}{d\mu}\,\mu, \tag{3.12}$$

$$|\psi_i^{\sigma_1}\rangle = |\psi_i^{(0)\,\sigma_1}\rangle + \left| \frac{d\psi_i^{\sigma_1}}{d\mu} \right\rangle \mu, \tag{3.13}$$

$$V_{\rm KS}^{[\mathbf{B}]\sigma_1\sigma_2} = V_{\rm KS}^{(0)\,[\mathbf{B}]\sigma_1\sigma_2} + \frac{dV_{\rm KS}^{[\mathbf{B}]\sigma_1\sigma_2}}{d\mu}\,\mu, \tag{3.14}$$

where the superscript (0) identifies the unperturbed quantities. In the US scheme, the overlap matrix is written in a similar way because the projectors $|\beta\rangle$ may depend on the external perturbation:

$$S^{\sigma_1\sigma_2} = S^{(0)\,\sigma_1\sigma_2} + \frac{dS^{\sigma_1\sigma_2}}{d\mu}\,\mu. \tag{3.15}$$

In the following, for the sake of simplicity we will drop the superscript (0) from the unperturbed quantities.

By introducing in the KS equations (Eq. (1.163)) the first-order expansions reported above, and keeping only the linear terms, we get the following linear system:

$$\sum_{\sigma_2} \left(H_{\rm KS}^{[\mathbf{B}]\sigma_1\sigma_2} - \epsilon_i S^{\sigma_1\sigma_2} \right) \left| \frac{d\psi_i^{\sigma_2}}{d\mu} \right\rangle = -\sum_{\sigma_2} \frac{dV_{\rm KS}^{[\mathbf{B}]\sigma_1\sigma_2}}{d\mu} |\psi_i^{\sigma_2}\rangle + \sum_{\sigma_2} \left(\frac{d\epsilon_i}{d\mu}\, S^{\sigma_1\sigma_2} + \epsilon_i \frac{dS^{\sigma_1\sigma_2}}{d\mu} \right) |\psi_i^{\sigma_2}\rangle\,, \tag{3.16}$$

whose solution is the first-order derivative of the KS orbitals. Eq. (3.16) is known in literature as *Sternheimer linear system*. The total derivative of the KS potential appearing on the right-hand side reads:

$$\frac{dV_{\mathrm{KS}}^{[\mathbf{B}]\sigma_1\sigma_2}}{d\mu} = \frac{\partial V_{\mathrm{KS}}^{[\mathbf{B}]\sigma_1\sigma_2}}{\partial\mu} + \sum_{\sigma_3\,\sigma_4}\int d^3r\,\frac{dV_{\mathrm{H,xc}}^{[\mathbf{B}]\sigma_3\sigma_4}(\mathbf{r})}{d\mu}\,K_{\sigma_1\sigma_2}^{\sigma_3\sigma_4}(\mathbf{r}), \tag{3.17}$$

and differs from the partial derivative of $V_{\mathrm{KS}}^{[\mathbf{B}]\sigma_1\sigma_2}$ (Eq. (3.8)) for the presence of the self-consistent term $dV_{\mathrm{H,xc}}^{[\mathbf{B}]\sigma_3\sigma_4}(\mathbf{r})/d\mu$ [49]:

$$\begin{aligned}\frac{dV_{\mathrm{H,xc}}^{[\mathbf{B}]\sigma_3\sigma_4}(\mathbf{r})}{d\mu} = &\left[\frac{\delta V_{\mathrm{H,xc}}}{\delta n(\mathbf{r})}\,\frac{dn(\mathbf{r})}{d\mu} + \sum_{\alpha=1}^{3}\frac{\delta V_{\mathrm{H,xc}}}{\delta m_\alpha(\mathbf{r})}\,\frac{dm_\alpha(\mathbf{r})}{d\mu}\right]\delta^{\sigma_3\sigma_4} - \mu_{\mathrm{B}}\sum_{\beta=1}^{3}\left[\frac{\delta B_{\mathrm{xc},\beta}}{\delta n(\mathbf{r})}\,\frac{dn(\mathbf{r})}{d\mu}\right.\\ &\left.+\sum_{\alpha=1}^{3}\frac{\delta B_{\mathrm{xc},\beta}}{\delta m_\alpha(\mathbf{r})}\,\frac{dm_\alpha(\mathbf{r})}{d\mu}\right]\sigma_\beta^{\sigma_3\sigma_4}.\end{aligned} \tag{3.18}$$

$dV_{\mathrm{H,xc}}^{[\mathbf{B}]\sigma_3\sigma_4}(\mathbf{r})/d\mu$ depends on the induced charge and magnetization densities, which in turn depend on the response of the wave functions (see Section 3.2.3), hence the right-hand side of the Sternheimer linear system depends on the solutions of the system itself: in practical calculations, Eq. (3.16) is solved with a self-consistent approach, similarly to that used for the KS equations.

$|d\psi_i^\sigma/d\mu\rangle$ can be alternatively expressed in the basis of the unperturbed wave functions: indeed, contraction of Eq. (3.16) with $\langle\psi_j^\sigma|$ $(j\neq i)$ gives:

$$\sum_{\sigma_1\,\sigma_2}\langle\psi_j^{\sigma_1}|\,S^{\sigma_1\sigma_2}\left|\frac{d\psi_i^{\sigma_2}}{d\mu}\right\rangle = -\sum_{\sigma_1\,\sigma_2}\frac{\left\langle\psi_j^{\sigma_1}\left|\dfrac{dV_{\mathrm{KS}}^{[\mathbf{B}]\sigma_1\sigma_2}}{d\mu} - \epsilon_i\dfrac{\partial S^{\sigma_1\sigma_2}}{\partial\mu}\right|\psi_i^{\sigma_2}\right\rangle}{\epsilon_j-\epsilon_i}. \tag{3.19}$$

The change of the energy levels, instead can be obtained by contracting Eq. (3.16) with $\langle\psi_i^\sigma|$:

$$\frac{d\epsilon_i}{d\mu} = \sum_{\sigma_1\,\sigma_2}\left\langle\psi_i^{\sigma_1}\left|\frac{dV_{\mathrm{KS}}^{[\mathbf{B}]\sigma_1\sigma_2}}{d\mu} - \epsilon_i\frac{\partial S^{\sigma_1\sigma_2}}{\partial\mu}\right|\psi_i^{\sigma_2}\right\rangle. \tag{3.20}$$

3.2.3 Induced densities

The induced charge and magnetization densities, appearing in the self-consistent term $dV_{\mathrm{H,xc}}^{\sigma_1\sigma_2}/d\mu$ (Eq. (3.18)) in the Sternheimer linear system, can be computed by taking the derivative of Eqs. (1.38) and (1.39):

$$\frac{dn(\mathbf{r})}{d\mu} = \sum_\sigma\frac{dn^{\sigma\sigma}(\mathbf{r})}{d\mu}, \tag{3.21}$$

$$\frac{dm_\alpha(\mathbf{r})}{d\mu} = \mu_{\mathrm{B}}\sum_{\sigma\,\sigma'}\frac{dn^{\sigma\sigma'}(\mathbf{r})}{d\mu}\,\sigma_\alpha^{\sigma\sigma'}. \tag{3.22}$$

$dn^{\sigma\sigma'}(\mathbf{r})/d\mu$ is the induced spin density: it can be computed by differentiating Eq. (1.161) and is made up of three terms. The first one is typical of metals and accounts for the change in the occupation numbers:

$$\left(\frac{dn^{\sigma\sigma'}(\mathbf{r})}{d\mu}\right)^{(a)} = \sum_i \sum_{\sigma_1\,\sigma_2} \frac{d\tilde{\theta}_{F,i}}{d\mu} \langle\psi_i^{\sigma_1}|K^{\sigma\sigma'}_{\sigma_1\sigma_2}(\mathbf{r})|\psi_i^{\sigma_2}\rangle\,, \tag{3.23}$$

the second one contains the change in the wave functions:

$$\left(\frac{dn^{\sigma\sigma'}(\mathbf{r})}{d\mu}\right)^{(b)} = \sum_i \sum_{\sigma_1\,\sigma_2} \tilde{\theta}_{F,i} \left[\left\langle \frac{d\psi_i^{\sigma_1}}{d\mu}\right| K^{\sigma\sigma'}_{\sigma_1\sigma_2}(\mathbf{r})|\psi_i^{\sigma_2}\rangle + \langle\psi_i^{\sigma_1}|K^{\sigma\sigma'}_{\sigma_1\sigma_2}(\mathbf{r})\left|\frac{d\psi_i^{\sigma_2}}{d\mu}\right\rangle\right], \tag{3.24}$$

and the third one characterizes the US scheme and contains the derivative of the kernel K:

$$\left(\frac{dn^{\sigma\sigma'}(\mathbf{r})}{d\mu}\right)^{(c)} = \sum_i \sum_{\sigma_1\,\sigma_2} \tilde{\theta}_{F,i} \left\langle \psi_i^{\sigma_1}\right| \frac{\partial K^{\sigma\sigma'}_{\sigma_1\sigma_2}(\mathbf{r})}{\partial\mu} \left|\psi_i^{\sigma_2}\right\rangle. \tag{3.25}$$

The terms (a) and (b) can be further manipulated. First of all, in term (a) the derivative of the occupation numbers can be written as:

$$\frac{d\tilde{\theta}_{F,i}}{d\mu} = \frac{1}{\eta}\,\tilde{\delta}_{F,i}\left(\frac{d\epsilon_{\mathrm{F}}}{d\mu} - \frac{d\epsilon_i}{d\mu}\right), \tag{3.26}$$

then we write explicitly $d\epsilon_i/d\mu$ using Eq. (3.20). In term (b), instead we exploit Eq. (3.19) together with analytical tricks to deal with the fractional occupation numbers. Finally, we introduce the following auxiliary quantities [47, 49]:

$$|\Delta^\mu\psi_i^{\sigma_1}\rangle = \frac{1}{2\eta}\,\tilde{\delta}_{F,i}\,\frac{d\epsilon_{\mathrm{F}}}{d\mu} + \sum_j \sum_{\sigma_2\,\sigma_3} \frac{\tilde{\theta}_{F,i} - \tilde{\theta}_{F,j}}{\epsilon_i - \epsilon_j}\,\theta_{j,i}\,|\psi_j^{\sigma_1}\rangle \left\langle \psi_j^{\sigma_2}\right| \left[\frac{dV_{\mathrm{KS}}^{[\mathbf{B}]\sigma_2\sigma_3}}{d\mu} - \epsilon_i \frac{\partial S^{\sigma_2\sigma_3}}{\partial\mu}\right] \left|\psi_i^{\sigma_3}\right\rangle, \tag{3.27}$$

$$|\delta^\mu\psi_i^{\sigma_1}\rangle = \sum_j \sum_{\sigma_2\sigma_3} \left(\tilde{\theta}_{F,i}\theta_{i,j} + \tilde{\theta}_{F,j}\theta_{j,i}\right) |\psi_j^{\sigma_1}\rangle \left\langle \psi_j^{\sigma_2}\right| \frac{\partial S^{\sigma_2\sigma_3}}{\partial\mu} \left|\psi_i^{\sigma_3}\right\rangle, \tag{3.28}$$

$$\Delta^\mu n^{\sigma\sigma'}(\mathbf{r}) = -\sum_i \sum_{\sigma_1\sigma_2} \langle\delta^\mu\psi_i^{\sigma_1}|K^{\sigma\sigma'}_{\sigma_1\sigma_2}(\mathbf{r})|\psi_i^{\sigma_2}\rangle + \sum_i \sum_{\sigma_1\sigma_2} \left\langle \psi_i^{\sigma_1}\right| \frac{\partial K^{\sigma\sigma'}_{\sigma_1\sigma_2}(\mathbf{r})}{\partial\mu} \left|\psi_i^{\sigma_2}\right\rangle, \tag{3.29}$$

where $\theta_{i,j} = \theta(\epsilon_i - \epsilon_j)$ and $\theta(x)$ is the Heaviside step function, while $\tilde{\theta}_{F,i} = \tilde{\theta}(\epsilon_{\mathrm{F}} - \epsilon_i)$ represents the occupation function approximated with the smearing technique (see Section 1.6). As a final result, summing up the three terms (a), (b), and (c), the induced spin density reads:

$$\frac{dn^{\sigma\sigma'}(\mathbf{r})}{d\mu} = \sum_i \sum_{\sigma_1\,\sigma_2} \left[\langle\psi_i^{\sigma_1}|K^{\sigma\sigma'}_{\sigma_1\sigma_2}(\mathbf{r})|\Delta^\mu\psi_i^{\sigma_2}\rangle + \langle\Delta^\mu\psi_i^{\sigma_1}|K^{\sigma\sigma'}_{\sigma_1\sigma_2}(\mathbf{r})|\psi_i^{\sigma_2}\rangle\right] + \Delta^\mu n^{\sigma\sigma'}(\mathbf{r}). \tag{3.30}$$

The quantities introduced in Eqs. (3.27), (3.28), and (3.29) to lighten the expression of the induced spin density generalize the formulation of DFPT to metallic systems and to the US

scheme. In particular, it is worthwhile to note that $|\Delta^\mu \psi_i^\sigma\rangle$ is directly linked to the derivative of the wave functions, as can be inferred from Eq. (3.19). Indeed, in insulators $d\epsilon_{\rm F}/d\mu = 0$ and $\tilde{\theta}(x) = \theta(x)$, thus Eq. (3.27) becomes:

$$|\Delta^\mu \psi_i^{\sigma_1}\rangle = \sum_{\sigma_2} P_c^{\sigma_1\sigma_2} \left| \frac{d\psi_i^{\sigma_2}}{d\mu} \right\rangle, \tag{3.31}$$

where:

$$P_c^{\sigma_1\sigma_2} = \sum_{j \in unocc.} \sum_{\sigma_3} |\psi_j^{\sigma_1}\rangle \langle \psi_j^{\sigma_3}| \, S^{\sigma_3\sigma_2} \tag{3.32}$$

is the projector over the conduction states. P_c is ubiquitous in DFPT, since all the relevant quantities, such as the charge density response and the force constants (see Section 3.2.5 below), can be expressed in terms of $P_c |d\psi_i^\sigma/d\mu\rangle$ in the NC PPs scheme, a milestone of DFPT presented in 1987 [42]. This is not strictly true in the US formulation, because the spin density response contains also the induced augmentation density matrix, $\Delta^\mu n^{\sigma\sigma'}(\mathbf{r})$, which depends on $|\delta^\mu \psi_i^\sigma\rangle$, a quantity reminiscent of the projection of $|d\psi_i^\sigma/d\mu\rangle$ over the occupied states, non-vanishing only if the orthonormalization constraints are variable.

Here we focus on the contributions to the induced spin density that contain $|\Delta^\mu \psi_i^\sigma\rangle$. In literature, they have been always written by exploiting the hermiticity of K, which implies that the two terms are the complex conjugate of each other [43, 46, 47, 49]:

$$\sum_{\sigma_1\,\sigma_2} \langle \Delta^\mu \psi_i^{\sigma_1} | K_{\sigma_1\sigma_2}^{\sigma\sigma'}(\mathbf{r}) | \psi_i^{\sigma_2}\rangle = \left[\sum_{\sigma_1\,\sigma_2} \langle \psi_i^{\sigma_1} | K_{\sigma_1\sigma_2}^{\sigma\sigma'}(\mathbf{r}) | \Delta^\mu \psi_i^{\sigma_2}\rangle \right]^*, \tag{3.33}$$

therefore Eq. (3.30) has been written as [49]:

$$\frac{dn^{\sigma\sigma'}(\mathbf{r})}{d\mu} = 2\,\mathrm{Re}\left[\sum_i \sum_{\sigma_1\,\sigma_2} \langle \psi_i^{\sigma_1} | K_{\sigma_1\sigma_2}^{\sigma\sigma'}(\mathbf{r}) | \Delta^\mu \psi_i^{\sigma_2}\rangle \right] + \Delta^\mu n^{\sigma\sigma'}(\mathbf{r}), \tag{3.34}$$

where Re identifies the real part. Eq. (3.34) is always valid and, in particular, it holds also for magnetic systems. However, it is not convenient to use when we specialize the formulation to a phonon perturbation in a non-collinear magnetic system (see Section 3.3 for more details). In this Thesis, we present a different approach which, by exploiting the properties of the time-reversal operator, allows to write the second term in the induced spin density (Eq. (3.30)) in terms of the time-reversed wave functions and the time-reversed responses [128]. The method, based on what has been recently proposed (in the NC scheme) for the calculation of magnons [52], *is necessary to deal with the non-collinear magnetic case where, after introducing the (complex) spin density response to a perturbation with wave vector* $\mathbf{q}$*, the two contributions that depend on the response of the wave functions are not related to each other.* We introduce the time-reversal operator:

$$\mathcal{T} = U\mathcal{K}, \tag{3.35}$$

an antiunitary operator [129] (see also Appendix B for a summary of the properties of antilinear operators and for a definition of the time-reversal operator, both in the spinless and the spin-1/2 cases) where:

$$U = i\sigma_y \tag{3.36}$$

is the unitary part, while $\mathcal{K}$ is the complex conjugation operator (an antilinear operator). Since $\mathcal{T}$ is antiunitary, it follows that $\mathcal{T}^\dagger\mathcal{T} = \mathbb{1}$, which can be inserted in the second term of Eq. (3.30) to get:

$$\begin{aligned}\frac{dn^{\sigma\sigma'}(\mathbf{r})}{d\mu} = &\sum_i \sum_{\sigma_1\sigma_2} \Big[\langle \psi_i^{\sigma_1} |\, K^{\sigma\sigma'}_{\sigma_1\sigma_2}(\mathbf{r})\, |\Delta^\mu \psi_i^{\sigma_2}\rangle \\ &+ \sum_{\sigma_3\sigma_4} \langle (\mathcal{T}\psi_i)^{\sigma_1}| \left(\mathcal{T}^{\sigma_1\sigma_3}\, K^{\sigma'\sigma}_{\sigma_3\sigma_4}(\mathbf{r})\, \mathcal{T}^{\dagger\sigma_4\sigma_2}\, |(\mathcal{T}\Delta^\mu\psi_i)^{\sigma_2}\rangle \right) \Big] + \Delta^\mu n^{\sigma\sigma'}(\mathbf{r}).\end{aligned} \tag{3.37}$$

As a result, the spin density response contains a term with the wave functions $|\psi_i^\sigma\rangle$ and the response $|\Delta^\mu\psi_i^\sigma\rangle$, and another term with the time-reversed wave functions $|(\mathcal{T}\psi_i)^\sigma\rangle$ and the time-reversed responses $|(\mathcal{T}\Delta^\mu\psi_i)^\sigma\rangle$. The induced charge density and magnetization density follow according to Eqs. (3.21) and (3.22). Following the complete derivation reported in Appendix G (see also Appendix D for an explanation on how to deal with the action of the time-reversal operator in the US kernel K), they read:

$$\begin{aligned}\frac{dn(\mathbf{r})}{d\mu} = &\sum_i \sum_\sigma \sum_{\sigma_1\,\sigma_2} \left[\langle \psi_i^{\sigma_1} | K^{\sigma\sigma}_{\sigma_1\sigma_2}(\mathbf{r}) | \Delta^\mu \psi_i^{\sigma_2}\rangle + \langle (\mathcal{T}\psi_i)^{\sigma_1}\, | K^{\sigma\sigma}_{\sigma_1\sigma_2}(\mathbf{r}) | (\mathcal{T}\Delta^\mu\psi_i)^{\sigma_2}\rangle \right] \\ &+ \sum_\sigma \Delta^\mu n^{\sigma\sigma}(\mathbf{r}),\end{aligned} \tag{3.38}$$

$$\begin{aligned}\frac{dm_\alpha(\mathbf{r})}{d\mu} = &\mu_\mathrm{B} \sum_i \sum_{\sigma\,\sigma'} \sum_{\sigma_1\,\sigma_2} \left[\langle \psi_i^{\sigma_1} | K^{\sigma\sigma'}_{\sigma_1\sigma_2}(\mathbf{r}) | \Delta^\mu \psi_i^{\sigma_2}\rangle - \langle (\mathcal{T}\psi_i)^{\sigma_1}\, | K^{\sigma\sigma'}_{\sigma_1\sigma_2}(\mathbf{r}) | (\mathcal{T}\Delta^\mu\psi_i)^{\sigma_2}\rangle \right] \sigma_\alpha^{\sigma\sigma'} \\ &+ \mu_\mathrm{B} \sum_{\sigma\sigma'} \Delta^\mu n^{\sigma\sigma'}(\mathbf{r})\, \sigma_\alpha^{\sigma\sigma'}.\end{aligned} \tag{3.39}$$

It is important to notice that the term containing the time-reversed wave functions contributes with a $-$ sign to the induced magnetization density, because the spin changes sign under the action of the time-reversal.

3.2.4 Sternheimer linear system

When dealing with metals, the response of the wave functions appearing in the induced spin density has to be generalized by introducing $|\Delta^\mu\psi_i^\sigma\rangle$ (Eq. (3.27)), therefore the Sternheimer linear system presented above (Eq. (3.16)) has to be generalized accordingly [45]. In the US case, this has been done in Ref. [47] for the spin-polarized case (in the LSDA formulation). Later, it has been generalized to the non-collinear FR case in the following way [49]:

$$\sum_{\sigma_2} \left[H^{[\mathbf{B}]\sigma_1\sigma_2}_\mathrm{KS} + Q^{\sigma_1\sigma_2} - \epsilon_i S^{\sigma_1\sigma_2} \right] |\overline{\Delta}^\mu \psi_i^{\sigma_2}\rangle = -\sum_{\sigma_2\sigma_3} P^{\dagger\sigma_1\sigma_2}_{c,i} \left[\frac{dV^{[\mathbf{B}]\sigma_2\sigma_3}_\mathrm{KS}}{d\mu} - \epsilon_i \frac{\partial S^{\sigma_2\sigma_3}}{\partial\mu} \right] \left| \psi_i^{\sigma_3} \right\rangle, \tag{3.40}$$

with

$$P^{\dagger\sigma_1\sigma_2}_{c,i} = \tilde{\theta}_{F,i}\, \delta^{\sigma_1\sigma_2} - \sum_j \sum_{\sigma_3} \beta_{ij}\, S^{\sigma_1\sigma_3}\, |\psi_j^{\sigma_3}\rangle\, \langle \psi_j^{\sigma_2}|\,. \tag{3.41}$$

$Q^{\sigma_1\sigma_2}$ in the left-hand side of Eq. (3.40) is an operator, non-vanishing only in the valence states, that makes the linear system non-singular [45, 47, 49]:

$$Q^{\sigma_1\sigma_2} = \sum_j \sum_{\sigma_3\,\sigma_4} \alpha_j \, S^{\sigma_1\sigma_3} \, |\psi_j^{\sigma_3}\rangle \, \langle \psi_j^{\sigma_4}| \, S^{\sigma_4\sigma_2}, \tag{3.42}$$

with

$$\alpha_j = \max(\epsilon_{\mathrm{F}} - 3\eta - \epsilon_j, 0), \tag{3.43}$$

where η is the smearing parameter. If one projects Eq. (3.40) on the unperturbed states, it follows that by choosing the coefficient β_{ij} as

$$\beta_{ij} = \tilde{\theta}_{F,i} \, \theta_{i,j} + \tilde{\theta}_{F,j} \, \theta_{j,i} + \alpha_j \, \frac{\tilde{\theta}_{F,i} - \tilde{\theta}_{F,j}}{\epsilon_i - \epsilon_j} \, \theta_{j,i}, \tag{3.44}$$

the solution $|\overline{\Delta}^{\mu}\psi_i^{\sigma}\rangle$ is [49]:

$$|\overline{\Delta}^{\mu}\psi_i^{\sigma_1}\rangle = |\Delta^{\mu}\psi_i^{\sigma_1}\rangle - \frac{1}{2\eta}\tilde{\delta}_{F,i} \, \frac{d\epsilon_{\mathrm{F}}}{d\mu}, \tag{3.45}$$

with $|\Delta^{\mu}\psi_i^{\sigma}\rangle$ being the wave functions response given by Eq. (3.27).

In Eq. (3.40), the right-hand side depends on the derivative of the spin-dependent, self-consistent, Hartree and exchange-correlation potential. Using Eq. (3.17) we can write:

$$\sum_{\sigma_3} \left[\frac{dV_{\mathrm{KS}}^{[\mathbf{B}]\sigma_2\sigma_3}}{d\mu} - \epsilon_i \frac{\partial S^{\sigma_2\sigma_3}}{\partial \mu} \right] \left| \psi_i^{\sigma_3} \right\rangle = |\phi_i^{\mu[\mathbf{B}]\sigma_2}\rangle + \sum_{\sigma_3\,\sigma_4\,\sigma_5} \int d^3r \, \frac{dV_{\mathrm{H,xc}}^{[\mathbf{B}]\sigma_4\sigma_5}(\mathbf{r})}{d\mu} \, K_{\sigma_2\sigma_3}^{\sigma_4\sigma_5}(\mathbf{r}) \, |\psi_i^{\sigma_3}\rangle \,, \tag{3.46}$$

where $|\phi_i^{\mu[\mathbf{B}]\sigma}\rangle$ is the non-self-consistent part of the induced potential:

$$|\phi_i^{\mu[\mathbf{B}]\sigma_2}\rangle = \sum_{\sigma_3} \left[\frac{\partial V_{\mathrm{KS}}^{[\mathbf{B}]\sigma_2\sigma_3}}{\partial \mu} - \epsilon_i \frac{\partial S^{\sigma_2\sigma_3}}{\partial \mu} \right] \left| \psi_i^{\sigma_3} \right\rangle. \tag{3.47}$$

In the alternative approach introduced in this Thesis and discussed for the induced spin density in Section 3.2.3, we need also the time-reversed response of the wave functions, $|(\mathcal{T}\Delta^{\mu}\psi_i)^{\sigma}\rangle$, which can be obtained as the solution of the following linear system:

$$\begin{aligned} \sum_{\sigma_2} \left[H_{\mathrm{KS}}^{[-\mathbf{B}]\sigma_1\sigma_2} + Q^{\sigma_1\sigma_2} - \epsilon_i S^{\sigma_1\sigma_2} \right] |\left(\mathcal{T}\overline{\Delta}^{\mu}\psi_i\right)^{\sigma_2}\rangle = -\sum_{\sigma_2} \Pi_{c,i}^{\dagger\sigma_1\sigma_2} \Bigg[|\phi_{T\,i}^{\mu[-\mathbf{B}]\sigma_2}\rangle \\ + \sum_{\sigma_3\,\sigma_4\,\sigma_5} \int d^3r \, \frac{dV_{\mathrm{H,xc}}^{[-\mathbf{B}]\sigma_4\sigma_5}(\mathbf{r})}{d\mu} \, K_{\sigma_2\sigma_3}^{\sigma_4\sigma_5}(\mathbf{r}) |(\mathcal{T}\psi_i)^{\sigma_3}\rangle \Bigg], \end{aligned} \tag{3.48}$$

which has been obtained by applying $\mathcal{T}$ to both sides of the Sternheimer linear system (Eq. (3.40)), similarly to what proposed in Ref. [52] for the calculation of magnons in the NC

case. In particular, we introduced the time-reversed non-self-consistent contribution to the induced potential, represented by the vector:

$$\begin{aligned} |\phi_{Ti}^{\mu[-\mathbf{B}]\sigma_2}\rangle &= \sum_{\sigma_3} \mathcal{T}^{\sigma_2\sigma_3}\, |\phi_i^{\mu[\mathbf{B}]\sigma_3}\rangle \\ &= \sum_{\sigma_3} \left[\frac{\partial V_{\mathrm{KS}}^{[-\mathbf{B}]\sigma_2\sigma_3}}{\partial\mu} - \epsilon_i \frac{\partial S^{\sigma_2\sigma_3}}{\partial\mu} \right] \Big| \, (\mathcal{T}\psi_i)^{\sigma_3} \Big\rangle, \end{aligned} \tag{3.49}$$

and the time-reversed projector on the conduction manifold [52], namely:

$$\Pi_{c,i}^{\dagger\sigma_1\sigma_2} = \sum_{\sigma_3\sigma_4} \mathcal{T}^{\sigma_1\sigma_3} P_{c,i}^{\dagger\sigma_3\sigma_4} \mathcal{T}^{\dagger\,\sigma_4\sigma_2}, \tag{3.50}$$

Notably, the effect of the time-reversal operator in Eq. (3.48) is to change sign to every term that contains a linear coupling with the spin, represented by the Pauli matrices (because $\mathcal{T}\sigma_\alpha\mathcal{T}^\dagger = -\sigma_\alpha$), an effect that can be equivalently achieved by changing sign to the exchange-correlation magnetic field $\mathbf{B}_{\mathrm{xc}}$. In the Sternheimer linear system, the objects that depend on $\mathbf{B}_{\mathrm{xc}}$ are the KS Hamiltonian, appearing on the left-hand side, and the non-self-consistent and the self-consistent terms of the induced potential, appearing on the right-hand side. In particular, we have:

$$\sum_{\sigma_3\,\sigma_4} \mathcal{T}^{\sigma_1\sigma_3}\, H_{\mathrm{KS}}^{[\mathbf{B}]\sigma_3\sigma_4}\, \mathcal{T}^{\dagger\,\sigma_4\sigma_2} = H_{\mathrm{KS}}^{[-\mathbf{B}]\sigma_1\sigma_2}, \tag{3.51}$$

$$\sum_{\sigma_3\,\sigma_4} \mathcal{T}^{\sigma_1\sigma_3}\, \frac{\partial V_{\mathrm{KS}}^{[\mathbf{B}]\sigma_3\sigma_4}(\mathbf{r})}{\partial\mu}\, \mathcal{T}^{\dagger\,\sigma_4\sigma_2} = \frac{\partial V_{\mathrm{KS}}^{[-\mathbf{B}]\sigma_1\sigma_2}(\mathbf{r})}{\partial\mu}, \tag{3.52}$$

$$\sum_{\sigma_3\,\sigma_4} \mathcal{T}^{\sigma_1\sigma_3}\, \frac{dV_{\mathrm{H,xc}}^{[\mathbf{B}]\sigma_3\sigma_4}(\mathbf{r})}{d\mu}\, \mathcal{T}^{\dagger\,\sigma_4\sigma_2} = \frac{dV_{\mathrm{H,xc}}^{[-\mathbf{B}]\sigma_1\sigma_2}(\mathbf{r})}{d\mu}. \tag{3.53}$$

3.2.5 Second-order energy derivatives: further analysis

The second-order derivative of the total energy may be further manipulated. Starting from the expression of the terms (a), b, and c presented above (Eqs. (3.9), (3.10), and (3.11), respectively), we use Eq. (3.26) in $d^2E_{\mathrm{tot}}^{(a)}/d\mu d\lambda$, then we write explicitly the quantity $d/d\mu(\partial V_{\mathrm{KS}}^{[\mathbf{B}]\sigma_1\sigma_2}/\partial\lambda)$ appearing in $d^2E_{\mathrm{tot}}^{(c)}/d\mu d\lambda$:

$$\frac{d}{d\mu}\left(\frac{\partial V_{\mathrm{KS}}^{[\mathbf{B}]\sigma_1\sigma_2}}{\partial\lambda}\right) = \frac{\partial^2 V_{\mathrm{KS}}^{[\mathbf{B}]\sigma_1\sigma_2}}{\partial\mu\partial\lambda} + \sum_{\sigma_3\sigma_4}\int d^3r\, \frac{dV_{\mathrm{H,xc}(\mathbf{r})}^{[\mathbf{B}]\sigma_3\sigma_4}}{d\mu}\, \frac{\partial K_{\sigma_1\sigma_2}^{\sigma_3\sigma_4}(\mathbf{r})}{\partial\lambda}, \tag{3.54}$$

where the explicit expression of the second-order partial derivative of the KS potential is:

$$\begin{aligned} \frac{\partial^2 V_{\mathrm{KS}}^{[\mathbf{B}]\sigma_1\sigma_2}}{\partial\mu\partial\lambda} =& \frac{\partial^2 V_{\mathrm{NL}}^{\sigma_1\sigma_2}}{\partial\mu\partial\lambda} + \sum_{\sigma_3}\int d^3r\, \frac{\partial^2 V_{\mathrm{loc}}(\mathbf{r})}{\partial\mu\partial\lambda}\, K_{\sigma_1\sigma_2}^{\sigma_3\sigma_3}(\mathbf{r}) + \sum_{\sigma_3\sigma_4}\int d^3r\, V_{\mathrm{LOC}}^{[\mathbf{B}]\sigma_3\sigma_4}(\mathbf{r})\, \frac{\partial^2 K_{\sigma_1\sigma_2}^{\sigma_3\sigma_4}(\mathbf{r})}{\partial\mu\partial\lambda} \\ &+ \sum_{\sigma_3}\left[\int d^3r\, \frac{\partial V_{\mathrm{loc}}(\mathbf{r})}{\partial\lambda}\, \frac{\partial K_{\sigma_1\sigma_2}^{\sigma_3\sigma_3}(\mathbf{r})}{\partial\mu} + \int d^3r\, \frac{\partial V_{\mathrm{loc}}(\mathbf{r})}{\partial\mu}\, \frac{\partial K_{\sigma_1\sigma_2}^{\sigma_3\sigma_3}(\mathbf{r})}{\partial\lambda}\right]. \end{aligned} \tag{3.55}$$

The presence of the fractional occupation numbers can be dealt with by using Eqs. (3.19) and (3.20), together with further bookkeeping techniques described in Refs. [45] and [47]. Finally, after introducing the two vectors $|\Delta^\mu\psi_i^\sigma\rangle$ and $|\delta^\mu\psi_i^\sigma\rangle$ (Eqs. (3.27) and (3.28)) and the induced augmentation density matrix $\Delta^\mu n^{\sigma\sigma'}(\mathbf{r})$ (Eq. (3.29)), $d^2E_{\rm tot}/d\mu d\lambda$ can be rewritten as a sum of the following four terms [49]. The first comes from the expectation value of the second-order derivative of the KS potential:

$$\frac{d^2E_{\rm tot}^{(1)}}{d\mu d\lambda} = \sum_i \sum_{\sigma_1\,\sigma_2} \tilde{\theta}_{F,i} \left\langle \psi_i^{\sigma_1} \middle| \frac{\partial^2 V_{\rm KS}^{[\mathbf{B}]\sigma_1\sigma_2}}{\partial\mu\partial\lambda} - \epsilon_i \frac{\partial^2 S^{\sigma_1\sigma_2}}{\partial\mu\partial\lambda} \middle| \psi_i^{\sigma_2} \right\rangle, \tag{3.56}$$

the second results from the change in the wave functions:

$$\frac{d^2E_{\rm tot}^{(2)}}{d\mu d\lambda} = \sum_i \sum_{\sigma_1} \left[\langle \phi_i^{\lambda[\mathbf{B}]\sigma_1} | \Delta^\mu \psi_i^{\sigma_1} \rangle + \langle \Delta^\mu \psi_i^{\sigma_1} | \phi_i^{\lambda[\mathbf{B}]\sigma_1} \rangle \right]. \tag{3.57}$$

Finally, the third and the fourth terms are peculiar of the US PPs scheme, and contain the derivatives of the overlap matrix S and of the kernel K:

$$\frac{d^2E_{\rm tot}^{(3)}}{d\mu d\lambda} = \sum_{\sigma_1\,\sigma_2} \int d^3r \, \frac{dV_{\rm H,xc}^{[\mathbf{B}]\sigma_1\sigma_2}(\mathbf{r})}{d\mu} \, \Delta^\lambda n^{\sigma_1\sigma_2}(\mathbf{r}), \tag{3.58}$$

$$\frac{d^2E_{\rm tot}^{(4)}}{d\mu d\lambda} = -\sum_i \sum_{\sigma_1} \left[\langle \delta^\mu \psi_i^{\sigma_1} | \phi_i^{\lambda[\mathbf{B}]\sigma_1} \rangle + \langle \delta^\lambda \psi_i^{\sigma_1} | \phi_i^{\mu[\mathbf{B}]\sigma_1} \right\rangle \Bigg]. \tag{3.59}$$

We focus on the term $d^2E_{\rm tot}^{(2)}/d\mu d\lambda$. Since $V_{\rm KS}$ and S are hermitian operators, we have:

$$\sum_{\sigma_1} \langle \Delta^\mu \psi_i^{\sigma_1} | \phi_i^{\lambda[\mathbf{B}]\sigma_1} \rangle = \left[\sum_{\sigma_1} \langle \phi_i^{\lambda[\mathbf{B}]\sigma_1} | \Delta^\mu \psi_i^{\sigma_1} \rangle \right]^*, \tag{3.60}$$

whence Eq. (3.57) is tipically written as [43, 46, 47, 49]:

$$\frac{d^2E_{\rm tot}^{(2)}}{d\mu d\lambda} = 2\,{\rm Re}\, \left[\sum_i \sum_{\sigma_1} \langle \phi_i^{\lambda[\mathbf{B}]\sigma_1} | \Delta^\mu \psi_i^{\sigma_1} \rangle \right], \tag{3.61}$$

therefore $d^2E_{\rm tot}^{(2)}/d\mu d\lambda$ is computed from the scalar product of $|\Delta^\mu\psi_i^\sigma\rangle$ and the non-self-consistent part in the right-hand side of the Sternheimer linear system.

As discussed above for the induced spin density, Eq. (3.61) is always valid and holds also in the non-collinear magnetic case because it follows from the hermiticity of $V_{\rm KS}$ and S, however it is not convenient to use because it requires both the responses at $\mathbf{q}$ and $-\mathbf{q}$. Here, instead we apply the alternative approach proposed in this Thesis, based on the usage of the time-reversal operator, to deal with Eq. (3.57) [128]. We insert the identity $\mathcal{T}^\dagger\mathcal{T} = \mathbb{1}$ in the second term of Eq. (3.57) to get:

$$\begin{aligned}
\sum_i \sum_{\sigma_1} \langle \Delta^\mu \psi_i^{\sigma_1} | \phi_i^{\lambda[\mathbf{B}]\sigma_1} \rangle &= \sum_i \sum_{\sigma_1\,\sigma_2\,\sigma_3} \langle \Delta^\mu \psi_i^{\sigma_1} | \Big(\mathcal{T}^{\dagger\,\sigma_1\sigma_2} \mathcal{T}^{\sigma_2\sigma_3} | \phi_i^{\lambda[\mathbf{B}]\sigma_3} \rangle \Big) \\
&= \sum_i \sum_{\sigma_1\,\sigma_2\,\sigma_3} \Big[\big(\langle \Delta^\mu \psi_i^{\sigma_1} | \mathcal{T}^{\dagger\,\sigma_1\sigma_2} \big) \Big(\mathcal{T}^{\sigma_2\sigma_3} | \phi_i^{\lambda[\mathbf{B}]\sigma_3} \rangle \Big) \Big]^* \\
&= \sum_i \sum_{\sigma_2} \langle \phi_{Ti}^{\lambda[-\mathbf{B}]\sigma_2} | (\mathcal{T} \Delta^\mu \psi_i)^{\sigma_2} \rangle,
\end{aligned} \tag{3.62}$$

where the second equality follows by applying the properties of antilinear operators. As a final result, Eq. (3.57) becomes:

$$\frac{d^2E^{(2)}_{\rm tot}}{d\mu d\lambda} = \sum_i \sum_{\sigma_1} \left[\langle \phi_i^{\lambda[\mathbf{B}]\sigma_1} | \Delta^\mu \psi_i^{\sigma_1} \rangle + \langle \phi_{Ti}^{\lambda[-\mathbf{B}]\sigma_1} | (\mathcal{T}\Delta^\mu \psi_i)^{\sigma_1} \rangle \right], \tag{3.63}$$

hence it is computed as the sum of the scalar products of the solutions of the two linear systems (Eqs. (3.40) and (3.48)) and the non-self-consistent contributions of the perturbation in the right-hand side of the two linear systems.

3.3 Formulation for lattice dynamics

In this Section, we focus on the particular case of lattice dynamics in extended systems, briefly introduced in Section 3.1. We introduce $\lambda = u_{\mu s\alpha}$, which represents a generic displacement of the atom s inside the μ-th unit cell along the direction α, and, similarly $\mu = u_{\nu s'\beta}$, and we consider the case of a phonon perturbation of wave vector $\mathbf{q}$.

3.3.1 Induced densities

As before, we start from the calculation of the induced densities. We introduce the spin density and the augmentation density matrix induced by a phonon perturbation at finite wave vector $\mathbf{q}$, $u_{s\alpha}(\mathbf{q})$ [49]:

$$\frac{dn^{\sigma\sigma'}(\mathbf{r})}{du_{s'\beta}(\mathbf{q})} = \sum_\nu e^{i\mathbf{q}\cdot\mathbf{R}_\nu} \frac{dn^{\sigma\sigma'}(\mathbf{r})}{du_{\nu s'\beta}}, \tag{3.64}$$

$$\Delta^{u_{s'\beta}(\mathbf{q})} n^{\sigma\sigma'}(\mathbf{r}) = \sum_\nu e^{i\mathbf{q}\cdot\mathbf{R}_\nu} \Delta^{u_{\nu s'\beta}} n^{\sigma\sigma'}(\mathbf{r}). \tag{3.65}$$

Similarly, after introducing the wave vector $\mathbf{k}$ and the band index v on the wave functions, as appropriate for solids , we define the change on the wave functions induced by a phonon perturbation in the following way:

$$|\Delta^{u_{s'\beta}(\mathbf{q})} \psi^{\sigma_1}_{\mathbf{k}v}\rangle = \sum_\mu e^{i\mathbf{q}\cdot\mathbf{R}_\mu} \, |\Delta^{u_{\nu s'\beta}} \psi^{\sigma_1}_{\mathbf{k}v}\rangle \,, \tag{3.66}$$

thus Eq. (3.37) becomes:

$$\begin{aligned} \frac{dn^{\sigma\sigma'}(\mathbf{r})}{du_{s'\beta}(\mathbf{q})} = & \sum_{\mathbf{k}v} \sum_{\sigma_1\sigma_2} \Bigg[\langle \psi^{\sigma_1}_{\mathbf{k}v} | \, K^{\sigma\sigma'}_{\sigma_1\sigma_2}(\mathbf{r}) \, |\Delta^{u_{s'\beta}(\mathbf{q})} \psi^{\sigma_2}_{\mathbf{k}v}\rangle \\ & + \sum_{\sigma_3\sigma_4} \langle (\mathcal{T}\psi_{-\mathbf{k}v})^{\sigma_1} | \, \mathcal{T}^{\sigma_1\sigma_3} K^{\sigma'\sigma}_{\sigma_3\sigma_4}(\mathbf{r}) \mathcal{T}^{\dagger\sigma_4\sigma_2} \, | \big(\mathcal{T}\Delta^{u_{s'\beta}(-\mathbf{q})} \psi_{-\mathbf{k}v}\big)^{\sigma_2} \rangle \Bigg] \\ & + \Delta^{u_{s'\beta}(\mathbf{q})} n^{\sigma\sigma'}(\mathbf{r}). \end{aligned} \tag{3.67}$$

This result represents an important starting point to understand the difference between the theoretical formulations for magnetic and non-magnetic systems. We consider a system

described by the Hamiltonian $H_{\rm KS}^{[\mathbf{B}]}$, $\mathbf{B}$ being the exchange-correlation magnetic field or, in general, even an external magnetic field: in particular, let us focus on the two self-consistent KS problems with $\mathbf{B}$ and $-\mathbf{B}$. To distinguish the two cases we label the eigenvalues and the eigenstates with the superscript $[\mathbf{B}]$ or $[-\mathbf{B}]$ (above, we did not specify such label in the wave functions, the energies, and the response of the wave functions because we always considered only the problem with $\mathbf{B}$). By comparing the solutions of the two problems, it can be proved that:

$$\epsilon_{-\mathbf{k}v}^{[\mathbf{B}]} = \epsilon_{\mathbf{k}v}^{[-\mathbf{B}]}, \tag{3.68}$$

$$|\mathcal{T}\psi_{-\mathbf{k}v}^{[\mathbf{B}]}\rangle = |\psi_{\mathbf{k}v}^{[-\mathbf{B}]}\rangle\,. \tag{3.69}$$

Similarly, if we extend the argument to the first-order perturbation theory, we have:

$$|\mathcal{T}\Delta^{u_{s'\beta}(-\mathbf{q})}\psi_{-\mathbf{k}v}^{[\mathbf{B}]}\rangle = |\Delta^{u_{s'\beta}(\mathbf{q})}\psi_{\mathbf{k}v}^{[-\mathbf{B}]}\rangle\,. \tag{3.70}$$

In the non-magnetic case, $\mathbf{B} = (0,0,0)$, therefore the wave functions at $\mathbf{k}$ and $-\mathbf{k}$ (and, similarly, their responses at $\mathbf{q}$ and $-\mathbf{q}$) are connected via the time-reversal operator and the eigenvalues at $\mathbf{k}$ and $-\mathbf{k}$ are equal. In particular, $|(\mathcal{T}\psi_{-\mathbf{k}v})^\sigma\rangle = |\psi_{\mathbf{k}v}^\sigma\rangle$ and $|\left(\mathcal{T}\Delta^{u_{s'\beta}(-\mathbf{q})}\psi_{-\mathbf{k}v}\right)^\sigma\rangle = |\Delta^{u_{s'\beta}(\mathbf{q})}\psi_{\mathbf{k}v}^\sigma\rangle$, therefore the two terms in square brackets in Eq. (3.67) become identical: in a practical calculation only the first term is computed, and the induced spin density reads

$$\frac{dn^{\sigma\sigma'}(\mathbf{r})}{du_{s'\beta}(\mathbf{q})} = 2\sum_{\mathbf{k}v}\sum_{\sigma_1\sigma_2}\langle\psi_{\mathbf{k}v}^{\sigma_1}|\,K_{\sigma_1\sigma_2}^{\sigma\sigma'}(\mathbf{r})\,|\Delta^{u_{s'\beta}(\mathbf{q})}\psi_{\mathbf{k}v}^{\sigma_2}\rangle\,. \tag{3.71}$$

Instead, in magnetic systems the eigenfunctions at $\mathbf{k}$ *of the KS problem with magnetic field* $\mathbf{B}$ *can be linked only to the time-reversed eigenfunctions at* $-\mathbf{k}$ *of the KS problem with magnetic field* $-\mathbf{B}$*, therefore Eq.* (3.67) *requires the solutions to two different problems, already introduced above in Section 3.2.4 and explicitly discussed for lattice dynamics in the following subsection.*

Once the induced spin density is computed, the responses of the charge and magnetization densities can be obtained by summing, with the appropriate phase factor, Eqs. (3.21) and (3.22), respectively, for each atomic displacement:

$$\frac{dn(\mathbf{r})}{du_{s'\beta}(\mathbf{q})} = \sum_\sigma \frac{dn^{\sigma\sigma}(\mathbf{r})}{du_{s'\beta}(\mathbf{q})}, \tag{3.72}$$

$$\frac{dm_\alpha(\mathbf{r})}{du_{s'\beta}(\mathbf{q})} = \mu_{\rm B}\sum_{\sigma\,\sigma'}\frac{dn^{\sigma\sigma'}(\mathbf{r})}{du_{s'\beta}(\mathbf{q})}\,\sigma_\alpha^{\sigma\sigma'}. \tag{3.73}$$

3.3.2 Linear system

In the magnetic case, the two vectors $|\Delta^{u_{s'\beta}(\mathbf{q})}\psi_{\mathbf{k}v}^\sigma\rangle$ and $|\left(\mathcal{T}\Delta^{u_{s'\beta}(-\mathbf{q})}\psi_{-\mathbf{k}v}\right)^\sigma\rangle$, appearing in Eq. (3.67), can be computed by solving two different problems. In particular, similarly to what reported in Section 3.2.4, they are obtained by adding a term (due to the change of the Fermi energy) to the solution of a Sternheimer linear system for a phonon perturbation.

These linear systems follow by adding, with the appropriate phase factor, Eqs. (3.40) and (3.48), respectively, for each atomic displacement, and read:

$$\sum_{\sigma_2}\left[H^{[\mathbf{B}]\sigma_1\sigma_2}+Q^{\sigma_1\sigma_2}-\epsilon_{\mathbf{k}v}\,S^{\sigma_1\sigma_2}\right]|\overline{\Delta}^{u_{s'\beta}(\mathbf{q})}\psi^{\sigma_2}_{\mathbf{k}v}\rangle=-\sum_{\sigma_2}P^{\dagger\sigma_1\sigma_2}_{c,\mathbf{k}v}\Bigg[|\phi^{u_{s'\beta}(\mathbf{q})[\mathbf{B}]\sigma_2}_{\mathbf{k}v}\rangle + \sum_{\sigma_3}\sum_{\sigma_4\sigma_5}\int d^3r\,\frac{dV^{[\mathbf{B}]\sigma_4\sigma_5}_{\mathrm{H,xc}}(\mathbf{r})}{du_{s'\beta}(\mathbf{q})}\,K^{\sigma_4\sigma_5}_{\sigma_2\sigma_3}(\mathbf{r})\,|\psi^{\sigma_3}_{\mathbf{k}v}\rangle\Bigg], \tag{3.74}$$

$$\sum_{\sigma_2}\left[H^{[-\mathbf{B}]\sigma_1\sigma_2}+Q^{\sigma_1\sigma_2}-\epsilon_{-\mathbf{k}v}\,S^{\sigma_1\sigma_2}\right]|(\mathcal{T}\overline{\Delta}^{u_{s'\beta}(-\mathbf{q})}\psi_{-\mathbf{k}v})^{\sigma_2}\rangle=-\sum_{\sigma_2}\Pi^{\dagger\sigma_1\sigma_2}_{c,-\mathbf{k}v}\Bigg[|\phi^{u_{s'\beta}(\mathbf{q})[-\mathbf{B}]\sigma_2}_{T-\mathbf{k}v}\rangle + \sum_{\sigma_3}\sum_{\sigma_4\sigma_5}\int d^3r\,\frac{dV^{[-\mathbf{B}]\sigma_4\sigma_5}_{\mathrm{H,xc}}(\mathbf{r})}{du_{s'\beta}(\mathbf{q})}\,K^{\sigma_4\sigma_5}_{\sigma_2\sigma_3}(\mathbf{r})\,|(\mathcal{T}\psi_{-\mathbf{k}v})^{\sigma_3}\rangle\Bigg], \tag{3.75}$$

where the expression of the vector $|\phi^{\lambda[\mathbf{B}]\sigma}_i\rangle$, appearing in the right-hand side, has been properly generalized to the case of a phonon perturbation:

$$|\phi^{u_{s'\beta}(\mathbf{q})[\mathbf{B}]\sigma_2}_{\mathbf{k}v}\rangle=\sum_{\sigma_3}\left[\frac{\partial V^{[\mathbf{B}]\sigma_2\sigma_3}_{\mathrm{KS}}}{\partial u_{s'\beta}(\mathbf{q})}-\epsilon_{\mathbf{k}v}\frac{\partial S^{\sigma_2\sigma_3}}{\partial u_{s'\beta}(\mathbf{q})}\right]\left|\psi^{\sigma_3}_{\mathbf{k}v}\right\rangle, \tag{3.76}$$

where, similarly to Eqs. (3.64) and (3.65), we defined:

$$\frac{\partial V^{[\mathbf{B}]\sigma_2\sigma_3}_{\mathrm{KS}}}{\partial u_{s'\beta}(\mathbf{q})}=\sum_{\nu}e^{i\mathbf{q}\cdot\mathbf{R}_\nu}\,\frac{\partial V^{[\mathbf{B}]\sigma_2\sigma_3}_{\mathrm{KS}}}{\partial u_{\nu s'\beta}}, \tag{3.77}$$

$$\frac{\partial S^{\sigma_2\sigma_3}}{\partial u_{s'\beta}(\mathbf{q})}=\sum_{\nu}e^{i\mathbf{q}\cdot\mathbf{R}_\nu}\,\frac{\partial S^{\sigma_2\sigma_3}}{\partial u_{\nu s'\beta}}. \tag{3.78}$$

We mention that, as a further possible alternative approach, it would be possible to write the spin density induced by a phonon perturbation starting from Eq. (3.30), without introducing the time-reversal operator, similarly to what has been done for the calculation of magnons in Ref. [51]. In that case, at variance with the approach discussed above, the second set of solutions needed to compute the induced spin density would require the solution of a Sternheimer linear system with magnetic field $\mathbf{B}$, but on the right-hand side we would have the responses to a perturbation at $-\mathbf{q}$.

Once more, we remark that instead, in non-magnetic systems, only $|\Delta^{u_{s'\beta}(\mathbf{q})}\psi^{\sigma}_{\mathbf{k}v}\rangle$ is needed, therefore only the first linear system, Eq. (3.74), is solved.

3.3.3 Dynamical matrix

Finally, we discuss the calculation of the dynamical matrix (Eq. (3.5)) in DFPT, given the expression of the second-order derivatives of the total energy reported above for generic perturbations λ and μ. Among the contributions coming from the four terms discussed in

Section 3.2.5, we consider that obtained from $d^2E^{(2)}_{\rm tot}/d\mu d\lambda$, which contains the response of the wave functions.

We start from Eq. (3.63). If we introduce the quantities defined above, the term $\Phi^{(2)}_{s\alpha s'\beta}(\mathbf{q})$ obtained from $d^2E^{(2)}_{\rm tot}/d\mu d\lambda$ reads:

$$\Phi^{(2)}_{\substack{s\alpha\\ s'\beta}}(\mathbf{q}) = \frac{1}{N}\sum_{\mathbf{k}v}\sum_{\sigma_1}\left[\langle\phi^{u_{s\alpha}(\mathbf{q})[\mathbf{B}]\sigma_1}_{\mathbf{k}v}|\Delta^{u_{s'\beta}(\mathbf{q})}\psi^{\sigma_1}_{\mathbf{k}v}\rangle + \langle\phi^{u_{s\alpha}(\mathbf{q})[-\mathbf{B}]\sigma_1}_{T\,-\mathbf{k}v}|\left(\mathcal{T}\Delta^{u_{s'\beta}(-\mathbf{q})}\psi_{-\mathbf{k}v}\right)^{\sigma_1}\rangle\right]. \tag{3.79}$$

Similarly to the discussion for the induced spin density above, in a time-reversal invariant (i.e. non-magnetic) system, the two terms in Eq. (3.79) are identical, because $|\phi^{u_{s\alpha}(\mathbf{q})[-\mathbf{B}]\sigma}_{T\,-\mathbf{k}v}\rangle = |\phi^{u_{s\alpha}(\mathbf{q})[\mathbf{B}]\sigma}_{\mathbf{k}v}\rangle$ and $|\left(\mathcal{T}\Delta^{u_{s'\beta}(-\mathbf{q})}\psi_{-\mathbf{k}v}\right)^{\sigma}\rangle = |\Delta^{u_{s'\beta}(\mathbf{q})}\psi^{\sigma}_{\mathbf{k}v}\rangle$, and therefore, in a practical implementation, the second term is not explicitly computed. This leads to the way Eq. (3.79) is usually presented in the literature (see, e.g. [47] for the LSDA spin-polarized case):

$$\Phi^{(2)}_{\substack{s\alpha\\ s'\beta}}(\mathbf{q}) = \frac{2}{N}\sum_{\mathbf{k}v}\sum_{\sigma_1}\langle\phi^{u_{s\alpha}(\mathbf{q})[\mathbf{B}]\sigma_1}_{\mathbf{k}v}|\Delta^{u_{s'\beta}(\mathbf{q})}\psi^{\sigma_1}_{\mathbf{k}v}\rangle\,. \tag{3.80}$$

On the other hand, a magnetic system is not time-reversal invariant, *hence the two terms in Eq.* (3.79) *are different and must be computed separately* [128].

3.4 Symmetrization

The induced spin density and, consequently, the induced charge and magnetization densities, and the dynamical matrix depend on summations over the **k**-points in the BZ. By exploiting a symmetrization procedure, it is possible to reduce the number of **k**-points in the sums, considering only the points inside the IBZ (thus decreasing the computational cost in practical calculations), similarly to what previously discussed for the charge and magnetization densities (see Section 1.7). We consider the symmetry operations $\{\mathcal{S}|\mathbf{f}\}$ of the space group of the crystal. In a magnetic solid, we have to consider also the operations $\mathcal{S}$ such that $\{\mathcal{T}\mathcal{S}|\mathbf{f}\}$ is a symmetry of the crystal. The full set of symmetries identifies the so-called *antiunitary space group* of the crystal.

Since, for a phonon perturbation, the charge (and magnetization) density response and the dynamical matrix are computed at a given finite wave vector **q**, we use as symmetry operations only those N_S operations of the *antiunitary small space group of* **q**, the subgroup of the antiunitary space group of the crystal, which contains only the symmetry operations $\{\mathcal{S}|\mathbf{f}\}$ such that:

$$\mathcal{S}\mathbf{q} = \mathbf{q} + \mathbf{G}_{\mathcal{S}}, \tag{3.81}$$

if $\{\mathcal{S}|\mathbf{f}\}$ is a symmetry of the crystal, or:

$$\mathcal{S}\mathbf{q} = -\mathbf{q} + \mathbf{G}_{\mathcal{S}}, \tag{3.82}$$

if $\{\mathcal{T}\mathcal{S}|\mathbf{f}\}$ is a symmetry of the crystal. Here, $\mathbf{G}_{\mathcal{S}}$ is a reciprocal lattice vector that might appear when **q** is at zone border. In order to distinguish the two cases we introduce a variable $\tau(\mathcal{S})$ which may take the values $\tau = 0$ or $\tau = 1$ if Eq. (3.81) or Eq. (3.82) holds, respectively.

We compute the non-symmetrized induced spin density by summing over the Irreducible Brillouin Zone (IBZ) in Eqs. (3.72) and (3.73), introducing a weight proportional to the number of elements in the star of $\mathbf{q}$. Then, we calculate the non-symmetrized induced charge and magnetization densities $\widetilde{dn}^{\mathrm{NS}}(\mathbf{r})/du_{s'\beta}(\mathbf{q})$ and $\widetilde{dm}_{\delta}^{\mathrm{NS}}(\mathbf{r})/du_{s'\beta}(\mathbf{q})$ using Eqs. (H.20) and (H.21). Finally, the complete responses are obtained through the following relationships:

$$\frac{\widetilde{dn}(\mathbf{r})}{du_{s'\beta}(\mathbf{q})} = \frac{1}{N_S}\sum_{\{\mathcal{S}|\mathbf{f}\}}\mathcal{O}_{\tau(\mathcal{S})}\left[\sum_{\gamma} S_{\gamma\beta}\frac{\widetilde{dn}^{\mathrm{NS}}(\{\mathcal{S}|\mathbf{f}\}\mathbf{r})}{du_{\bar{s}'\gamma}(\mathbf{q})}e^{i\mathbf{G}_{\mathcal{S}^{-1}}\cdot\mathbf{r}}e^{-i\mathbf{q}\cdot\mathbf{R}^{\mathcal{S}}_{s'}}\right], \tag{3.83}$$

$$\frac{\widetilde{dm}_{\delta}(\mathbf{r})}{du_{s'\beta}(\mathbf{q})} = \frac{1}{N_S}\sum_{\{\mathcal{S}|\mathbf{f}\}}(-1)^{\tau(\mathcal{S})}\mathcal{O}_{\tau(\mathcal{S})}\left[\sum_{\gamma\eta}\widetilde{S}^{-1}_{\delta\eta}S_{\gamma\beta}\frac{\widetilde{dm}_{\eta}^{\mathrm{NS}}(\{\mathcal{S}|\mathbf{f}\}\mathbf{r})}{du_{\bar{s}'\gamma}(\mathbf{q})}e^{i\mathbf{G}_{\mathcal{S}^{-1}}\cdot\mathbf{r}}e^{-i\mathbf{q}\cdot\mathbf{R}^{\mathcal{S}}_{s'}}\right], \tag{3.84}$$

where $\widetilde{S}$ is the proper part of S, $\mathcal{O}_{\tau(\mathcal{S})}$ is the identity if $\tau(\mathcal{S})=0$, or $\mathcal{O}_{\tau(\mathcal{S})}=\mathcal{K}$ if $\tau(\mathcal{S})=1$. Moreover, $\mathbf{R}^{\mathcal{S}}_{s'}=\mathcal{S}\mathbf{d}_{s'}-\mathbf{d}_{\bar{s}'}$, where $\mathbf{d}_{s'}$ identifies the position of the atom s' with respect to the origin of its primitive cell, while $\mathbf{d}_{\bar{s}'}$ is obtained by applying the rotation $\mathcal{S}$ to the atom s' ($\{\mathcal{S}|\mathbf{f}\}(\mathbf{R}_{\nu}+\mathbf{d}_{s'})=\mathbf{R}_{\bar{\nu}}+\mathbf{d}_{\bar{s}'}$). Similarly, the dynamical matrix becomes:

$$\Phi_{\substack{s\alpha\\ s'\beta}}(\mathbf{q}) = \frac{1}{N_S}\sum_{\{\mathcal{S}|\mathbf{f}\}}\mathcal{O}_{\tau(\mathcal{S})}\left[\sum_{\gamma\delta} S_{\gamma\alpha}\,S_{\delta\beta}\,\Phi^{\mathrm{NS}}_{\substack{\bar{s}\gamma\\ \bar{s}'\delta}}(\mathbf{q})e^{i\mathbf{q}\cdot(\mathbf{R}^{\mathcal{S}}_{s}-\mathbf{R}^{\mathcal{S}}_{s'})}\right], \tag{3.85}$$

where $\Phi^{\mathrm{NS}}_{\bar{s}\gamma\bar{s}'\delta}(\mathbf{q})$ is obtained summing over the IBZ.

A complete derivation of Eqs. (3.83), (3.84), and (3.85) presented here is reported in Appendix I.

3.5 Theory validation: applications to fcc Ni and Pt nanowire

In this section we use the theory described above to compute the phonon dispersions of ferromagnetic fcc Ni and of a monatomic ferromagnetic Pt nanowire. We validate the theory by comparing the phonon frequencies obtained by diagonalizing the dynamical matrix (Eq. (3.5)) with those obtained by the frozen phonon method.

3.5.1 Methods

First-principle calculations were performed within the Local Density Approximation (LDA) [56] and the Perdew-Burke-Ernzerhof (PBE) [65] schemes, as implemented in the `Quantum ESPRESSO` [119–121] and `thermo_pw` [1]. packages. The atoms are described by FR US PPs [40], with $4s$ and $3d$ valence electrons for Ni (PPs `Ni.rel-pz-n-rrkjus_psl.0.1.UPF` and `Ni.rel-pbe-n-rrkjus_psl.0.1.UPF` from pslibrary 0.1) and with $6s$ and $5d$ valence electrons for Pt (`PP Pt.rel-pz-n-rrkjus_psl.1.0.0.UPF` from pslibrary 1.0.0 [123] [2]).

[1] `thermo_pw` is a driver of the Quantum ESPRESSO (QE) routines which provides an alternative organization of the QE work-flow for the most common tasks. For more information see `https://dalcorso.github.io/thermo_pw`

[2] See `https://dalcorso.github.io/pslibrary`

DFPT calculations on ferromagnetic fcc Ni are at the theoretical LDA and PBE lattice constants, $a = 6.483$ a.u. and $a = 6.658$ a.u., which are 2.6% and 0.02% smaller than experiment [124] ($a = 6.659$ a.u.), respectively. The pseudo wavefunctions (charge density) are expanded in a plane waves basis set with a kinetic energy cut-off of 120 (600) Ry. The BZ integrations were done using a shifted uniform Monkhorst-Pack [74] **k**-point mesh of $28 \times 28 \times 28$ points for the phonon calculations at a single wave vector **q**. The same computational parameters, except the **k**-point mesh which has been reduced to $18 \times 18 \times 18$ points, have been used for the phonon dispersions. The dynamical matrices have been computed by DFPT on a $6 \times 6 \times 6$ **q**-point mesh, and Fourier interpolated to obtain the complete dispersions. Phonon frequencies of ferromagnetic Ni with the frozen phonon method, were calculated with a simple cubic supercell with 4 Ni atoms. The kinetic energy cut-offs used are the same as for the DFPT calculations, while the BZ integrations were performed on a **k**-point mesh of $24 \times 24 \times 24$ points. The presence of a Fermi surface has been dealt with by the Methfessel-Paxton smearing method [71] with a smearing parameter $\sigma = 0.02$ Ry.

DFPT calculations on monatomic ferromagnetic Pt nanowire were done at a stretched geometry with interatomic distance $d = 4.927$ a.u.. The wire replicas have been separated by a vacuum space of 20 a.u.. We have checked that by increasing the vacuum space the computed frequencies do not change more than 0.2 cm^{-1}. The system has been studied in a ferromagnetic configuration, with magnetization either parallel or perpendicular to the wire. The kinetic energy cut-off was 60 (400) Ry for the wave functions (charge density). The **k**-point mesh is a shifted uniform Monkhorst-Pack mesh of 300 points. Frozen phonon calculations were performed with supercells with 2 and 4 Pt atoms, and Monkhorst-Pack meshes of 150 and 75 **k**-points, respectively. The smearing parameter was $\sigma = 0.002$ Ry.

3.5.2 Fcc Ni

We start our discussion from the computation of the phonon frequencies of ferromagnetic fcc Ni with the magnetization along [001] (and with a magnitude that turns out to be $0.62\,\mu_{\mathrm{B}}$ per atom), and compare the DFPT and the frozen phonon method at the Y and Z points. The results obtained are reported in Table 3.1. The frequencies of the transverse modes at $\mathbf{q} = (0, 0, 2\pi/a)$ (Z) are degenerate with both methods, as a consequence of the tetragonal magnetic symmetry ($D_{4h}(C_{4h})$): indeed both transverse modes have atomic displacements perpendicular to the magnetization. Instead, the transverse modes at $\mathbf{q} = (0, 2\pi/a, 0)$ (Y) show a small splitting of $0.04\,\mathrm{cm}^{-1}$. The two modes are actually different because the atomic displacements are either parallel or perpendicular to the magnetization. A frequency splitting arises as a consequence of spin-orbit coupling. The DFPT and frozen phonon methods agree within $0.3\,\mathrm{cm}^{-1}$. The DFPT and the frozen phonon method predict the same splitting, which however is small compared to the agreement of the absolute values of the frequencies obtained with the two methods, hence it is not possible to give an accurate quantitative prediction, but only an order of magnitude. With the kinetic energy cut-offs and **k**-point mesh used, the frequencies obtained are converged within $5 \times 10^{-3}\,\mathrm{cm}^{-1}$, the same order of magnitude as the errorbar reported in Table 3.1 and due to the fit.

In Fig. 3.1 we show the complete phonon dispersion of fcc Ni obtained by DFPT. Both LDA and PBE theoretical dispersions are shown, together with inelastic neutron scattering data [130]. The agreement between the LDA result and the experiment is poor, mainly

	DFPT $\nu(\mathrm{cm}^{-1})$	Frozen phonon $\nu(\mathrm{cm}^{-1})$
$T_x^{(0,1,0)}$	232.438	232.691 ± 0.006
$T_z^{(0,1,0)}$	232.397	232.648 ± 0.006
$T_{\{xy\}}^{(0,0,1)}$	232.433	232.688 ± 0.006

Table 3.1: Computed FR LDA phonon frequencies at $\mathbf{q} = (0, 2\pi/a, 0)$ and $\mathbf{q} = (0, 0, 2\pi/a)$ with DFPT and the frozen phonon method for fcc Ni. The magnetization is oriented along the z axis. The subscripts indicate the polarization of the phonon modes.

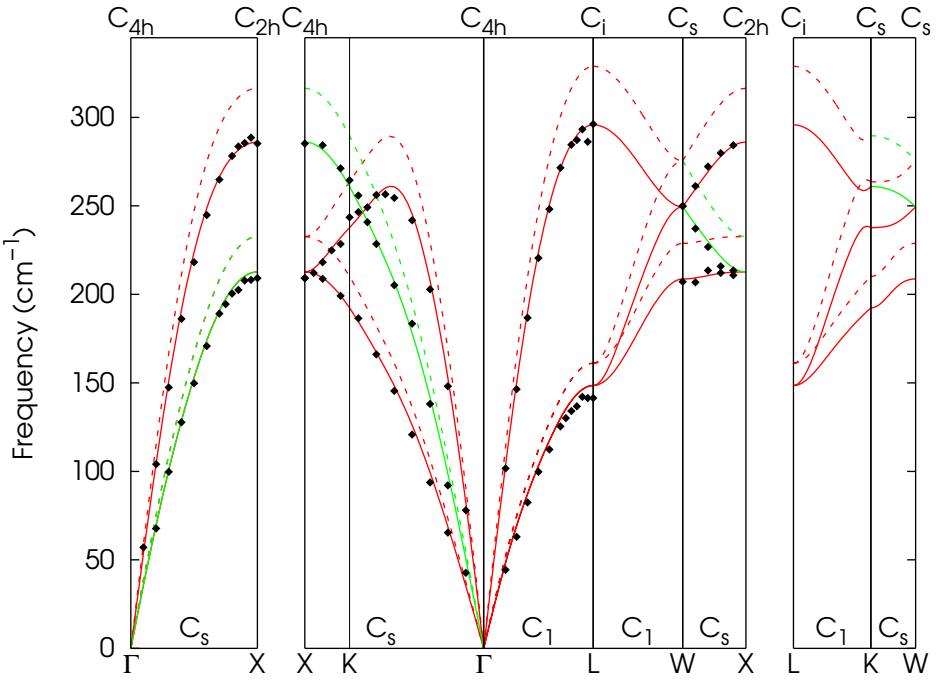

Figure 3.1: Computed FR LDA (dashed lines) and PBE (solid lines) phonon dispersions of ferromagnetic fcc Ni, compared to inelastic neutron scattering data (solid diamonds). Phonon modes are classified using symmetry, but only the operations that do not require $\mathcal{T}$ are used.

because LDA underestimates the lattice constant: the highest frequencies of the dispersion (e.g. at the X and L points) are about $30\,\mathrm{cm}^{-1}$ higher than the experiment. On the other hand, the PBE phonon dispersions are in excellent agreement with the experiment. Note however that this agreement is slightly worsened by temperature effects [131] not included in the present study.

q		$\mathbf{m} \parallel x$		$\mathbf{m} \parallel z$	
		DFPT $\nu(\mathrm{cm}^{-1})$	Frozen phonon $\nu(\mathrm{cm}^{-1})$	DFPT $\nu(\mathrm{cm}^{-1})$	Frozen phonon $\nu(\mathrm{cm}^{-1})$
π/a	T_x	36.51	37.02 ± 0.03	45.71	46.10 ± 0.03
	T_y	37.00	37.34 ± 0.03	45.71	46.10 ± 0.03
	L	113.98	114.21 ± 0.03	110.30	110.51 ± 0.03
$\pi/2a$	T_x	25.1	25.5 ± 0.1	39.17	39.63 ± 0.03
	T_y	32.1	31.8 ± 0.1	39.17	39.65 ± 0.03
	L	54.2	53.8 ± 0.1	62.66	63.14 ± 0.03

Table 3.2: Computed FR LDA phonon frequencies at $q = \pi/a$ and $q = \pi/2a$ with DFPT and the frozen phonon method for a monatomic ferromagnetic Pt nanowire. The nanowire is oriented along the z axis. Results are shown with both $\mathbf{m} \parallel x$ and $\mathbf{m} \parallel z$. The subscripts indicate the polarization of the phonon modes.

3.5.3 Pt monatomic wire

In this section we consider a monatomic Pt nanowire, a metal with ferromagnetic ordering. It has been shown [53, 132] that at its equilibrium geometry (atomic distance $d = 4.441$ a.u.) the system shows a colossal magnetic anisotropy, since the preferred orientation of the magnetization is parallel to the wire and the magnetization vanishes when forced to be perpendicular to the wire. Instead, for stretched geometries with atomic distance higher than 4.913 a.u. a non-zero magnetization perpendicular to the wire is allowed. Here we consider a stretched geometry with $d = 4.927$ a.u. and compute the phonon dispersions with both a magnetization parallel and perpendicular to the wire. In the following the nanowire is along the z direction. In Table 3.2 we compare the phonon frequencies, at $q = \pi/a$ and $q = \pi/2a$ with $\mathbf{m} \parallel x$ and $\mathbf{m} \parallel z$, computed by the DFPT and with the frozen phonon method. With a magnetization $\mathbf{m} \parallel z$ ($m = 0.65\,\mu_\mathrm{B}$ per atom), the frequencies of the transverse modes are degenerate, while with $\mathbf{m} \parallel x$ ($m = 0.13\,\mu_\mathrm{B}$ per atom) at $q = \pi/a$ the two transverse modes show a splitting of about $0.5\,\mathrm{cm}^{-1}$, which is of the same order of magnitude as the overall agreement of the two methods. At $q = \pi/2a$ this splitting is about $7\,\mathrm{cm}^{-1}$, one order of magnitude larger than at $q = \pi/a$. In both cases the polarization of the transverse mode with higher frequency is perpendicular to the magnetization. As discussed above for fcc Ni, the two transverse modes are not equivalent due to the presence of the magnetization and of spin-orbit coupling. Pt atoms are heavier than Ni and show a stronger spin-orbit interaction: indeed, the splitting reported for Pt is $1 - 2$ orders of magnitudes higher than in Ni. The DFPT and frozen phonon results agree within $0.4\,\mathrm{cm}^{-1}$ on average. As before, the errorbars reported in Table 3.2 come from the linear fit. With the kinetic energy cut-offs and the $\mathbf{k}$-point mesh used all the frequencies reported are converged within $0.03\,\mathrm{cm}^{-1}$

In Fig. 3.2 we show the phonon branches along $\Gamma-$ Z for a ferromagnetic wire with magnetization parallel (left panel) or perpendicular to the wire (right panel). The two dispersions show evident differences: at $q = \pi/a$, the longitudinal mode for the wire with $\mathbf{m} \parallel z$ is lower in frequency than for the wire with $\mathbf{m} \parallel x$, while the transverse modes are higher in frequency. In the central part of the BZ, around $q = \pi/2a$, the longitudinal mode

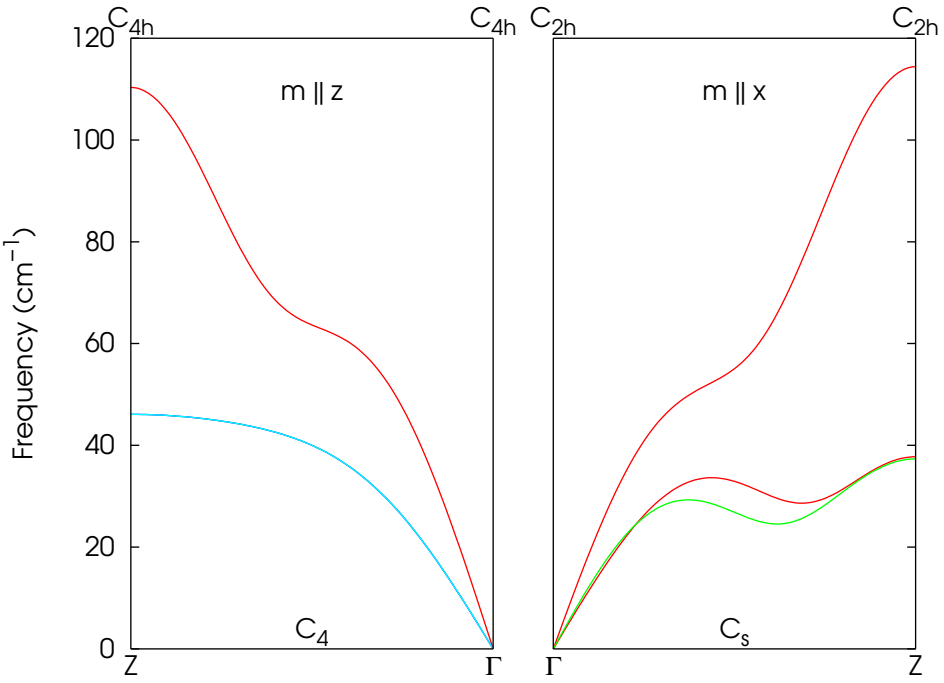

Figure 3.2: Computed FR LDA phonon dispersions of ferromagnetic Pt nanowire. Left panel: magnetization parallel to the wire. Right panel: magnetization perpendicular to the wire.

of the wire with $\mathbf{m} \parallel z$ has a higher frequency at the Kohn anomaly than the wire with $\mathbf{m} \parallel x$, while the transverse modes show a Kohn anomaly only for $\mathbf{m} \parallel x$. We remark that at the stretched geometry studied ($d = 4.927$ a.u.) the phonon modes are still stable, but the range of atomic distances at which both modes are stable is quite narrow.

Chapter 4

Lattice dynamics effects on the magnetocrystalline anisotropy energy: application to MnBi

Recently, there has been a significant effort towards the realization of rare-earth-free permanent magnets [133, 134]. Due to its magnetic properties, such as a high Curie temperature, well above room temperature, and a large *uniaxial magnetic anisotropy*, the intermetallic MnBi compound [134–137] has emerged as a promising candidate among the transition-metal-based materials.

4.1 A brief overview on MnBi: magnetic properties, magnetocrystalline anisotropy, spin-reorientation transition

In the low-temperature phase (LTP), MnBi is a ferromagnet and crystallizes in the NiAs structure (see Fig. 4.1). As reported by C. Guillaud in 1951 [135], the compound remains ferromagnetic upon heating, up to $T \approx 630$ K, whereas a non-vanishing net magnetization reappears upon cooling at $T \approx 610$ K [135]. The presence of a latent heat and the abrupt drop of the net magnetization (see, e.g., Ref. [138]) suggests that the transition is of the first order, in contrast with the usual ferromagnetic-paramagnetic second-order phase transitions [1]. These experimental evidences have been interpreted in different ways [135, 136, 139, 140]. The current explanation of the LTP-HTP phase is that of Ref. [140], where it was proposed that the HTP is a separate compound with a chemical formula of $Mn_{1.08}Bi$: according to

[1] The estimation of an hypothetical Curie temperature T_c for MnBi would lead to $T_c = 680$ K [138], ≈ 50 K higher than the transition temperature reported by experiments.

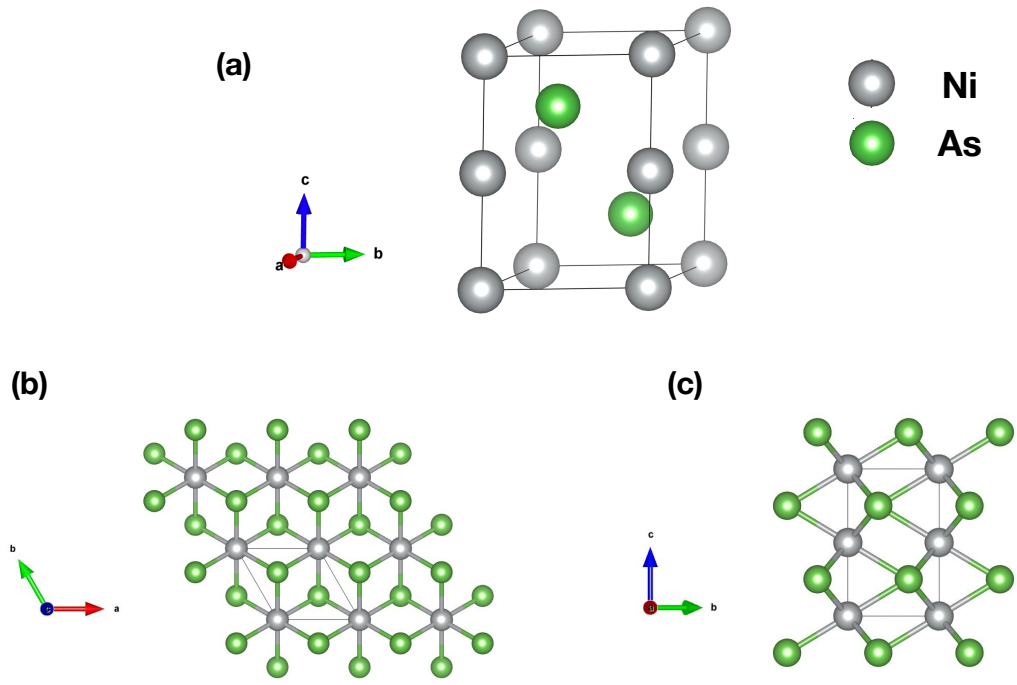

Figure 4.1: The NiAs structure. (a) Unit cell. (b) Top view. (c) Side view. The edges of the unit cell are indicated with black solid lines.

the MnBi phase diagram, the phase transition upon heating is associated with a peritectic decomposition of MnBi (LTP) into $Mn_{1.08}Bi$ (HTP) and liquid Bi. On the other hand, upon cooling the HTP undergoes a transformation of solid-solid decomposition of $Mn_{1.08}Bi$ into MnBi + Mn. In the same work, Ref. [140], a second phase transition occurring at $T \approx 720$ K was identified to be a decomposition of $Mn_{1.08}Bi$ into Mn and liquid Bi.

The electronic structure of the LTP MnBi has been studied, e.g., in Ref. [141]. The bands near the Fermi level are made up of Bi-p and Mn-d orbitals, whereas the Bi-s bands lie lower in energy and are fully occupied, and the Mn-s bands are empty. With spin-polarized calculations, the Mn-d bands are split by the exchange interaction: as a consequence, the majority channel of Mn-d states is fully occupied, while the minority channel is occupied by ≈ 0.8 electrons per Mn, leading to a magnetic moment of approximately $4\,\mu_B$ per Mn (see Table 4.1 for some reference values taken from theoretical and experimental references).

The presence of a relevant spin-orbit coupling in the system, due to the heavy element Bi, together with a strong ferromagnetism, is responsible for evident magnetocrystalline anisotropy effects in MnBi, that were reported by experimental studies already in the 50s [142]. Being an hexagonal crystal, MnBi possesses a single axis of high symmetry (a 6 axis), hence the magnetocrystalline anisotropy is of the *uniaxial* type. In a hexagonal crystal, the magnetocrystalline anisotropy energy (MAE) reads [143]:

$$E_A = K_1 \sin^2\theta + K_2 \sin^4\theta + (K_3 + K_4 \cos 6\phi) \sin^6\theta, \tag{4.1}$$

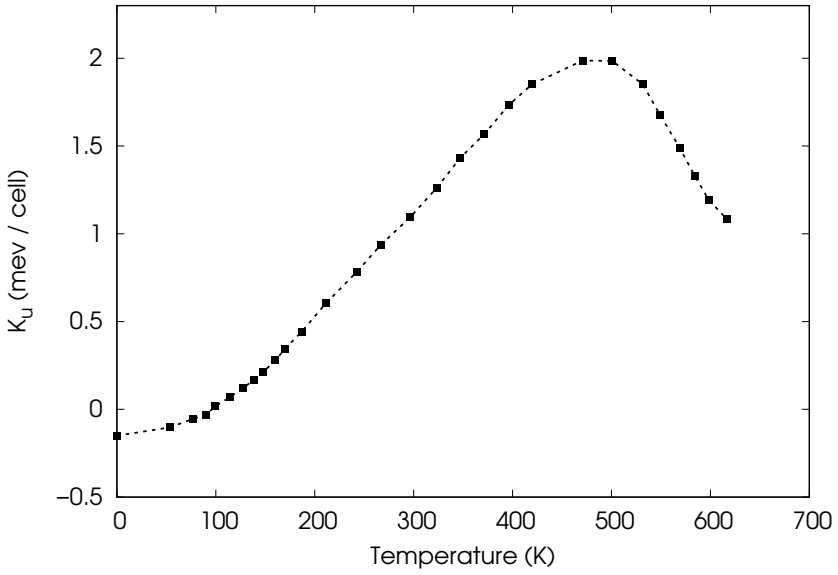

Figure 4.2: Experimental MAE constant K_u as a function of temperature. Experimental data are reported in Ref. [143].

where θ and ϕ are the angular polar coordinates that identify the direction of the magnetization. A study of the magnetocrystalline anisotropy in the basal plane led to determine $\phi = 15°$ [143], hence the term containing K_4 in Eq. (4.1) vanishes. The quantity that is typically reported in experiments is $K_\mathrm{u} = K_1 + K_2 + K_3$, usually referred to as *MAE constant*: conceptually, K_u corresponds to the energy difference between the configurations with magnetization perpendicular to the c axis and magnetization parallel to the c axis, corresponding to $\theta = \pi/2$ and $\theta = 0$ in Eq. (4.1), respectively.

The behavior of the MAE as a function of temperature in MnBi is peculiar: at $T = 0$ K K_u is negative, its reported experimental value being -0.2 MJ / m^3 (≈ -0.12 meV / cell) with an easy axis in the basal plane [142, 143], and increases with T (see Fig. 4.2), unlike most magnetic systems [136, 143]. At $T \approx 90$ K K_u becomes positive, thus leading to a *spin-reorientation transition*: from 90 K to 140 K, the easy axis rotates outside the basal plane, and above 140 K it is parallel to the c axis [144].

Several studies, both experimental and theoretical, have been carried out during the decades to understand this intriguing property. In experiments, the spin-reorientation transition was observed also by neutron diffraction [139,145] and nuclear magnetic resonance [144]. Several other properties of MnBi have been studied, including the thermal expansion. In particular, the spin-reorientation transition comes together with a small kink in the lattice parameters (see Fig. 4.3) at $T \approx 90$ K [146, 147], which has been interpreted as the sign of a phase transition. Theoretical calculations, based on DFT within the LDA and the GGA approximations for the exchange-correlation functional, correctly predict MnBi to be a metal

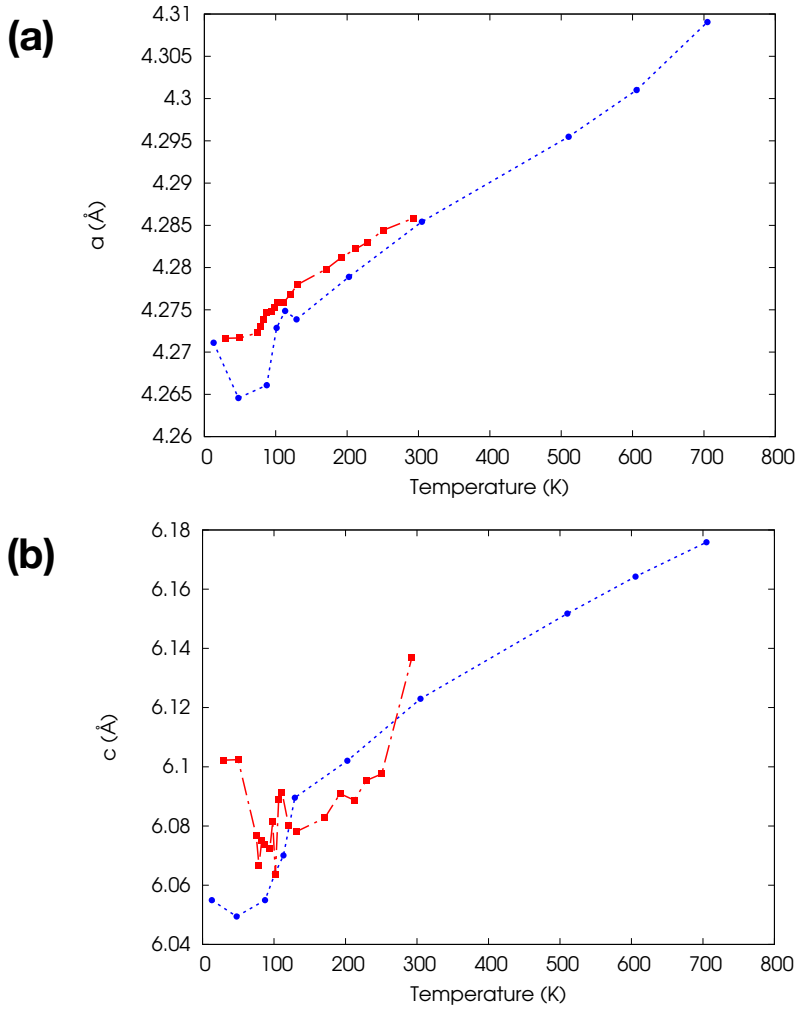

Figure 4.3: Experimental thermal expansion data. (a) a and (b) c lattice constants as a function of temperature. Blue and red dots and lines represent experimental data taken from Refs. [146, 147], respectively.

and a ferromagnet in the low-temperature phase, and to have a negative K_u, in qualitative agreement with experiments. Yet, they are believed to overestimate the magnitude of K_u by nearly an order of magnitude and are often not able to reproduce the correct behavior of K_u as a function of temperature. Refs. [148] and [149] showed that the treatment of correlation effects by means of the DFT+U approach is important to get the correct behavior of K_u as a function of temperature. In particular, in Ref. [149] the inclusion of the thermal expansion effects on K_u allowed to get a spin-reorientation temperature in agreement with experiments and a theoretical MAE constant in good agreement with experimental results, especially in the temperature range 150-450 K.

More recently, in Ref. [141] it was suggested that the spin-reorientation phenomenon might be partially due to lattice dynamics. Such statement was supported by the calculation of the lattice dynamics contribution to K_u, obtained by averaging the MAE over

configurations in which the Mn and Bi atoms were displaced according to the mean square atomic displacements as a function of temperature.

The extension of DFPT for lattice dynamics with FR US-PPs to magnetic materials [150], presented in Chapter 3, allows to detect differences in the phonon frequencies for different orientations of the magnetization, thus making possible to evaluate the vibrational free energy contribution to the MAE.

In this Chapter we study, by means of *ab initio* techniques, the lattice dynamics of ferromagnetic MnBi for two different orientations of the magnetization: 1. in-plane; 2. perpendicular to the plane. We find that the two phonon dispersions mainly differ in the high-frequency optical branches, where the phase with magnetic moments pointing in the out-of-plane direction shows, on average, phonon modes of 2 cm^{-1} lower in frequency. Starting from the difference of the vibrational density of states of the two phases we compute the vibrational contribution to MAE. We find that, if the energy contribution to MAE is computed by the PBEsol exchange-correlation functional, the phonon contribution is of the same order of magnitude as the ground state MAE, hence it plays a relevant role in the calculation of K_{u} and to determine the spin-reorientation transition temperature T_{SR}.

4.2 Methods

First-principle calculations were carried out by means of DFT [34,35] within the LDA [56] and the Perdew-Burke-Ernzerhof optimized for solids (PBEsol) [66] schemes for the exchange-correlation functional approximation, as implemented in the `Quantum ESPRESSO` [119–121] and `thermo_pw` [2] packages. The atoms are described by FR US-PPs [40], with $3p$, $4s$, and $3d$ electrons for Mn (PPs `Mn.rel-pz-spn-rrkjus_psl.0.3.1.UPF` and `Mn.rel-pbesol-spn-rrkjus_psl.0.3.1.UPF` , from pslibrary 0.3.1 [123] [3]) and with $6s$, $5d$, and $6p$ electrons for Bi (PPs `Bi.rel-pz-dn-rrkjus_psl.1.0.0.UPF` and `Bi.rel-pbesol-dn-rrkjus_psl.1.0.0.UPF`, from pslibrary 1.0.0 [123]).

MnBi crystallizes in the NiAs structure (Fig. 4.1), with an hexagonal lattice described by the point group D_{6h}. The inclusion of magnetism differentiates the structures into a low-symmetry phase ($\mathbf{m} \perp \mathbf{c}$ henceforth), below T_{SR}, and a high-symmetry phase ($\mathbf{m} \parallel \mathbf{c}$ henceforth), above T_{SR}. In particular, the $\mathbf{m} \parallel \mathbf{c}$ phase is described by the magnetic point group $D_{6h}(C_{6h})$, compatible with an hexagonal Bravais lattice, while the $\mathbf{m} \perp \mathbf{c}$ phase has a magnetic point group $D_{2h}(C_{2h})$, compatible with a base-centered orthorhombic Bravais lattice. We checked the relevance of the lattice parameter b, which is not constrained by symmetry in the $\mathbf{m} \perp \mathbf{c}$ phase, and concluded that it is not crucial to make the structure more stable than the $\mathbf{m} \parallel \mathbf{c}$ phase, hence in the rest of the chapter we use the ideal value $b = \sqrt{3}a$. In Table 4.1 we summarize the data relative to the lattice constants and to the magnetic moment of Mn atoms, obtained with the LDA and PBEsol functionals, and compare them with previous theoretical results and with experiments. The LDA geometry is in good agreement with the theoretical results reported in Ref. [141], but both lattice constants

[2] `thermo_pw` is a driver of the `Quantum ESPRESSO` (QE) routines which provides an alternative organization of the QE work-flow for the most common tasks. For more information see `https://dalcorso.github.io/thermo_pw`.

[3] See `https://dalcorso.github.io/pslibrary`

Exchange-correlation functional	a (Å)	c (Å)	m_{Mn} (μ_{B})
LDA (this work)	4.16	5.57	3.2
LDA (Ref. [141])	4.20	5.54	3.29
GGA-PBEsol (this work)	4.24	5.67	3.5
GGA-PBEsol (Ref. [141])	4.28	5.63	3.56
GGA-PBE (Ref. [141])	4.35	5.76	3.69
GGA-PBE (Ref. [148])	4.31	5.74	3.45
GGA-PBE + U (Ref. [148])	4.39	6.12	3.96
exp. (Ref. [146])	4.27	6.05	3.8-4.2

Table 4.1: Computed (FR LDA and PBEsol), theoretical reference (LDA, PBEsol, PBE, and PBE+U), and experimental lattice constants and Mn magnetic moments.

underestimate the experimental values: in particular, a is 2 % smaller than experiment, while c is 8 % smaller than experiment. The PBEsol geometry gives lattice constants slightly smaller than PBE (reported in Ref. [141]) and experiments: a and c are 0.5 % and 6 % smaller than experiment, respectively. The $\mathbf{m} \perp \mathbf{c}$ and $\mathbf{m} \parallel \mathbf{c}$ phases have slightly different lattice constants a and c, but in Table 4.1 we report only one structure because the differences in the lattice constants are beyond the significative digits reported. We use the LDA to compute the phonon frequencies and their contribution to the MAE, while the PBEsol is used to compute the energy contribution to the MAE and to correct it for thermal expansion effects. The LDA and the PBEsol (at $T = 0$ K) calculations are performed at the geometry reported in Table 4.1. The computed Mn magnetic moment m_{Mn} is in agreement with previous calculations reported in literature [141, 148]: m_{Mn} is 10 % (20 %) smaller than experiment within the PBEsol (LDA) approximation.

The pseudowave functions (charge density) have been expanded in a PWs basis set with a kinetic energy cut-off of 110 Ry (440 Ry). The BZ integrations have been performed using a shifted uniform Monkhorst-Pack mesh [74] of $12 \times 12 \times 8$ **k**-points. The presence of a Fermi surface has been dealt with by the Methfessel-Paxton smearing method [71], with a smearing parameter $\sigma = 0.015$ Ry. The dynamical matrices have been computed on a uniform $4 \times 4 \times 3$ **q**-points mesh, and a Fourier interpolation was used to obtain the complete phonon dispersions and the free energy. The latter has been obtained approximating the BZ integral with a $300 \times 300 \times 300$ **q**-points mesh.

4.3 Results and discussion

MnBi is a magnetic binary compound, in which magnetism is carried mainly by the Mn atoms, while Bi is responsible for a strong spin-orbit interaction. As a consequence, strong magnetocrystalline anisotropy effects are expected.

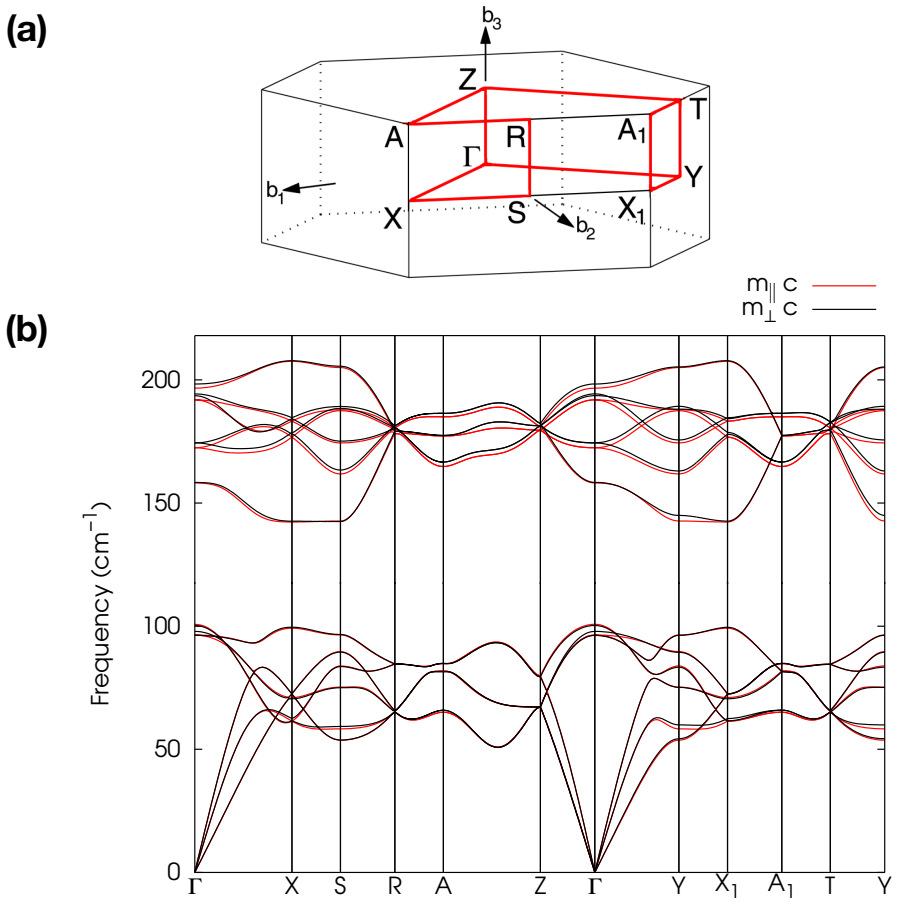

Figure 4.4: (a) BZ of the base-centered orthorhombic Bravais lattice. The high-symmetry lines are highlighted in red. (b) Computed FR LDA phonon dispersions of MnBi with magnetic moments oriented in plane ($\mathbf{m} \perp \mathbf{c}$, black line), and out of plane ($\mathbf{m} \parallel \mathbf{c}$, red line).

4.3.1 Phonon dispersions

Here we consider the phonon dispersions of MnBi with two different orientations of the magnetic moments, $\mathbf{m} \perp \mathbf{c}$ (in-plane) and $\mathbf{m} \parallel \mathbf{c}$ (out-of-plane), and among all the possible in-plane orientations $\mathbf{m} \perp \mathbf{c}$, we choose $\mathbf{m} \parallel \mathbf{a}$, $\mathbf{a}$ and $\mathbf{c}$ being the primitive vectors of the hexagonal Bravais lattice). The presence of a magnetization leads to a difference in the Bravais lattice the magnetic point group is compatible with, as discussed in the previous Section. In order to compare the phonon dispersions in the same BZ, we choose to set the geometry in the base-centered orthorhombic Bravais lattice, which is compatible with the low-symmetry phase (magnetic point group $D_{2h}(C_{2h})$).

The BZ and the phonon dispersions are illustrated in Fig. 4.4. The phonon modes are split in two groups, separated by a gap. The low-frequency branches (up to ~ 100 cm $^{-1}$) are dominated by displacements of the heavy element Bi, while the high-frequency branches (from ~ 150 cm $^{-1}$ to ~ 200 cm $^{-1}$) are mainly displacements of the Mn atoms. The main difference between the phonon frequencies of the two phases is a rigid shift: the phonon

q	$\mathbf{m} \parallel \mathbf{c}$		$\mathbf{m} \perp \mathbf{c}$	
	ν (cm $^{-1}$)	degeneracy	ν (cm $^{-1}$)	degeneracy
Z	67.135	4	67.212	2
			67.231	2
	180.245	4	181.263	2
			181.340	2
X_1	61.427	2	61.554	1
			62.503	1
	72.461	2	72.467	1
			72.577	1
	176.735	2	178.156	1
			178.556	1
	184.374	2	185.195	1
			185.395	1

Table 4.2: Computed FR LDA phonon frequencies at high-symmetry points Z and X_1 for the configurations $\mathbf{m} \parallel \mathbf{c}$ and $\mathbf{m} \perp \mathbf{c}$. Only the degenerate modes are shown for the configuration $\mathbf{m} \parallel \mathbf{c}$, and how the degeneracy is lowered or lifted if $\mathbf{m} \perp \mathbf{c}$.

frequencies of the phase with in-plane magnetization are higher than those of the phase with out-of-plane magnetization. The shift is about 0.5 cm $^{-1}$ in the low-frequency branches, while it is about 2 cm $^{-1}$ in the high-frequency branches. Moreover, there are differences due to symmetry. The system with in-plane magnetization has lower symmetry and some modes, degenerate when the magnetization is along **c**, split. As an example, in Table 4.2 we report the phonon modes at Z and X_1. At Z, in the phase with $\mathbf{m} \parallel \mathbf{c}$ there are two groups of four-fold degenerate modes, which become four couples of degenerate modes in the phase $\mathbf{m} \perp \mathbf{c}$: the splittings are quite small, in the range 0.02-0.08 cm^{-1}. At X_1, in the configuration $\mathbf{m} \parallel \mathbf{c}$ there are four two-fold degenerate modes, which split from 0.1 cm^{-1} to 1 cm^{-1}. Similar splittings are found also along the other high-symmetry lines.

4.3.2 MAE

In previous works, the spin-reorientation transition, due to the change of K_u from negative to positive at $T_\mathrm{SR} \approx 90$ K, has been explained as an effect of thermal expansion of the crystal parameters a and c.

In Refs. [148] and [149] $K_\mathrm{u}^{\mathrm{th.\ exp.}}$, the function K_u obtained accounting for thermal expansion effects, has been computed within the LSDA + SO + U scheme using the experimental lattice constants as a function of the temperature, reported in Refs. [146, 147] and finding in this way a good agreement with experiments. Here instead we compute $K_\mathrm{u}^{\mathrm{th.\ exp.}}$ within the FR PBEsol scheme. In Fig. 4.5(a) we show $\bar{K}_\mathrm{u}$, the contribution to K_u given by the energy difference of the electronic groundstates, for a mesh of geometries and on top of it we indicate with black and white points the thermal expansion data added to the theoretical PBEsol $T = 0$ K crystal parameters. The resulting $K_\mathrm{u}^{\mathrm{th.\ exp.}}$ is reported in Fig. 4.5(b). $K_\mathrm{u}^{\mathrm{th.\ exp.}}$ is negative and slightly increases with increasing a and c. Yet, such an increase is not sufficient

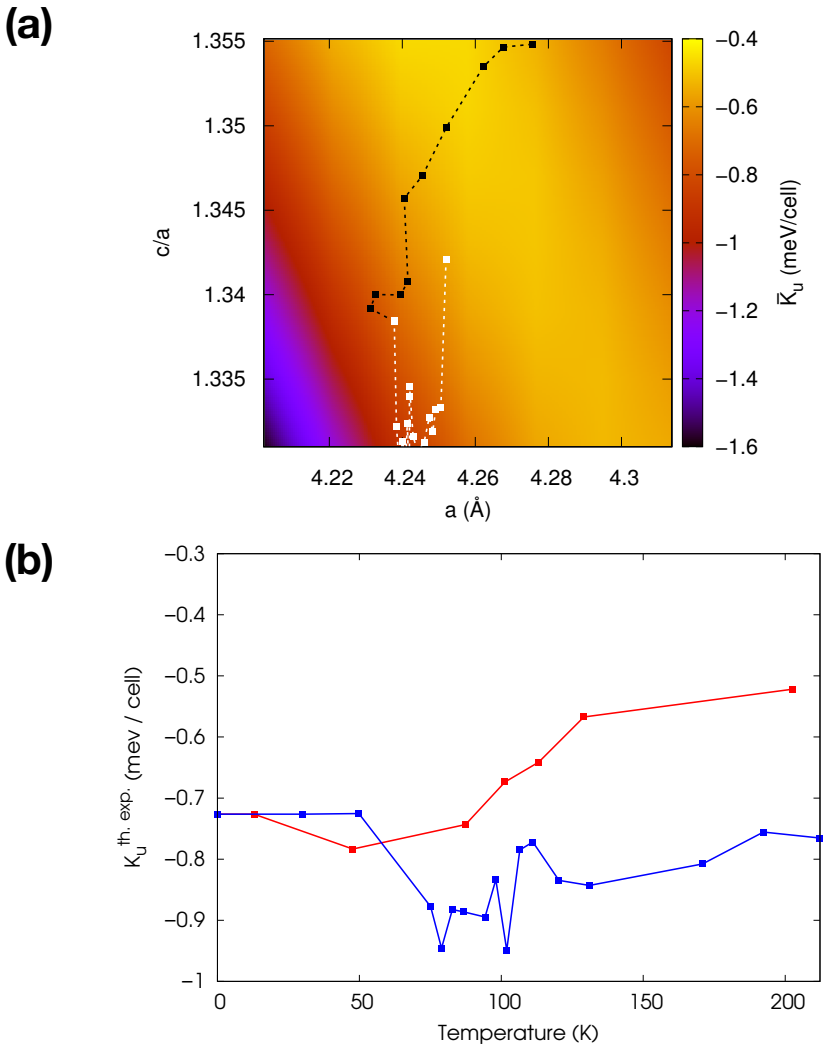

Figure 4.5: Energy contribution to the MAE constant, $\bar{K}_u$, computed in the FR PBEsol scheme. (a) $\bar{K}_u$ as a function of lattice constants. Black and white dashed lines represent the geometries at different temperatures, obtained from Refs. [146] and [147], respectively, as explained in the main text. (b) $K_u^{\text{th. exp.}}$ as a function of temperature. Red and blue lines represent the values of $K_u^{\text{th. exp.}}$ obtained from the black and white dashed lines in panel (a), respectively.

to cross the value $K_u^{\text{th. exp.}} = 0$ because the $T = 0$ K energy difference (≈ -0.73 meV/cell) is significantly lower than the experimental value (≈ -0.15 meV / cell), similarly to what found within the LDA and GGA approximations in Refs. [148] and [149], and because the energy difference landscape shows a local maximum of about -0.4 meV / cell.

In addition to the thermal expansion effect we consider also the effect of the lattice dynamics on K_u: in fact, since the two phases have slightly different phonon frequencies, they have different vibrational entropies that give a temperature-dependent contribution to the MAE defined as the difference of the vibrational free energies of the two phases. We

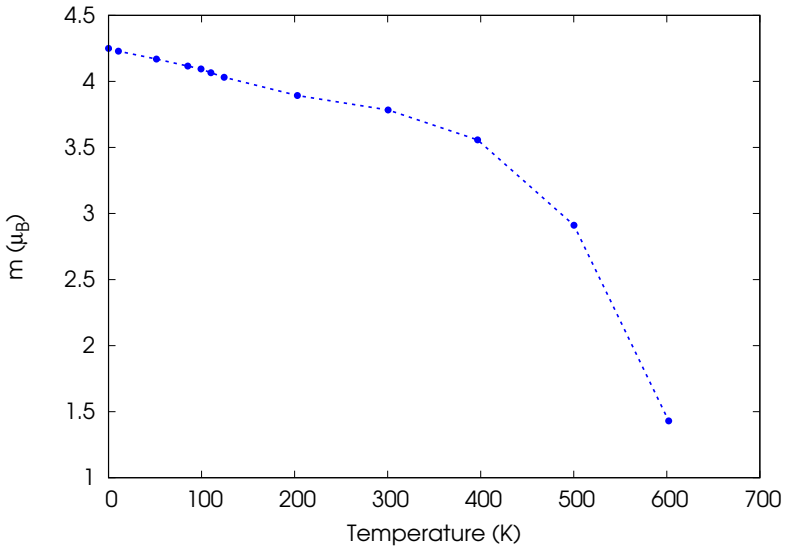

Figure 4.6: Experimental magnetization of MnBi as a function of temperature. Experimental data are reported in Ref. [146].

write the constant K_{u} as [151]:

$$K_{\mathrm{u}} = K_{\mathrm{u}}^{\text{th. exp.}} + K_{\mathrm{u}}^{\mathrm{vib}} + K_{\mathrm{u}}^{\mathrm{mag}}, \tag{4.2}$$

where $K_{\mathrm{u}}^{\text{th. exp.}}$ is the thermal expansion contribution, $K_{\mathrm{u}}^{\mathrm{vib}}$ is the lattice dynamics contribution, and $K_{\mathrm{u}}^{\mathrm{mag}}$ is the magnon contribution. In our analysis we do not consider $K_{\mathrm{u}}^{\mathrm{mag}}$, which should not be crucial to explain the spin-reorientation transition: indeed, if the contribution of the spin fluctuations is similar to the one computed, e.g., for FePt in Ref. [152], it would not explain by itself the behavior of K_{u} as a function of T. Furthermore, it should not be important at low temperatures because it increases when the magnetization varies rapidly, which happens at high temperatures (see Fig. 4.6).

In the following we consider the term $K_{\mathrm{u}}^{\mathrm{vib}}$, which can be computed from the phonon frequencies using the harmonic approximation:

$$K_{\mathrm{u}}^{\mathrm{vib}} = \int_0^{+\infty} d\omega \, \frac{1}{2} \hbar\omega \, \left[g_{\perp}(\omega) - g_{\parallel}(\omega) \right] + k_{\mathrm{B}} T \int_0^{+\infty} d\omega \, \left[g_{\perp}(\omega) - g_{\parallel}(\omega) \right] \ln \left(1 - e^{-\hbar\omega / k_{\mathrm{B}} T} \right), \tag{4.3}$$

where $g_{\perp}(\omega)$ ($g_{\parallel}(\omega)$) is the phonon density of states relative to the phase with $\mathbf{m} \perp \mathbf{c}$ ($\mathbf{m} \parallel \mathbf{c}$).

$K_{\mathrm{u}}^{\mathrm{vib}}$, in Eq. (4.3), is made up of two terms: the first one is the zero-point vibrational free energy contribution, it is temperature-independent and hence it produces a rigid shift of the function $K_{\mathrm{u}}(T)$; the second one is temperature-dependent and stems from the thermal population of the phonon modes. In our case, $K_{\mathrm{u}}^{\mathrm{vib}}$ is positive and increases with increasing temperature, as shown in Fig. 4.7: its magnitude is comparable with that of $K_{\mathrm{u}}^{\text{th. exp.}}$, hence it gives a crucial contribution in determining the MAE constant K_{u}. In

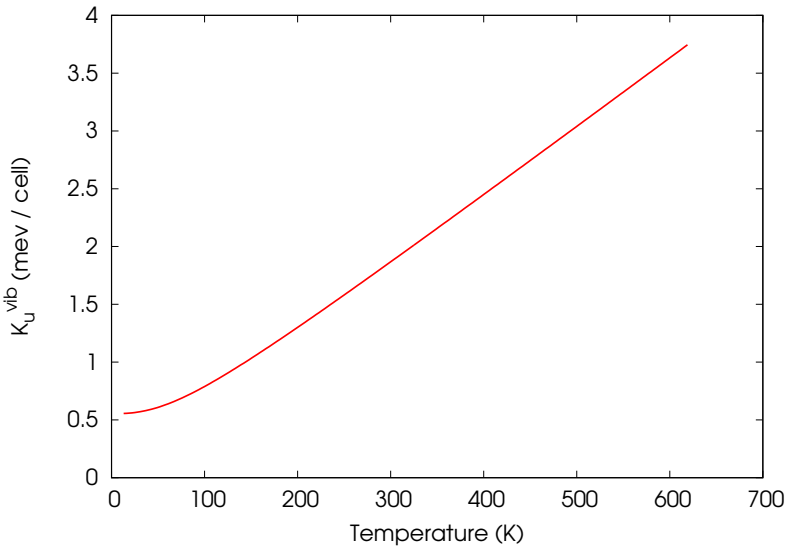

Figure 4.7: Vibrational contribution to the MAE constant K_{u}, computed from the phonon frequencies within the harmonic approximation (Eq. (1.7)).

particular, the zero-point contribution amounts to 0.5 meV / cell and is dominated by the high-frequency branches because the weight function is proportional to ω; the thermal contribution is dominated by the low-frequency branches at low temperatures, whereas the high-frequency branches start to give a relevant contribution at higher temperatures, when their thermal occupation becomes non-negligible. The huge difference in the thermal population function at low temperatures between the two sets of phonon branches is partially compensated by the difference in the phonon densities of states, hence the high-frequency phonon modes give a relevant contribution already at low temperatures, as shown in Fig. 4.8, where we present the relative contribution of the two groups of modes to the second term of $K_{\mathrm{u}}^{\mathrm{vib}}$. As an example, at the spin-reorientation temperature the high-frequency modes account for about 25 % of the thermal vibrational free energy difference.

In Ref. [141] a first estimate of the vibrational contribution to MAE was given, which led to $T_{\mathrm{SR}} \approx 450$ K, far from the experimental value. In this work we find a vibrational contribution of the same order of magnitude as found in Ref. [141], and we include also the zero-point vibrational free energy difference, which gives an important contribution. In Figs. 4.9(a)-(b) we show the total K_{u} defined in Eq. (4.2), and compare it with the experimental data. By comparison with Fig. 4.5(b), it is clear that the addition of the vibrational contribution is important. In particular, the zero-point vibrational free energy difference allows to have a $T = 0$ K value of K_{u} in good agreement with experiments and, together with the thermal contribution (second term of Eq. (4.3)), to get a transition temperature T_{SR} in reasonable agreement with the experiments ($T_{\mathrm{SR}} \approx 90$ K and $T_{\mathrm{SR}} \approx 110$ K with the data given by Refs. [146] and [147], respectively). We remark that the electronic contribution to K_{u} has been computed with the PBEsol functional: the use of other functionals such as LDA

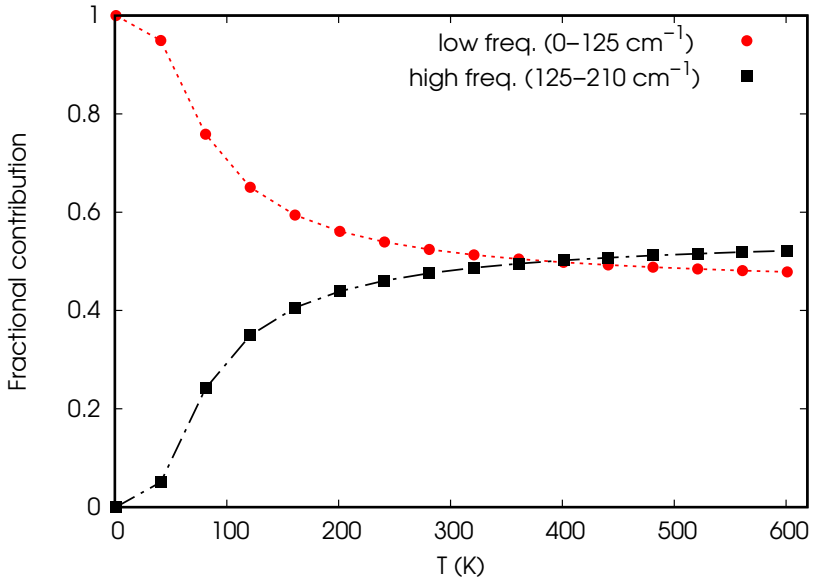

Figure 4.8: Relative fractional contribution of the low-frequency ($0\ \text{cm}^{-1} < \omega < 125\ \text{cm}^{-1}$) and high-frequency ($125\ \text{cm}^{-1} < \omega < 210\ \text{cm}^{-1}$) branches to the thermal part of $K_{\text{u}}^{\text{vib}}$ (second term in Eq. (4.2)).

would give instead a lower value of the MAE at $T = 0$ K than that predicted by PBEsol [4], and would lead to predict $T_{\text{SR}} \approx 500$ K. On the other hand, the use of the Hubbard U correction would result, instead, in a higher value of K_{u} at $T = 0$ K [149] and, as a consequence, we would get $K_{\text{u}} > 0$ when adding the vibrational contribution, thus the spin-reorientation transition would not be explained. As shown in Fig. 4.9 (b), the vibrational contribution allows to have a fair agreement with experimental data [143] in a rather large temperature range. At variance with Ref. [149], we do not find a maximum in K_{u} because the $T = 0$ K geometry corresponds to the theoretical geometry (and hence our geometries do not allow to go beyond the local maximum of the MAE landscape reported in Fig. 4.5), and because the vibrational contribution increases with T. At high temperatures ($T > 500$ K) our results do not agree with the experiment, suggesting that additional contributions may become important in this temperature range, in particular the term $K_{\text{u}}^{\text{mag}}$ in Eq. (4.2), which affects the magnetization (see Fig. 4.6) and can result in a decreasing K_{u} with T [152]. Moreover, we mention that in the high-temperature limit additional effects not included in Eq. (4.2), as the magnon-phonon coupling [153, 154], might be non negligible.

[4] One of the reasons is the underestimation of the lattice constants, typical of LDA, together with the concavity of the electronic MAE landscape as a function of the lattice constants (see Fig. 4.5)

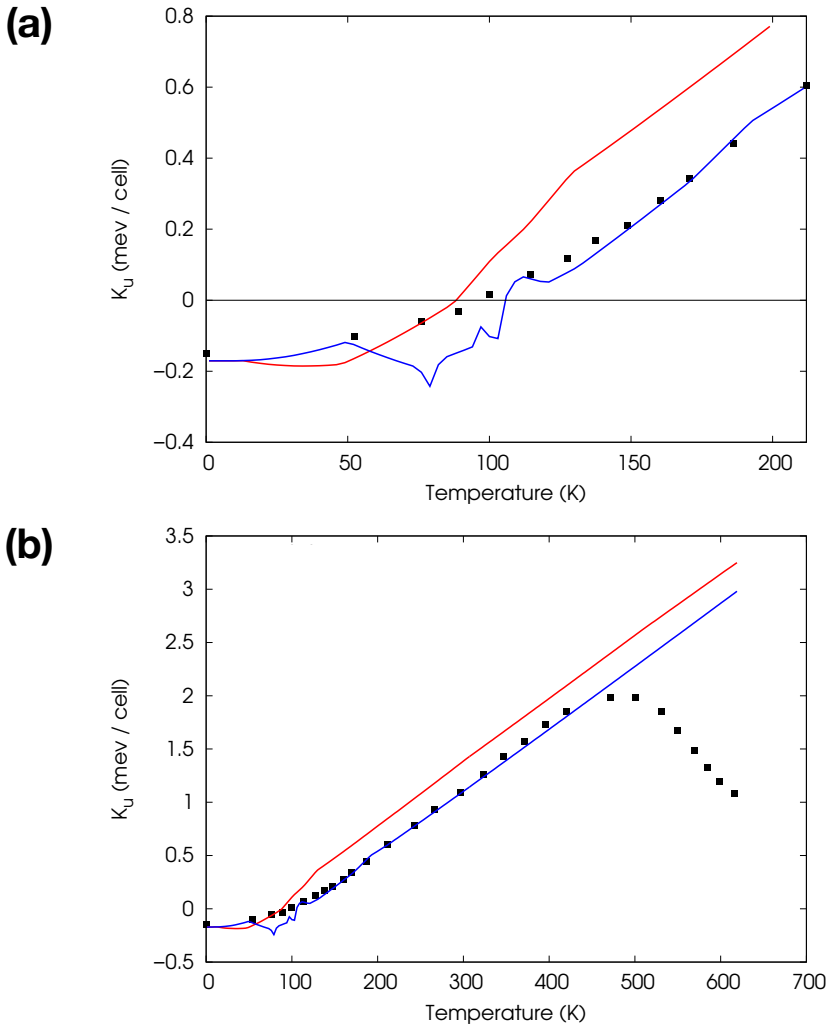

Figure 4.9: Comparison between computed and experimental MAE constant K_{u}. Black squares represent experimental data [143], red and blue lines represent the total K_{u} computed, where the $K_{\mathrm{u}}^{\mathrm{th.\ exp.}}$ contribution has been obtained from Refs. [146] and [147], respectively, as explained in the main text. (a) Detailed comparison in the temperature range $0 - 200$ K, to highlight T_{SR}. (b) Comparison in a wider range of temperatures ($0 - 600$ K).

Summary and Outlook

The work presented in this Ph.D. Thesis falls within the fields of spin-orbit effects in condensed matter and the development of *ab initio* techniques. In particular, our research activity has been focused on the study of few selected cases and, especially, on the methodological development of DFPT for lattice dynamics of magnetic systems, within the FR PPs approach. In the following, we summarize the main findings and outcomes of the work, and we mention presently open questions and future perspectives.

In the first part of the project, addressed in Chapter 2, we performed a FR PAW LDA calculation of the electronic surface states of the clean Os(0001) and Re(0001) surfaces. We described the nature and localization of the main surface states and resonances analyzing their charge density contour levels and planar averages. In both surfaces we found a gap in the PBS at $\bar{\Gamma}$, similar to the L-gap typical of the (111) surfaces of the fcc lattice. Like in Ir(111) [102] and at variance with Au(111), this gap does not host any surface state. Below the "L-gap", we found two resonances that cross the Fermi energy and show a downward energy dispersion, as in Ir(111). In Os(0001) it has been possible to fit their energy dispersion with two Rashba-split parabolas with parameters $\gamma_{\mathrm{SO}} = (6.1 \pm 0.1) \times 10^{-9}$ eV cm and $m^*/m = -0.280 \pm 0.002$. Conversely, in Re(0001) it has not been possible to perform a similar fit because the energy dispersion crossing predicted at $\bar{\Gamma}$ has not been found with our slab thickness: yet, the computed spin texture of the states at the Fermi energy is similar to the one predicted by the Rashba model. We found and characterized several other surface states, present also in previously studied surfaces [99, 102], although few of them differ somewhat from the states found, e.g., in Ir(111). Remarkably, also the so-called S_2 surface states show a Rashba splitting, and we fitted their dispersion with parameters $\gamma_{\mathrm{SO}} = (0.288 \pm 0.003) \times 10^{-9}$ eV cm and $m^*/m = (0.732 \pm 0.005)$ in Os(0001) and $\gamma_{\mathrm{SO}} = (0.200 \pm 0.005) \times 10^{-9}$ eV cm and $m^*/m = (0.661 \pm 0.003)$ in Re(0001). Moreover we analyzed the magnetization density of some selected surface states and computed their spin polarization.

In the second part of the project, we extended and implemented DFPT for lattice dynamics with both FR NC and US PPs to deal with magnetic systems, as described in Chapter 3. Moreover, we extended the symmetrization of the induced densities and of the dynamical matrix to include also the symmetries operations of the antiunitary space group of the crystal that require the time-reversal operator. We validated the implementation of the theory by comparing the phonon frequencies computed with DFPT and with the frozen phonon method for ferromagnetic fcc Ni and for a monatomic ferromagnetic Pt nanowire. The agreement between the two methods is within $0.5\,\mathrm{cm}^{-1}$. For both systems, we computed by DFPT the complete phonon dispersions and discussed their features, showing that magnetism together with spin-orbit coupling may lift the degeneracy of some phonon modes. For our systems

these splittings range from $10^{-2}\,\mathrm{cm}^{-1}$, in Ni, to a few cm^{-1}, in Pt nanowire. Moreover, we showed that the phonon frequencies may depend on the orientation of the magnetization, an effect particularly evident in the Pt nanowire.

The implementation is currently public and available in both the `thermo_pw` (since version 1.0.0) and Quantum `ESPRESSO` (since version 6.6) open source packages.

In the final part of the project we applied our developments to study the effect of the orientation of the magnetization on the phonon frequencies and the vibrational free energy of a realistic system. In particular, we studied the lattice dynamics of the MnBi ferromagnet for two orientations of the magnetization, $\mathbf{m} \perp \mathbf{c}$ and $\mathbf{m} \parallel \mathbf{c}$, as presented in Chapter 4. We have shown that the differences in the phonon frequencies give rise to a contribution to the MAE comparable with the electronic one. We have found that the vibrational contribution is relevant to explain the behavior of the MAE constant K_u as a function of temperature. We could also get an estimate of the spin-reorientation temperature T_SR in fair agreement with the experimental value using the PBEsol approximation to evaluate the energy contribution to the MAE. We mention that in Ref. [141] a first estimate of the vibrational contribution to MAE was given, which led to $T_\mathrm{SR} \approx 450$ K, far from the experimental value. Our computed vibrational contribution is of the same order of magnitude as found in Ref. [141], and we have included also the zero-point vibrational free energy difference, which gives an important contribution and leads to an estimated spin-reorientation temperature $T_\mathrm{SR} \approx 100$ K, when used together with the energy MAE given by PBEsol.

The computed K_u as a function of temperature does not reproduce the experimental results at high temperatures ($T > 450$ K), a regime where magnon (and, possibly, magnon-phonon coupling) contributions may become important. The quantitative estimation of the contribution of magnons to the MAE is presently an open question and certainly represents an interesting future direction of investigation.

Our work can now be extended along several directions. From a methodological point of view, we mention the possibility to extend the formulation for the magnetic case to the FR PAW scheme.

We mention that the magnetic and the mixed *magnetoelectric* responses of a material can influence the long-wavelength phonon modes. In particular, in Ref. [155] it has been explained that, similarly to the dielectric response, they give a contribution (although expected to be small) to the non-analytic term of the dynamical matrix at Γ. In particular, the additional term depends on the *dynamical magnetic charges*, Z_m, related to the net magnetization induced by a phonon mode, and the *linear magnetoelectric tensor* α [156–158], related to the magnetic response to an electric field (or, similarly, to the electric response to a magnetic field). Both Z_m and α can be computed in the non-collinear DFPT formalism for magnetic systems presented in this Thesis. In particular, the dynamical magnetic charges can be computed by integrating over the unit cell the magnetization density response induced by a phonon perturbation at Γ, thus avoiding a further frozen phonon calculation. Together with the calculation of the Born effective charges, already available in Quantum `ESPRESSO`, it would be then possible to compute directly also the lattice-mediated contribution to the linear magnetoelectric tensor. Similarly, the integration of the magnetization density induced by an electric field would allow to compute the electronic contribution to α [156]. Currently, we are working to implement in the DFPT code the calculation of Z_m, both the lattice-mediated and

electronic contributions to α, and the magnetic and magnetoelectric non-analytic terms in the dynamical matrix at Γ, and we are testing the implementation for Cr_2O_3, a prototypical example of a magnetoelectric material [159–165].

APPENDIX A

Antilinear operators

A.1 Definition

An operator is antilinear if it is linear and moreover it takes the complex conjugate of the scalars it is acting on. Briefly, an operator $\mathcal{A} : |\psi\rangle \to \mathcal{A}\,|\psi\rangle$ is antilinear if its action on a given ket provides:

$$\mathcal{A}(\alpha_1\,|\psi_1\rangle + \alpha_2\,|\psi_2\rangle) = \alpha_1^*\,\mathcal{A}\,|\psi_1\rangle + \alpha_2^*\,\mathcal{A}\,|\psi_2\rangle\,. \tag{A.1}$$

As a consequence, antilinear operators and complex scalars do not commute. In fact, given a complex constant c, from (A.1) it follows immediately that:

$$\mathcal{A}\,c = c^*\mathcal{A}. \tag{A.2}$$

The product of operators in which at least one operator is antilinear is defined in the same way as for linear operators. The product of an antilinear operator with a linear operator is an antilinear operator, whereas the product of two antilinear operators is a linear operator. In general, the product of $p + q$ operators, of which p are antilinear and q are linear, is a linear (antilinear) operator if p is even (odd).

Two operators can commute or not: the commutator and anticommutator are defined in the same way as for linear operators.

A.2 Action in dual space and definition of the Hermitian conjugate

The action on a dual space element $\langle\psi|$ is defined in the same way as for the ket, namely:

$$(\langle\psi_1|\,\alpha_1 + \langle\psi_2|\,\alpha_2)\mathcal{A} = (\langle\psi_1|\,\mathcal{A})\alpha_1^* + (\langle\psi_2|\,\mathcal{A})\alpha_2^*. \tag{A.3}$$

As a consequence, in the definition of the scalar product $\langle\phi|\,\mathcal{A}\,|\psi\rangle$ it is important to specify whether $\mathcal{A}$ acts to the left or to the right. In fact, expressing $\langle\phi|$ as a linear combination of two vectors, namely $\langle\phi| = \langle\phi_1|\,\alpha_1 + \langle\phi_2|\,\alpha_2$, if $\mathcal{A}$ acts to the right we have:

$$\langle\phi|\,(\mathcal{A}\,|\psi\rangle) = [\langle\phi_1|\,\alpha_1 + \langle\phi_2|\,\alpha_2](\mathcal{A}\,|\psi\rangle) = \alpha_1\,\langle\phi_1|\,(\mathcal{A}\,|\psi\rangle) + \alpha_2\,\langle\phi_2|\,(\mathcal{A}\,|\psi\rangle), \tag{A.4}$$

while if $\mathcal{A}$ acts to the left we have:

$$(\langle\phi|\,\mathcal{A})\,|\psi\rangle = [(\langle\phi_1|\,\alpha_1 + \langle\phi_2|\,\alpha_2)\mathcal{A}]\,|\psi\rangle = \alpha_1^*(\langle\phi_1|\,\mathcal{A})\,|\psi\rangle + \alpha_2^*(\langle\phi_2|\,\mathcal{A})\,|\psi\rangle\,. \tag{A.5}$$

Comparing the two expressions it can be seen that if we take the complex conjugate of Eq. (A.4) we get (A.5), so:

$$(\langle\phi|\,\mathcal{A})\,|\psi\rangle = [\langle\phi|\,(\mathcal{A}\,|\psi\rangle)]^*. \tag{A.6}$$

As a result, the parenthesis cannot be omitted and one has to specify whether the operator acts to the left or to the right.

The hermitian conjugate is defined in the same fashion as for linear operators, i.e.:

$$(\mathcal{A}\,|\psi\rangle)^\dagger = (\langle\psi|\,\mathcal{A}^\dagger), \tag{A.7}$$

but, due to Eq. (A.6) we have:

$$\langle\phi|\,(\mathcal{A}\,|\psi\rangle) = [(\langle\psi|\,\mathcal{A}^\dagger)\,|\phi\rangle]^* = \langle\psi|\,(\mathcal{A}^\dagger\,|\phi\rangle). \tag{A.8}$$

A.3 Antiunitarity

Finally, we define the antiunitarity property. A given operator $\mathcal{U}$ is called antiunitary if it is antilinear and unitary at the same time. We recall that an operator is unitary if its hermitian conjugate coincides with its inverse, namely:

$$\mathcal{U}^\dagger\mathcal{U} = \mathbb{1}, \tag{A.9}$$

where $\mathbb{1}$ is the identity.

APPENDIX B

Symmetry operations in state space: a general discussion

In this section we consider the effects of a given symmetry operation $\mathcal{S}$ on wave functions. To keep the discussion as general as possible we will consider the action on both the space $\mathbb{R}^n$ and the spin space, so we will consider spinors rather than one-component wave functions. In the following discussion we refer to Complements B_{VI} and A_{IX} of Ref. [166]. We will start from rotations, then we will include inversion and fractional translations. Finally we will describe in more detail the time-reversal operation.

B.1 Rotations in state space

The generator of a rotation is the orbital angular momentum, so that the operator associated with a rotation of angle θ about an axis whose direction is expressed by the unit vector $\mathbf{n}$, is given by:

$$\mathcal{R}_{\mathbf{n}}(\theta) = e^{-\frac{i}{\hbar}\theta \mathbf{L}\cdot\mathbf{n}}, \tag{B.1}$$

where $\mathbf{L}$ is the orbital angular momentum. Eq. (B.1) is valid for a rotation applied to a quantum state defined in the conventional vector space $\mathbb{R}^3$, that we will call $\mathcal{V}_{\mathbf{r}}$. If the state is defined also in the spin space, it must be represented by a tensor product of a ket defined in $\mathcal{V}_{\mathbf{r}}$ and a ket defined in the spin space $\mathcal{V}_{\mathbf{s}}$:

$$|\psi\rangle = |\phi\rangle \otimes |\chi\rangle\,, \tag{B.2}$$

where $|\phi\rangle \in \mathcal{V}_{\mathbf{r}}$, while $|\chi\rangle \in \mathcal{V}_{\mathbf{s}}$. In this case a rotation defined by the operator $\mathcal{R}_{\mathbf{n}}(\theta)$ must act also on the spin part of the state. Consequently, Eq. (B.1) is generalized in the following way:

$$\mathcal{R}_{\mathbf{n}}(\theta) = e^{-\frac{i}{\hbar}\theta \mathbf{J}\cdot\mathbf{n}}, \tag{B.3}$$

where $\mathbf{J}$ is the total angular momentum, defined as $\mathbf{J} = \mathbf{L} + \mathbf{S}$. Basically, now the rotation operator is made up of two parts, $\mathcal{R}^{(\mathbf{r})}_{\mathbf{n}}(\theta) = e^{-\frac{i}{\hbar}\theta \mathbf{L}\cdot\mathbf{n}}$, whose action is defined in $\mathcal{V}_{\mathbf{r}}$, and $\mathcal{R}^{(\mathbf{s})}_{\mathbf{n}}(\theta) = e^{-\frac{i}{\hbar}\theta \mathbf{S}\cdot\mathbf{n}}$, that acts in $\mathcal{V}_{\mathbf{s}}$. The action of $\mathcal{R}_{\mathbf{n}}(\theta)$ on a given ket $|\psi\rangle$ is defined as:

$$|\psi'\rangle = \mathcal{R}_{\mathbf{n}}(\theta)\,|\psi\rangle = [\mathcal{R}^{(\mathbf{r})}_{\mathbf{n}}(\theta)\,|\phi\rangle] \otimes [\mathcal{R}^{(\mathbf{s})}_{\mathbf{n}}(\theta)\,|\chi\rangle]. \tag{B.4}$$

B.2 Rotation of two-component spinors

Let us consider now the specific case of a spin-1/2 particle. Its state is described by the spinor $[\psi](\mathbf{r})$, whose components are:

$$\psi^{\sigma}(\mathbf{r}) = \langle \mathbf{r}, \sigma|\psi\rangle\,, \tag{B.5}$$

where σ represents the components in the spin space. Applying a rotation $\mathcal{R} = \mathcal{R}^{(\mathbf{r})} \otimes \mathcal{R}^{(\mathbf{s})}$ to the spinor $[\psi](\mathbf{r})$, the ket transforms as $|\psi'\rangle = \mathcal{R}\,|\psi\rangle$ and its components are:

$$\psi'^{\sigma}(\mathbf{r}) = \langle \mathbf{r}, \sigma|\psi'\rangle = \langle \mathbf{r}, \sigma|\,\mathcal{R}\,|\psi\rangle\,. \tag{B.6}$$

Inserting the completeness relation relative to the basis $\{|\mathbf{r}, \sigma\rangle\}$ we get:

$$\psi'^{\sigma}(\mathbf{r}) = \sum_{\sigma'} \int d^3r'\ \langle \mathbf{r}, \sigma|\,\mathcal{R}\,|\mathbf{r}', \sigma'\rangle\,\langle \mathbf{r}', \sigma'|\psi\rangle\,. \tag{B.7}$$

Since the vectors of the basis $\{|\mathbf{r}, \sigma\rangle\}$ are given by tensor products, the matrix elements of the operator $\mathcal{R}$ can be written in the following way:

$$\langle \mathbf{r}, \sigma|\,\mathcal{R}\,|\mathbf{r}', \sigma'\rangle = \langle \mathbf{r}|\,\mathcal{R}^{(\mathbf{r})}\,|\mathbf{r}'\rangle\,\langle \sigma|\,\mathcal{R}^{(\mathbf{s})}\,|\sigma'\rangle\,. \tag{B.8}$$

Since $\mathcal{R}^{(\mathbf{r})}$ is unitary we have that $\langle \mathbf{r}|\,\mathcal{R}^{(\mathbf{r})}\,|\mathbf{r}'\rangle = \langle (\mathcal{R}^{(\mathbf{r})})^{-1}\mathbf{r}|\mathbf{r}'\rangle = \delta[\mathbf{r}' - (\mathcal{R}^{(\mathbf{r})})^{-1}\mathbf{r}]$. Furthermore, calling $\mathcal{R}^{\sigma\sigma'}_{1/2}$ the matrix element $\langle \sigma|\,\mathcal{R}^{(\mathbf{s})}\,|\sigma'\rangle$, Eq. (B.7) becomes:

$$\psi'^{\sigma}(\mathbf{r}) = \sum_{\sigma'} \mathcal{R}^{\sigma\sigma'}_{1/2}\,\psi^{\sigma'}(\mathcal{R}^{-1}\mathbf{r}), \tag{B.9}$$

where we dropped the superscript $(\mathbf{r})$ for simplicity.

B.3 Inversion symmetry

The inversion symmetry reverses the sign of all spatial coordinates:

$$\mathcal{I}\mathbf{r} = -\mathbf{r}. \tag{B.10}$$

Since the spin is an angular momentum, it possesses all its properties. In particular it is an axial vector, which means that it is invariant upon inversion. Consequently, inversion symmetry does not modify the spin part $|\chi\rangle$ of a given state $|\psi\rangle$, so we must care only about the action of $\mathcal{I}$ on $|\phi\rangle$. We have:

$$\psi'^{\sigma}(\mathbf{r}) = \langle \mathbf{r}, \sigma|\,\mathcal{I}\,|\psi\rangle = \langle -\mathbf{r}, \sigma|\psi\rangle = \psi_{\sigma}(-\mathbf{r}). \tag{B.11}$$

The results obtained can be extended to a reflection symmetry, also known as mirror. A mirror is an improper symmetry obtained by the composition of a proper rotation $\mathcal{R}$ with the inversion $\mathcal{I}$ (improper rotation). When applied to a given spinor $[\psi](\mathbf{r})$, the component $|\phi\rangle$ defined in $\mathcal{V}_{\mathbf{r}}$ gets transformed by the whole symmetry operation (i.e. the mirror symmetry), while the spin part $|\chi\rangle$ is transformed according to the SU(2) matrix $\mathcal{R}_{1/2}$ representing, in spin space, the proper rotation $\mathcal{R}$. In general, given a point symmetry operation $\mathcal{S}$, the spinor $[\psi](\mathbf{r})$ transforms in the following way:

$$\psi'^{\sigma}(\mathbf{r}) = \sum_{\sigma'} \mathcal{R}^{\sigma\sigma'}_{1/2}\, \psi^{\sigma'}(\mathcal{S}^{-1}\mathbf{r}). \tag{B.12}$$

B.4 Space groups

Above we discussed point symmetry operations. Yet, the space group of a crystal may contain operations for which a fractional translation is required. In the most general case we represent a symmetry with the symbol $\{\mathcal{S}|\mathbf{f}\}$, where $\mathbf{f}$ is the fractional translation associated to $\mathcal{S}$. The action of $\{\mathcal{S}|\mathbf{f}\}$ on a given vector $\mathbf{r}$ of $\mathbb{R}^3$ is:

$$\{\mathcal{S}|\mathbf{f}\}\mathbf{r} = \mathcal{S}\mathbf{r} + \mathbf{f}. \tag{B.13}$$

Being a translation, $\mathbf{f}$ does not affect the spin, so Eq. (B.12) becomes, in the case in which also fractional translations are present:

$$\psi'^{\sigma}(\mathbf{r}) = \sum_{\sigma'} \mathcal{R}^{\sigma\sigma'}_{1/2}\, \psi^{\sigma'}(\{\mathcal{S}|\mathbf{f}\}^{-1}\mathbf{r}). \tag{B.14}$$

The inverse of $\{\mathcal{S}|\mathbf{f}\}$ can be obtained requiring that $\{\mathcal{S}_j|\mathbf{f}_j\}\{\mathcal{S}_i|\mathbf{f}_i\}\mathbf{r} = \mathbf{r}$, where $\{\mathcal{S}_j|\mathbf{f}_j\} = \{\mathcal{S}_i|\mathbf{f}_i\}^{-1}$. We have:

$$\begin{aligned} \{\mathcal{S}_j|\mathbf{f}_j\}\{\mathcal{S}_i|\mathbf{f}_i\}\mathbf{r} &= \{\mathcal{S}_j|\mathbf{f}_j\}(\mathcal{S}_i\mathbf{r} + \mathbf{f}_i) \\ &= \mathcal{S}_j\mathcal{S}_i\mathbf{r} + \mathcal{S}_j\mathbf{f}_i + \mathbf{f}_j \\ &= \mathbf{r} \end{aligned} \tag{B.15}$$

From the last equality it follows that:

$$\mathcal{S}_j = \mathcal{S}_i^{-1} \tag{B.16}$$

$$\mathbf{f}_j = -\mathcal{S}_j\,\mathbf{f}_i = -\mathcal{S}_i^{-1}\,\mathbf{f}_i, \tag{B.17}$$

so $\{\mathcal{S}|\mathbf{f}\}^{-1}\mathbf{r} = \mathcal{S}^{-1}\mathbf{r} - \mathcal{S}^{-1}\mathbf{f}$. As a result, Eq. (B.14) becomes:

$$\psi'^{\sigma}(\mathbf{r}) = \sum_{\sigma'} \mathcal{R}^{\sigma\sigma'}_{1/2}\, \psi^{\sigma'}(\mathcal{S}^{-1}\mathbf{r} - \mathcal{S}^{-1}\mathbf{f}). \tag{B.18}$$

B.5 Time-reversal symmetry

Time translations

A well known symmetry operation in the time domain is the time-translation symmetry. We know from Classical Mechanics that a time-translational-invariant system is conservative: its

total energy is a constant of motion. In Quantum Mechanics, the time-translation symmetry implies the possibility to separate the time variable t and the spatial variable $\mathbf{r}$. As a consequence the time-dependent Schrödinger equation:

$$i\hbar\frac{\partial\Psi(\mathbf{r},t)}{\partial t} = H\Psi(\mathbf{r},t) \tag{B.19}$$

can be recast into the time-independent one:

$$H\psi(\mathbf{r}) = E\,\psi(\mathbf{r}), \tag{B.20}$$

by getting

$$\Psi(\mathbf{r},t) = e^{-\frac{i}{\hbar}E\,t}\,\psi(\mathbf{r}) \tag{B.21}$$

Time-reversal in Classical Mechanics

Physical systems are often not only conservative, but also time-reversal invariant. The time-reversal operation is defined as a particular time translation such that:

$$t \to -t, \tag{B.22}$$

which implies that:

$$\mathbf{r} \to \mathbf{r} \tag{B.23}$$

$$\mathbf{p} \to -\mathbf{p}. \tag{B.24}$$

Since $\mathbf{p} \to -\mathbf{p}$, time-reversal-invariant systems must be described by an Hamiltonian that contains only even powers of the linear momentum $\mathbf{p}$. In Classical Mechanics, the time-reversal operation is completely described by Eqs. (B.22) and (B.24). As a consequence the time-reversed trajectory of a particle can be obtained by just reversing the time and the velocity at each point of the trajectory.

Time-reversal in Quantum Mechanics: spinless particle

In Quantum Mechanics the situation is more subtle, since we have to specify how the time-reversal operator acts on a wave function. Basically, if we want a system to be time-reversal invariant, the Schrödinger equation must be invariant when the time-reversal operation is applied. If we change the sign of t in Eq. (B.19) we get:

$$-\,i\hbar\frac{\partial\Psi(\mathbf{r},-t)}{\partial t} = H\Psi(\mathbf{r},-t), \tag{B.25}$$

that is equal to the Schrödinger equation if we further take the complex conjugate of both sides (note that in the spinless case H is real):

$$i\hbar\frac{\partial\Psi^*(\mathbf{r},-t)}{\partial t} = H\Psi^*(\mathbf{r},-t). \tag{B.26}$$

As a consequence the time-reversed wave function is the complex conjugate of the original one:

$$\Psi(\mathbf{r}, t) \to \Psi^*(\mathbf{r}, -t), \tag{B.27}$$

which implies that the time-reversal operator $\mathcal{T}$, in the spinless case, is represented by the complex-conjugation operator $\mathcal{K}$. If we consider the wave function multiplied by a complex scalar α, we have $\mathcal{K}\alpha\,|\Psi\rangle = \alpha^*\mathcal{K}\,|\Psi\rangle$, so $\mathcal{K}$ is an antilinear operator. Moreover, $\mathcal{K}$ does not change the norm of the state it acts on, so $\mathcal{K}$ is antiunitary. Finally, if we apply $\mathcal{K}$ twice the state is not modified, so $\mathcal{K}^2 = \mathbb{1}$. As a result:

$$\mathcal{K}^\dagger = \mathcal{K}^{-1} = \mathcal{K}. \tag{B.28}$$

Time-reversal: a general definition

Because of Eq. (B.24), not only $\mathbf{p}$ is affected by time-reversal, but also all the quantities that depend on $\mathbf{p}$ or, obviously, on t. Among them we focus on the angular momentum. Since $\mathbf{L} = \mathbf{r} \times \mathbf{p}$ we have:

$$\mathcal{T}^\dagger(\mathbf{r} \times \mathbf{p})\mathcal{T} = -(\mathbf{r} \times \mathbf{p}), \tag{B.29}$$

so $\mathbf{L}$ changes sign if time-reversal $\mathcal{T}$ is applied. In order to have a more general definition of the operator $\mathcal{T}$ we must define the time-reversed spin variables. Since the spin $\mathbf{S}$ is a particular angular momentum we require that:

$$\mathcal{T}^\dagger\,\mathbf{S}\,\mathcal{T} = -\mathbf{S}. \tag{B.30}$$

If we consider $\mathcal{T} = \mathcal{K}$, as for a spinless particle, we have:

$$\mathcal{K}\,S_x\,\mathcal{K} = S_x \tag{B.31}$$
$$\mathcal{K}\,S_y\,\mathcal{K} = -S_y \tag{B.32}$$
$$\mathcal{K}\,S_z\,\mathcal{K} = S_z, \tag{B.33}$$

so the complex-conjugation operator is not sufficient. To be able to reverse the spin we define the time-reversal operator in a more general form:

$$\mathcal{T} = U\,\mathcal{K}, \tag{B.34}$$

where U is a unitary operator. Since $\mathcal{T}^\dagger = \mathcal{K}\,U^\dagger$, our requirements become:

$$U^\dagger\,\mathbf{r}\,U = \mathbf{r}, \tag{B.35}$$
$$U^\dagger\,\mathbf{p}\,U = \mathbf{p}, \tag{B.36}$$
$$U^\dagger\,S_x\,U = -S_x, \tag{B.37}$$
$$U^\dagger\,S_y\,U = S_y, \tag{B.38}$$
$$U^\dagger\,S_z\,U = -S_z, \tag{B.39}$$

therefore U represents a rotation, only for the spin variables, of $-\pi$ about the S_y axis. Given the discussion about rotation operators in spin space we can write $U = e^{i\pi S_y/\hbar}$, which, for

the particular case of a spin-1/2 particle, is $e^{i\pi\sigma_y/2}$. If we write it using a Taylor expansion, we get:

$$U = \sum_{k=0}^{+\infty} \frac{1}{k!} \left(i \, \frac{\pi}{2} \, \sigma_y \right)^k \tag{B.40}$$

Since σ_y^k is equal to $\mathbb{1}$ (σ_y) if k is even (odd), we can split the even powers from the odd ones to have:

$$U = \cos\left(\frac{\pi}{2}\right) + i \, \sigma_y \sin\left(\frac{\pi}{2}\right) = i \, \sigma_y, \tag{B.41}$$

whence the time-reversal operator for a spin-1/2 particle can be written as:

$$\mathcal{T} = i \, \sigma_y \, \mathcal{K}. \tag{B.42}$$

APPENDIX C

Spin-angle functions

C.1 Dirac Hamiltonian and total angular momentum

We consider the Dirac Hamiltonian, introduced in Section 1.9:

$$H = c\,\boldsymbol{\alpha}\cdot\mathbf{p} + \beta mc^2 + V. \tag{C.1}$$

If we take a central external potential $V(r)$, the eigenfunctions of H can be written as the product of a radial function and an angular part. V commutes with both the orbital angular momentum $\mathbf{L}$ and the spin angular momentum $\mathbf{S}$ that, in the relativistic case are defined in four dimensions in the following way:

$$\mathbf{L} = \mathbf{r}\times\mathbf{p}\,\mathbb{1}_{4\times4} \tag{C.2}$$

$$\mathbf{S} = \frac{\hbar}{2}\boldsymbol{\Sigma} = \frac{\hbar}{2}\begin{pmatrix}\boldsymbol{\sigma} & 0\\ 0 & \boldsymbol{\sigma}\end{pmatrix}. \tag{C.3}$$

However, the presence of a term linear in the momentum in the Dirac Hamiltonian implies that H does not commute with $\mathbf{L}$ and $\mathbf{S}$ separately. Indeed:

$$[H,\mathbf{L}] = -i\,\hbar\,c\,\boldsymbol{\alpha}\times\mathbf{p}, \tag{C.4}$$

and

$$[H,\mathbf{S}] = i\,\hbar\,c\,\boldsymbol{\alpha}\times\mathbf{p}. \tag{C.5}$$

Eqs. C.4 and C.5 imply that $[H,\mathbf{L}+\mathbf{S}]=0$, hence the Dirac Hamiltonian commutes with the total angular momentum $\mathbf{J}=\mathbf{L}+\mathbf{S}$. As a consequence, the angular part of the eigenfunctions of H must be an eigenfunction of J^2 and J_z as well. We identify them as four-component spinors Y^{jm_j}, where j and m_j are related to the eigenvalues of J^2 and J_z, following the secular equations:

$$J^2\,Y^{jm_j} = j(j+1)\,\hbar^2\,Y^{jm_j} \tag{C.6}$$

$$J_z\,Y^{jm_j} = m_j\,\hbar\,Y^{jm_j}. \tag{C.7}$$

C.2 Spin-angle functions

Given the definitions of $\mathbf{L}$ and $\mathbf{S}$ (Eqs. (C.2) and (C.3)), the four-dimensional total angular momentum can be written in a diagonal block form, where the two blocks in the diagonal are equal and correspond to the two-dimensional total angular momentum operator, $\mathbf{J}_{2\times2}$. As a consequence, Y^{jm_j} is made up of two two-component spinors corresponding to the eigenfunctions $Y^{jm_j}_{l1/2}$ of $\mathbf{J}_{2\times2}$ (see below for more details), called *spin-angle functions*. Given the eigenstates of $\mathbf{S}$, $\chi_{s\,m_s}$, that for $s = 1/2$ read:

$$\chi_{\substack{1/2\\1/2}} = \begin{pmatrix}1\\0\end{pmatrix} \tag{C.8}$$

$$\chi_{\substack{1/2\\-1/2}} = \begin{pmatrix}0\\1\end{pmatrix}, \tag{C.9}$$

and the eigenstates of $\mathbf{L}$, the spherical harmonics $Y_{l\,m}$, the spin-angle functions can be obtained by applying the rules for the addition of angular momenta and read:

$$Y^{jm_j}_{l\,1/2} = \sum_{m_l\,m_s} c(l\,m_l, 1/2\,m_s, j\,m_j)\,Y_{lm_l}\,\chi_{1/2\,m_s}, \tag{C.10}$$

where $c(l\,m_l, 1/2\,m_s, j\,m_j)$ are Clebsch-Gordan coefficients. The addition of angular momenta implies that $m_j = m_l + m_s$ and that j runs from $|l - s|$ to $l + s$: in our case, since $s = 1/2$ two different values of j are allowed for each l, namely $j = l - 1/2$ and $j = l + 1/2$ (the only exception being the case $l = 0$, for which only $j = 1/2$ is allowed). In particular, Eq. (C.10) provides

$$Y^{jm_j}_{l\,1/2} = \begin{pmatrix} \left(\dfrac{l + m_l + 1}{2l + 1}\right)^{1/2} Y_{lm_l} \\ \left(\dfrac{l - m_l}{2l + 1}\right)^{1/2} Y_{l\,m_l+1} \end{pmatrix} \tag{C.11}$$

for $j = l + 1/2$ (here, $m_l = m_j - 1/2$), and

$$Y^{jm_j}_{l\,1/2} = \begin{pmatrix} \left(\dfrac{l - m_l + 1}{2l + 1}\right)^{1/2} Y_{l\,m_l-1} \\ -\left(\dfrac{l + m_l}{2l + 1}\right)^{1/2} Y_{lm_l} \end{pmatrix} \tag{C.12}$$

for $j = l - 1/2$ (here, $m_l = m_j + 1/2$).

The eigenfunctions of the four-dimensional total angular momentum $\mathbf{J}$, Y^{jm_j}, are built using two spin-angle functions with the same j and m_j, and with orbital numbers l and l'. A given j can be obtained with different values of l: It can be proved that the large and the small component of the four-dimensional eigenfunctions of H must have different parity, hence $l = l' \pm 1$ and:

$$Y^{jm_j} = \begin{pmatrix} Y^{jm_j}_{l\,1/2} \\ \\ Y^{jm_j}_{l\pm1\,1/2} \end{pmatrix}, \tag{C.13}$$

C.2.1 Relationship with real spherical harmonics

Eq. (C.10) allows to write the spin-angle functions as a linear combination of spherical harmonics Y_{lm_l}. Y_{lm_l} are complex functions and can, in turn, be written in terms of the real form of spherical harmonics, Y'_{lm_l} (see, for instance, Ref. [167]), that are used in `Quantum ESPRESSO`, by means of a unitary matrix U in the following way:

$$Y_{lm_l} = \sum_{m'_l=-l}^{l} U^l_{m_l m'_l} Y'_{lm'_l}. \tag{C.14}$$

Eq. (C.10) can then be written as:

$$Y^{jm_j\sigma}_{l\,1/2} = \sum_{m_l=-l}^{l} c^{lj\sigma}_{m_j m_l} Y'_{lm_l}, \tag{C.15}$$

where

$$c^{lj\sigma}_{m_j m_l} = \sum_{m'_l\, m_s} c(l\, m'_l, 1/2\, m_s, j\, m_j)\, U^l_{m'_l m_l}\, \chi^\sigma_{s m_s}. \tag{C.16}$$

C.2.2 Effect of the time-reversal operator

We consider the action of the time-reversal operator $\mathcal{T} = i\,\sigma_y\,\mathcal{K}$ (see Appendix B) on the spin-angle functions, that will be useful when we will discuss the action of $\mathcal{T}$ on the US PPs kernel K below. The spin-dependent part of $\mathcal{T}$, $i\,\sigma_y$, acts on the spinors $\chi_{1/2m_s}$ appearing in Eq. (C.10). In particular:

$$i\,\sigma_y \begin{pmatrix} 1 \\ 0 \end{pmatrix} = -\begin{pmatrix} 0 \\ 1 \end{pmatrix} \tag{C.17}$$

$$i\,\sigma_y \begin{pmatrix} 0 \\ 1 \end{pmatrix} = \begin{pmatrix} 1 \\ 0 \end{pmatrix}. \tag{C.18}$$

Being the Clebsch-Gordan coefficients and the spinors $\chi_{1/2m_s}$ real quantities, the complex-conjugation operator $\mathcal{K}$ modifies only the spherical harmonics, whose properties imply that:

$$\mathcal{K}\, Y_{lm_l} = Y^*_{lm_l} = (-1)^{m_l}\, Y_{l\,-m_l}. \tag{C.19}$$

We start from the case $j = l + 1/2$. Using Eqs. (1.38), (1.98), and (1.100), the spin-angle function $Y^{jm_j\sigma}_{l\,1/2}$ transforms in the following way:

$$\mathcal{T}\, Y^{jm_j}_{l\,1/2} = (-1)^{m_l} \begin{pmatrix} \left(\dfrac{l-m_l}{2l+1}\right)^{1/2} Y_{l\,-m_l-1} \\ \left(\dfrac{l-m_l+1}{2l+1}\right)^{1/2} Y_{l\,-m_l} \end{pmatrix}. \tag{C.20}$$

By substituting $m_l = m_j - 1/2$, it follows that the spinor on the right-hand side of Eq. (C.20) is the spin-angle function with $-m_j$ (and $j = l + 1/2$), hence:

$$\mathcal{T}\, Y^{jm_j}_{l\,1/2} = (-1)^{m_l}\, Y^{j\,-m_j}_{l\,1/2}. \tag{C.21}$$

A similar argument holds for the $j = l - 1/2$ case as well, therefore Eq. (C.21) is always valid.

APPENDIX D

Effect of time-reversal on the ultrasoft kernel K

The properties of the spin-angle functions discussed in Appendix C can be used when applying the time-reversal operator to the US kernel $K^{\sigma\sigma'}_{\sigma_1\sigma_2}$, namely:

$$\sum_{\sigma_3\,\sigma_4} \mathcal{T}^{\sigma_1\sigma_3}\, K^{\sigma\sigma'}_{\sigma_3\sigma_4}\, \mathcal{T}^{\dagger\sigma_4\sigma_2}, \tag{D.1}$$

which appears in the induced spin-density, Eq. (3.37). The explicit form of $K^{\sigma\sigma'}_{\sigma_1\sigma_2}$ is [40]:

$$\begin{aligned} K^{\sigma\sigma'}_{\sigma_1\sigma_2}(\mathbf{r},\mathbf{r}_1,\mathbf{r}_2) = {} & \delta(\mathbf{r}-\mathbf{r}_1)\,\delta(\mathbf{r}-\mathbf{r}_2)\,\delta^{\sigma\sigma_1}\,\delta^{\sigma'\sigma_2} \\ & + \sum_I \sum_{\tau\,\tau'} \sum_{l\,l'} \sum_{j\,j'} \sum_{m_j\,m'_j} \frac{1}{r^2}\, Q^I_{\substack{\tau lj \\ \tau' l' j'}}(r)\, Y^{*\,Ijm_j\sigma}_{l\,1/2}(\Omega)\, Y^{Ij'm'_j\sigma'}_{l'\,1/2}(\Omega) \\ & \times \beta^I_{\tau lj}(r_1)\, Y^{Ijm_j\sigma_1}_{l\,1/2}(\Omega_1)\, \beta^I_{\tau' l' j'}(r_2)\, Y^{*\,Ij'm'_j\sigma_2}_{l'\,1/2}(\Omega_2). \end{aligned} \tag{D.2}$$

As a first step, we shall prove that:

$$\sum_{\sigma''\,\sigma'''} \sum_{\sigma_1\,\sigma_2} U^{\sigma\sigma''}\, \mathcal{T}^{\sigma_1\sigma_3}\, K^{\sigma''\sigma'''}_{\sigma_3\sigma_4}\, \mathcal{T}^{\dagger\sigma_4\sigma_2} U^{\dagger\sigma'''\sigma'} = K^{\sigma\sigma'}_{\sigma_1\sigma_2}, \tag{D.3}$$

where U is the unitary part of $\mathcal{T}$. U and $\mathcal{T}$ do not affect the quantities $Q^I_{\substack{\tau lj \\ \tau' l' j'}}(r)$, $\beta^I_{\tau lj}(r_1)$, and $\beta^I_{\tau' l' j'}(r_2)$ appearing in $K^{\sigma''\sigma'''}_{\sigma_3\sigma_4}$, because they are real and are not spin-dependent. Consequently, in Eq. (D.3) the operators U, $U^\dagger$, $\mathcal{T}$, and $\mathcal{T}^\dagger$ act only on the four spin-angle functions contained in $K^{\sigma''\sigma'''}_{\sigma_3\sigma_4}$, therefore we consider the product:

$$\sum_{\sigma''\,\sigma'''} \sum_{\sigma_3\,\sigma_4} U^{\sigma\sigma''}\, \mathcal{T}^{\sigma_1\sigma_3}\, Y^{Ijm_j\sigma_3}_{l\,1/2}(\Omega_1)\, Y^{*\,Ijm_j\sigma''}_{l\,1/2}(\Omega)\, Y^{Ij'm'_j\sigma'''}_{l'\,1/2}(\Omega)\, Y^{*\,Ij'm'_j\sigma_4}_{l'\,1/2}(\Omega_2) \mathcal{T}^{\dagger\sigma_4\sigma_2} U^{\dagger\sigma'''\sigma'}. \tag{D.4}$$

In particular, U and $U^\dagger$ act on the two spin-angle functions computed at Ω, the spin-dependent parts of $\mathcal{T}$ and $\mathcal{T}^\dagger$ act on the spin-angle functions computed at Ω_1 and Ω_2, respectively, whereas the complex-conjugation operator contained in $\mathcal{T}$ acts on all four spin-angle functions. Therefore, we can exploit Eq. (C.21) to get:

$$\begin{aligned}&\sum_{\sigma''\,\sigma'''}\sum_{\sigma_3\,\sigma_4} U^{\sigma\sigma''}\,\mathcal{T}^{\sigma_1\sigma_3}\,Y_{l\,1/2}^{Ijm_j\sigma_3}(\Omega_1)\,Y_{l\,1/2}^{*\,Ijm_j\sigma''}(\Omega)\,Y_{l'\,1/2}^{Ij'm'_j\sigma'''}(\Omega)\,Y_{l'\,1/2}^{*\,Ij'm'_j\sigma_4}(\Omega_2)\mathcal{T}^{\dagger\sigma_4\sigma_2}U^{\dagger\sigma'''\sigma'}\\ &=(-1)^{2(m_l+m'_l)}\,Y_{l\,1/2}^{Ij\,-m_j\sigma_1}(\Omega_1)\,Y_{l\,1/2}^{*\,Ij\,-m_j\sigma}(\Omega)\,Y_{l'\,1/2}^{Ij'\,-m'_j\sigma'}(\Omega)\,Y_{l'\,1/2}^{*\,Ij'\,-m'_j\sigma_2}(\Omega_2).\end{aligned} \tag{D.5}$$

Since m_l and m'_l are integers ($m_l = m_j \pm 1/2$, $m'_l = m'_j \pm 1/2$) we have $(-1)^{2(m_l+m'_l)} = 1$, therefore the action of U, $U^\dagger$, $\mathcal{T}$, and $\mathcal{T}^\dagger$ on $K_{\sigma_3\sigma_4}^{\sigma''\sigma'''}$ changes the sign of the numbers m_j and m'_j in the spin-angle functions. However, since the sums over m_j and m'_j in Eq. (D.2) run from $-j$ to j and from $-j'$ to j', respectively, the kernel is overall unchanged, which proves Eq. (D.3).

Finally, we can get the quantity reported in Eq. (D.1) by multiplying Eq. (D.3) by $U^\dagger$ and U on the left and on the right, respectively:

$$\sum_{\sigma_3\,\sigma_4} \mathcal{T}^{\sigma_1\sigma_3}\,K_{\sigma_3\sigma_4}^{\sigma\sigma'}\,\mathcal{T}^{\dagger\sigma_4\sigma_2} = \sum_{\sigma''\,\sigma'''} U^{\dagger\sigma\sigma''}\,K_{\sigma_1\sigma_2}^{\sigma''\sigma'''}\,U^{\sigma'''\sigma'}. \tag{D.6}$$

APPENDIX E

Consequences of symmetry on the charge and magnetization densities of solids

In this Appendix we apply to a crystalline system the general discussion of Appendix B. In particular, our aim is to understand the consequences of symmetries on the charge and magnetization densities associated to a single state or, in a more general fashion, to a group of degenerate states. We first describe the consequences of a space group symmetry, then we generalize the discussion including the time-reversal symmetry.

E.1 Bloch states and charge density in the spinless case: the small group of k

We consider a crystalline system described by the Hamiltonian H and a symmetry operation $\{\mathcal{S}|\mathbf{f}\}$ of the crystal space group. Being a symmety of the crystal, its operator $\mathcal{O}_{\{\mathcal{S}|\mathbf{f}\}}$ commutes with the Hamiltonian:

$$\left[H, \mathcal{O}_{\{\mathcal{S}|\mathbf{f}\}}\right] = 0. \tag{E.1}$$

Given the Schrödinger equation for the crystal:

$$H\psi_{\mathbf{k}n}(\mathbf{r}) = \epsilon_{\mathbf{k}n}\psi_{\mathbf{k}n}(\mathbf{r}), \tag{E.2}$$

where $\mathbf{k}$ identifies the wave vector, we apply $\mathcal{O}_{\{\mathcal{S}|\mathbf{f}\}}$ on both sides and exploit Eq. (E.1) to get:

$$H\mathcal{O}_{\{\mathcal{S}|\mathbf{f}\}}\psi_{\mathbf{k}n}(\mathbf{r}) = \epsilon_{\mathbf{k}n}\mathcal{O}_{\{\mathcal{S}|\mathbf{f}\}}\psi_{\mathbf{k}n}(\mathbf{r}), \tag{E.3}$$

which means that $\mathcal{O}_{\{\mathcal{S}|\mathbf{f}\}}\psi_{\mathbf{k}n}(\mathbf{r})$ is an eigenstate of H relative to the same eigenvalue $\epsilon_{\mathbf{k}n}$ as $\psi_{\mathbf{k}n}(\mathbf{r})$. From Appendix B (Eq. (B.18)) we recall that:

$$\mathcal{O}_{\{\mathcal{S}|\mathbf{f}\}}\psi_{\mathbf{k}n}(\mathbf{r}) = \psi_{\mathbf{k}n}(\mathcal{S}^{-1}\mathbf{r} - \mathcal{S}^{-1}\mathbf{f}). \tag{E.4}$$

Since $\psi_{\mathbf{k}n}(\mathbf{r})$ is a Bloch state, the right-hand side can be written as $\psi_{\mathcal{S}\mathbf{k}n}(\mathbf{r})$. In the following we consider only the set of symmetry operations such that $\mathcal{S}\mathbf{k} = \mathbf{k} + \mathbf{G}$, which defines subgroup of the crystal space group called *small group* of $\mathbf{k}$. In this case the relationship $\psi_{\mathbf{k}n}(\mathcal{S}^{-1}\mathbf{r} - \mathcal{S}^{-1}\mathbf{f}) = \psi_{\mathcal{S}\mathbf{k}n}(\mathbf{r})$ becomes $\psi_{\mathbf{k}n}(\mathcal{S}^{-1}\mathbf{r} - \mathcal{S}^{-1}\mathbf{f}) = \psi_{\mathbf{k}n}(\mathbf{r})$. As a consequence:

$$|\psi_{\mathbf{k}n}(\mathcal{S}^{-1}\mathbf{r} - \mathcal{S}^{-1}\mathbf{f})|^2 = |\psi_{\mathbf{k}n}(\mathbf{r})|^2, \tag{E.5}$$

therefore the symmetries of the charge density associated to a Bloch state with wave vector $\mathbf{k}$ are described by the operations of the small group of $\mathbf{k}$.

It is possible to generalize the previous discussion to the case in which the state $\psi_{\mathbf{k}n}(\mathbf{r})$ at $\mathbf{k}$ is N-fold degenerate. In this case, if $\mathcal{S}\mathbf{k} = \mathbf{k} + \mathbf{G}$ the application of $\mathcal{O}_{\{\mathcal{S}|\mathbf{f}\}}$ to $\psi_{\mathbf{k}n}(\mathbf{r})$ gives a Bloch state defined in the N-dimensional subspace of Bloch states with wavevector $\mathbf{k}$, so it can be expressed as a linear combination in the basis of this subspace:

$$\mathcal{O}_{\{\mathcal{S}|\mathbf{f}\}}\psi_{\mathbf{k}n}(\mathbf{r}) = \sum_{m=1}^{N} \Gamma_{nm}\, \psi_{\mathbf{k}m}(\mathbf{r}). \tag{E.6}$$

To analyze the symmetries of the charge density, as discussed above for the non-degenerate case, we should consider the sum of the contribution to the charge density of each of the N degenerate states. Indeed, since the basis of the N-dimensional subspace is not unique, the charge density associated to a single state is physically meaningless. Using Eq. (E.6) we have:

$$\begin{aligned}
\sum_{n=1}^{N} |\mathcal{O}_{\{\mathcal{S}|\mathbf{f}\}}\psi_{\mathbf{k}n}(\mathbf{r})|^2 &= \sum_{n=1}^{N} \left(\sum_{m=1}^{N} \Gamma^*_{nm}\, \psi^*_{\mathbf{k}m}(\mathbf{r}) \right) \left(\sum_{m'=1}^{N} \Gamma_{nm'} \psi_{\mathbf{k}m'}(\mathbf{r}) \right) \\
&= \sum_{m=1}^{N} \sum_{m'=1}^{N} \sum_{n=1}^{N} \Gamma^\dagger_{mn}\, \Gamma_{nm'}\, \psi^*_{\mathbf{k}m}(\mathbf{r})\, \psi_{\mathbf{k}m'}(\mathbf{r}) \\
&= \sum_{m=1}^{N} \psi^*_{\mathbf{k}m}(\mathbf{r})\, \psi_{\mathbf{k}m}(\mathbf{r}) \\
&= \sum_{m=1}^{N} |\psi_{\mathbf{k}m}(\mathbf{r})|^2,
\end{aligned} \tag{E.7}$$

where we used the unitarity of Γ ($\sum_{n=1}^{N} \Gamma^\dagger_{mn}\, \Gamma_{nm'} = \delta_{mm'}$). The same sum of charge densities can be dealt with using Eq. (E.4). We get:

$$\sum_{n=1}^{N} |\mathcal{O}_{\{\mathcal{S}|\mathbf{f}\}}\psi_{\mathbf{k}n}(\mathbf{r})|^2 = \sum_{n=1}^{N} |\psi_{\mathbf{k}n}(\mathcal{S}^{-1}\mathbf{r} - \mathcal{S}^{-1}\mathbf{f})|^2. \tag{E.8}$$

By comparing the right-hand sides of Eqs. (E.7) and (E.8) we get the final result:

$$\sum_{n=1}^{N} |\psi_{\mathbf{k}n}(\mathbf{r})|^2 = \sum_{n=1}^{N} |\psi_{\mathbf{k}n}(\mathcal{S}^{-1}\mathbf{r} - \mathcal{S}^{-1}\mathbf{f})|^2, \tag{E.9}$$

that is the generalization of Eq. (E.5).

E.2 Magnetization density: the spin-1/2 case

Below we consider the spin-1/2 case. Our goal is to generalize to the magnetization density the arguments discussed above for the charge density in the spinless case. We recall that the magnetization density is defined as:

$$m_\alpha(\mathbf{r}) = \mu_\mathrm{B} \sum_{n=1}^{N} \sum_{\sigma_1\sigma_2} \psi^{*\sigma_1}_{\mathbf{k}n}(\mathbf{r})\, \sigma_\alpha^{\sigma_1\sigma_2}\, \psi^{\sigma_2}_{\mathbf{k}n}(\mathbf{r}), \tag{E.10}$$

where α identifies the cartesian component we are considering, σ_α are the Pauli matrices, and $\sigma_1 = 1, 2$, $\sigma_2 = 1, 2$ identify the components in spin space. Here we are already considering the more general case of degenerate states. We apply a given symmetry operation $\{\mathcal{S}|\mathbf{f}\}$ of the small group of $\mathbf{k}$. Using Eq. (E.6) we get for the transformed magnetization:

$$\begin{aligned}
&\mu_\mathrm{B} \sum_{n=1}^{N} \sum_{\sigma_1\sigma_2} \left(\mathcal{O}_{\{\mathcal{S}|\mathbf{f}\}}\psi_{\mathbf{k}n}(\mathbf{r})\right)^{*\sigma_1}\, \sigma_\alpha^{\sigma_1\sigma_2}\, \left(\mathcal{O}_{\{\mathcal{S}|\mathbf{f}\}}\psi_{\mathbf{k}n}(\mathbf{r})\right)^{\sigma_2} \\
&= \mu_\mathrm{B} \sum_{n=1}^{N} \sum_{\sigma_1\sigma_2} \left(\sum_{m=1}^{N} \Gamma^*_{nm}\, \psi^{*\sigma_1}_{\mathbf{k}m}(\mathbf{r})\right) \sigma_\alpha^{\sigma_1\sigma_2} \left(\sum_{m'=1}^{N} \Gamma_{nm'}\, \psi^{\sigma_2}_{\mathbf{k}m'}(\mathbf{r})\right) \\
&= \mu_\mathrm{B} \sum_{m=1}^{N} \sum_{m'=1}^{N} \sum_{n=1}^{N} \sum_{\sigma_1\sigma_2} \Gamma^\dagger_{mn}\, \Gamma_{nm'}\, \psi^{*\sigma_1}_{\mathbf{k}m}(\mathbf{r})\, \sigma_\alpha^{\sigma_1\sigma_2}\, \psi^{\sigma_2}_{\mathbf{k}m'}(\mathbf{r}) \\
&= \mu_\mathrm{B} \sum_{m=1}^{N} \sum_{\sigma_1\sigma_2} \psi^{*\sigma_1}_{\mathbf{k}m}(\mathbf{r})\, \sigma_\alpha^{\sigma_1\sigma_2}\, \psi^{\sigma_2}_{\mathbf{k}m}(\mathbf{r}) \\
&= m_\alpha(\mathbf{r}).
\end{aligned} \tag{E.11}$$

On the other hand, if we exploit Eq. (B.18) we get:

$$\begin{aligned}
&\mu_\mathrm{B} \sum_{n=1}^{N} \sum_{\sigma_1\sigma_2} \left(\mathcal{O}_{\{\mathcal{S}|\mathbf{f}\}}\psi_{\mathbf{k}n}(\mathbf{r})\right)^{*\sigma_1}\, \sigma_\alpha^{\sigma_1\sigma_2}\, \left(\mathcal{O}_{\{\mathcal{S}|\mathbf{f}\}}\psi_{\mathbf{k}n}(\mathbf{r})\right)^{\sigma_2} \\
&= \mu_\mathrm{B} \sum_{n=1}^{N} \sum_{\sigma_1\sigma_2} \sum_{\sigma_3\sigma_4} \psi^{*\sigma_3}_{\mathbf{k}n}(\mathcal{S}^{-1}\mathbf{r} - \mathcal{S}^{-1}\mathbf{f})\, \mathcal{R}^{\dagger\,\sigma_3\sigma_1}_{1/2}\, \sigma_\alpha^{\sigma_1\sigma_2}\, \mathcal{R}^{\sigma_2\sigma_4}_{1/2}\, \psi^{\sigma_4}_{\mathbf{k}n}(\mathcal{S}^{-1}\mathbf{r} - \mathcal{S}^{-1}\mathbf{f}) \\
&= \mu_\mathrm{B} \sum_{n=1}^{N} \sum_{\beta} \sum_{\sigma_3\sigma_4} \psi^{*\sigma_3}_{\mathbf{k}n}(\mathcal{S}^{-1}\mathbf{r} - \mathcal{S}^{-1}\mathbf{f})\, \tilde{\mathcal{S}}_{\alpha\beta}\, \sigma_\beta^{\sigma_3\sigma_4}\, \psi^{\sigma_4}_{\mathbf{k}n}(\mathcal{S}^{-1}\mathbf{r} - \mathcal{S}^{-1}\mathbf{f}) \\
&= \sum_{n=1}^{N} \sum_{\beta} \tilde{\mathcal{S}}_{\alpha\beta}\, m_\beta(\mathcal{S}^{-1}\mathbf{r} - \mathcal{S}^{-1}\mathbf{f}),
\end{aligned} \tag{E.12}$$

where $\tilde{\mathcal{S}}$ (called $\mathcal{R}$ previously in Appendix B) is the proper part of the operation $\mathcal{S}$, and we used the following relationship:

$$\sum_{\sigma_1\sigma_2} \mathcal{R}^{\dagger\,\sigma_3\sigma_1}_{1/2} \sigma_\alpha^{\sigma_1\sigma_2} \mathcal{R}^{\sigma_2\sigma_4}_{1/2} = \sum_{\beta} \tilde{\mathcal{S}}_{\alpha\beta} \sigma_\beta^{\sigma_3\sigma_4}, \tag{E.13}$$

whose proof is shown in detail in Appendix F. By comparing the right-hand sides of Eqs. (E.11) and (E.12) we get the final result:

$$\mathbf{m}(\mathbf{r}) = \tilde{\mathcal{S}}\,\mathbf{m}(\mathcal{S}^{-1}\mathbf{r} - \mathcal{S}^{-1}\mathbf{f}). \tag{E.14}$$

If $\{\mathcal{S}|\mathbf{f}\}$ is a symmetry operation of the small group of $\mathbf{k}$ when composed with the time-reversal, we must generalize Eq. (E.14). In particular, Eq. (E.6) holds also if time-reversal is applied:

$$\mathcal{T}\mathcal{O}_{\{\mathcal{S}|\mathbf{f}\}}\psi_{\mathbf{k}n}(\mathbf{r}) = \sum_{m=1}^{N} \Gamma_{nm}\psi_{\mathbf{k}m}(\mathbf{r}). \tag{E.15}$$

Γ is, as in the previous case, a unitary matrix, so the calculations in Eq. (E.11) can be done in a similar way, to get:

$$\mu_{\mathrm{B}} \sum_{n=1}^{N}\sum_{\sigma_1\sigma_2} \left(\mathcal{T}\mathcal{O}_{\{\mathcal{S}|\mathbf{f}\}}\psi_{\mathbf{k}n}(\mathbf{r})\right)^{*\,\sigma_1} \sigma_\alpha^{\sigma_1\sigma_2} \left(\mathcal{T}\mathcal{O}_{\{\mathcal{S}|\mathbf{f}\}}\psi_{\mathbf{k}n}(\mathbf{r})\right)^{\sigma_2} = m_\alpha(\mathbf{r}). \tag{E.16}$$

Instead, calculations similar to those in Eq. (E.12) can be performed in the following way:

$$\begin{aligned}
&\mu_{\mathrm{B}} \sum_{n=1}^{N}\sum_{\sigma_1\sigma_2} \left(\mathcal{T}\mathcal{O}_{\{\mathcal{S}|\mathbf{f}\}}\psi_{\mathbf{k}n}(\mathbf{r})\right)^{*\,\sigma_1} \sigma_\alpha^{\sigma_1\sigma_2} \left(\mathcal{T}\mathcal{O}_{\{\mathcal{S}|\mathbf{f}\}}\psi_{\mathbf{k}n}(\mathbf{r})\right)^{\sigma_2} \\
&= \mu_{\mathrm{B}} \sum_{n=1}^{N}\sum_{\sigma_1\sigma_2}\sum_{\sigma_3\sigma_4} \left[\left(\mathcal{O}_{\{\mathcal{S}|\mathbf{f}\}}\psi_{\mathbf{k}n}(\mathbf{r})\right)^{*\,\sigma_3} \mathcal{T}^{\dagger\,\sigma_3\sigma_1}\right] \sigma_\alpha^{\sigma_1\sigma_2} \left[\mathcal{T}^{\sigma_2\sigma_4} \left(\mathcal{O}_{\{\mathcal{S}|\mathbf{f}\}}\psi_{\mathbf{k}n}(\mathbf{r})\right)^{\sigma_4}\right] \\
&= \mu_{\mathrm{B}} \sum_{n=1}^{N}\sum_{\sigma_3\sigma_4} \left(\mathcal{O}_{\{\mathcal{S}|\mathbf{f}\}}\psi_{\mathbf{k}n}(\mathbf{r})\right)^{\sigma_3} \left[\sum_{\sigma_1\sigma_2} \mathcal{T}^{\sigma_1\sigma_3}\, \sigma_\alpha^{*\,\sigma_1\sigma_2}\, \mathcal{T}^{*\,\sigma_2\sigma_4} \left(\mathcal{O}_{\{\mathcal{S}|\mathbf{f}\}}\psi_{\mathbf{k}n}(\mathbf{r})\right)^{*\,\sigma_4}\right] \\
&= \mu_{\mathrm{B}} \sum_{n=1}^{N}\sum_{\sigma_3\sigma_4} \left(\mathcal{O}_{\{\mathcal{S}|\mathbf{f}\}}\psi_{\mathbf{k}n}(\mathbf{r})\right)^{*\,\sigma_4} \left[\mathcal{T}^{\dagger\,\sigma_4\sigma_2}\, \sigma_\alpha^{\sigma_2\sigma_1}\, \mathcal{T}^{\sigma_1\sigma_3} \left(\mathcal{O}_{\{\mathcal{S}|\mathbf{f}\}}\psi_{\mathbf{k}n}(\mathbf{r})\right)^{\sigma_3}\right] \\
&= -\,\mu_{\mathrm{B}} \sum_{n=1}^{N}\sum_{\sigma_3\sigma_4} \left(\mathcal{O}_{\{\mathcal{S}|\mathbf{f}\}}\psi_{\mathbf{k}n}(\mathbf{r})\right)^{*\,\sigma_4} \sigma_\alpha^{\sigma_4\sigma_3} \left(\mathcal{O}_{\{\mathcal{S}|\mathbf{f}\}}\psi_{\mathbf{k}n}(\mathbf{r})\right)^{\sigma_3} \\
&= -\sum_{n=1}^{N}\sum_{\beta} \tilde{\mathcal{S}}_{\alpha\beta}\, m_\beta(\mathcal{S}^{-1}\mathbf{r} - \mathcal{S}^{-1}\mathbf{f}),
\end{aligned} \tag{E.17}$$

where in the third line we used the properties of antilinear operators, while in the fifth line we used the relationship $\mathcal{T}^\dagger\sigma_\alpha\mathcal{T} = -\sigma_\alpha$, a property of the time-reversal operator discussed in Appendix B. The last equality in Eq. (E.17) follows from Eq. (E.12). Finally, the generalization of Eq. (E.14) reads like:

$$\mathbf{m}(\mathbf{r}) = \pm\tilde{\mathcal{S}}\,\mathbf{m}(\mathcal{S}^{-1}\mathbf{r} - \mathcal{S}^{-1}\mathbf{f}), \tag{E.18}$$

where the sign depends on the presence of time-reversal in the symmetry considered. In particular, if $\mathcal{S}$ ($\mathcal{T}\mathcal{S}$) belongs to the small group of $\mathbf{k}$ we must consider the $+$ ($-$) sign.

APPENDIX F

Rotation of Pauli matrices

In this Appendix we consider the rotation in spin space introduced in Appendix B and used explicitly in Appendix E to compute the transformed magnetization. The proof presented below is partially based on Problem 9.4 of Ref. [168]. We shall show that:

$$\sum_{\sigma_1\sigma_2} \mathcal{R}_{1/2}^{\dagger\,\sigma_3\sigma_1}\, \sigma_\alpha^{\sigma_1\sigma_2}\, \mathcal{R}_{1/2}^{\sigma_2\sigma_4} = \sum_\beta \tilde{\mathcal{S}}_{\alpha\beta}\, \sigma_\beta^{\sigma_3\sigma_4}, \tag{F.1}$$

or, in a more compact way:

$$R_{1/2}^\dagger \boldsymbol{\sigma} R_{1/2} = \tilde{\mathcal{S}}\, \boldsymbol{\sigma}, \tag{F.2}$$

where $\boldsymbol{\sigma}$ is a vector whose components are the Pauli matrices $\sigma_\alpha (\alpha = 1, 2, 3)$, while $\tilde{\mathcal{S}}$ is the proper rotation associated to the symmetry operation $\mathcal{S}$.

From Appendix B we recall that:

$$R_{1/2} = e^{-\frac{i}{\hbar}\theta \mathbf{S}\cdot\mathbf{n}} = e^{-i\frac{\theta}{2}\boldsymbol{\sigma}\cdot\mathbf{n}}, \tag{F.3}$$

where $\mathbf{n}$ (a unit vector) represents the rotation axis, while θ is the rotation angle. We consider the Taylor expansion of $R_{1/2}$. To compute the quantity $(\boldsymbol{\sigma}\cdot\mathbf{n})^k$, we use the following relationship:

$$(\boldsymbol{\sigma}\cdot\mathbf{A})\,(\boldsymbol{\sigma}\cdot\mathbf{B}) = \mathbf{A}\cdot\mathbf{B} + i\boldsymbol{\sigma}\cdot(\mathbf{A}\times\mathbf{B}), \tag{F.4}$$

a property of the Pauli matrices, to get:

$$(\boldsymbol{\sigma}\cdot\mathbf{n})^2 = \mathbb{1} + i\,\boldsymbol{\sigma}\cdot(\mathbf{n}\times\mathbf{n}) = \mathbb{1}, \tag{F.5}$$

and, as a consequence:

$$(\boldsymbol{\sigma}\cdot\mathbf{n})^{2k} = \mathbb{1}, \tag{F.6}$$

$$(\boldsymbol{\sigma}\cdot\mathbf{n})^{2k+1} = \boldsymbol{\sigma}\cdot\mathbf{n}. \tag{F.7}$$

Using Eqs. (F.6) and (F.7) it is possible to separate the even and the odd powers in the Taylor expansion of $R_{1/2}$. As a result we get:

$$R_{1/2} = \mathbb{1}\cos\left(\frac{\theta}{2}\right) - i(\boldsymbol{\sigma}\cdot\mathbf{n})\sin\left(\frac{\theta}{2}\right). \tag{F.8}$$

Using the expression of $R_{1/2}$ it is possible to compute $R_{1/2}^{\dagger}\,\boldsymbol{\sigma}\,R_{1/2}$. We consider a given component α of the vector $\boldsymbol{\sigma}$:

$$\begin{aligned} R_{1/2}^{\dagger}\,\sigma_\alpha\,R_{1/2} &= \left[\mathbb{1}\cos\left(\frac{\theta}{2}\right) + i(\boldsymbol{\sigma}\cdot\mathbf{n})\sin\left(\frac{\theta}{2}\right)\right]\sigma_\alpha\left[\mathbb{1}\cos\left(\frac{\theta}{2}\right) - i(\boldsymbol{\sigma}\cdot\mathbf{n})\sin\left(\frac{\theta}{2}\right)\right] \\ &= \cos^2\left(\frac{\theta}{2}\right)\sigma_\alpha - i\sin\left(\frac{\theta}{2}\right)\cos\left(\frac{\theta}{2}\right)\left[\sigma_\alpha\,(\boldsymbol{\sigma}\cdot\mathbf{n}) - (\boldsymbol{\sigma}\cdot\mathbf{n})\,\sigma_\alpha\right] \\ &\quad + \sin^2\left(\frac{\theta}{2}\right)(\boldsymbol{\sigma}\cdot\mathbf{n})\,\sigma_\alpha\,(\boldsymbol{\sigma}\cdot\mathbf{n}). \end{aligned} \tag{F.9}$$

We analyze separately the following two terms: $[\sigma_\alpha\,(\boldsymbol{\sigma}\cdot\mathbf{n}) - (\boldsymbol{\sigma}\cdot\mathbf{n})\,\sigma_\alpha]$ and $(\boldsymbol{\sigma}\cdot\mathbf{n})\,\sigma_\alpha\,(\boldsymbol{\sigma}\cdot\mathbf{n})$. We have:

$$\begin{aligned} \sigma_\alpha\,(\boldsymbol{\sigma}\cdot\mathbf{n}) - (\boldsymbol{\sigma}\cdot\mathbf{n})\,\sigma_\alpha &= \sum_\beta n_\beta[\sigma_\alpha,\sigma_\beta] \\ &= 2\,i\sum_{\beta\gamma}\epsilon_{\alpha\beta\gamma}\,n_\beta\,\sigma_\gamma \\ &= 2\,i\,(\mathbf{n}\times\boldsymbol{\sigma})_\alpha, \end{aligned} \tag{F.10}$$

where $\epsilon_{\alpha\beta\gamma}$ is the totally antisymmetric Levi-Civita tensor and we used the property of the Pauli matrices $[\sigma_\alpha,\sigma_\beta] = 2\,i\sum_k\epsilon_{\alpha\beta\gamma}\,\sigma_\gamma$. To deal with the second term we recall another property of the Pauli matrices, namely $\sigma_\alpha\sigma_\beta = \delta_{\alpha\beta} + i\sum_\gamma\epsilon_{\alpha\beta\gamma}\sigma_\gamma$. We get:

$$\begin{aligned} (\boldsymbol{\sigma}\cdot\mathbf{n})\,\sigma_\alpha\,(\boldsymbol{\sigma}\cdot\mathbf{n}) &= \sum_{\beta\gamma} n_\beta\,n_\gamma\,\sigma_\beta\,\sigma_\alpha\,\sigma_\gamma \\ &= \sum_{\beta\gamma} n_\beta\,n_\gamma\,\sigma_\beta\,\delta_{\alpha\gamma} + i\sum_{\beta\gamma\delta} n_\beta\,n_\gamma\,\epsilon_{\alpha\gamma\delta}\,\sigma_\beta\,\sigma_\delta. \end{aligned} \tag{F.11}$$

The first term gives $n_\alpha\,(\mathbf{n}\cdot\boldsymbol{\sigma})$. The second term can be further expanded getting:

$$i\sum_{\beta\gamma} n_\beta\,n_\gamma\,\epsilon_{\alpha\gamma\beta} + \sum_{\beta\gamma}\sum_{\delta\eta} n_\beta\,n_\gamma\,\epsilon_{\alpha\gamma\delta}\,\epsilon_{\delta\beta\eta}\,\sigma_\eta. \tag{F.12}$$

The first term is $-i\,(\mathbf{n}\times\mathbf{n})_\alpha = 0$, while the second can be rearranged in the following way:

$$\begin{aligned} \sum_{\gamma\delta}\epsilon_{\alpha\gamma\delta}\,n_\gamma\sum_{\beta\eta}\epsilon_{\delta\beta\eta}\,n_\beta\,\sigma_\eta &= \sum_{\gamma\delta}\epsilon_{\alpha\gamma\delta}\,n_\gamma\,(\mathbf{n}\times\boldsymbol{\sigma})_\delta \\ &= \left[\mathbf{n}\times(\mathbf{n}\times\boldsymbol{\sigma})\right]_\alpha \end{aligned} \tag{F.13}$$

To summarize, we have:

$$(\boldsymbol{\sigma}\cdot\mathbf{n})\,\sigma_\alpha\,(\boldsymbol{\sigma}\cdot\mathbf{n}) = n_\alpha\,(\mathbf{n}\cdot\boldsymbol{\sigma}) + \left[\mathbf{n}\times(\mathbf{n}\times\boldsymbol{\sigma})\right]_\alpha. \tag{F.14}$$

Finally, in order to complete the rearrangement of the quantity $R^{\dagger}_{1/2}\sigma_\alpha R_{1/2}$ we consider once more the term $\sum_{\beta\gamma}\sum_{\delta\eta} n_\beta\, n_\gamma\, \epsilon_{\alpha\gamma\delta}\, \epsilon_{\delta\beta\eta}\, \sigma_\eta$, that before we wrote explicitly as $[\mathbf{n}\times(\mathbf{n}\times\boldsymbol{\sigma})]_\alpha$. It is possible to compute it in a different way, using the following property of the totally antisymmetric tensor: $\sum_\gamma \epsilon_{\alpha\beta\gamma}\,\epsilon_{\gamma\delta\eta} = \delta_{\alpha\delta}\delta_{\beta\eta} - \delta_{\alpha\eta}\delta_{\beta\gamma}$. We get:

$$\begin{aligned}\sum_{\beta\gamma}\sum_{\delta\eta} n_\beta\, n_\gamma\, \epsilon_{\alpha\gamma\delta}\, \epsilon_{\delta\beta\eta}\, \sigma_\eta &= \sum_{\beta\gamma\eta} n_\beta\, n_\gamma\, \sigma_\eta\, (\delta_{\alpha\beta}\delta_{\gamma\eta} - \delta_{\alpha\eta}\delta_{\beta\gamma}) \\ &= n_\alpha \sum_\gamma n_\gamma\, \sigma_\gamma - \sigma_\alpha \sum_\gamma n_\gamma^2 \\ &= n_\alpha\, (\mathbf{n}\cdot\boldsymbol{\sigma}) - \sigma_\alpha,\end{aligned} \tag{F.15}$$

from which we can get an expression for the Pauli matrix σ_α, which multiplies $\cos^2(\theta/2)$ in the expression of $R^{\dagger}_{1/2}\,\sigma_\alpha\, R_{1/2}$, Eq. (F.9). In particular, we have:

$$\sigma_\alpha = n_\alpha\, (\mathbf{n}\cdot\boldsymbol{\sigma}) - [\mathbf{n}\times(\mathbf{n}\times\boldsymbol{\sigma})]_\alpha\,. \tag{F.16}$$

Finally, we substitute the computed terms in the expression of $R^{\dagger}_{1/2}\,\sigma_\alpha\, R_{1/2}$ and we exploit the trigonometric identities to reach the following result:

$$R^{\dagger}_{1/2}\,\sigma_\alpha\, R_{1/2} = n_\alpha\, (\mathbf{n}\cdot\boldsymbol{\sigma}) - \cos\theta\, [\mathbf{n}\times(\mathbf{n}\times\boldsymbol{\sigma})]_\alpha + \sin\theta\, (\mathbf{n}\times\boldsymbol{\sigma})_\alpha. \tag{F.17}$$

This expression can be further expanded to factor out the Pauli matrices, so that we can write $R^{\dagger}_{1/2}\;\boldsymbol{\sigma}\, R_{1/2}$ as a matrix-vector product. By writing explicitly the dot and cross products, Eq. (F.17) becomes:

$$R^{\dagger}_{1/2}\,\sigma_\alpha\, R_{1/2} = n_\alpha \sum_\beta n_\beta\, \sigma_\beta - \cos\theta \sum_{\beta\gamma}\sum_{\delta\eta} \epsilon_{\alpha\beta\gamma}\, n_\beta\, \epsilon_{\gamma\delta\eta}\, n_\delta\, \sigma_\eta + \sin\theta \sum_{\beta\gamma} \epsilon_{\alpha\beta\gamma} n_\beta \sigma_\gamma. \tag{F.18}$$

The sum over γ in the second term can be computed using the identity $\sum_\gamma \epsilon_{\alpha\beta\gamma}\epsilon_{\gamma\delta\eta} = \delta_{\alpha\delta}\delta_{\beta\eta} - \delta_{\alpha\eta}\delta_{\beta\delta}$, that allows to compute the sums over δ and η as well. The third term can be slightly rearranged exchanging the indices β and γ in order to have σ_β instead of σ_γ. Moreover, recalling that $\sum_\beta n_\beta^2 = 1$ and collecting the similar terms, we get:

$$R^{\dagger}_{1/2}\,\sigma_\alpha\, R_{1/2} = n_\alpha\, (1-\cos\theta) \sum_\beta n_\beta\, \sigma_\beta + \cos\theta \sum_\beta \delta_{\alpha\beta}\, \sigma_\beta + \sin\theta \sum_{\beta\gamma} \epsilon_{\alpha\gamma\beta}\, n_\gamma\, \sigma_\beta, \tag{F.19}$$

that can be written as the product of a matrix $\mathcal{M}$ and the vector $\boldsymbol{\sigma}$, whose entries are the Pauli matrices. The entries of the matrix can be computed from Eq. (F.19) by inserting $\alpha = 1,2,3$ and $\beta = 1,2,3$. The final result is:

$$\mathcal{M} = \begin{pmatrix} \cos\theta + n_x^2(1-\cos\theta) & n_x n_y(1-\cos\theta) - n_z\sin\theta & n_x n_z(1-\cos\theta) + n_y\sin\theta \\ n_x n_y(1-\cos\theta) + n_z\sin\theta & \cos\theta + n_y^2(1-\cos\theta) & n_y n_z(1-\cos\theta) - n_x\sin\theta \\ n_x n_z(1-\cos\theta) - n_y\sin\theta & n_y n_z(1-\cos\theta) + n_x\sin\theta & \cos\theta + n_z^2(1-\cos\theta) \end{pmatrix}, \tag{F.20}$$

which can be proved to represent a rotation of angle θ about the axis $\mathbf{n}$ (see [169] for more details). This is the proper rotation associated to the symmetry operation $\mathcal{S}$ we started from

in Appendix E. Its form does not depend on the presence of improper rotations (inversion) in $\mathcal{S}$, because the improper rotations do not affect the spin variables, hence they do not change the form of $R_{1/2}$. We can conclude that $\mathcal{M}$ is the proper part of $\mathcal{S}$, therefore:

$$\sum_{\sigma_1\sigma_2} \mathcal{R}_{1/2}^{\dagger\,\sigma_3\sigma_1}\, \sigma_\alpha^{\sigma_1\sigma_2}\, \mathcal{R}_{1/2}^{\sigma_2\sigma_4} = \sum_\beta \tilde{\mathcal{S}}_{\alpha\beta}\, \sigma_\beta^{\sigma_3\sigma_4}. \tag{F.21}$$

APPENDIX G

Analysis of the term $\langle \Delta^\mu \psi | K | \psi \rangle$ in the induced spin density

In this Appendix we consider the second term appearing in the induced spin density (Eq. (3.30)) and discuss how to introduce the time-reversal operator $\mathcal{T}$. Moreover, we explain how to apply this expression to the induced charge and magnetization densities.

We start our discussion from the induced spin density (Eq. (3.30)), which reads:

$$\frac{dn^{\sigma\sigma'}(\mathbf{r})}{d\mu} = \sum_i \sum_{\sigma_1\,\sigma_2} \left[\langle \psi_i^{\sigma_1} | K^{\sigma\sigma'}_{\sigma_1\sigma_2}(\mathbf{r}) | \Delta^\mu \psi_i^{\sigma_2} \rangle + \langle \Delta^\mu \psi_i^{\sigma_1} | K^{\sigma\sigma'}_{\sigma_1\sigma_2}(\mathbf{r}) | \psi_i^{\sigma_2} \rangle \right] + \Delta^\mu n^{\sigma\sigma'}(\mathbf{r}). \quad \text{(G.1)}$$

We label the first and the second terms with the superscripts (1) and (2), respectively, and we focus on $(dn^{\sigma\sigma'}(\mathbf{r})/d\mu)^{(2)}$. Inserting the identity $\mathcal{T}^\dagger\mathcal{T} = \mathbb{1}$ between $\langle \Delta^\mu \psi_i^\sigma |$ and K and between K and $|\psi_i^\sigma\rangle$ we have:

$$\begin{aligned}\left(\frac{dn^{\sigma\sigma'}(\mathbf{r})}{d\mu}\right)^{(2)} &= \sum_i \sum_{\sigma_1\,\sigma_2} \langle \Delta^\mu \psi_i^{\sigma_1} | K^{\sigma\sigma'}_{\sigma_1\sigma_2}(\mathbf{r}) | \psi_i^{\sigma_2} \rangle \\ &= \sum_i \sum_{\sigma_1\,\sigma_2} \sum_{\sigma_3\,\sigma_4} \sum_{\sigma_5\,\sigma_6} \langle \Delta^\mu \psi_i^{\sigma_1} | \left(\mathcal{T}^{\dagger\,\sigma_1\sigma_3}\, \mathcal{T}^{\sigma_3\sigma_4}\, K^{\sigma\sigma'}_{\sigma_4\sigma_5}(\mathbf{r})\, \mathcal{T}^{\dagger\,\sigma_5\sigma_6}\, \mathcal{T}^{\sigma_6\sigma_2}\, |\psi_i^{\sigma_2}\rangle \right).\end{aligned} \quad \text{(G.2)}$$

In the bottom line the round brackets are necessary because $\mathcal{T}$ is an antilinear operator, hence it is essential to specify whether it acts to the right or to the left. By applying the

properties of antilinear operators we can write:

$$\begin{aligned}\left(\frac{dn^{\sigma\sigma'}(\mathbf{r})}{d\mu}\right)^{(2)} &= \sum_i \sum_{\sigma_1\,\sigma_2} \sum_{\sigma_3\,\sigma_4} \sum_{\sigma_5\,\sigma_6} \left[\left(\langle \Delta^\mu \psi_i^{\sigma_1} | \, \mathcal{T}^{\dagger\,\sigma_1\sigma_3} \right) \left(\mathcal{T}^{\sigma_3\sigma_4} \, K^{\sigma\sigma'}_{\sigma_4\sigma_5}(\mathbf{r}) \, \mathcal{T}^{\dagger\,\sigma_5\sigma_6} \, \mathcal{T}^{\sigma_6\sigma_2} \, |\psi_i^{\sigma_2}\rangle \right) \right]^* \\ &= \sum_i \sum_{\sigma_3\,\sigma_4} \sum_{\sigma_5\,\sigma_6} \langle (\mathcal{T}\psi_i)^{\sigma_6} | \left(\mathcal{T}^{\sigma_6\sigma_5} \, K^{\sigma'\sigma}_{\sigma_5\sigma_4}(\mathbf{r}) \, \mathcal{T}^{\dagger\,\sigma_4\sigma_3} \, |(\mathcal{T}\Delta^\mu\psi_i)^{\sigma_3}\rangle \right),\end{aligned} \tag{G.3}$$

where the second line follows from the hermiticity of the kernel K, namely $K^{\sigma\sigma'\,*}_{\sigma_4\sigma_5} = K^{\sigma'\sigma}_{\sigma_5\sigma_4}$. Then we can exploit Eq. (D.6), a property of K discussed in detail in Appendix D. As a result:

$$\left(\frac{dn^{\sigma\sigma'}(\mathbf{r})}{d\mu}\right)^{(2)} = \sum_i \sum_{\sigma_1\,\sigma_2} \sum_{\sigma''\,\sigma'''} U^{\dagger\,\sigma'\sigma''} \left[\langle (\mathcal{T}\psi_i)^{\sigma_1} | \, K^{\sigma''\sigma'''}_{\sigma_1\sigma_2}(\mathbf{r}) \, |(\mathcal{T}\Delta^\mu\psi_i)^{\sigma_2}\rangle \right] U^{\sigma'''\sigma}. \tag{G.4}$$

When computing the contribution to the induced charge and magnetization densities given by $(dn^{\sigma\sigma'}(\mathbf{r})/d\mu)^{(2)}$, Eq. (G.4) implies that:

$$\begin{aligned}\left(\frac{dn(\mathbf{r})}{d\mu}\right)^{(2)} &= \sum_\sigma \left(\frac{dn^{\sigma\sigma}(\mathbf{r})}{d\mu}\right)^{(2)} \\ &= \sum_\sigma \sum_{\sigma''\,\sigma'''} \sum_{\sigma_1\,\sigma_2} U^{\dagger\,\sigma\sigma''} \left[\langle (\mathcal{T}\psi_i)^{\sigma_1} | \, K^{\sigma''\sigma'''}_{\sigma_1\sigma_2}(\mathbf{r}) \, |(\mathcal{T}\Delta^\mu\psi_i)^{\sigma_2}\rangle \right] U^{\sigma'''\sigma} \\ &= \sum_{\sigma''} \sum_{\sigma_1\,\sigma_2} \langle (\mathcal{T}\psi_i)^{\sigma_1} | \, K^{\sigma''\sigma''}_{\sigma_1\sigma_2}(\mathbf{r}) \, |(\mathcal{T}\Delta^\mu\psi_i)^{\sigma_2}\rangle\end{aligned} \tag{G.5}$$

for the charge density response. In particular, the bottom line follows from $\sum_\sigma U^{\sigma'''\sigma} \, U^{\dagger\,\sigma\sigma''} = \delta^{\sigma'''\sigma''}$ (U is a unitary matrix). For the induced magnetization density, instead we have:

$$\begin{aligned}\left(\frac{dm_\alpha(\mathbf{r})}{d\mu}\right)^{(2)} &= \sum_{\sigma\,\sigma'} \left(\frac{dn^{\sigma\sigma'}(\mathbf{r})}{d\mu}\right)^{(2)} \sigma_\alpha^{\sigma\sigma'} \\ &= \sum_{\sigma\,\sigma'} \sum_{\sigma''\,\sigma'''} U^{\dagger\,\sigma'\sigma''} \left[\langle (\mathcal{T}\psi_i)^{\sigma_1} | \, K^{\sigma''\sigma'''}_{\sigma_1\sigma_2}(\mathbf{r}) \, |(\mathcal{T}\Delta^\mu\psi_i)^{\sigma_2}\rangle \right] \sigma_\alpha^{\sigma\sigma'} \, U^{\sigma'''\sigma} \\ &= -\sum_{\sigma''\,\sigma'''} \left[\langle (\mathcal{T}\psi_i)^{\sigma_1} | \, K^{\sigma''\sigma'''}_{\sigma_1\sigma_2}(\mathbf{r}) \, |(\mathcal{T}\Delta^\mu\psi_i)^{\sigma_2}\rangle \right] \sigma_\alpha^{\sigma''\sigma'''},\end{aligned} \tag{G.6}$$

where in the last step we used the explicit expression of U ($U = i\,\sigma_y$), so that:

$$\begin{aligned}\sum_{\sigma\,\sigma'} U^{\sigma'''\sigma} \sigma_\alpha^{\sigma\sigma'} U^{\dagger\,\sigma'\sigma''} &= (-1)^\alpha \, \sigma_\alpha^{\sigma'''\sigma''} \\ &= (-1)^\alpha \, \sigma_\alpha^{*\,\sigma''\sigma'''} \\ &= -\sigma_\alpha^{\sigma''\sigma'''},\end{aligned} \tag{G.7}$$

where, in the first line we used the anti-commutation relation $\{\sigma_\alpha, \sigma_\beta\} = 2\,\delta_{\alpha\beta}\,\mathbb{1}$, in the second step we exploited the hermiticity of the Pauli matrices, and in the last step we made use of the property $\sigma_\alpha^{*\,\sigma''\sigma'''} = (-1)^{\alpha-1} \, \sigma_\alpha^{\sigma''\sigma'''}$.

APPENDIX H

DFPT IN THE NON-COLLINEAR MAGNETIC CASE: FORMULATION FOR PERIODIC SOLIDS

In this Appendix, we write the theory formulated in Chapter 3 in a more explicit way for periodic solids. From a practical point of view, we will write explicitly the KS potential V_{KS} (Eq. (1.164)), the kernel K (Eq. (1.162)), and the overlap matrix S (Eq. (1.168)), and we will exploit Bloch's theorem to introduce the periodic parts of the wave functions, wherever possible. The purpose is to write the equations presented in Chapter 3 in a way similar to how they are implemented in the code. In particular, we will generalize the main equations reported in Appendix A of Ref. [47].

H.1 Preliminary discussion

H.1.1 Effects of periodicity

As a preliminary information, we discuss the effects of periodicity on the responses to a phonon perturbation with wave vector $\mathbf{q}$. When computing the response of a quantity F having the same periodicity as the crystal, it is possible to write it as a lattice-periodic function modulated by a phase factor $e^{i\mathbf{q}\cdot\mathbf{r}}$. If F is a local function, this is done in a straightforward way. The response of F is defined as:

$$\frac{\partial F(\mathbf{r})}{\partial u_{s\alpha}(\mathbf{q})} = \sum_{\mu} e^{i\mathbf{q}\cdot\mathbf{R}_{\mu}} \frac{\partial F(\mathbf{r})}{\partial u_{\mu s\alpha}}. \tag{H.1}$$

We take its Fourier transform:

$$\frac{\partial F}{\partial u_{s\alpha}(\mathbf{q})}(\mathbf{k}) = \frac{1}{V}\int d^3r\, e^{-i\mathbf{k}\cdot\mathbf{r}} \sum_{\mu} e^{i\mathbf{q}\cdot\mathbf{R}_{\mu}} \frac{\partial F(\mathbf{r})}{\partial u_{\mu s\alpha}}. \tag{H.2}$$

The translational invariance of the solid implies that:

$$\frac{\partial F(\mathbf{r}-\mathbf{R}_\mu)}{\partial u_{0s\alpha}} = \frac{\partial F(\mathbf{r})}{\partial u_{\mu s\alpha}}, \tag{H.3}$$

which, inserted in the expression of the Fourier component (and after introducing $\mathbf{r}' = \mathbf{r} + \mathbf{R}_\mu$), gives:

$$\frac{\partial F}{\partial u_{s\alpha}(\mathbf{q})}(\mathbf{k}) = \frac{1}{V}\int d^3r' \, \frac{\partial F(\mathbf{r}')}{\partial u_{0s\alpha}} \, e^{-i\mathbf{k}\cdot\mathbf{r}'} \sum_\mu e^{i(\mathbf{q}-\mathbf{k})\cdot\mathbf{R}_\mu}, \tag{H.4}$$

that is non-vanishing only if $\mathbf{k} = \mathbf{q} + \mathbf{G}$. As a consequence:

$$\frac{\partial F(\mathbf{r})}{\partial u_{s\alpha}(\mathbf{q})} = e^{i\mathbf{q}\cdot\mathbf{r}} \sum_{\mathbf{G}} \frac{\partial F}{\partial u_{s\alpha}(\mathbf{q})}(\mathbf{q}+\mathbf{G}) \, e^{i\mathbf{G}\cdot\mathbf{r}}, \tag{H.5}$$

and the sum over $\mathbf{G}$ yields a lattice-periodic function, therefore we can write:

$$\frac{\partial F(\mathbf{r})}{\partial u_{s\alpha}(\mathbf{q})} = e^{i\mathbf{q}\cdot\mathbf{r}} \, \widetilde{\frac{\partial F(\mathbf{r})}{\partial u_{s\alpha}(\mathbf{q})}}, \tag{H.6}$$

where the tilde symbol $\sim$ identifies the periodic part of the function. As an example, the responses of the local and of the Hartree and exchange-correlation potentials become:

$$\frac{\partial V_{\mathrm{loc}}(\mathbf{r})}{\partial u_{s\alpha}(\mathbf{q})} = e^{i\mathbf{q}\cdot\mathbf{r}} \, \widetilde{\frac{\partial V_{\mathrm{loc}}(\mathbf{r})}{\partial u_{s\alpha}(\mathbf{q})}}, \tag{H.7}$$

$$\frac{\partial V_{\mathrm{H,xc}}(\mathbf{r})}{\partial u_{s\alpha}(\mathbf{q})} = e^{i\mathbf{q}\cdot\mathbf{r}} \, \widetilde{\frac{\partial V_{\mathrm{H,xc}}(\mathbf{r})}{\partial u_{s\alpha}(\mathbf{q})}}. \tag{H.8}$$

Instead, if F is a non-local quantity it contains the projectors $|\beta^I_m\rangle$ ($I = \{\rho, s''\}$) or their derivatives. In this case, we remark that quantities such as $\sum_\rho e^{i\mathbf{q}\cdot\mathbf{R}_\rho} |\beta^I_m\rangle$, $\sum_\rho e^{i\mathbf{q}\cdot\mathbf{R}_\rho} |\partial\beta^I_m/\partial u_{\mu s\alpha}\rangle$, and $\sum_\rho e^{i\mathbf{q}\cdot\mathbf{R}_\rho} |\partial^2\beta^I_m/\partial u_{\mu s\alpha}\partial u_{\nu s'\beta}\rangle$ can be treated as Bloch sums because $|\beta^I_m\rangle$ are localized and centered about the atom I. Then, using Bloch's theorem they can be written as the product of a phase factor $e^{i\mathbf{q}\cdot\mathbf{r}}$ and a lattice-periodic function. As an example, $\sum_\rho e^{i\mathbf{q}\cdot\mathbf{R}_\rho} |\beta^I_m\rangle$ becomes:

$$\sum_\rho e^{i\mathbf{q}\cdot\mathbf{R}_\rho} |\beta^I_m\rangle = e^{i\mathbf{q}\cdot\mathbf{r}} |\widetilde{\beta}^I_m\rangle \, . \tag{H.9}$$

The same argument holds also for the augmentation functions $Q^I_{mn}(\mathbf{r})$:

$$\sum_\rho e^{i\mathbf{q}\cdot\mathbf{R}_\rho} \, Q^I_{mn}(\mathbf{r}) = e^{i\mathbf{q}\cdot\mathbf{r}} \, \widetilde{Q}^{s''\mathbf{q}}_{mn}(\mathbf{r}). \tag{H.10}$$

By exploiting Bloch's theorem and the consequences of periodicity mentioned above, the wave function response can be written as the product of a phase factor and a lattice-periodic

function. In an insulator this is done in a straightforward way: indeed, Bloch's theorem and Eq. (H.6) imply that

$$\left|\frac{\partial\psi^{\sigma_1}_{\mathbf{k}v}}{\partial u_{s\alpha}(\mathbf{q})}\right\rangle = e^{i(\mathbf{k}+\mathbf{q})\cdot\mathbf{r}}\left|\widetilde{\frac{\partial u^{\sigma_1}_{\mathbf{k}v}}{\partial u_{s\alpha}(\mathbf{q})}}\right\rangle. \tag{H.11}$$

In a metal, the wave function response contains also non-local terms (see Eq. (3.27)): using Eqs. (H.9) and (H.10) we can write it in a way similar to the insulating case, i.e.:

$$|\Delta^{u_{s\alpha}(\mathbf{q})}\psi^{\sigma_1}_{\mathbf{k}v}\rangle = e^{i(\mathbf{k}+\mathbf{q})\cdot\mathbf{r}}\ |\widetilde{\Delta^{u_{s\alpha}(\mathbf{q})}u^{\sigma_1}_{\mathbf{k}v}}\rangle\,. \tag{H.12}$$

H.1.2 Remarks on scalar products

When addressing the non-local contributions in the induced densities, in the Sternheimer linear system, and in the dynamical matrix, we often deal with scalar products of the wave functions and of the projectors or their derivatives. Such scalar products can be manipulated and we can extract a phase factor. Following Ref. [47] we have:

$$\langle\beta^I_{m_1}|\psi^{\sigma_1}_{\mathbf{k}v}\rangle = e^{i\mathbf{k}\cdot\mathbf{R}_\rho}\,\beta^{s''m_1\sigma_1}_{\mathbf{k}v}, \tag{H.13}$$

$$\left\langle\frac{\partial\beta^I_{m_1}}{\partial u_{\mu s\alpha}}\middle|\psi^{\sigma_1}_{\mathbf{k}v}\right\rangle = e^{i\mathbf{k}\cdot\mathbf{R}_\rho}\,\alpha^{s''\alpha m_1\sigma_1}_{\mathbf{k}v}, \tag{H.14}$$

$$\left\langle\frac{\partial^2\beta^I_{m_1}}{\partial u_{\mu s\alpha}u_{\nu s'\beta}}\middle|\psi^{\sigma_1}_{\mathbf{k}v}\right\rangle = e^{i\mathbf{k}\cdot\mathbf{R}_\rho}\,\gamma^{s''\alpha\beta m_1\sigma_1}_{\mathbf{k}v}. \tag{H.15}$$

The scalar product of the projectors $|\beta^I_{m_1}\rangle$ with the wave function response can be manipulated in a similar way, namely:

$$\langle\beta^I_{m_1}|\Delta^{u_{s\alpha}(\mathbf{q})}\psi^{\sigma_1}_{\mathbf{k}v}\rangle = e^{i(\mathbf{k}+\mathbf{q})\cdot\mathbf{R}_\rho}\,\Delta^{u_{s\alpha}(\mathbf{q})}\beta^{s''m_1\sigma_1}_{\mathbf{k}v}. \tag{H.16}$$

H.2 Induced densities

Following the same order as in Chapter 3, we start from the induced spin density, Eq. (3.67), which may be further manipulated by writing explicitly $K^{\sigma\sigma'}_{\sigma_1\sigma_2}(\mathbf{r})$. Introducing the periodic parts of the Bloch functions and of the responses of the wave functions (Eq. (H.12)), we obtain the periodic part of the induced spin density:

$$\begin{aligned}\widetilde{\frac{dn^{\sigma\sigma'}(\mathbf{r})}{du_{s'\beta}(\mathbf{q})}} =& \sum_{\mathbf{k}v}\left[u^{*\,\sigma}_{\mathbf{k}v}(\mathbf{r})\,\widetilde{\Delta^{u_{s'\beta}(\mathbf{q})}}u^{\sigma'}_{\mathbf{k}v}(\mathbf{r}) + \sum_{\sigma_1\sigma_2}U^{\sigma'\sigma_1}\,(\mathcal{T}u_{-\mathbf{k}v}(\mathbf{r}))^{*\,\sigma_1}\,(\mathcal{T}\widetilde{\Delta^{u_{s'\beta}(-\mathbf{q})}}\,u_{-\mathbf{k}v}(\mathbf{r}))^{\sigma_2}\,U^{\dagger\,\sigma_2\sigma}\right]\\ &+\sum_{s''}\sum_{m\,n}\left(\widetilde{Q}^{s''\mathbf{q}}_{mn}(\mathbf{r})\,\Delta^{u_{s'\beta}(\mathbf{q})}\rho^{s''\sigma\sigma'}_{mn}\right) + \widetilde{\Delta^{u_{s'\beta}(\mathbf{q})}n^{\sigma\sigma'}}(\mathbf{r}),\end{aligned} \tag{H.17}$$

where we defined the quantity $\Delta^{u_{s'\beta}(\mathbf{q})}\rho^{s''\sigma\sigma'}_{mn}$ as:

$$\begin{aligned}\Delta^{u_{s'\beta}(\mathbf{q})}\rho^{s''\sigma\sigma'}_{mn} =& \sum_{m_1n_1}\sum_{\sigma_1\sigma_2}\sum_{\mathbf{k}v}\Big(\beta^{*\,s''m_1\sigma_1}_{\mathbf{k}v}\,f^{\sigma_1\sigma}_{m_1m}\,f^{\sigma'\sigma_2}_{nn_1}\,\Delta^{u_{s'\beta}(\mathbf{q})}\beta^{s''n_1\sigma_2}_{\mathbf{k}v}\\ &+\sum_{\sigma''\sigma'''}\beta^{*\,s''m_1\sigma_1}_{T-\mathbf{k}v}\,f^{\sigma_1\sigma''}_{m_1m}\,U^{\sigma''\sigma'}\,U^{\dagger\,\sigma\sigma'''}\,f^{\sigma'''\sigma_2}_{nn_1}\,\Delta^{u_{s'\beta}(-\mathbf{q})}\beta^{s''n_1\sigma_2}_{T-\mathbf{k}v}\Big),\end{aligned} \tag{H.18}$$

where we used the fact that (See Appendix D, Eq. (D.6)):

$$\sum_{\sigma_3\sigma_4} \mathcal{T}^{\sigma_1\sigma_3}\, K^{\sigma'\sigma}_{\sigma_3\sigma_4}\, \mathcal{T}^{\dagger\,\sigma_4\sigma_2} = \sum_{\sigma''\sigma'''} U^{\sigma'\sigma''}\, K^{\sigma''\sigma'''}_{\sigma_1\sigma_2}\, U^{\dagger\,\sigma'''\sigma}. \tag{H.19}$$

The periodic part of the induced charge and magnetization densities can be computed from the periodic part of the induced spin density (Eq. (H.17)) as:

$$\frac{\widetilde{dn}(\mathbf{r})}{du_{s'\beta}(\mathbf{q})} = \sum_{\sigma} \frac{\widetilde{dn^{\sigma\sigma}}(\mathbf{r})}{du_{s'\beta}(\mathbf{q})}, \tag{H.20}$$

$$\frac{\widetilde{dm}_\alpha(\mathbf{r})}{du_{s'\beta}(\mathbf{q})} = \mu_{\mathrm{B}} \sum_{\sigma\,\sigma'} \frac{\widetilde{dn^{\sigma\sigma'}}(\mathbf{r})}{du_{s'\beta}(\mathbf{q})} \sigma_\alpha^{\sigma\sigma'}. \tag{H.21}$$

H.3 Linear system

The periodic parts of the response of the wave functions, $|\widetilde{\Delta^{u_{s'\beta}(\mathbf{q})}} u^{\sigma_1}_{\mathbf{k}v}\rangle$ and $|(\mathcal{T}\widetilde{\Delta^{u_{s'\beta}(-\mathbf{q})}} u_{-\mathbf{k}v})^{\sigma_1}\rangle$, are the solutions of the Sternheimer linear systems reported in Eqs. (3.40) and (3.48), which can be written in an explicit form and in terms of lattice-periodic functions in the following way:

$$\begin{aligned}\sum_{\sigma_2} \left(H^{[\mathbf{B}]\sigma_1\sigma_2}_{\mathbf{k}+\mathbf{q}} + Q^{\sigma_1\sigma_2}_{\mathbf{k}+\mathbf{q}} - \epsilon_{\mathbf{k}v} S^{\sigma_1\sigma_2}_{\mathbf{k}+\mathbf{q}}\right) |\widetilde{\overline{\Delta}^{u_{s'\beta}(\mathbf{q})}} u^{\sigma_2}_{\mathbf{k}v}\rangle = -\sum_{\sigma_2} P^{\dagger\sigma_1\sigma_2,\mathbf{k}+\mathbf{q}}_{c,\mathbf{k}v} \Bigg[|\widetilde{\phi}^{u_{s'\beta}(\mathbf{q})[\mathbf{B}]\sigma_2}_{\mathbf{k}v}\rangle \\ + \sum_{\sigma_3} \frac{\widetilde{dV}^{[\mathbf{B}]\sigma_2\sigma_3}_{H,xc}}{du_{s'\beta}(\mathbf{q})} \Big| u^{\sigma_3}_{\mathbf{k}v} \Big\rangle + \sum_{\sigma_3}\sum_{s''}\sum_{m_1 n_1} {}^3I^{u_{s'\beta}(\mathbf{q})[\mathbf{B}]\sigma_2\sigma_3}_{s''m_1n_1}\, \beta^{s''n_1\sigma_3}_{\mathbf{k}v}\, |\widetilde{\beta}^{s''\,\mathbf{k}+\mathbf{q}}_{m_1}\rangle \Bigg],\end{aligned} \tag{H.22}$$

$$\begin{aligned}\sum_{\sigma_2} \left(H^{[-\mathbf{B}]\sigma_1\sigma_2}_{\mathbf{k}+\mathbf{q}} + Q^{\sigma_1\sigma_2}_{\mathbf{k}+\mathbf{q}} - \epsilon_{-\mathbf{k}v} S^{\sigma_1\sigma_2}_{\mathbf{k}+\mathbf{q}}\right) |(\mathcal{T}\widetilde{\overline{\Delta}^{u_{s'\beta}(-\mathbf{q})}} u_{-\mathbf{k}v})^{\sigma_2}\rangle = -\sum_{\sigma_2} \Pi^{\dagger\sigma_1\sigma_2,-\mathbf{k}-\mathbf{q}}_{c,-\mathbf{k}v} \Bigg[|\widetilde{\phi}^{u_{s'\beta}(\mathbf{q})[-\mathbf{B}]\sigma_2}_{T\,-\mathbf{k}v}\rangle \\ + \sum_{\sigma_3} \frac{\widetilde{dV}^{[-\mathbf{B}]\sigma_2\sigma_3}_{H,xc}}{du_{s'\beta}(\mathbf{q})} \Big| (\mathcal{T}u_{-\mathbf{k}v})^{\sigma_3} \Big\rangle + \sum_{\sigma_3}\sum_{s''}\sum_{m_1 n_1} {}^3I^{u_{s'\beta}(\mathbf{q})[-\mathbf{B}]\sigma_2\sigma_3}_{s''m_1n_1}\, \beta^{s''n_1\sigma_3}_{T\,-\mathbf{k}v}\, |\widetilde{\beta}^{s''\,\mathbf{k}+\mathbf{q}}_{m_1}\rangle \Bigg],\end{aligned} \tag{H.23}$$

where $H^{[\mathbf{B}]\sigma_1\sigma_2}_{\mathbf{k}+\mathbf{q}}$, $S^{\sigma_1\sigma_2}_{\mathbf{k}+\mathbf{q}}$, and $Q^{\sigma_1\sigma_2}_{\mathbf{k}+\mathbf{q}}$ are defined as:

$$H^{[\mathbf{B}]\sigma_1\sigma_2}_{\mathbf{k}+\mathbf{q}} = e^{-i(\mathbf{k}+\mathbf{q})\cdot\mathbf{r}}\, H^{[\mathbf{B}]\sigma_1\sigma_2}\, e^{i(\mathbf{k}+\mathbf{q})\cdot\mathbf{r}}, \tag{H.24}$$

$$S^{\sigma_1\sigma_2}_{\mathbf{k}+\mathbf{q}} = e^{-i(\mathbf{k}+\mathbf{q})\cdot\mathbf{r}}\, S^{\sigma_1\sigma_2}\, e^{i(\mathbf{k}+\mathbf{q})\cdot\mathbf{r}}, \tag{H.25}$$

$$Q^{\sigma_1\sigma_2}_{\mathbf{k}+\mathbf{q}} = e^{-i(\mathbf{k}+\mathbf{q})\cdot\mathbf{r}}\, Q^{\sigma_1\sigma_2}\, e^{i(\mathbf{k}+\mathbf{q})\cdot\mathbf{r}}. \tag{H.26}$$

${}^3I^{u_{s'\beta}(\mathbf{q})[\mathbf{B}]\sigma_2\sigma_3}_{s''m_1n_1}$ in the right-hand side of the linear systems is obtained by generalizing to the non-collinear FR formulation the integral of the self-consistent part of the response of the KS potential with the augmentation functions (${}^3I^{u_{s'\beta}(\mathbf{q})[\mathbf{B}]}_{s''mn\alpha}$ in Ref. [47]), namely:

$${}^3I^{u_{s'\beta}(\mathbf{q})[\mathbf{B}]\sigma_2\sigma_3}_{s''m_1n_1} = \sum_{mn}\sum_{\sigma_4\sigma_5}\sum_{\eta} f^{\sigma_2\sigma_4}_{m_1m}\, A^{\sigma_4\sigma_5}_{\eta}\, {}^3I^{u_{s'\beta}(\mathbf{q})[\mathbf{B}]}_{s''mn\eta}\, f^{\sigma_5\sigma_3}_{nn_1}, \tag{H.27}$$

with

$$ {}^3I^{u_{s'\beta}(\mathbf{q})[\mathbf{B}]}_{s''mn\eta} = \int d^3r\, Q^{s''}_{mn}(\mathbf{r})\, \frac{dC^{[\mathbf{B}]}_\eta(\mathbf{r})}{du_{s'\beta}(\mathbf{q})}, \tag{H.28} $$

where $\mathbf{C}^{[\mathbf{B}]} = (V_{\mathrm{H,xc}}, -\mu_\mathrm{B} B_{\mathrm{xc},x}, -\mu_\mathrm{B} B_{\mathrm{xc},y}, -\mu_\mathrm{B} B_{\mathrm{xc},z})$. Moreover, in the right-hand side of the linear systems we introduced the periodic part of the vector $|\phi^{u_{s'\beta}(\mathbf{q})[\mathbf{B}]\sigma_1}_{\mathbf{k}v}\rangle$, which contains the non-self-consistent contribution of the perturbation of the KS potential. It reads:

$$ \begin{aligned} |\widetilde{\phi}^{u_{s'\beta}(\mathbf{q})[\mathbf{B}]\sigma_1}_{\mathbf{k}v}\rangle = &\sum_{\sigma_2}\sum_{m_1\, n_1}\Bigg[\left(\widetilde{D}^{I\,\sigma_1\sigma_2}_{m_1 n_1} - \epsilon_{\mathbf{k}v}\, q^{\gamma(I)\,\sigma_1\sigma_2}_{m_1 n_1}\right)\left(\beta^{s' n_1\sigma_2}_{\mathbf{k}v}\left|\widetilde{\frac{\partial \beta^{s'\,\mathbf{k}+\mathbf{q}}_{m_1}}{\partial u_{\nu s'\beta}}}\right\rangle + \alpha^{s'\beta n_1\sigma_2}_{\mathbf{k}v}\,|\widetilde{\beta}^{s'\,\mathbf{k}+\mathbf{q}}_{m_1}\rangle\right) \\ &+ \left({}^1I^{u_{\nu s'\beta}[\mathbf{B}]\sigma_1\sigma_2}_{m_1 n_1} + {}^2I^{u_{\nu s'\beta}\,\sigma_1\sigma_2}_{m_1 n_1}\right)\beta^{s' n_1\sigma_2}_{\mathbf{k}v}\,|\widetilde{\beta}^{s'\,\mathbf{k}+\mathbf{q}}_{m_1}\rangle\Bigg] + \widetilde{\frac{\partial V_\mathrm{loc}}{\partial u_{s'\beta}(\mathbf{q})}}\left|u^{\sigma_1}_{\mathbf{k}v}\right\rangle, \end{aligned} \tag{H.29} $$

where the integrals ${}^1I^{u_{\nu s'\beta}[\mathbf{B}]\sigma_1\sigma_2}_{m_1 n_1}$ and ${}^2I^{u_{\nu s'\beta}}_{m_1 n_1}$ are properly generalized to the non-collinear FR case. In particular:

$$ {}^1I^{u_{\nu s'\beta}[\mathbf{B}]\sigma_1\sigma_2}_{m_1 n_1} = \sum_{m\, n}\sum_{\sigma_3\,\sigma_4}\sum_{\eta} f^{\sigma_1\sigma_3}_{m_1 m}\, A^{\sigma_3\sigma_4}_\eta\, {}^1I^{u_{\nu s'\beta}[\mathbf{B}]}_{mn\eta}\, f^{\sigma_4\sigma_2}_{n n_1}, \tag{H.30} $$

with

$$ {}^1I^{u_{\nu s'\beta}[\mathbf{B}]}_{mn\eta} = \int d^3r\, C'^{[\mathbf{B}]}_\eta\, \frac{\partial Q^I_{mn}(\mathbf{r})}{\partial u_{\nu s'\beta}}, \tag{H.31} $$

where $\mathbf{A}$ and $\mathbf{C}'$ are four-component vectors defined in Section 1.9.2. Similarly:

$$ {}^2I^{u_{\nu s'\beta}\,\sigma_1\sigma_2}_{m_1 n_1} = \sum_{m\, n}\sum_{\sigma_3} f^{\sigma_1\sigma_3}_{m_1 m}\, {}^2I^{u_{\nu s'\beta}}_{mn}\, f^{\sigma_3\sigma_2}_{n n_1}, \tag{H.32} $$

with [47]

$$ {}^2I^{u_{\nu s'\beta}}_{m_1 n_1} = \int d^3r\, \frac{\partial V_\mathrm{loc}(\mathbf{r})}{\partial u_{\nu s'\beta}}\, Q^I_{mn}(\mathbf{r}). \tag{H.33} $$

The periodic part of $|\phi^{u_{s'\beta}(\mathbf{q})[-\mathbf{B}]\sigma_1}_{T-\mathbf{k}v}\rangle$ is defined in a similar way. Starting from Eq. (3.49), its explicit expression is:

$$ \begin{aligned} |\widetilde{\phi}^{u_{s'\beta}(\mathbf{q})[-\mathbf{B}]\sigma_1}_{T-\mathbf{k}v}\rangle = &\sum_{\sigma_2}\sum_{m_1\, n_1}\Bigg[\left(\widetilde{D}^{I\,\sigma_1\sigma_2}_{m_1 n_1} - \epsilon_{\mathbf{k}v}\, q^{\gamma(I)\,\sigma_1\sigma_2}_{m_1 n_1}\right)\left(\beta^{s n_1\sigma_2}_{T-\mathbf{k}v}\left|\widetilde{\frac{\partial \beta^{s\,\mathbf{k}+\mathbf{q}}_{m_1}}{\partial u_{\nu s'\beta}}}\right\rangle + \alpha^{s'\beta n_1\sigma_2}_{T-\mathbf{k}v}\,|\widetilde{\beta}^{s'\,\mathbf{k}+\mathbf{q}}_{m_1}\rangle\right) \\ &+ \left({}^1I^{u_{\nu s'\beta}[-\mathbf{B}]\sigma_1\sigma_2}_{m_1 n_1} + {}^2I^{u_{\nu s'\beta}\,\sigma_1\sigma_2}_{m_1 n_1}\right)\beta^{s n_1\sigma_2}_{T-\mathbf{k}v}\,|\widetilde{\beta}^{s'\,\mathbf{k}+\mathbf{q}}_{m_1}\rangle\Bigg] + \widetilde{\frac{\partial V_\mathrm{loc}}{\partial u_{s'\beta}(\mathbf{q})}}\left|(\mathcal{T}\, u_{-\mathbf{k}v})^{\sigma_1}\right\rangle, \end{aligned} \tag{H.34} $$

where the coefficients $\beta^{s' n_1\sigma_2}_{T-\mathbf{k}v}$ and $\alpha^{s'\beta n_1\sigma_2}_{T-\mathbf{k}v}$ are defined in a similar way to Eqs. (H.13) and (H.14), but they contain the time-reversed wave functions at wave vector $-\mathbf{k}$:

$$ \langle \beta^I_{m_1}|(\mathcal{T}\psi_{-\mathbf{k}v})^{\sigma_1}\rangle = e^{i\mathbf{k}\cdot\mathbf{R}_\rho}\, \beta^{s'' m_1\sigma_1}_{T-\mathbf{k}v}, \tag{H.35} $$

$$ \left\langle \frac{\partial \beta^I_{m_1}}{\partial u_{\nu s'\beta}}\right|(\mathcal{T}\psi_{-\mathbf{k}v})^{\sigma_1}\Big\rangle = e^{i\mathbf{k}\cdot\mathbf{R}_\rho}\, \alpha^{s''\beta m_1\sigma_1}_{T-\mathbf{k}v}. \tag{H.36} $$

H.4 Dynamical matrix

Considering the dynamical matrix, defined in Eq. (3.5), the contribution coming from $d^2E^{(2)}_{\rm tot}/d\mu d\lambda$ is split into three parts. The first one stems from the expectation value of the mixed derivatives of the electron-ion potential. In the NC case, this term is diagonal in the atomic indices s, s'. In the US scheme there is a similar term:

$$\begin{aligned}
\Phi^{(1a)}_{\substack{s\alpha\\ s'\beta}}(\mathbf{q}) &= \frac{1}{N}\sum_{\mu}\delta_{ss'}\Bigg\{\sum_{\mathbf{k}v}\tilde{\theta}_{F,\mathbf{k}v}\sum_{I}\sum_{m_1\,n_1}\sum_{\sigma_1\sigma_2}\Bigg[\left(\widetilde{D}^{I\,\sigma_1\sigma_2}_{m_1n_1}-\epsilon_{\mathbf{k}v}\,q^{\gamma(I)\,\sigma_1\sigma_2}_{m_1n_1}\right)\\
&\quad\times\left\langle\psi^{\sigma_1}_{\mathbf{k}v}\middle|\frac{\partial^2}{\partial u_{\mu s\alpha}\partial u_{\mu s\beta}}\left(|\beta^I_{m_1}\rangle\,\langle\beta^I_{n_1}|\right)\middle|\psi^{\sigma_2}_{\mathbf{k}v}\right\rangle\Bigg]+\int d^3r\,\frac{\partial^2 V_{\rm loc}(\mathbf{r})}{\partial u_{\mu s\alpha}\partial u_{\mu s\beta}}\,n(\mathbf{r})\Bigg\}\\
&= \frac{1}{N}\sum_{\mu}\delta_{ss'}\Bigg\{\sum_{\mathbf{k}v}\tilde{\theta}_{F,\mathbf{k}v}\sum_{m_1\,n_1}\sum_{\sigma_1\sigma_2}\Bigg[\left(\widetilde{D}^{s\,\sigma_1\sigma_2}_{m_1n_1}-\epsilon_{\mathbf{k}v}\,q^{\gamma(s)\,\sigma_1\sigma_2}_{m_1n_1}\right)\\
&\quad\times\left(\gamma^{*\,s\alpha\beta m_1\sigma_1}_{\mathbf{k}v}\,\beta^{sn_1\sigma_2}_{\mathbf{k}v}+\beta^{*\,sm_1\sigma_1}_{\mathbf{k}v}\,\gamma^{s\alpha\beta n_1\sigma_2}_{\mathbf{k}v}+2\,\alpha^{*\,s\alpha m_1\sigma_1}_{\mathbf{k}v}\,\alpha^{s\beta n_1\sigma_2}_{\mathbf{k}v}\right)\Bigg]\\
&\quad+\int d^3r\,\frac{\partial^2 V_{\rm loc}(\mathbf{r})}{\partial u_{\mu s\alpha}\partial u_{\mu s\beta}}\,n(\mathbf{r})\Bigg\}.
\end{aligned}\tag{H.37}$$

In the US formulation there is also a second term diagonal in s and s', that contains integrals of the effective potential (and, similarly, of the exchange-correlation magnetic field) with the derivatives of the augmentation functions:

$$\begin{aligned}
\Phi^{(1b)}_{\substack{s\alpha\\ s'\beta}}(\mathbf{q}) &= \frac{1}{N}\sum_{\mu}\delta_{ss'}\Bigg\{\sum_{\mathbf{k}v}\tilde{\theta}_{F,\mathbf{k}v}\sum_{I}\sum_{m_1\,n_1}\sum_{\sigma_1\,\sigma_2}\delta_{I,(\mu,s)}\,{}^4I^{u_{\mu s\alpha}\beta\,\sigma_1\sigma_2}_{m_1n_1}\,\langle\psi^{\sigma_1}_{\mathbf{k}v}|\beta^I_{m_1}\rangle\,\langle\beta^I_{n_1}|\psi^{\sigma_2}_{\mathbf{k}v}\rangle\\
&\quad+\sum_{\mathbf{k}v}\tilde{\theta}_{F,\mathbf{k}v}\sum_{I}\sum_{m_1\,n_1}\sum_{\sigma_1\,\sigma_2}\left[{}^1I^{u_{\mu s\alpha}\,\sigma_1\sigma_2}_{m_1n_1}\left\langle\psi^{\sigma_1}_{\mathbf{k}v}\middle|\frac{\partial}{\partial u_{\mu s\beta}}\left(|\beta^I_{m_1}\rangle\,\langle\beta^I_{n_1}|\right)\middle|\psi^{\sigma_2}_{\mathbf{k}v}\right\rangle+(\alpha\leftrightarrow\beta)\right]\Bigg\}\\
&= \frac{1}{N}\sum_{\mu}\delta_{ss'}\Bigg\{\sum_{\mathbf{k}v}\tilde{\theta}_{F,\mathbf{k}v}\sum_{m_1\,n_1}\sum_{\sigma_1\,\sigma_2}{}^4I^{u_{\mu s\alpha}\beta\,\sigma_1\sigma_2}_{m_1n_1}\,\beta^{*\,sm_1\sigma_1}_{\mathbf{k}v}\,\beta^{sn_1\sigma_2}_{\mathbf{k}v}\\
&\quad+\sum_{\mathbf{k}v}\tilde{\theta}_{F,\mathbf{k}v}\sum_{m_1\,n_1}\sum_{\sigma_1\,\sigma_2}\left[{}^1I^{u_{\mu s\alpha}\,\sigma_1\sigma_2}_{m_1n_1}(\alpha^{*\,s\alpha m_1\sigma_1}_{\mathbf{k}v}\,\beta^{sn_1\sigma_2}_{\mathbf{k}v}+\beta^{*\,sm_1\sigma_1}_{\mathbf{k}v}\,\alpha^{s\alpha m_1\sigma_1\,*}_{\mathbf{k}v})+(\alpha\leftrightarrow\beta)\right]\Bigg\},
\end{aligned}\tag{H.38}$$

where $(\alpha\leftrightarrow\beta)$ is a short-hand notation that indicates the presence of a similar term obtained by exchanging the indices α and β. The integral ${}^4I^{u_{\mu s\alpha}\beta[\mathbf{B}]\sigma_1\sigma_2}_{m_1n_1}$ is properly generalized to the non-collinear FR case, namely:

$${}^4I^{u_{\mu s\alpha}\beta[\mathbf{B}]\sigma_1\sigma_2}_{m_1n_1}=\sum_{m\,n}\sum_{\sigma_3\,\sigma_4}\sum_{\eta}f^{\sigma_1\sigma_3}_{m_1m}\,A^{\sigma_3\sigma_4}_{\eta}\,{}^4I^{u_{\mu s\alpha}\beta[\mathbf{B}]}_{mn\,\eta}\,f^{\sigma_4\sigma_2}_{nn_1},\tag{H.39}$$

with

$$ {}^4I_{mn\,\eta}^{u_{\mu s\alpha}\beta[\mathbf{B}]} = \int d^3r\, C_\eta'^{[\mathbf{B}]}\, \frac{\partial^2 Q_{mn}^I(\mathbf{r})}{\partial u_{\mu s\alpha}\partial u_{\mu s\beta}}, \tag{H.40} $$

Finally, in the US case the contribution of $d^2E_{\mathrm{tot}}^{(1)}/d\mu d\lambda$ to the dynamical matrix shows also a third term, non-vanishing on the non-diagonal elements as well, which contains integrals of the derivative of the local potential with the augmentation function and its derivative:

$$ \begin{aligned} \Phi_{\substack{s\alpha\\ s'\beta}}^{(1c)}(\mathbf{q}) = \frac{1}{N}\sum_{\mu\,\nu} e^{-i\mathbf{q}\cdot\mathbf{R}_\mu} \Bigg\{ \sum_{\mathbf{k}v} \tilde{\theta}_{F,\mathbf{k}v} \sum_I \sum_{m_1\,n_1} \sum_{\sigma_1\,\sigma_2} \Bigg[\delta_{I,(\mu,s)}\, {}^5I_{m_1n_1}^{u_{\mu s\alpha}u_{\nu s'\beta}\,\sigma_1\sigma_2} \langle\psi_{\mathbf{k}v}^{\sigma_1}|\beta_{m_1}^I\rangle \langle\beta_{n_1}^I|\psi_{\mathbf{k}v}^{\sigma_2}\rangle \\ + {}^2I_{m_1n_1}^{u_{\mu s\alpha}\,\sigma_1\sigma_2} \left\langle \psi_{\mathbf{k}v}^{\sigma_1} \middle| \frac{\partial}{\partial u_{\nu s'\beta}} \left(|\beta_{m_1}^I\rangle \langle\beta_{n_1}^I| \right) \middle| \psi_{\mathbf{k}v}^{\sigma_2} \right\rangle + (u_{\mu s\alpha} \leftrightarrow u_{\nu s'\beta}) \Bigg] \Bigg\} e^{i\mathbf{q}\cdot\mathbf{R}_\nu} \\ = \frac{1}{N}\sum_{\mu\,\nu} e^{-i\mathbf{q}\cdot\mathbf{R}_\mu} \Bigg\{ \sum_{\mathbf{k}v} \tilde{\theta}_{F,\mathbf{k}v} \sum_{m_1\,n_1} \sum_{\sigma_1\,\sigma_2} \Bigg[{}^5I_{m_1n_1}^{u_{\mu s\alpha}u_{\nu s'\beta}\,\sigma_1\sigma_2} \beta_{\mathbf{k}v}^{*\,sm_1\sigma_1}\, \beta_{\mathbf{k}v}^{sn_1\sigma_2} \\ + {}^2I_{m_1n_1}^{u_{\mu s\alpha}\,\sigma_1\sigma_2} (\alpha_{\mathbf{k}v}^{*\,s\alpha m_1\sigma_1}\, \beta_{\mathbf{k}v}^{sn_1\sigma_2} + \beta_{\mathbf{k}v}^{*\,sm_1\sigma_1}\, \alpha_{\mathbf{k}v}^{s\alpha m_1\sigma_1}) + (u_{\mu s\alpha} \leftrightarrow u_{\nu s'\beta}) \Bigg] \Bigg\} e^{i\mathbf{q}\cdot\mathbf{R}_\nu}, \end{aligned} \tag{H.41} $$

where

$$ {}^5I_{m_1n_1}^{u_{\mu s\alpha}u_{\nu s'\beta}\,\sigma_1\sigma_2} = \sum_{m\,n}\sum_{\sigma_3} f_{m_1m}^{\sigma_1\sigma_3}\, {}^5I_{mn}^{u_{\mu s\alpha}u_{\nu s'\beta}}\, f_{nn_1}^{\sigma_3\sigma_2}, \tag{H.42} $$

has been obtained by transforming with the matrices of f coefficients the integral ${}^5I_{mn}^{u_{\mu s\alpha}u_{\nu s'\beta}}$ defined in Ref. [47]:

$$ {}^5I_{mn}^{u_{\mu s\alpha}u_{\nu s'\beta}} = \int d^3r\, \frac{\partial V_{\mathrm{loc}}(\mathbf{r})}{\partial u_{\mu s\alpha}}\, \frac{Q_{mn}^I(\mathbf{r})}{\partial u_{\nu s'\beta}}, \tag{H.43} $$

The other parts of the dynamical matrix are found using the definitions introduced above. The second term, coming from $d^2E_{\mathrm{tot}}^{(1)}/d\mu d\lambda$, reads:

$$ \Phi_{\substack{s\alpha\\ s'\beta}}^{(2)}(\mathbf{q}) = \frac{1}{N}\sum_{\mathbf{k}v}\sum_{\sigma_1} \left[\langle \widetilde{\phi}_{\mathbf{k}v}^{u_{s\alpha}(\mathbf{q})[\mathbf{B}]\sigma_1} | \widetilde{\Delta^{u_{s'\beta}(\mathbf{q})} u_{\mathbf{k}v}^{\sigma_1}} \rangle + \langle \widetilde{\phi}_{T\,-\mathbf{k}v}^{u_{s\alpha}(\mathbf{q})[-\mathbf{B}]\sigma_1} | \widetilde{(\mathcal{T}\Delta^{u_{s'\beta}(-\mathbf{q})} u_{-\mathbf{k}v})^{\sigma_1}} \rangle \right]. \tag{H.44} $$

Finally, the third and the fourth term of $\Phi_{s\alpha s'\beta}(\mathbf{q})$, which come from the interaction of the moving augmentation charge with the variation of $V_{\mathrm{H,xc}}^{[\mathbf{B}]\sigma_1\sigma_2}$ and from the change in the orthonormalization constraints, respectively, read:

$$ \Phi_{\substack{s\alpha\\ s'\beta}}^{(3)}(\mathbf{q}) = \sum_{\sigma_1\,\sigma_2} \int d^3r\, \frac{\widetilde{dV}_{H,xc}^{[\mathbf{B}]\sigma_1\sigma_2}(\mathbf{r})}{du_{s\alpha}(\mathbf{q})}\, \widetilde{\Delta^{u_{s'\beta}(\mathbf{q})}} n^{\sigma_1\sigma_2}(\mathbf{r}), \tag{H.45} $$

$$\Phi^{(4)}_{\substack{s\alpha\\ s'\beta}}(\mathbf{q}) = -\frac{1}{N}\sum_{\nu}\Bigg\{\sum_{\mathbf{k}v}\sum_{\mathbf{k}'v'}\Big(\tilde{\theta}_{F,\mathbf{k}v}\,\theta_{\mathbf{k}v,\mathbf{k}'v'} + \tilde{\theta}_{F,\mathbf{k}'v'}\,\theta_{\mathbf{k}'v',\mathbf{k}v}\Big)\sum_{I}\sum_{m_1\,n_1}\sum_{\sigma_2\,\sigma_3} q^{\gamma(I)\,\sigma_2\sigma_3}_{m_1 n_1}$$
$$\times\Big\langle \psi^{\sigma_2}_{\mathbf{k}'v'}\Big|\frac{\partial}{\partial u_{\nu s'\beta}}\left(|\beta^I_{m_1}\rangle\,\langle\beta^I_{n_1}|\right)\Big|\psi^{\sigma_3}_{\mathbf{k}v}\Big\rangle\sum_{\sigma_1}\langle\psi^{\sigma_1}_{\mathbf{k}'v'}|\phi^{u_{s\alpha}(\mathbf{q})[\mathbf{B}]\sigma_1}_{\mathbf{k}v}\rangle\Bigg\}e^{i\mathbf{q}\cdot\mathbf{R}_\nu}. \tag{H.46}$$
$$= -\frac{1}{N}\sum_{\nu}\Bigg\{\sum_{\mathbf{k}}\sum_{vv'}\Big(\tilde{\theta}_{F,\mathbf{k}v}\,\theta_{\mathbf{k}v,\mathbf{k}+\mathbf{q}v'} + \tilde{\theta}_{F,\mathbf{k}+\mathbf{q}v'}\,\theta_{\mathbf{k}+\mathbf{q}v',\mathbf{k}v}\Big)\sum_{m_1\,n_1}\sum_{\sigma_2\,\sigma_3} q^{\gamma(s')\,\sigma_2\sigma_3}_{m_1 n_1}$$
$$\times\Big(\alpha^{*\,s'\beta m_1\sigma_2}_{\mathbf{k}+\mathbf{q}v'}\,\beta^{s'n_1\sigma_3}_{\mathbf{k}v} + \beta^{*\,s'm_1\sigma_2}_{\mathbf{k}+\mathbf{q}v'}\,\alpha^{s'\beta n_1\sigma_3}_{\mathbf{k}v}\Big)\sum_{\sigma_1}\langle u^{\sigma_1}_{\mathbf{k}+\mathbf{q}v'}|\widetilde{\phi}^{u_{s\alpha}(\mathbf{q})[\mathbf{B}]\sigma_1}_{\mathbf{k}v}\rangle\Bigg\}e^{i\mathbf{q}\cdot\mathbf{R}_\nu}.$$

APPENDIX I

SYMMETRIZATION: INDUCED CHARGE AND MAGNETIZATION DENSITIES, AND DYNAMICAL MATRIX

In this Appendix we present a complete derivation of Eqs. (3.83) and (3.84), which allow to symmetrize the periodic parts of the induced charge density and magnetization density, and the dynamical matrix.

I.1 Induced charge density and magnetization density

We consider the symmetry operations $\{\mathcal{S}|\mathbf{f}\}$ and $\{\mathcal{T}\mathcal{S}|\mathbf{f}\}$ of the antiunitary space group of the crystal. Since

$$\begin{aligned}\{\mathcal{S}|\mathbf{f}\}(\mathbf{R}_\nu + \mathbf{d}_{s'}) &= \mathcal{S}\mathbf{R}_\nu + \mathcal{S}\mathbf{d}_{s'} + \mathbf{f} \\ &= \mathbf{R}_{\bar{\nu}} + \mathbf{d}_{\bar{s}'},\end{aligned} \tag{I.1}$$

the application of the operation $\mathcal{S}$ to the atomic displacement $u_{\nu s'\beta}$ gives:

$$u_{\bar{\nu}\bar{s}'\gamma} = \sum_\alpha S_{\gamma\beta}\, u_{\nu s'\beta}. \tag{I.2}$$

In order to compute the symmetrized induced charge density, we take the derivative of Eq. (1.82) with respect to $u_{\nu s'\beta}$ and, moreover, we apply the chain rule on the right-hand side:

$$\begin{aligned}\frac{dn(\mathbf{r})}{du_{\nu s'\beta}} &= \frac{1}{N_S}\sum_{\{\mathcal{S}|\mathbf{f}\}}\sum_\gamma \frac{dn^{\mathrm{NS}}(\{\mathcal{S}|\mathbf{f}\}\mathbf{r})}{du_{\bar{\nu}\bar{s}'\gamma}}\,\frac{du_{\bar{\nu}\bar{s}'\gamma}}{du_{\nu s'\beta}} \\ &= \frac{1}{N_S}\sum_{\{\mathcal{S}|\mathbf{f}\}}\sum_\gamma \frac{dn^{\mathrm{NS}}(\mathbf{r})}{du_{\bar{\nu}\bar{s}'\gamma}}\,S_{\gamma\beta},\end{aligned} \tag{I.3}$$

where the second line follows from Eq. (I.2). At a second stage, we switch to the response to a phonon perturbation: in Eq. (I.3) we multiply both sides by the phase factor $e^{i\mathbf{q}\cdot\mathbf{R}_\nu}$ and we sum over ν. Moreover, in the right-hand side we insert the phase factors $e^{i\mathcal{S}\mathbf{q}\cdot\mathbf{R}_{\bar{\nu}}}$ and $e^{-i\mathcal{S}\mathbf{q}\cdot\mathbf{R}_{\bar{\nu}}}$ [1] and we sum over $\bar{\nu}$:

$$\frac{dn(\mathbf{r})}{du_{s'\beta}(\mathbf{q})} = \frac{1}{N}\sum_{\nu\,\bar{\nu}}\frac{1}{N_S}\sum_{\{\mathcal{S}|\mathbf{f}\}}\sum_{\gamma} S_{\gamma\beta}\,\frac{dn^{\mathrm{NS}}(\{\mathcal{S}|\mathbf{f}\}\mathbf{r})}{du_{\bar{\nu}\bar{s}'\gamma}}\,e^{i\mathcal{S}\mathbf{q}\cdot\mathbf{R}_{\bar{\nu}}}\,e^{i\mathbf{q}\cdot(\mathbf{R}_\nu-\mathcal{S}^{-1}\mathbf{R}_{\bar{\nu}})}. \tag{I.4}$$

We remark that from Eq. (I.1) it follows that:

$$\mathbf{R}_\nu - \mathcal{S}^{-1}\mathbf{R}_{\bar{\nu}} = \mathcal{S}^{-1}\mathbf{d}_{\bar{s}'} - \mathcal{S}^{-1}\mathbf{f} - \mathbf{d}_{s'}, \tag{I.5}$$

hence the phase factors in the right-hand side of Eq. (I.4) do not depend on ν. As a consequence, the sum over ν cancels the factor $1/N$, while the sum over $\bar{\nu}$ leads to the response of the non-symmetrized charge density to a phonon perturbation with wave vector $\mathcal{S}\mathbf{q}$. By introducing the vector $\mathbf{R}^{\mathcal{S}}_{s'} = \mathcal{S}\mathbf{d}_{s'} - \mathbf{d}_{\bar{s}'}$, Eq. (I.4) becomes:

$$\frac{dn(\mathbf{r})}{du_{s'\beta}(\mathbf{q})} = \frac{1}{N_S}\sum_{\{\mathcal{S}|\mathbf{f}\}}\sum_{\gamma} S_{\gamma\beta}\,\frac{dn^{\mathrm{NS}}(\{\mathcal{S}|\mathbf{f}\}\mathbf{r})}{du_{\bar{s}'\beta}(\mathcal{S}\mathbf{q})}\,e^{-i\mathcal{S}\mathbf{q}\cdot(\mathbf{R}^{\mathcal{S}}_{s'}+\mathbf{f})}. \tag{I.6}$$

Finally, we pass to the periodic parts. In particular, $dn^{\mathrm{NS}}(\{\mathcal{S}|\mathbf{f}\}\mathbf{r})/du_{\bar{s}'\gamma}(\mathcal{S}\mathbf{q})$ can be written as:

$$\frac{dn^{\mathrm{NS}}(\{\mathcal{S}|\mathbf{f}\}\mathbf{r})}{du_{\bar{s}'\gamma}(\mathcal{S}\mathbf{q})} = e^{i\mathcal{S}\mathbf{q}\cdot(\mathcal{S}\mathbf{r}+\mathbf{f})}\,\frac{\widetilde{dn}^{\mathrm{NS}}(\{\mathcal{S}|\mathbf{f}\}\mathbf{r})}{du_{\bar{s}'\gamma}(\mathcal{S}\mathbf{q})}, \tag{I.7}$$

therefore Eq. (I.6) becomes:

$$\frac{\widetilde{dn}(\mathbf{r})}{du_{s'\beta}(\mathbf{q})} = \frac{1}{N_S}\sum_{\{\mathcal{S}|\mathbf{f}\}}\sum_{\gamma} S_{\gamma\beta}\,\frac{\widetilde{dn}^{\mathrm{NS}}(\{\mathcal{S}|\mathbf{f}\}\mathbf{r})}{du_{\bar{s}'\beta}(\mathcal{S}\mathbf{q})}\,e^{-i\mathcal{S}\mathbf{q}\cdot\mathbf{R}^{\mathcal{S}}_{s'}}. \tag{I.8}$$

As explained in Section 3.4, here we consider only the symmetry operations $\{\mathcal{S}|\mathbf{f}\}$ such that:

$$\mathcal{S}\mathbf{q} = \mathbf{q} + \mathbf{G}_{\mathcal{S}}, \tag{I.9}$$

if $\{\mathcal{S}|\mathbf{f}\}$ is a symmetry of the crystal, or:

$$\mathcal{S}\mathbf{q} = -\mathbf{q} + \mathbf{G}_{\mathcal{S}}, \tag{I.10}$$

if $\{\mathcal{T}\mathcal{S}|\mathbf{f}\}$ is a symmetry of the crystal, and we introduce the variable $\tau(\mathcal{S})$ to distinguish the two cases. Since $\mathbf{q}+\mathbf{G}_{\mathcal{S}}$ ($-\mathbf{q}+\mathbf{G}_{\mathcal{S}}$) is equivalent to $\mathbf{q}$ ($-\mathbf{q}$), the non-symmetrized induced charge density appearing in the right-hand side of Eq. (I.6) becomes:

$$\begin{aligned}\frac{dn^{\mathrm{NS}}(\{\mathcal{S}|\mathbf{f}\}\mathbf{r})}{du_{\bar{s}'\gamma}(\mathcal{S}\mathbf{q})} &= \frac{dn^{\mathrm{NS}}(\{\mathcal{S}|\mathbf{f}\}\mathbf{r})}{du_{\bar{s}'\gamma}(\pm\mathbf{q}+\mathbf{G}_{\mathcal{S}})} \\ &= \frac{dn^{\mathrm{NS}}(\{\mathcal{S}|\mathbf{f}\}\mathbf{r})}{du_{\bar{s}'\gamma}(\pm\mathbf{q})},\end{aligned} \tag{I.11}$$

[1] The latter will be written as $e^{-i\mathbf{q}\cdot\mathcal{S}^{-1}\mathbf{R}_{\bar{\nu}}}$.

where the $\pm$ sign holds if $\tau(\mathcal{S}) = 0$ or $\tau(\mathcal{S}) = 1$, respectively. Passing to the periodic parts of the response, we have:

$$\begin{aligned}\frac{\widetilde{dn}^{\mathrm{NS}}(\{\mathcal{S}|\mathbf{f}\}\mathbf{r})}{du_{\bar{s}'\gamma}(\mathcal{S}\mathbf{q})} &= \frac{\widetilde{dn}^{\mathrm{NS}}(\{\mathcal{S}|\mathbf{f}\}\mathbf{r})}{du_{\bar{s}'\gamma}(\pm\mathbf{q}+\mathbf{G}_{\mathcal{S}})} \\ &= e^{-i\mathbf{G}_{\mathcal{S}}\cdot(\{\mathcal{S}|\mathbf{f}\}\mathbf{r})}\,\frac{\widetilde{dn}^{\mathrm{NS}}(\{\mathcal{S}|\mathbf{f}\}\mathbf{r})}{du_{\bar{s}'\gamma}(\pm\mathbf{q})} \\ &= e^{-i\mathcal{S}^{-1}\mathbf{G}_{\mathcal{S}}\cdot\mathbf{r}}\,e^{-i\mathbf{G}_{\mathcal{S}}\cdot\mathbf{f}}\,\frac{\widetilde{dn}^{\mathrm{NS}}(\{\mathcal{S}|\mathbf{f}\}\mathbf{r})}{du_{\bar{s}'\gamma}(\pm\mathbf{q})}.\end{aligned} \tag{I.12}$$

The vector $\mathcal{S}^{-1}\mathbf{G}_{\mathcal{S}}$ appearing in the first phase factor can be written in a more compact form. Starting from the $\tau(\mathcal{S}) = 0$ case, we write Eq. (I.9) for $\mathcal{S}^{-1}$:

$$\mathcal{S}^{-1}\mathbf{q} = \mathbf{q} + \mathbf{G}_{\mathcal{S}^{-1}}. \tag{I.13}$$

If we apply $\mathcal{S}^{-1}$ to both sides of Eq. (I.9), we get:

$$\mathcal{S}^{-1}\mathbf{q} = \mathbf{q} - \mathcal{S}^{-1}\mathbf{G}_{\mathcal{S}}, \tag{I.14}$$

which implies, by comparing with Eq. (I.13), $\mathcal{S}^{-1}\mathbf{G}_{\mathcal{S}} = -\mathbf{G}_{\mathcal{S}^{-1}}$. Applying the same procedure to Eq. (I.10), we get $\mathcal{S}^{-1}\mathbf{G}_{\mathcal{S}} = \mathbf{G}_{\mathcal{S}^{-1}}$ for the $\tau(\mathcal{S}) = 1$ case.

As a final step, we introduce Eq. (I.12) in the expression of the symmetrized induced charge density (Eq. (I.8)). After dropping the phase factor $e^{-i\mathbf{G}_{\mathcal{S}}\cdot(\mathbf{R}^{\mathcal{S}}_{s'}+\mathbf{f})}$, that is 1 because $\mathbf{R}^{\mathcal{S}}_{s'} + \mathbf{f} = \mathcal{S}\mathbf{R}_{\nu} - \mathbf{R}_{\bar{\nu}}$ is a direct lattice vector, Eq. (I.8) is finally written as:

$$\frac{\widetilde{dn}(\mathbf{r})}{du_{s'\beta}(\mathbf{q})} = \frac{1}{N_S}\sum_{\{\mathcal{S}|\mathbf{f}\}}\mathcal{O}_{\tau(\mathcal{S})}\left[\sum_{\gamma} S_{\gamma\beta}\frac{\widetilde{dn}^{\mathrm{NS}}(\{\mathcal{S}|\mathbf{f}\}\mathbf{r})}{du_{\bar{s}'\gamma}(\mathbf{q})}\,e^{i\mathbf{G}_{\mathcal{S}^{-1}}\cdot\mathbf{r}}\,e^{-i\mathbf{q}\cdot\mathbf{R}^{\mathcal{S}}_{s'}}\right], \tag{I.15}$$

where the operator $\mathcal{O}_{\tau(\mathcal{S})}$ is the identity if $\tau(\mathcal{S}) = 0$, or $\mathcal{O}_{\tau(\mathcal{S})} = \mathcal{K}$ if $\tau(\mathcal{S}) = 1$.

The induced magnetization density can be symmetrized in a similar way. Starting from the derivative of Eq. (1.85) with respect to $u_{\nu s'\beta}$ and following the steps described in detail above for the charge density response, we reach the final result:

$$\frac{\widetilde{dm}_{\delta}(\mathbf{r})}{du_{s'\beta}(\mathbf{q})} = \frac{1}{N_S}\sum_{\{\mathcal{S}|\mathbf{f}\}}(-1)^{\tau(\mathcal{S})}\,\mathcal{O}_{\tau(\mathcal{S})}\left[\sum_{\gamma\eta}\tilde{S}^{-1}_{\delta\eta}\,S_{\gamma\beta}\,\frac{\widetilde{dm}^{\mathrm{NS}}_{\eta}(\{\mathcal{S}|\mathbf{f}\}\mathbf{r})}{du_{\bar{s}'\gamma}(\mathbf{q})}\,e^{i\mathbf{G}_{\mathcal{S}^{-1}}\cdot\mathbf{r}}\,e^{-i\mathbf{q}\cdot\mathbf{R}^{\mathcal{S}}_{s'}}\right]. \tag{I.16}$$

I.2 Dynamical matrix

The dynamical matrix can be symmetrized with an approach similar to the one described above. We start from the total energy of the system perturbed by the atomic displacements $u_{\nu s'\beta}$. If we consider the second-order derivatives of the total energy with respect to $\mathbf{u}$ (computed at $\mathbf{u} = \mathbf{0}$), exploit the chain rule and make use of Eq. (I.2), similarly to what done for the induced charge density, we can write:

$$\frac{d^2E_{\mathrm{tot}}}{du_{\mu s\alpha}du_{\nu s'\beta}} = \frac{1}{N_S}\sum_{\{\mathcal{S}|\mathbf{f}\}}\sum_{\gamma\delta}S_{\gamma\alpha}\,S_{\delta\beta}\,\frac{d^2E^{\mathrm{NS}}_{\mathrm{tot}}}{du_{\bar{\mu}\bar{s}\gamma}du_{\bar{\nu}\bar{s}'\delta}}, \tag{I.17}$$

where we introduced the non-symmetrized second-order energy derivative, obtained by summing over the IBZ in all the expressions that include a sum over $\mathbf{k}$. In order to extend Eq. (I.17) to the dynamical matrix, we multiply both sides by the factors $e^{-i\mathbf{q}\cdot\mathbf{R}_\mu}$, $e^{i\mathbf{q}\cdot\mathbf{R}_\nu}$, and $1/N$, where N is the number of unit cells in the solid, and we sum over μ and ν. Moreover, in the right-hand side we insert the phase factors $e^{-i\mathcal{S}\mathbf{q}\cdot\mathbf{R}_{\bar{\mu}}}$ and $e^{i\mathcal{S}\mathbf{q}\cdot\mathbf{R}_{\bar{\nu}}}$ and we sum over $\bar{\mu}$ and $\bar{\nu}$. As a result:

$$\Phi^{\,s\alpha}_{\,s'\beta}(\mathbf{q}) = \frac{1}{N_S}\frac{1}{N^3}\sum_{\{\mathcal{S}|\mathbf{f}\}}\sum_{\mu\bar{\mu}}\sum_{\nu\bar{\nu}}\sum_{\gamma\delta}\left[S_{\gamma\alpha}\,S_{\delta\beta}\,e^{-i\mathcal{S}\mathbf{q}\cdot\mathbf{R}_{\bar{\mu}}}\,\frac{d^2E^{\mathrm{NS}}_{\mathrm{tot}}}{du_{\bar{\mu}\bar{s}\gamma}du_{\bar{\nu}\bar{s}'\delta}}\,e^{i\mathcal{S}\mathbf{q}\cdot\mathbf{R}_{\bar{\nu}}}\,e^{-i\mathbf{q}\cdot(\mathbf{R}_\mu-\mathcal{S}^{-1}\mathbf{R}_{\bar{\mu}})}\right.$$
$$\left.\times\, e^{i\mathbf{q}\cdot(\mathbf{R}_\nu-\mathcal{S}^{-1}\mathbf{R}_{\bar{\nu}})}\right] \tag{I.18}$$

From Eq. (I.5) (and a similar one for $\mathbf{R}_\nu-\mathcal{S}^{-1}\mathbf{R}_{\bar{\nu}}$), it follows that the phase factors appearing in the right-hand side do not depend on μ and ν, hence the sums over μ and ν give a factor N^2. By further introducing the vectors $\mathbf{R}^{\mathcal{S}}_s$ (already defined above) and, in a similar way, $\mathbf{R}^{\mathcal{S}}_{s'}$, Eq. (I.18) becomes:

$$\Phi^{\,s\alpha}_{\,s'\beta}(\mathbf{q}) = \frac{1}{N_S}\sum_{\{\mathcal{S}|\mathbf{f}\}}\sum_{\gamma\delta}S_{\gamma\alpha}\,S_{\delta\beta}\left[\frac{1}{N}\sum_{\bar{\mu}\bar{\nu}}e^{-i\mathcal{S}\mathbf{q}\cdot\mathbf{R}_{\bar{\mu}}}\,\frac{d^2E^{\mathrm{NS}}_{\mathrm{tot}}}{du_{\bar{\mu}\bar{s}\gamma}du_{\bar{\nu}\bar{s}'\delta}}\,e^{i\mathcal{S}\mathbf{q}\cdot\mathbf{R}_{\bar{\nu}}}\right]e^{i\mathcal{S}\mathbf{q}\cdot(\mathbf{R}^{\mathcal{S}}_s-\mathbf{R}^{\mathcal{S}}_{s'})}. \tag{I.19}$$

The quantity inside the square brackets is the non-symmetrized dynamical matrix at wave vector $\mathcal{S}\mathbf{q}$. We consider only the symmetry operations of the antiunitary small group of $\mathbf{q}$ and we distinguish the two cases represented by Eqs. (I.9) and (I.10). Moreover, we exploit the property $\Phi(-\mathbf{q}) = \Phi^*(\mathbf{q})$, following from the definition of the dynamical matrix, and we introduce the operator $\mathcal{O}_{\tau(\mathcal{S})}$ to get the final result mentioned in Section 3.4:

$$\Phi^{\,s\alpha}_{\,s'\beta}(\mathbf{q}) = \frac{1}{N_S}\sum_{\{\mathcal{S}|\mathbf{f}\}}\mathcal{O}_{\tau(\mathcal{S})}\left[\sum_{\gamma\delta}S_{\gamma\alpha}\,S_{\delta\beta}\,\Phi^{\mathrm{NS}}_{\bar{s}\gamma\,\bar{s}'\delta}(\mathbf{q})\,e^{i\mathbf{q}\cdot(\mathbf{R}^{\mathcal{S}}_s-\mathbf{R}^{\mathcal{S}}_{s'})}\right]. \tag{I.20}$$

Bibliography

[1] P. Pyykkö, Chem. Rev. **88**, 563-594 (1988).

[2] I. Žutić, J. Fabian, and S. Das Sarma, Rev. Mod. Phys. **76**, 323 (2004).

[3] A. Hirohata, K. Yamada, Y. Nakatani, L. Prejbeanu, B. Diény, P. Pirro, and B. Hillebrands, J. Magn. Magn. Mater. **509**, 166711 (2020).

[4] A. Manchon, J. Železný, I. M. Miron, T. Jungwirth, J. Sinova, A. Thiaville, K. Garello, and P. Gambardella, Rev. Mod. Phys. **91**, 035004 (2019).

[5] Y.A. Bychkov, E.I. Rashba, JETP Lett. **39**, 78 (1984).

[6] M. I. Dyakonov and V. I. Perel, J. Exp. Theor. Phys. Lett. **13**, 467 (1971).

[7] J. E. Hirsch, Phys. Rev. Lett. **83**, 1834 (1999).

[8] J. Sinova, S. O. Valenzuela, J. Wunderlich, C.H. Back, and T. Jungwirth, Rev. Mod. Phys. **87**, 1213 (2015).

[9] A. Fert, N. Reyren, and V. Cros, Nat. Rev. Mater. **2**, 17031 (2017).

[10] J. E. Moore, Nature **464**, 194 (2010).

[11] M. Z. Hasan, J. E. Moore, Annu. Rev. Condens. Matter Phys., **2**, 55 (2011).

[12] Y. Ando, Journal of the Physical Society of Japan **82**, 102001 (2013).

[13] S. Chikazumi, Physics of Ferromagnetism. New York: Oxford University press Inc., 1997.

[14] P. A. M. Dirac, Proc. R. Soc. Lond. A **117**, 610 (1928).

[15] C. G. Darwin, Proc. R. Soc. London A **118**, 654 (1928).

[16] W. Gordon, Z. Phys. **48**, 11 (1928).

[17] R. D. Cowan and D. C. Griffin, J. Opt. Soc. Am. **66**, 1010 (1976).

[18] J. L. Schonfelder, Proc. Phys. Soc. **87**, 163 (1966).

[19] D. E. Ellis, J. Phys. B **10**, 1 (1977).

[20] D. E. Ellis, Int. J. Quantum Chem. **S11**, 201 (1977).

[21] L. D. Miller, Phys. Rev. A **7**, 1433 (1973).

[22] M. A. Coulthard, Proc. Phys. Soc. **90**, 615 (1967).

[23] M. A. Coulthard, Proc. Phys. Soc. **91**, 44 (1967).

[24] F. C. Smith and W. R. Johnson, Phys. Rev. **160**, 136 (1967).

[25] P. Pyykkö, Adv. Quantum Chem. **11**, 353 (1978).

[26] J. Callaway, R. D. Woods, and V. Sirounian, Phys. Rev. **107**, 934 (1957).

[27] F. Herman, C. D. Kuglin, K. F. Cuff, and R. L. Kortum, Phys. Rev. Lett. **11**, 541 (1963).

[28] L. E. Johnson, J. B. Conklin, and G. W. Pratt, Jr., Phys. Rev. Lett. **11**, 538 (1963).

[29] P. Soven, Phys. Rev. **137**, A1706 (1965).

[30] T. L. Loucks, Phys. Rev. **139**, A1333 (1965).

[31] Y. Onodera and M. Okazaki, J. Phys. Soc. Jpn. **21**, 1273 (1966).

[32] Y. Onodera and M. Okazaki, J. Phys. Soc. Jpn. **21**, 2400 (1966).

[33] A. O. E. Animalu, Philos. Mag. **13**, 53 (1966).

[34] P. Hohenberg and W. Kohn, Phys. Rev. **136**, B864 (1964).

[35] W. Kohn and L. J. Sham, Phys. Rev. **140**, A1133 (1965).

[36] A. H. MacDonald and S. H. Vosko, J. Phys. C **12**, 2977 (1979).

[37] L. Kleinman, Phys. Rev. B **21**, 2630 (1980).

[38] L. A. Hemstreet, C. Y. Fong, J. S. Nelson, Phys. Rev. B **47**, 4238 (1993).

[39] G. Theurich and N. A. Hill, Phys. Rev. B **64**, 073106 (2001).

[40] A. Dal Corso and A. M. Conte, Phys. Rev. B **71**, 115106 (2005).

[41] K. Kunc, *Recent results in semiconductor dynamics by ab initio 'direct' approach.* In Electronic Structure, dynamics, and quantum structural properties of condensed matter. J. T. Devreese and P. van Camp eds., NATO ASI, Series B, 121. Plenum Press, New York, 1985.

[42] S. Baroni, P. Giannozzi, and A. Testa, Phys. Rev. Lett. **58**, 1861 (1987).

[43] S. Baroni, S. de Gironcoli, A. Dal Corso, and P. Giannozzi, Rev. Mod. Phys. **73**, 515 (2001).

[44] P. Giannozzi, S. de Gironcoli, P. Pavone, and S. Baroni, Phys. Rev. B **43**, 7231 (1991).

[45] S. de Gironcoli, Phys. Rev. B **51**, 6773 (1995).

[46] A. Dal Corso, A. Pasquarello, and A. Baldereschi, Phys. Rev. B **56**, R11369(R) (1997).

[47] A. Dal Corso, Phys. Rev. B **64**, 235118 (2001).

[48] A. Dal Corso, Phys. Rev. B **81**, 075123 (2010).

[49] A. Dal Corso, Phys. Rev. B **76**, 054308 (2007).

[50] I. Timrov, N. Vast, R. Gebauer, and S. Baroni, Comput. Phys. Commun. **196**, 460 (2015).

[51] K. Cao, H. Lambert, P. G. Radaelli, and F. Giustino, Phys. Rev. B **97**, 024420 (2018).

[52] T. Gorni, I. Timrov, and S. Baroni, Eur. Phys. J. B **91**, 249 (2018).

[53] A. Smogunov, A. Dal Corso, A. Delin, R. Weht, and E. Tosatti, Nature Nanotechnology **3**, 22 (2008).

[54] D. M. Ceperley and B. J. Alder, Phys. Rev. Lett. **45**, 566 (1980).

[55] S. H. Vosko, L. Wilk, and M. Nusair, Can. J. Phys., **58**, 1200 (1980).

[56] J. P. Perdew and A. Zunger, Phys. Rev. B **23**, 5048 (1981).

[57] L. A. Cole and J. P. Perdew, Phys. Rev. A **25**, 1265 (1982).

[58] R.O. Jones and O. Gunnarsson, Rev. Mod. Phys. **61**, 689 (1989).

[59] J. P. Perdew, Phys. Rev. B, **33**, 8822 (1986).

[60] J. P. Perdew and Y. Wang, Phys. Rev. B **33**, 8800 (1986).

[61] A. D. Becke, Phys. Rev. A **38**, 3098 (1988).

[62] C. Lee, W. Yang, and R. G. Parr, Phys. Rev. B **37**, 785 (1988).

[63] J. P. Perdew and Y. Wang, Phys. Rev. B **45**, 13244 (1992).

[64] J. P. Perdew, J. A. Chevary, S. H. Vosko, K. A. Jackson, M. R. Pederson, D. J. Singh, and C. Fiolhais, Phys. Rev. B **46**, 6671 (1992).

[65] J. P. Perdew, K. Burke, and M. Ernzerhof, Phys. Rev. Lett. **77**, 3865 (1996).

[66] J. P. Perdew, A. Ruzsinszky, G. I. Csonka, O. A. Vydrov, G. E. Scuseria, L. A. Constantin, X. Zhou, and K. Burke, Phys. Rev. Lett. **100**, 136406 (2008).

[67] U. von Barth and L. Hedin, J. Phys. C: Solid State Phys. **5**, 1629 (1972).

[68] H. Hellmann, *Einjuhrung in die Quantenchemie* p. 285, Franz Deuticke, Leipzig, 1937.

[69] R. P. Feynman, Phys. Rev. **56**, 340 (1939).

[70] C. -L. Fu and K. -M. Ho, Phys. Rev. B **28**, 5480 (1983).

[71] M. Methfessel and A. T. Paxton, Phys. Rev. B **40**, 3616 (1989).

[72] N. Marzari, D. Vanderbilt, A. De Vita, and M. C. Payne, Phys. Rev. Lett. **82**, 3296 (1999).

[73] R. M. Wentzcovitch, J. L. Martins, and P. B. Allen, Phys. Rev. B **45**, 11372 (1992).

[74] J. Monkhorst and J.D. Pack, Phys. Rev. B **13**, 5188 (1976).

[75] C. Herring, Phys. Rev. **57**, 1169 (1940).

[76] J. C. Phillips and L. Kleinman, Phys. Rev. **116**, 287 (1959).

[77] G. P. Kerker, J. Phys. C: Solid St. Phys. **13**, L189 (1980).

[78] N. Troullier and J. M. Martins, Phys. Rev. B **43**, 1993 (1991).

[79] N. Troullier and J. M. Martins, Phys. Rev. B **43**, 8861 (1991).

[80] A. M. Rappe, K. Rabe, E. Kaxiras, and J. D. Joannopoulos, Phys. Rev. B **41**, 1227 (1990).

[81] D. R. Hamann, M. Schlüter, and C. Chiang, Phys. Rev. Lett. **43**, 1494 (1979).

[82] L. Kleinman and D. M. Bylander, Phys. Rev. Lett. **48**, 1425 (1982).

[83] D. Vanderbilt, Phys. Rev. B **41**, 7892(R) (1990).

[84] K. Laasonen, A. Pasquarello, R. Car, C. Lee, and D. Vanderbilt, Phys. Rev. B **47**, 10142 (1993).

[85] P. E. Blöchl, Phys. Rev. B **50**, 17953 (1994).

[86] G. Kresse and D. Joubert, Phys. Rev. B **59**, 1758 (1999).

[87] D. F. Mayers, Proc. R. Soc. London, Ser. A, **A241**, 93 (1957).

[88] R. G. Boyd, A. C. Larson, and J. T. Waber, Phys. Rev. **129**, 1629 (1963).

[89] P. Pyykkö and J. P. Desclaux, Acc. Chem. Res. **12**, 276 (1979).

[90] P. Romaniello and P. L. de Boeij, J. Chem. Phys. **122**, 164303 (2005).

[91] P. Romaniello and P. L. de Boeij, J. Chem. Phys. **127**, 174111 (2007).

[92] P. Pyykkö, J. G. Snijders, and E. J. Baerends, Chem. Phys. Lett. **83**, 432 (1981).

[93] D. D. Koelling and B. N. Harmon, J. Phys. C: Solid State Phys. **10** 3107 (1977).

[94] G. B. Bachelet and M. Schlüter, Phys. Rev. B **25**, 2103 (1982).

[95] A. Zangwill, *Physics at Surfaces*, Cambridge University Press, 1988.

[96] G. Nicolay, F. Reinert, S. Hüfner, Phys. Rev. B **65**, 033407 (2001).

[97] J. Henk, A. Ernst, P. Bruno, Surf. Sci. **566-568**, 482 (2004).

[98] J. Henk, M. Hoesch, J. Osterwalder, A. Ernst, P. Bruno, J. Phys. Condens. Matter **16**, 7581-7597 (2004).

[99] R. Mazzarello, A. Dal Corso, E. Tosatti, Surf. Sci. **602**, 893 (2008).

[100] S. Bornemann, O. Šipr, S. Mankovsky, S. Polesya, J. B. Staunton, W. Wurth, H. Ebert, J. Minár, Phys. Rev. B **86**, 104436 (2012).

[101] R. Requist, Polina M. Sheverdyaeva, Paolo Moras, Sanjoy K. Mahatha, Carlo Carbone, Erio Tosatti, Phys. Rev. B **91**, 045432 (2015).

[102] A. Dal Corso, Surf. Sci. **637-638**, 106 (2015).

[103] A. Urru and A. Dal Corso, Surf. Sci. **671**, 17 (2018).

[104] S. Hüfner, *Photoelectron Spectroscopy*, 3rd ed., Springer, Berlin, 2003.

[105] S. LaShell, B. A. McDougall, E. Jensen, Phys. Rev. Lett. **77**, 3419 (1996).

[106] F. Reinert, G. Nicolay, S. Schmidt, D. Ehm, S. Hüfner, Phys. Rev. B **63**, 115415 (2001).

[107] W. Di, K.E. Smith, S.D. Kevan, Phys. Rev. B **45**, 3652 (1992).

[108] A. Ramstad, S. Raaen, N. Barrett, Surf. Sci. **448**, 179 (2000).

[109] J. Wiebe, F. Meier, K. Hashimoto, G. Bihlmayer, S. Blügel, P. Ferriani, S. Heinze, R. Wiesendanger, Phys. Rev. B **72**, 193406 (2005).

[110] E. Frantzeskakis, S. Pons, A. Crepaldi, H. Brune, K. Kern, M. Grioni, Phys. Rev. B **84**, 245443 (2011).

[111] I. Pletikosić, M. Kralj, D. Šokčević, R. Brako, P. Lazić, P. Pervan, J. Phys. Condens. Matter **22**, 135006 (2010).

[112] A. Varykhalov, D. Marchenko, M.R. Scholz, E.D.L. Rienks, T.K. Kim, G. Bihlmayer, J. Sánchez-Barriga, Phys. Rev. Lett. **108**, 066804 (2012).

[113] E. Starodub, A. Bostwick, L. Moreschini, S. Nie, F. El Gabaly, K.F. McCarty, E. Rotenberg, Phys. Rev. B **83**, 125428 (2011).

[114] V. Pallassana, M. Neurock, L. B. Hansen, B. Hammer, J. K. Nørskov, Phys. Rev. B **60**, 6146 (1999).

[115] E. Miniussi, E. R. Hernández, M. Pozzo, A. Baraldi, E. Vesselli, G. Comelli, S. Lizzit, D. Alfé, J. Phys. Chem. C **116**, 23297 (2012).

[116] J. Ontaneda, R. A. Bennett, R. Grau-Crespo, J. Phys. Chem. C **119**, 23436 (2015).

[117] H. Kim, A. Palacio-Morales, T. Posske, L. Rózsa, K. Palotás, L. Szunyogh, M. Thorwart, and R. Wiesendanger, Sci. Adv. **4**, eaar5251 (2018).

[118] N. H. Long, P. Mavropoulos, B. Zimmermann, D. S. G. Bauer, S. Blügel, and Y. Mokrousov, Phys. Rev. B **90**, 064406 (2014).

[119] P. Giannozzi, S. Baroni, N. Bonini, M. Calandra, R. Car, C. Cavazzoni, D. Ceresoli, G. L. Chiarotti, M. Cococcioni, I. Dabo, et al., J. Phys. Condens. Matter **21**, 395502 (2009) (See `http://www.quantum-espresso.org`).

[120] P. Giannozzi, O. Andreussi, T. Brumme, O. Bunau, M. B. Nardelli, M. Calandra, R. Car, C. Cavazzoni, D. Ceresoli, M. Cococcioni, et al., J. Phys. Condens. Matter **29**, 465901 (2017).

[121] P. Giannozzi, O. Baseggio, P. Bonfá, D. Brunato, R. Car, I. Carnimeo, C. Cavazzoni, S. de Gironcoli, P. Delugas, F. Ferrari Ruffino, J. Chem. Phys. **152**, 154105 (2020).

[122] A. Dal Corso, Phys. Rev. B **82**, 075116 (2010).

[123] A. Dal Corso, Comp. Mat. Sci. **95**, 337 (2014).

[124] R. W. G. Wyckoff, Crystal Structures, John Wiley & Sons, Inc. (Wiley, New York, 1963), Volume 1, 7-83.

[125] T. Oguchi, T. Shishidou, J. Phys. Condens. Matter **21**, 092001 (2009).

[126] H. Bentmann, T. Kuzumaki, G. Bihlmayer, S. Blügel, E. V. Chulkov, F. Reinert, and K. Sakamoto, Phys. Rev. B **84**, 115426 (2011).

[127] A. Dal Corso, J. Phys. Condens. Matter **20**, 445202 (2008).

[128] A. Urru and A. Dal Corso, Phys. Rev. B **100**, 045115 (2019).

[129] K. Konishi and G. Paffuti, *Quantum Mechanics: A New Introduction*. Oxford University Press, 2009.

[130] R. J. Birgeneau, J. Cordes, G. Dolling, and A. D. B. Woods, Phys. Rev. **136**, A1359 (1964).

[131] A. Dal Corso, J. Phys. Condens. Matter **25**, 145401 (2013).

[132] A. Smogunov, A. Dal Corso, and E. Tosatti, Phys. Rev. B **78** 014423 (2008).

[133] D. J. Sellmyer, B. Balamurugan, W. Y. Zhang, B. Das, R. Skomski, P. Kharel, and Y. Liu, Advances in Rare-Earth-Free Permanent Magnets. In: Marquis F. (eds) Proceedings of the 8th Pacific Rim International Congress on Advanced Materials and Processing. Springer, Cham (2013).

[134] J. Cui, M. Kramer, L. Zhou, F. Liu, A. Gabay, G. Hadjipanayis, B. Balasubramanian, D. Sellmyer, Acta Materialia **158**, 118 (2018).

[135] C. Guillaud, J. Phys. Radium **12**, 143 (1951).

[136] B. W. Roberts, Phys. Rev. **104**, 607 (1956).

[137] J. B. Yang, K. Kamaraju, W. B. Yelon, and W. J. James, Appl. Phys. Lett. **79**, 1846 (2001).

[138] M. A. McGuire, H. Cao, B. C. Chakoumakos, and B. C. Sales, Phys. Rev. B **90**, 174425 (2014).

[139] A. F. Andresen, W. Hälg, P. Fischer, and E. Stoll, Acta Chem. Scand. **21**, 1543 (1967).

[140] T. Chen, J. Appl. Phys. **45**, 2358 (1974).

[141] K. V. Shanavas, D. Parker, and D. J. Singh, Sci. Reports **4**, 7222 (2014).

[142] C. Guillaud, J. Phys. Radium **12**, 492 (1951).

[143] W. E. Stutius, T. Chen, and T. R. Sandin, Magnetism and magnetic materials - 1973: Nineteenth Annual Conference (1974).

[144] T. Hihara and Y. K$\bar{o}$i, J. Phys. Soc. Jpn. **29**, 343 (1970).

[145] J. B. Yang, W. B. Yelon, W. J. James, Q. Cai, M. Kornecki, S. Roy, N. Ali, and Ph. l'Heritier, J. Phys.: Condens. Matter **14**, 6509 (2002).

[146] J. B. Yang, Y. B. Yang, X. G. Chen, X. B. Ma, J. Z. Han, Y. C. Yang, S. Guo, A. R. Yan, Q. Z. Huang, M. M. Wu et al., Appl. Phys. Lett. **99**, 082505 (2011)

[147] K. Koyama, Y. Mitsui, and K. Watanabe, Sci. Technol. Adv. Mater. **9**, 024204 (2008).

[148] N. A. Zarkevich, L.L. Wang, and D. D. Johnson, APL Mater. **2**, 032103 (2014).

[149] V. P. Antropov, V. N. Antonov, L. V. Bekenov, A. Kutepov, and G. Kotliar, Phys. Rev. B **90** 054404 (2014).

[150] A. Urru and A. Dal Corso, Phys. Rev. B **100**, 045115 (2019).

[151] F. Körmann, A. Dick, B. Grabowski, B. Hallstedt, T. Hickel, and J. Neugebauer, Phys. Rev. B **78**, 033102 (2008).

[152] J. B. Staunton, S. Ostanin, S. S. A. Razee, B. L. Gyorffy, L. Szunyogh, B. Ginatempo, and E. Bruno, Phys. Rev. Lett. **93**, 257204 (2004).

[153] F. Körmann, A. Dick, B. Grabowski, T. Hickel, and J. Neugebauer, Phys. Rev. B **85**, 125104 (2012).

[154] J. Hellsvik, D. Thonig, K. Modin, D. Iusan, A. Bergman, O. Eriksson, L. Bergqvist, and A. Delin, Phys. Rev B **99**, 104302 (2019).

[155] R. Resta, Phys. Rev. B **84**, 214428 (2011).

[156] D. Vanderbilt, *Berry phases in electronic structure theory*, Cambridge University Press, 2018.

[157] M. Fiebig, J. Phys. D **38**, R123 (2005).

[158] J. P. Rivera, Eur. Phys. J. B **71**, 299 (2009).

[159] D. N. Astrov, Sov. Phys. JETP **13**, 729 (1961).

[160] G. T. Rado and V. J. Folen, Phys. Rev. Lett. **7**, 310 (1961).

[161] V. J. Folen, G. T. Rado, and E. W. Stalder, Phys. Rev. Lett. **6**, 607 (1961).

[162] J. P. Rivera, Ferroelectrics **161**, 165 (1994).

[163] J. Íñiguez, Phys. Rev. Lett. **101**, 117201 (2008).

[164] E. Bousquet, N. A. Spaldin, and K. T. Delaney, Phys. Rev. Lett. **106**, 107202 (2011).

[165] M. Ye and D. Vanderbilt, Phys. Rev. B **89**, 064301 (2014).

[166] C. Cohen-Tannoudji, B. Diu, and F. Laloe, *Quantum Mechanics*, John Wiley & Sons Inc. (Wiley, New York, 1996), Volumes 1-2.

[167] B. H. Bransden and C. J. Joachain, *Physics of Atoms and Molecules*, 2nd ed., Prentice Hall, Englewood Cliffs, NJ, 2003.

[168] F. Schwabl, *Quantum Mechanics*, 3rd ed., Springer, Berlin, 2002.

[169] S. K. Kim, *Group Theoretical Methods*, Cambridge University Press, 1999.